

DISSERTATION

ZUR

ERLANGUNG DER DOKTORWÜRDE (DR. RER. NAT.)

DER

GESAMTFAKULTÄT FÜR

MATHEMATIK, INGENIEUR- UND NATURWISSENSCHAFTEN

DER

RUPRECHT-KARLS-UNIVERSITÄT HEIDELBERG

VORGELEGT VON

NICOLAS FREDERIC ZORN

GEBOREN IN ESSLINGEN AM NECKAR

TAG DER MÜNDLICHEN PRÜFUNG

05.05.2023

CHARGE TRANSPORT IN
AND LUMINESCENCE FROM
COVALENTLY FUNCTIONALIZED
CARBON NANOTUBE NETWORKS

GUTACHTER

PROF. DR. JANA ZAUMSEIL

PROF. DR. RALPH KRUPKE

Abstract

Their high ambipolar charge carrier mobilities and narrowband emission in the near-infrared make semiconducting single-walled carbon nanotubes (SWCNTs) a promising material for optoelectronic devices. The controlled low-level decoration of SWCNTs with covalently bound sp^3 defects gives rise to red-shifted luminescence and single-photon emission, thus strongly expanding their application potential. While the spectroscopic properties of sp^3 -functionalized SWCNT dispersions under optical excitation are already well-understood, little research efforts have been directed at the impact of luminescent defects on charge transport as well as defect population and emission in thin films and under electrical excitation. A fundamental understanding of these aspects is a prerequisite for the realization of light-emitting devices based on functionalized SWCNTs.

This thesis demonstrates high ambipolar charge carrier mobilities and red-shifted defect-state electroluminescence in light-emitting field-effect transistors with randomly oriented networks of functionalized SWCNTs as active layers. The results imply that luminescent defects act as shallow trapping potentials for charge carriers that still allow for fast detrapping at room temperature, thus explaining the moderate decrease in network mobilities upon functionalization. Time-resolved terahertz spectroscopy corroborates the impact of these defects on the intrinsic nanotube conductivity and provides further evidence that charge transport in semiconducting SWCNT networks, as opposed to the widespread belief, is not solely determined by the inter-nanotube junctions.

To achieve better control over the spectroscopic properties of SWCNT thin films deposited on surfaces, substrate passivation with a cross-linked polymer is demonstrated to reduce peak broadening and suppress sideband emission that is assigned to the uncontrolled formation of lattice defects through nanotube–substrate interactions. The realization of pristine and sp^3 -functionalized SWCNT network transistors with near-intrinsic electroluminescence on passivated substrates showcases the compatibility of the developed method with standard semiconductor processing steps and device fabrication. Moreover, the selective introduction of luminescent defects with a larger spectral red-shift pushes the electroluminescence from SWCNT networks further towards telecommunication wavelengths and highlights their potential for optoelectronic applications such as electrically-pumped single-photon sources.

Kurzfassung

Ihre hohen ambipolaren Ladungsträgerbeweglichkeiten und schmalbandige Emission im nahen Infrarotbereich machen halbleitende einwandige Kohlenstoffnanoröhren (engl. *single-walled carbon nanotubes*, SWCNTs) zu einem vielversprechenden Material für optoelektronische Bauelemente. Die kontrollierte Einführung einer geringen Anzahl an kovalent gebundenen sp^3 -Defekten in SWCNTs führt zu rotverschobener Lumineszenz und Einzelphotonenemission und vergrößert damit die Bandbreite der potentiellen Anwendungen. Mittlerweile sind die spektroskopischen Eigenschaften von sp^3 -funktionalisierten SWCNTs in Dispersion und unter optischer Anregung gut verstanden, wohingegen der Einfluss der lumineszenten Defekte auf den Ladungstransport sowie die Defektemission in dünnen Filmen und bei elektrischer Anregung bislang wenig untersucht wurden. Ein tiefgreifendes Verständnis dieser Aspekte ist die Voraussetzung für die Realisierung von lichtemittierenden Bauelementen basierend auf funktionalisierten SWCNTs.

Diese Arbeit zeigt erstmals hohe ambipolare Ladungsträgerbeweglichkeiten und rotverschobene Elektrolumineszenz von Defektzuständen in leuchtenden Feldeffekttransistoren mit Netzwerken funktionalisierter SWCNTs als aktiver Schicht. Die Ergebnisse deuten darauf hin, dass lumineszente Defekte flache Fallenzustände für Ladungsträger darstellen, aus denen die Ladungen bei Raumtemperatur jedoch leicht wieder entkommen können. Dadurch lässt sich auch die geringfügige Änderung der Beweglichkeiten durch die Funktionalisierung erklären. Untersuchungen mittels zeitaufgelöster Terahertz-Spektroskopie bestätigen den direkten Einfluss der Defekte auf die intrinsische Leitfähigkeit der Nanoröhren und liefern Hinweise darauf, dass der Ladungstransport in halbleitenden SWCNT-Netzwerken entgegen der weitverbreiteten Annahme nicht ausschließlich durch den Ladungsübertrag zwischen einzelnen Nanoröhren bestimmt ist.

Im Hinblick auf eine bessere Kontrolle der spektroskopischen Eigenschaften von dünnen SWCNT-Filmen auf Substraten wird eine Methode zur Oberflächenpassivierung mittels eines quervernetzten Polymers eingeführt. Diese Passivierung verringert die Verbreiterung der Emissionsbande der SWCNTs und unterdrückt die Lumineszenz einer rotverschobenen Seitenbande, welche durch die unkontrollierten Einführung von Defekten aufgrund von Wechselwirkungen zwischen den Nanoröhren und der Substratoberfläche verursacht wird. Der Nach-

weis nahezu intrinsischer Elektrolumineszenzspektren von Transistoren sowohl mit unbehandelten als auch mit funktionalisierten SWCNT-Netzwerken auf passivierten Substraten stellt die Kompatibilität der entwickelten Methode mit standardmäßigen Prozessierungsschritten in der Halbleitertechnik und der Bauelementherstellung unter Beweis. Des Weiteren führt die selektive Einführung strahlender Defekte mit einer größeren spektralen Rotverschiebung zu Elektrolumineszenz von SWCNT-Netzwerken nahe des Telekommunikationswellenlängenbereichs und unterstreicht damit deren Potenzial für optoelektronische Anwendungen wie beispielsweise elektrisch gepumpte Einzelphotonenquellen.

Danksagung

Diese Dissertation wäre nicht möglich gewesen ohne die Unterstützung vieler Personen, denen ich an dieser Stelle danken möchte.

Zuallererst möchte ich mich bei **Prof. Dr. Jana Zaumseil** für die Möglichkeit bedanken, meine Doktorarbeit in ihrer Arbeitsgruppe zu solch einem spannenden und interdisziplinären Thema anfertigen zu können und meine Ergebnisse auf diversen internationalen Konferenzen präsentieren zu dürfen. Danke für das in mich gesetzte Vertrauen, die frühe Übertragung von Verantwortung, die Einbindung in viele verschiedene Projekte und internationale Kooperationen, Deinen fachlichen Rat, Deine Bereitschaft für Diskussionen, sowie für alles, was Du mir in den letzten Jahren beigebracht hast.

Ganz herzlich möchte ich mich auch bei **Prof. Dr. Ralph Krupke** für die bereitwillige Übernahme des Zweitgutachtens bedanken.

Allen derzeitigen und ehemaligen Kolleginnen und Kollegen der **Nanomaterials for Optoelectronics** und **Physical Chemistry of Layered Nanomaterials** Forschungsgruppen danke ich für die angenehme Arbeitsatmosphäre, die Hilfsbereitschaft, den Einsatz bei der Betreuung und Reparatur von Geräten und Messaufbauten, sowie die gute Zeit bei und außerhalb der Arbeit und auf Konferenzen. Besonders hervorheben möchte ich dabei das **TRIFECTs Team**. Mit Euch zu arbeiten hat mir immer großen Spaß bereitet, und unsere gute Zusammenarbeit und der ständige Austausch von Ideen haben viele unserer Errungenschaften erst möglich gemacht. Außerdem danke ich der **SFM Crew**, die durch den niemals endenden Nachschub an selektierten Nanoröhren die Arbeit wesentlich erleichtert hat.

Ein großer Dank gilt **Constantin Tormann, Christoph Bendel, und Finn Sebastian**, die ich während ihrer Abschlussarbeiten oder Praktika betreuen durfte. Ich habe dabei selbst viel dazugelernt, und ich danke Euch für Eure tolle Arbeit, Eure Motivation, und die lustige Zeit im Labor.

Bedanken möchte ich mich auch bei allen externen **Kooperationspartnern**, mit denen ich im Laufe meiner Promotion zusammenarbeiten durfte. Ein besonderer Dank gilt hierbei denjenigen, die mich im Rahmen von Forschungsaufenthalten in ihre Labore eingeladen und mir dabei detailliertes Wissen vermittelt, neue Methoden beigebracht, sowie tolle persönliche

Erfahrungen ermöglicht haben: **Dr. Yuichiro Kato**, **Dr. Daiki Yamashita**, und **Dr. Keigo Otsuka** am RIKEN in Wako, Japan, sowie **Dr. Hai Wang** und **Wenhao Zheng** am Max-Planck-Institut für Polymerforschung in Mainz. Des Weiteren danke ich **Prof. Dr. Alexander Högele** (Ludwig-Maximilians-Universität München) und **Dr. Benjamin Flavel** (Karlsruher Institut für Technologie) sowie deren Mitarbeitern für ihre Beiträge zu dieser Arbeit, sowie **Dr. Mario Caironi** (Istituto Italiano di Tecnologia, Mailand, Italien) für hilfreiche Diskussionen zu Modulationsspektroskopie und viele Folgeprojekte zu meiner Masterarbeit.

Darüber hinaus gilt mein Dank allen Mitarbeiterinnen und Mitarbeitern des Lehrstuhls für Angewandte Physikalische Chemie für die unkomplizierte Zusammenarbeit und tatkräftige Unterstützung bei Problemen jeglicher Art: **Günter Meinus**, **Peter Jeschka**, und die Mitarbeiter der **Feinmechanikwerkstatt** für die unschätzbare Hilfe bei technischen Fragen, sowie **Swetlana Duchnay**, **Isabella Haffelder**, **Anja Ihli**, **Karin Jordan**, und **Benjamin Scherke** für die Unterstützung bei administrativen Angelegenheiten.

Die Promotion und das Studium waren eine unglaublich spannende und herausfordernde Zeit und ich bin dankbar für die dabei entstandenen Freundschaften, die zu tollen Erlebnissen geführt und vieles vereinfacht haben. Insbesondere danke ich **Alex**, **Moritz**, **Franzi**, **Sonja**, **Marvin**, **Sara**, **Max**, und **Marc**, und ich hoffe, dass wir auch weiterhin in Kontakt bleiben. Außerdem danke ich **Jule** und **Joris** für die Ablenkung und die mittlerweile traditionellen gemeinsamen Jahreswechsel.

Ein ganz besonderer Dank geht an meine Eltern **Carola** und **Stefan**, meine Schwestern **Isabel** und **Katharina**, und meine Großeltern. Danke, dass Ihr mir meinen bisherigen Weg ermöglicht habt und immer für mich da seid. Mein größter Dank gilt meiner Freundin **Lina** für ihren Rückhalt. Danke für Deine unermüdliche Unterstützung und unsere schöne gemeinsame Zeit, und ich freue mich auf das, was vor uns liegt.

Contents

Abstract	i
Kurzfassung	iii
Danksagung	v
Abbreviations	xi
1 Introduction	1
2 Theoretical Background	5
2.1 Single-walled carbon nanotubes	6
2.1.1 Structure and synthesis	6
2.1.2 Purification and sorting	8
2.1.3 Electronic structure	10
2.1.4 Optical properties of SWCNTs and excitons	13
2.2 Luminescent defects in SWCNTs	17
2.2.1 Exciton localization and spectroscopic properties	17
2.2.2 Role of defect structure	21
2.2.3 Covalent functionalization of SWCNTs	23
2.2.4 Impact on charge transport	25
2.3 Field-effect transistors	26
2.3.1 Basic principle of unipolar FETs	27
2.3.2 Ambipolar and light-emitting FETs	29
2.3.3 SWCNT network transistors	30
2.4 Charge transport in semiconducting SWCNTs	32
2.4.1 Charge transport in individual nanotubes	32
2.4.2 Charge transport in nanotube networks	33
2.4.3 Experimental techniques	37
3 Experimental Details and Methods	41
3.1 SWCNT dispersions	42

3.1.1	Selective dispersion of (6,5) SWCNTs in toluene	42
3.1.2	Selective dispersion of (7,5) SWCNTs in toluene	42
3.1.3	Aqueous dispersion of (6,5) SWCNTs	42
3.2	Covalent functionalization of polymer-wrapped SWCNTs	43
3.2.1	Functionalization with aryldiazonium salts	43
3.2.2	Functionalization with aniline derivatives	43
3.3	SWCNT thin film deposition and FET fabrication	44
3.3.1	Spin-coating of SWCNT networks	44
3.3.2	Aerosol-jet printing of SWCNT networks	44
3.3.3	Membrane transfer of SWCNT films	45
3.3.4	Fabrication of BCB-covered substrates	45
3.3.5	Fabrication of <i>h</i> -BN flakes on Si/SiO ₂ substrates	46
3.3.6	Field-effect transistor fabrication	46
3.4	Spectroscopic characterization	47
3.4.1	Luminescence microscopy setup	47
3.4.2	Voltage-dependent PL and EL spectroscopy	49
3.4.3	Charge modulation PL spectroscopy	49
3.4.4	Time-correlated single-photon counting	50
3.4.5	PL quantum yield determination	50
3.4.6	EL imaging	51
3.4.7	External quantum efficiency measurements	51
3.4.8	Low-temperature and temperature-dependent PL spectroscopy	51
3.4.9	Hyperspectral PL imaging on <i>h</i> -BN flakes	53
3.4.10	Optical-pump THz-probe and THz time-domain spectroscopy	53
3.5	Other characterization techniques	54
3.5.1	Absorption spectroscopy	54
3.5.2	Raman spectroscopy	54
3.5.3	Profilometry	55
3.5.4	Atomic force microscopy	55
3.5.5	Electrical characterization	55
4	Charge Transport in SWCNT Networks with Luminescent Defects	57
4.1	Introduction	58
4.2	Functionalization and characterization	59
4.3	FETs with functionalized SWCNT networks	61
4.4	Electroluminescence from defect states	65
4.5	EL efficiencies of LEFETs with functionalized SWCNT networks	69
4.6	Interaction of charge carriers with luminescent defects and defect-localized excitons	71

4.7	Temperature-dependent charge transport	77
4.8	Summary and conclusion	82
5	Carrier Dynamics in Functionalized SWCNTs Probed by Terahertz Spectroscopy	85
5.1	Introduction	86
5.2	Functionalization and characterization	87
5.3	OTTP spectroscopy of SWCNT dispersions	90
5.4	Mechanism of photoinduced free-carrier generation	95
5.5	Macroscopic charge transport in SWCNT network FETs	97
5.6	Temperature-dependent OTTP spectroscopy of SWCNT films	102
5.7	Summary and conclusion	106
6	Near-Intrinsic Emission Spectra from SWCNT Thin Films on BCB-Passivated Substrates	109
6.1	Introduction	110
6.2	PL spectra of SWCNT films on BCB-passivated substrates	111
6.3	Origin of the Y_1 sideband	116
6.4	Polymer-wrapped (7,5) and surfactant-coated (6,5) SWCNT films	120
6.5	SWCNT films on <i>h</i> -BN flakes	122
6.6	SWCNT LEFETs on BCB-passivated substrates	124
6.7	Covalently functionalized SWCNT films on BCB	128
6.8	Summary and conclusion	132
7	Further Red-Shifted Electroluminescence from Functionalized SWCNT Networks	133
7.1	Introduction	134
7.2	(6,5) SWCNT network LEFETs with further red-shifted defects	135
7.3	Impact of binding configuration on defect–carrier interaction	139
7.4	Functionalized (7,5) SWCNT network LEFETs	145
7.5	Impact of SWCNT chirality on defect–carrier interaction	148
7.6	Defect-state EL at telecommunication wavelengths	151
7.7	Summary and conclusion	155
8	Conclusion and Outlook	159
	Bibliography	165
	Eidesstattliche Versicherung	185

Abbreviations

0D	Zero-dimensional
1D	One-dimensional
2D	Two-dimensional
AFM	Atomic force microscopy
ALD	Atomic layer deposition
ATPE	Aqueous two-phase extraction
BCB	Divinyltetramethylsiloxane-bis-benzocyclobutene
CMPL	Charge modulation photoluminescence
CMS	Charge modulation spectroscopy
CoMoCAT	Cobalt–molybdenum catalyst
CVD	Chemical vapor deposition
cw	Continuous wave
DC	Direct current
DMSO	Dimethyl sulfoxide
DOC	Sodium deoxycholate
DOS	Density of states
DzBr	4-Bromobenzenediazonium tetrafluoroborate
DzNO ₂	4-Nitrobenzenediazonium tetrafluoroborate
EL	Electroluminescence
EQE	External electroluminescence quantum efficiency
EVET	Electronic-to-vibrational energy transfer
FET	Field-effect transistor
FIT	Fluctuation-induced tunneling
<i>h</i> -BN	Hexagonal boron nitride
HOMO	Highest occupied molecular orbital
IRF	Instrument response function
KOtBu	Potassium <i>tert</i> -butoxide
LEFET	Light-emitting field-effect transistor
LUMO	Lowest unoccupied molecular orbital
MeCN	Acetonitrile

MPD	Multi-phonon decay
NIR	Near-infrared
NMP	<i>N</i> -Methyl-2-pyrrolidone
OPTP	Optical-pump terahertz-probe
PFO	Poly(9,9-dioctylfluorene)
PFO-BPy	Poly[(9,9-dioctylfluorenyl-2,7-diyl)- <i>alt</i> -(6,6'-2,2'-bipyridine)]
PL	Photoluminescence
PLQY	Photoluminescence quantum yield
PMMA	Poly(methyl methacrylate)
PTFE	Poly(tetrafluoroethylene)
SWCNT	Single-walled carbon nanotube
TCSPC	Time-correlated single-photon counting
TD	Thermal detrapping
THF	Tetrahydrofuran
THz	Terahertz
THz-TDS	Terahertz time-domain spectroscopy
UV	Ultraviolet
vis	Visible
VRH	Variable range hopping

Chapter 1

Introduction

The rapid technological evolution in the past decades is strongly linked to the tremendous progress that has been made in the high-speed transfer of information and data. In today's telecommunication systems, modulated light pulses serve as information carriers that are transmitted through optical fibers.¹ For this fiber-optic communication to be efficient over long distances, signal attenuation and dispersion in the fiber material need to be minimized by choosing light with a suitable wavelength.² Currently used optical sources, whose emission spectrum matches the transmission windows (*i.e.*, wavelength ranges with the lowest attenuation coefficients) of standard silica fibers in the near-infrared (NIR, 1.3–1.6 μm), consist of light-emitting diodes or lasers that are made from inorganic III-V compound semiconductors.^{1,3} Nevertheless, the continuous progress and emerging technologies such as quantum information processing⁴ and flexible electronics⁵ require the development of new material systems with well-controlled mechanical, electrical, and optical properties.

A promising material in this regard are semiconducting single-walled carbon nanotubes (SWCNTs), as they combine mechanical flexibility and solution-processability with narrow-band, diameter-specific optical transitions in the NIR.⁶ Especially networks of SWCNTs can be easily and reproducibly deposited from solution and exhibit high ambipolar charge carrier mobilities as well as electroluminescence (EL) upon electrical excitation, which makes them highly suitable as active layers in light-emitting devices.⁷ However, the emission spectra of SWCNT thin films are markedly different from those in dispersion and typically suffer from peak broadening due to luminescence from undesired sidebands.⁸ Furthermore, their application has been hindered by the low emission efficiencies of SWCNT films (photoluminescence (PL) quantum yield $\sim 0.1\%$) and devices (external quantum efficiency $\sim 0.01\%$),^{9,10} despite the reasonable light output enabled by the high current densities.⁷

In recent years, the controlled covalent functionalization of semiconducting SWCNTs with luminescent sp^3 defects has emerged as a versatile approach to enhance their optical properties.^{11–14} These defects can be chemically implanted in the nanotube lattice, hence creating new optically active states that give rise to localized, red-shifted emission.¹⁵ For solution-dispersed nanotubes, functionalization typically leads to a brightening of the overall SWCNT PL emission.¹⁶ Synthetic variation of the attached groups and, more importantly, the introduction of defects with a specific molecular arrangement offers a certain degree of control over the defect emission wavelength and thus strongly expands the application potential of SWCNTs as tunable NIR emitters.¹⁷ Moreover, sp^3 defects exhibit high-purity single-photon emission at room temperature, since they can host only one exciton at any given time by virtue of their zero-dimensional character.^{18,19} Owing to this non-classical light emission, SWCNTs with luminescent defects have emerged as strong candidates for future technologies such as quantum cryptography or quantum computing.²⁰

However, there are still several challenges that need to be faced en route towards electrically-pumped single-photon sources in the NIR based on covalently functionalized SWCNTs.²¹

Thus far, the optical properties of sp^3 defects were predominantly investigated in dispersion and under optical excitation. Consequently, little is known about the effect of a changing environment on defect luminescence, especially when it comes to substrate-deposited SWCNTs and thin films. On top of that, the integration of functionalized nanotubes into optoelectronic devices as well as the demonstration of efficient defect emission upon electrical excitation are prerequisites for practical applications. Most importantly, the realization and optimization of such light-emitting devices demands a fundamental understanding of the impact of luminescent defects not only on the optical properties but also on charge transport.

This thesis addresses the issues outlined above by using a wide range of experimental techniques to investigate the charge transport and luminescence properties of covalently functionalized SWCNTs and their networks. The high purity and excellent processability of SWCNT dispersions prepared *via* selective polymer-wrapping, combined with recently developed, highly selective methods for covalent nanotube functionalization in organic solvents,^{22,23} enable their integration in light-emitting thin film field-effect transistors. To obtain a complete picture, the impact of sp^3 defects on the nanotube charge transport properties is studied on a microscopic and macroscopic level as a function of temperature and defect density. A facile substrate passivation method is developed to significantly enhance the emission spectra of SWCNT thin films and devices. Moreover, the choice of SWCNT species and control over the molecular arrangement of defect groups on the nanotube lattice are demonstrated as means to spectrally tune the defect EL to telecommunication wavelengths.

The outline of this thesis is as follows. Chapter 2 covers the structural description, synthesis, and optoelectronic properties of SWCNTs and luminescent defects. The working principle of field-effect transistors (FETs) is explained in general terms, before FETs based on SWCNT networks are introduced. Furthermore, the current state of research on charge transport in semiconducting SWCNT networks is summarized, including theoretical models for its description and an overview of experimental methods for its investigation.

Chapter 3 describes the materials and experimental techniques that were employed in this thesis. The protocols for the preparation of chirality-pure dispersions and covalent functionalization of polymer-wrapped SWCNTs are outlined in detail. A special focus is placed on SWCNT thin film deposition and device integration as well as the spectroscopic setups used for characterization.

In Chapter 4, networks of polymer-wrapped and functionalized SWCNTs are integrated as charge transport and emission layers in ambipolar, light-emitting FETs. The carrier mobility is studied as a function of defect density and temperature. Various spectroscopic techniques are used to explore the interaction of charge carriers with luminescent defects and defect-localized excitons in active optoelectronic devices, and EL from sp^3 defect states is demonstrated.

Chapter 5 uses time-resolved terahertz spectroscopy to investigate the intrinsic charge transport properties and carrier dynamics in functionalized SWCNT dispersions and films. Through assessment of the local nanotube conductivity depending on the degree of functionalization, optimum defect densities to achieve both favourable optical properties and high carrier mobilities are identified. The combination of terahertz spectroscopy and electrical measurements of SWCNT network transistors provides detailed insights into the factors that govern charge transport in SWCNT thin films on a microscopic and macroscopic level.

Chapter 6 introduces surface passivation with a cross-linked polymer as a general approach to enhance the luminescence spectra of SWCNT thin films on commonly used substrates. The origin of the pronounced sideband emission in nanotube films is elucidated, and the results are compared to those for SWCNT films on hexagonal boron nitride, which has been widely used as an encapsulation layer for low-dimensional materials. Furthermore, the fabrication of light-emitting SWCNT network transistors with near-intrinsic electroluminescence on passivated substrates demonstrates the applicability of the developed method for the realization of optoelectronic devices with improved emission spectra.

In Chapter 7, luminescent defects with a deeper optical trap depth are selectively introduced to (6,5) and (7,5) SWCNTs to further shift the emission spectrum of light-emitting SWCNT network FETs towards telecommunication wavelengths. The impact of covalent functionalization on charge transport in SWCNT networks is evaluated depending on the defect binding configuration and nanotube species. Moreover, the choice of nanotube chirality and control over the defect structure are highlighted as key factors to tune the emission wavelength of functionalized SWCNTs across the NIR spectral range.

Finally, Chapter 8 summarizes the main results of this thesis in a broader context and provides an outlook on future directions of research in this field.

Chapter 2

Theoretical Background

This Chapter covers the optical and electronic properties of single-walled carbon nanotubes and luminescent defects. It further discusses the working principle of field-effect transistors and charge transport in semiconducting nanotube networks.

2.1 Single-walled carbon nanotubes

In the past few decades, low-dimensional materials have been extensively explored both in the quest for fundamentally new physics and in the context of practical applications. Among these materials, the family of carbon allotropes is particularly versatile due to the ability of carbon atoms to bind to itself in a great variety of structural motifs, resulting in numerous modifications that each exhibit unique characteristics.²⁴ Zero-dimensional (0D) fullerenes, spherical structures consisting of five- and six-membered carbon rings, were first synthesized in 1985 and since then were also detected in nature and in interstellar space.^{25–27} Fullerene derivatives have been applied as vessels for drug delivery in nanomedicine²⁸ and are established acceptor materials in organic solar cells.²⁹ The two-dimensional (2D) graphene, first isolated in 2004 through exfoliation of graphite,³⁰ consists of a monolayer of sp^2 -hybridized carbon arranged in a honeycomb lattice and has been heavily investigated for its outstanding thermal, mechanical, electronic and optical properties.^{31–33} Initially discovered in 1991, carbon nanotubes are hollow cylindrical structures with diameters on the order of 1 nm and typical lengths of few micrometers.³⁴ Owing to their high aspect ratio, they are considered as one-dimensional (1D) materials and thus bridge the gap between fullerenes and graphene. Carbon nanotubes occur either as single-walled or as multi-walled species, with the latter comprising two or more concentric cylinders nested into each other. However, the well-defined and structure-dependent optical and electronic features of single-walled carbon nanotubes (SWCNTs) make them more attractive in terms of their application potential.^{35,36} Since this thesis is concerned with SWCNTs, their structure and properties will be derived from those of graphene in the following Sections.

2.1.1 Structure and synthesis

The structure of a SWCNT can be described conceptually as a seamless, rolled-up sheet of graphene, as depicted in Figure 2.1a.³⁷ Depending on the fashion of this imaginary roll-up process, a large variety of structurally different SWCNT species can be obtained. Each one of these nanotube structures is uniquely defined by their chiral vector \vec{C}_h , which connects pairs of carbon atoms that coincide after rolling-up and thus describes the circumference of the constructed SWCNT.³⁸ \vec{C}_h can be expressed as a linear combination according to

$$\vec{C}_h = n\vec{a}_1 + m\vec{a}_2 \quad (2.1)$$

with \vec{a}_1 and \vec{a}_2 being the unit vectors of the graphene lattice, whose length $a = \sqrt{3}a_{C-C} = 0.246$ nm is related to the carbon–carbon bond length $a_{C-C} = 0.142$ nm. n and m are integer numbers, and the index pair (n,m) directly determines the nanotube diameter d

$$d = \frac{|\vec{C}_h|}{\pi} = \frac{a}{\pi} \sqrt{n^2 + nm + m^2} \quad (2.2)$$

as well as the chiral angle θ

$$\cos(\theta) = \frac{2n + m}{2\sqrt{n^2 + nm + m^2}} \quad (2.3)$$

between the roll-up direction and the primitive vector \vec{a}_1 .^{39,40} Due to the hexagonal symmetry of the graphene lattice, only chiral angles between $0^\circ \leq \theta \leq 30^\circ$ lead to unique nanotube structures. SWCNTs with an index pair $(n,0)$ and a chiral angle of $\theta = 0^\circ$ are called zigzag nanotubes, whereas those with (n,n) and a chiral angle of $\theta = 30^\circ$ are denoted as armchair nanotubes. Species of either one of these types are achiral due to their mirror symmetry (Figure 2.1b). In contrast to that, all other species are chiral nanotubes. Enantiomeric pairs, *i.e.*, (n,m) and $(m,n) = (n+m,-m)$ SWCNTs, have the same diameter and properties except for their opposite circular dichroism.⁴¹ Irrespective of the symmetry, however, the helicity (n,m) is often referred to as the chirality of a given SWCNT species.

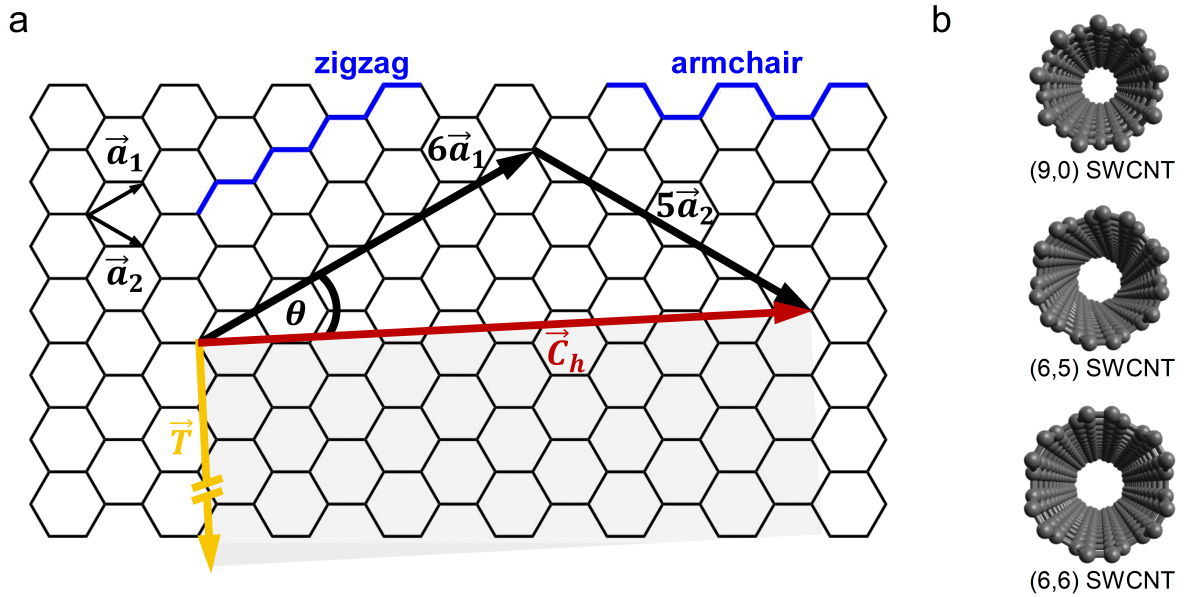


Figure 2.1: (a) Schematic construction of a (6,5) SWCNT by rolling up a graphene sheet. The roll-up vector \vec{C}_h defines the nanotube circumference, whereas the translational vector \vec{T} defines the periodicity in the direction of the nanotube axis. (b) Front view of a zigzag (9,0), a chiral (6,5), and an armchair (6,6) SWCNT.

In addition to \vec{C}_h , the translational vector \vec{T} can be constructed as the smallest possible vector perpendicular to the roll-up direction. A combination of both vectors defines the nanotube unit cell as a cylinder of diameter d and length $|\vec{T}|$. Even though the size of a unit cell can be markedly different depending on the nanotube chirality, SWCNTs typically

contain many of these repetition units and thus are frequently modelled as infinitely long.⁶ Moreover, the impact of nanotube ends, that may be either open or closed by fullerene caps,⁴² is commonly neglected.

Various methods have been developed for the synthesis of SWCNTs, and all of them involve a carbon-based precursor that is decomposed using a catalyst (typically transition metal nanoparticles or compounds thereof) to release the carbon atoms for nanotube growth.⁴³ Among these techniques are the conversion of carbon black or graphite in a plasma⁴⁴ or upon vaporization by laser ablation⁴⁵ or arc discharge,⁴⁶ which yield nanotubes with larger diameters ($d \sim 1\text{--}2$ nm) but require high temperatures of > 1000 °C. Nowadays, large-scale synthesis of commercially available SWCNTs predominantly relies on chemical vapor deposition (CVD) processes using gaseous carbon sources under milder processing conditions.⁴³ One example is the CoMoCAT process,⁴⁷ which produces a narrow range of small-diameter nanotubes ($d \sim 0.7\text{--}1.2$ nm) containing mostly (6,5) and (7,5) SWCNTs. Here, carbon monoxide is used as the feedstock gas, which disproportionates at temperatures between 700–850 °C on a silica- or magnesia-supported cobalt–molybdenum catalyst, before the as-synthesized SWCNTs are recovered by acid treatment to dissolve the support substrate.^{48,49}

All available synthesis methods, however, produce mixtures of SWCNTs with different diameters and, most importantly, different electronic type (metallic or semiconducting, see Chapter 2.1.3). In addition, nanotube soots contain impurities such as amorphous carbon or residual catalyst particles from the production process. While significant effort has been devoted to the development of methods that allow for selective growth of specific SWCNT chiralities,⁵⁰ for example by using tailored catalysts^{51,52} or templating end-caps,⁵³ they are still far from being suitable for large-scale production. Thus, the purification and sorting of SWCNT raw materials are crucial steps to enable the investigation of their structure-dependent properties and harness their potential for (opto-)electronic applications.

2.1.2 Purification and sorting

Aside from the mixture of all sorts of chiralities and residual impurities that are contained in commercial raw materials, as-grown SWCNTs occur as bundles held together by attractive van der Waals interactions between the extended π -systems of the nanotube sidewalls.⁵⁴ Moreover, SWCNTs are essentially insoluble in all solvents, with very few exceptions such as *N*-cyclohexyl-2-pyrrolidone or *N*-methyl-2-pyrrolidone that can disperse nanotubes in appreciable quantities.^{55,56} Consequently, different approaches have been developed for the exfoliation, stabilization, and sorting of SWCNTs in the liquid phase.^{54,57} All these strategies follow a common outline: First, SWCNTs are de-bundled in a solvent of choice typically through sonication methods (*e.g.*, tip sonication or bath sonication). To prevent immediate re-aggregation and to form colloidal dispersions, nanotubes are stabilized with the aid of a dispersing agent.⁵⁴ Then, a centrifugation step sediments the remaining bundles and impu-

rities, whereas the supernatant contains the individualized SWCNTs. Selectivity, *e.g.*, with respect to the electronic type (semiconducting *versus* metallic) or towards one or several chiralities, might be induced either in the dispersion step or *via* subsequent post-sorting techniques.

First reports of stable SWCNT dispersions in water involved the use of surfactants, such as sodium dodecyl sulfate or sodium (deoxy-)cholate,^{54,58} or nanotube wrapping with DNA.⁵⁹ However, these methods typically yield non-selective dispersions that need to be subjected to an additional sorting step.^{57,60} Commonly used techniques include density-gradient ultracentrifugation,^{61,62} gel chromatography,^{63,64} or dielectrophoresis.⁶⁵ In addition to that, aqueous two-phase extraction (ATPE) has emerged as a versatile and scalable approach for SWCNT separation.⁶⁶ ATPE is based on a system of two immiscible aqueous phases, usually formed by addition of the polymers dextran and poly(ethylene glycol), and the selective partitioning of SWCNTs between these two phases depending on their metallicity, diameter, surfactant coating, and pH value.⁶⁶⁻⁶⁸ Despite the recent progress of this method towards the separation of SWCNTs with small or large diameters and even their enantiomeric forms,⁶⁸⁻⁷⁰ small residual amounts of metallic SWCNTs even after multiple steps have hindered their application in devices.⁷¹

In contrast to that, semiconducting SWCNT dispersions with a superior purity can be obtained through stabilization with π -conjugated polymers in organic solvents (typically toluene or xylenes), as first introduced by Nish *et al.*⁷² This so-called polymer-wrapping approach is special since the dispersion step is selective itself, thus enabling the extraction of certain SWCNT species in a single step without the necessity of further sorting.⁷³ Upon exfoliation of the SWCNT raw material in a solution of the polymer through sonication or application of shear forces, the polymer chains selectively wrap around the preferred chiralities,⁷⁴ whereas other nanotubes quickly re-aggregate and can be separated by centrifugation together with unexfoliated material and impurities. Among the large variety of polymers that can be used in this process, polyfluorenes and their copolymers are those most frequently encountered.^{72,74-76} Figure 2.2 depicts the molecular structures of selected examples. The very high selectivity of these polymers towards exclusively semiconducting species has enabled the application of polymer-wrapped SWCNTs in electronic devices.^{77,78} Other classes of polymers that have been utilized for nanotube sorting include polythiophenes,⁷⁹ polycarbazoles,⁸⁰ and donor-acceptor copolymers.⁸¹ All these structures are comprised of a polymer backbone, which adsorbs to the nanotube sidewalls through strong π - π interactions, and long alkyl side chains to enhance the solubility of the polymers and thus, the colloidal stability of polymer-SWCNT hybrids.⁷⁵

Even though a large number of polymers suitable for dispersion of purely semiconducting SWCNTs are known by now, the origin of selectivity in polymer-wrapping remains poorly understood. Molecular dynamics simulations suggested that the polymer chains either wrap

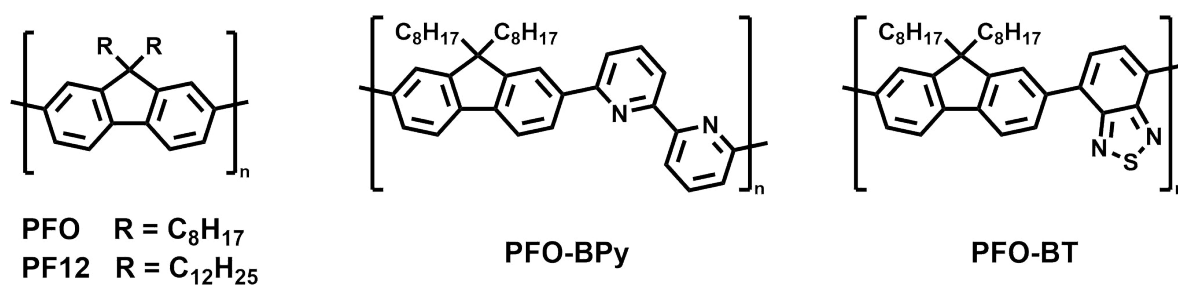


Figure 2.2: Structures of selected polyfluorene derivatives used for polymer-wrapping of semiconducting SWCNTs.

the nanotubes helically or are aligned along the tube axis, with the wrapping geometry depending on both the SWCNT chirality and polymer structure.^{72,74,75} Experimentally, different factors have been identified that affect the diameter of dispersed nanotubes as well as the yield and selectivity of the dispersion process. These include, amongst others, the length of the alkyl side chains,⁷⁵ the molecular weight of the polymer,^{78,82} the solvent viscosity,^{82,83} and the doping state of SWCNTs.⁸⁴ Nevertheless, while certain combinations of polymers and nanotube raw materials give rise to SWCNT dispersions with a broad diameter range,^{75,85} others were found to selectively disperse exclusively one single nanotube chirality.⁷² A prominent example is the selective extraction of small-diameter (6,5) SWCNTs from CoMoCAT raw material using the fluorene–bipyridine copolymer poly[(9,9-dioctylfluorenyl-2,7-diyl)-*alt*-(6,6'-2,2'-bipyridine)] (PFO-BPy), as introduced by Ozawa *et al.*⁷⁶ From the same raw material, (7,5) SWCNTs can be dispersed with poly(9,9-dioctylfluorene) (PFO).⁷²

Finally, it should be noted that harsh sonication used for SWCNT exfoliation shortens the nanotubes and introduces lattice defects that are detrimental to their electronic and optical properties.⁸⁶ Here, progress has been made through combination of polymer-wrapping with shear force mixing as a mild and scalable exfoliation method, as introduced by Graf *et al.*⁸⁷ This approach provides access to large quantities of long (6,5) SWCNTs with high quality and purity, and therefore served as the basis for the experiments carried out in this thesis.

2.1.3 Electronic structure

Along with their structure, the electronic properties of SWCNTs can be derived from those of graphene. For the highly symmetrical graphene lattice with only two carbon atoms per primitive unit cell, an analytical equation for its band structure is obtained within the nearest-neighbor tight-binding formalism.^{37,88} Within this model, only the bonding π - and antibonding π^* -bands (also referred to as valence and conduction band, respectively) dominate the charge transport properties and optical transitions in the visible (vis) and near-infrared (NIR) regions, owing to the large energy separation of the σ and σ^* bands that make up the hexagonal carbon lattice.³⁹ For energies around the Fermi level, electron–hole symmetry can be assumed, and the energy dispersion in reciprocal space is given by

$$E(\vec{k})^{\pm} = \pm\gamma\sqrt{1 + 4\cos\frac{\sqrt{3}k_x a}{2}\cos\frac{k_y a}{2} + 4\cos^2\frac{k_y a}{2}} \quad (2.4)$$

where \vec{k} is the wave vector, γ is the nearest-neighbor interaction energy (typically set to 3.1 eV), and the Fermi level is defined as zero.^{37,39} The band structure of graphene (see Figure 2.3a) reveals points of high symmetry, the so-called K and K' points, that are located at the vertices of the hexagonal Brillouin zone. At these points, the valence and conduction bands touch, and the energy dispersion is approximately linear (Figure 2.3b). Thus, graphene can be described as a zero-bandgap semiconductor or a semi-metal.

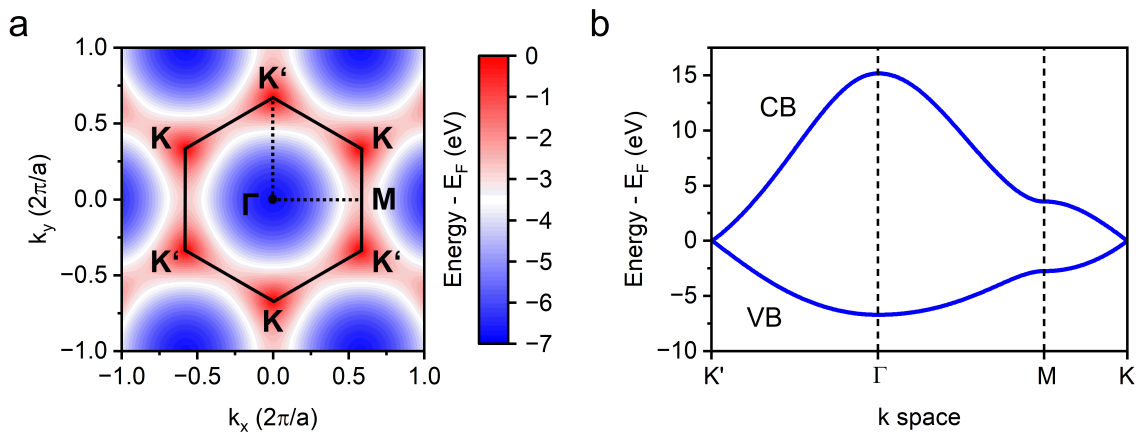


Figure 2.3: Graphene band structure in reciprocal space. (a) Contour plot of the valence band in the first Brillouin zone. The hexagonal symmetry and critical points (K, K', Γ , M) are indicated. (b) One-dimensional energy dispersion of the valence (VB) and conduction (CB) bands between the points indicated in (a) calculated *via* the tight-binding approach.

To calculate the electronic properties of a SWCNT, its reciprocal lattice is constructed from the real-space structure (compare Figure 2.1) under the reciprocity condition given by³⁷

$$\exp\left(i(\vec{K}_a + \vec{K}_c)(\vec{C}_h + \vec{T})\right) = 1 \quad (2.5)$$

where \vec{K}_a and \vec{K}_c are the reciprocal lattice vectors along the nanotube axis and circumference, respectively. Rolling up a sheet of graphene to form a nanotube results in the confinement of the wave function along the circumference, which imposes periodic boundary conditions on the wave vector in this direction. Consequently, a set of quantized wave vectors in the circumferential direction is obtained, as given by Equation 2.6. Notably, the same boundary conditions apply to the wave vector along the nanotube axis. However, the spacing between the k values vanishes in the limit of a very long nanotube ($L \gg |\vec{T}|$), and hence, the allowed wave vectors in the axial direction can be considered a quasi-continuous variable.^{37,39}

$$q = j|\vec{K}_c| = \frac{2\pi j}{|\vec{C}_h|} = \frac{2j}{d}, \quad j = 0, 1, \dots, j_{\max} \quad (2.6)$$

Consequently, the allowed wave vectors are composed of a series of lines that cut through the Brillouin zone of graphene, thus effectively creating a set of 1D cuts through the graphene band structure which are called the subbands of a nanotube. Based on the zone-folding approximation, the band structure of a SWCNTs is given by the sum of all subbands.^{39,89} Figure 2.4 visualizes these cutting lines and the resulting band structures for a chiral (6,5) SWCNT and an armchair (6,6) SWCNT, respectively. Depending on their orientation and spacing, the lines either do or do not intersect the K point (Figure 2.4a,d). Due to the intersection of the valence and conduction bands at this point, nanotubes whose subbands cut through the K point inherit metallic properties, whereas others possess a bandgap and exhibit semiconducting character (Figure 2.4b,e).³⁹

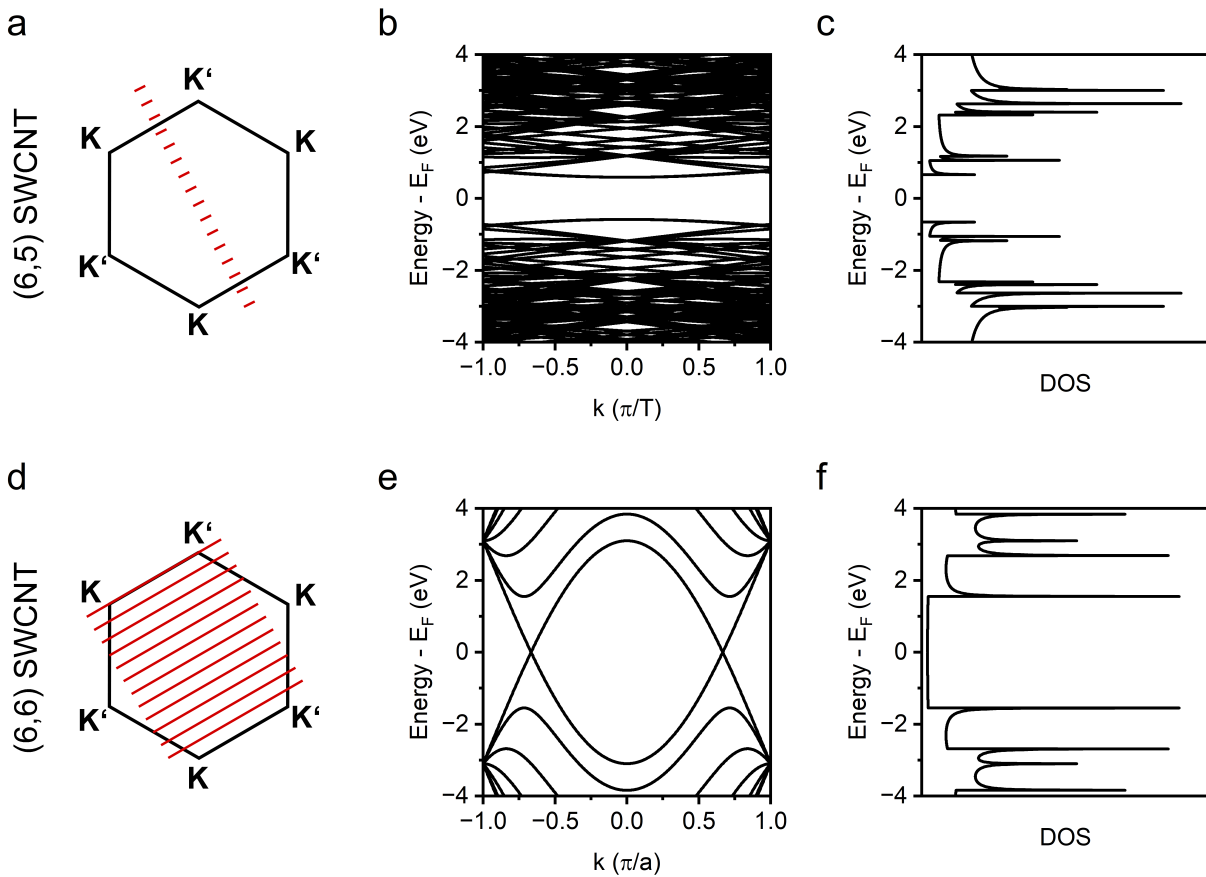


Figure 2.4: Band structure and DOS distribution of a (6,5) SWCNT and a (6,6) SWCNT calculated within the tight-binding and zone-folding formalisms. (a,d) Allowed wave vectors as line cuts through the first Brillouin zone in the band structure of graphene. (b,e) SWCNT band structure and (c,f) corresponding DOS distribution. The DOS at the Fermi level is zero for semiconducting (6,5) SWCNTs owing to their bandgap, whereas it is finite for metallic (6,6) SWCNTs.

To a first approximation, the bandgap E_g of a semiconducting SWCNT can be determined by $E_g = 2\gamma \frac{ac-c}{d}$ and thus primarily depends on the tube diameter rather than (n,m) species.³⁷ However, from the index pair, a general relation to predict the electronic type of a SWCNT can be derived, which reveals that a nanotube is metallic if $(n - m)$ is 0 or an integer multiple of 3, and it is semiconducting otherwise.³⁷ It follows that statistically, one third of all SWCNTs including all armchair species are metallic, and two thirds are semiconducting.^{39,90} From the SWCNT band structure, the total density of states (DOS) distribution $g_{\text{tot}}(E)$ can be calculated according to

$$g_{\text{tot}}(E) = \sum_j g(E, j) = \sum_j \frac{1}{\pi} \left| \frac{\partial k}{\partial E} \right| \quad (2.7)$$

where $g(E, j)$ is the DOS of the subband with index j (compare Equation 2.6). The DOS distributions, as shown for a (6,5) SWCNT and a (6,6) SWCNT in Figure 2.4c,f, feature a series of spikes denoted as van Hove singularities that are characteristic for electrons in a 1D solid.³⁷ At the Fermi level, the DOS is zero for the semiconducting (6,5) SWCNT, whereas it is finite for the metallic (6,6) SWCNT.

It should be noted that the presented nearest-neighbor tight-binding and zone-folding formalisms are based on several approximations, such as the neglect of curvature effects that become more pronounced as the nanotube diameter decreases.^{88,91} Nevertheless, the calculated DOS is in good agreement with experimental results from scanning tunneling microscopy⁹² and is very useful for the description of the charge transport (see Chapter 2.4) and thermoelectric properties of SWCNTs.^{93,94} Furthermore, their direct bandgap explains the observation of luminescence from semiconducting SWCNTs following optical or electrical excitation, whereas emission from metallic nanotubes is absent due to fast, non-radiative carrier relaxation. The next Section describes the optical properties of semiconducting SWCNTs.

2.1.4 Optical properties of SWCNTs and excitons

To a first approximation, the optical absorption transitions in semiconducting SWCNTs can be described within the single-particle picture as excitations of an electron from the valence to the conduction band, as shown in Figure 2.5a. Due to Fermi's golden rule, the transition rate depends on the density of initial and final states, and therefore, transitions between the van Hove singularities dominate the nanotube's optical response.⁹⁵ More specifically, only transitions between the i -th van Hove singularity in the valence (v1, v2, ...) and conduction (c1, c2, ...) band, labelled as E_{ii} transitions, are allowed for electric fields parallel to the tube axis to conserve angular momentum.⁹⁶ Even though E_{ij} transitions are allowed for excitation perpendicular to the nanotube, only E_{ii} features are visible in the SWCNT absorption spectrum (compare Figure 2.6a) due to the significantly larger absorption cross-section in the parallel

direction (antenna effect).⁹⁷ Within this picture, the energy of E_{11} corresponds to absorption or luminescence that occur directly across the bandgap, and thus, E_g .⁹⁵

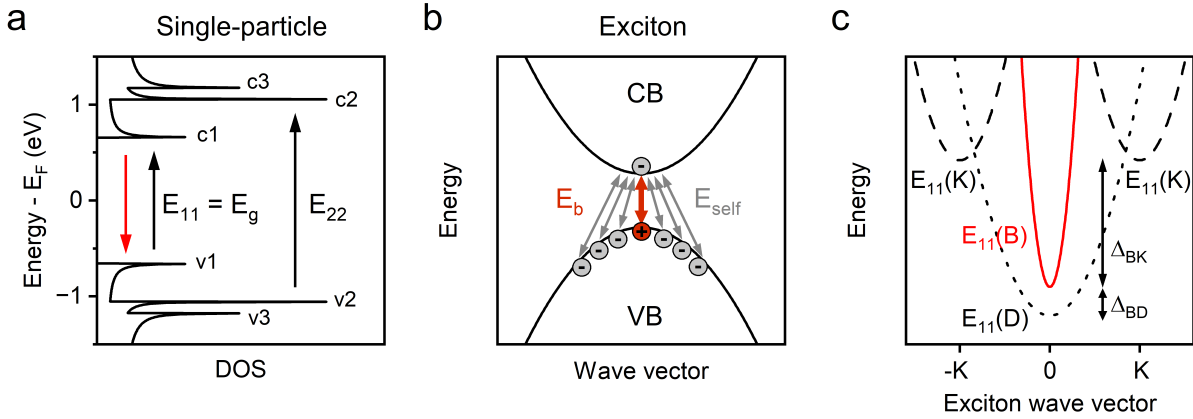


Figure 2.5: (a) Within the single-particle picture, optical transitions (absorption, black; emission, red) in semiconducting SWCNTs are described as transitions between the van Hove singularities in the valence and conduction band of the DOS. (b) Illustration of many-body effects in SWCNTs. The low dimensionality leads to strong attractive electron–hole (exciton binding energy E_b) and repulsive electron–electron (self-energy E_{self}) interactions. (c) Schematic energy dispersions of singlet E_{11} excitons. The bright $E_{11}(B)$ exciton is drawn in red, whereas optically forbidden $E_{11}(D)$ and $E_{11}(K)$ excitons are drawn in black.

However, analysis of the optical spectra for many different SWCNT species revealed pronounced discrepancies between the observed transition energies and those calculated from the tight-binding model, thus presenting evidence that the picture of a free electron and hole produced upon excitation is not sufficient.^{58,95,98,99} The reduced dimensionality of SWCNTs gives rise to poor dielectric screening and consequently strong electron–hole interactions, and hence requires many-body effects to be taken into account (Figure 2.5b).¹⁰⁰ Excitation of SWCNTs produces strongly-bound electron–hole pairs called excitons, which are stable at room temperature owing to their large binding energies (E_b). Using two-photon excitation spectroscopy, exciton binding energies on the order of several 100 meV were determined,^{101,102} which is substantially larger than in inorganic semiconductors. Aside from E_b which describes the attractive electron–hole interaction, many-body interactions include a second term to reflect the repulsive interaction between the excited electron in the conduction band and the remaining electrons in the valence band (self-energy E_{self}). Hence, the E_{11} transition energy in the excitonic picture is given by $E_{11} = E_g - E_b + E_{self}$.¹⁰³ In SWCNTs, E_{self} is larger than E_b , and thus, many-body effects lead to an increase in transition energy.^{100,103}

The degeneracy of the K and K' valleys in the graphene lattice gives rise to a four-fold degeneracy of each excitonic level in SWCNTs, with the different configurations labelled as KK, K'K', KK', and K'K to indicate the respective locations of the electron and hole. Due to the spin multiplicity of the involved carriers, each these configurations further splits into

one singlet and three triplets, resulting in a total of 16 excitons per E_{ii} state. However, since direct transitions require the momentum and spin to be conserved, intervalley (or K-momentum) excitons (*i.e.*, KK' and $K'K$) as well as all triplet configurations are optically forbidden (dark). For the intravalley, zero-momentum excitons, the wave functions split into a bonding and antibonding linear combination with odd and even parity, respectively. The latter is dark as well, since the selection rules require opposite parity between initial and final states for a transition to be allowed (*i.e.*, bright).³⁶ Consequently, only one of the 16 states, namely the odd-parity, zero-momentum singlet exciton, is optically active in a one-photon absorption or emission process. Within the currently used model, the parity-forbidden, zero-momentum exciton ($E_{11}(D)$) is located below the bright $E_{11}(B)$ exciton by only a few meV (Δ_{BD}).¹⁰⁴ Radiative transitions between the ground state and the K-momentum dark excitons $E_{11}(K)$, which are degenerate and located ~ 25 meV (Δ_{BK}) above $E_{11}(B)$, can be brightened through coupling to a D phonon as detailed below.¹⁰⁵ Figure 2.5c schematically depicts the energy dispersions of the four singlet E_{11} excitons. Note that the effective mass is lower for bright compared to dark excitons, thus explaining the steep dispersion of $E_{11}(B)$.¹⁰⁶ In the following, the absorption and photoluminescence (PL) spectra of (6,5) SWCNTs (Figure 2.6a) are used to discuss the common spectral features. The absorption spectrum exhibits strong resonances in the visible and NIR spectral range, corresponding to the E_{11} (~ 1000 nm) and E_{22} (~ 575 nm) transitions, respectively. Upon optical excitation into a higher excitonic state, *e.g.*, at the E_{22} transition, fast internal conversion (~ 100 fs) leads to relaxation to the E_{11} exciton manifold.^{107,108} Hence, only E_{11} PL is observed. Alternatively, E_{11} excitons may be generated electrically either *via* impact excitation or ambipolar carrier recombination (see Chapter 2.3.2).^{109,110} Radiative decay of the bright E_{11} exciton gives rise to a narrowband emission feature (linewidth ~ 20 meV for the data in Figure 2.6a) with a very small Stokes shift (~ 4 meV) that is associated with the small reorganization energy due to the rigidity of nanotube lattice.¹¹¹

In addition to the excitonic resonances, the absorption and emission spectra feature a series of lower-intensity peaks, as shown in Figure 2.6a.^{105,112,113} Absorption into, or emission from, the K-momentum dark excitonic state is brightened through coupling with a D phonon,^{105,112} which gives rise to a phonon sideband (also labelled as X_1 in emission). Population of the $E_{11}(K)$ state is hypothesized to occur *via* exciton scattering at lattice defects.^{114,115} In addition to that, coupling of the bright $E_{11}(B)$ exciton to a G phonon mode results in a weaker vibronic sideband (G_1) in the emission spectrum.¹⁰⁵ The lower-energy shoulder (Y_1) to the E_{11} emission has previously been assigned to extrinsic effects or brightened triplets, but its exact origin remains unclear.¹¹² A schematic energy level diagram depicting the main radiative emission transitions is shown in Figure 2.6b.

Owing to their high diffusion constant D on the order of $1\text{--}10$ cm²s⁻¹,^{116–118} excitons are highly mobile along individual SWCNTs and sample large parts of the nanotube during

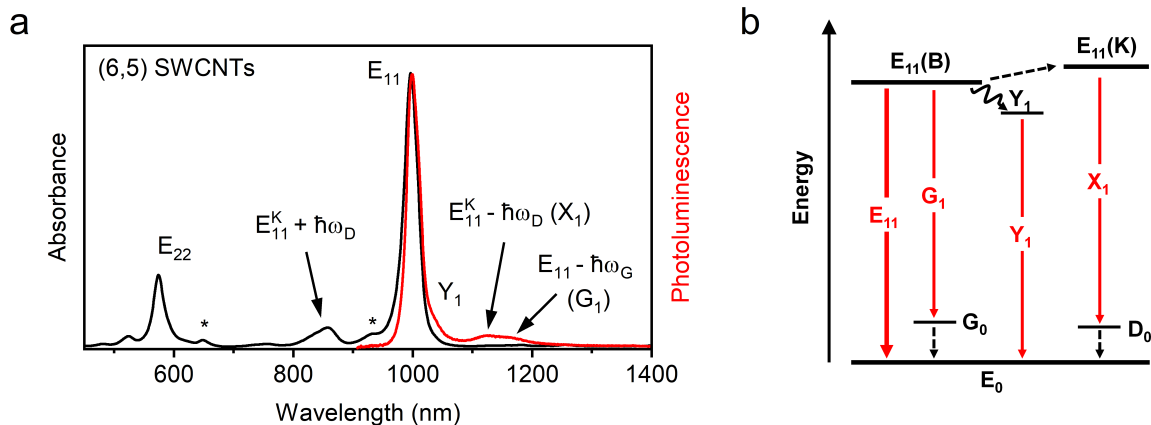


Figure 2.6: (a) Absorption (black) and photoluminescence (red) spectra of (6,5) SWCNTs. The main excitonic transitions and sidebands are labelled. The asterisk (*) marks impurities. (b) Schematic energy level diagram (energy axis not to scale) depicting the main radiative transitions (red arrows) from the E_{11} exciton manifold to the ground state. The main E_{11} transition is accompanied by weaker, lower-energy sidebands (Y_1 , X_1 , G_1). $E_{11}(B)$ is the bright, zero-momentum exciton; $E_{11}(K)$ denotes the K-momentum dark exciton. Transitions involving phonons are indicated as dashed lines.

their lifetime (~ 10 – 100 ps).³⁶ Additionally, exciton transfer in nanotube films was shown to take place on ultrafast time scales.^{119,120} As a consequence, excitons are highly sensitive to their environment and efficiently interact with, *e.g.*, other excitons, charge carriers, or SWCNT lattice defects (see Chapter 2.2).¹¹⁶ Optical transition energies in solution-dispersed compared to air-suspended SWCNTs of the same chirality are typically red-shifted, and the red-shift increases with dielectric constant of the solvent or surfactant.^{96,121,122} Moreover, for individual SWCNTs or films deposited on surfaces, nanotube–substrate and nanotube–nanotube interactions facilitate exciton quenching, which results in low emission efficiencies, peak broadening, and lifetime shortening.^{9,123,124} These effects can only partially be reduced by embedding the nanotubes in a polymer matrix¹²⁵ to create a homogeneous dielectric environment, or by depositing them on a substrate-passivating layer such as hexagonal boron nitride (*h*-BN).^{126,127} On top of that, saturation of the E_{11} PL at high excitation densities is associated with exciton–exciton annihilation,¹²³ and the presence of charge carriers results in efficient non-radiative Auger decay.^{128,129}

Aside from E_{11} emission, luminescence from trions – charged quasi-particles that are formed through binding of an exciton to an additional electron or hole – has been reported upon optical or electrical excitation of doped SWCNTs.^{130,131} As for excitons, the 1D structure of SWCNTs results in a large trion binding energy and thus, trions are observed as additional features in room-temperature emission spectra which are red-shifted by 100–200 meV with respect to the excitonic transition.^{8,132} Emission from (positive or negative) trions can even exceed the E_{11} emission intensity for high charge carrier densities, *e.g.*, in electrolyte-gated transistors.^{133,134}

2.2 Luminescent defects in SWCNTs

Since the first reports of luminescence from individual semiconducting SWCNTs in dispersion,⁵⁸ the origin of their low intrinsic PL quantum yields (PLQYs $\sim 1\%$) has been investigated intensely. While it has been proposed that the low emission efficiencies are due to the lowest excitonic state being optically dark,¹³⁵ the energetic difference to the bright E_{11} exciton is only a few meV and thus cannot fully account for this observation at least at room temperature.¹⁰⁴ Instead, diffusive quenching of bright excitons at nanotube lattice defects has been identified as the main source of non-radiative decay in solution-dispersed SWCNTs, as depicted in Figure 2.7a.^{116,136} Owing to the high exciton mobility, even a low number of such defects on a nanotube of typical length ($\sim 1 \mu\text{m}$) results in efficient exciton quenching. Lattice defects can either arise from imperfect growth, or are introduced by sonication in the de-bundling and dispersion process, which also leads to open and disordered tube ends.^{86,137}

In striking contrast to the prevailing notion that all lattice defects are exciton-quenching, seminal studies by Ghosh *et al.*¹³⁸ and Piao *et al.*¹⁶ reported the emergence of new, red-shifted emission features upon low-level decoration of SWCNTs with oxygen defects and aryl sp^3 defects, respectively. Such luminescent defects, also referred to as organic color centers or quantum defects, act as localization sites for mobile excitons (Figure 2.7a) and give rise to efficient radiative relaxation^{15,139} and even single-photon emission.^{18,19} Thus, the controlled introduction of such defects presents a powerful approach to enhance the optical properties of semiconducting SWCNTs, as has been covered extensively in recent reviews.^{11–14} The following Sections discuss the spectroscopic properties of luminescent defects in nanotubes, the synthetic methods for their controlled introduction, as well as their impact on charge transport. Since the main focus of this thesis are synthetic sp^3 defects, they will be reviewed in greater detail, but comparisons to oxygen defects will be drawn as well.

2.2.1 Exciton localization and spectroscopic properties

The creation of luminescent defects alters the electronic structure of the SWCNT and introduces a significant sp^3 character in the otherwise sp^2 -hybridized lattice, thus leading to a breaking of the local symmetry.¹⁴⁰ As a consequence, the zero-momentum $E_{11}(\text{B})$ and $E_{11}(\text{D})$ excitons, which are linear combinations of the KK and K'K' excitonic states (see Chapter 2.1.4) and only separated by few meV in pristine SWCNTs,¹⁰⁴ split into a lower-energy, stabilized E_{11}^* state and a higher-energy, destabilized E_{11}^{up} state (Figure 2.7b).¹³⁸ Because of the energetically lower potential of the E_{11}^* state, mobile excitons that diffuse along the SWCNT are localized at the defect site. Hence, exciton trapping at luminescent defects, which occurs on picosecond time scales as shown by transient absorption spectroscopy,¹⁴¹ effectively poses a competing pathway to diffusive quenching. Owing to the large energetic difference ($\sim 100 \text{ meV}$),¹⁴² excitons remain localized at sp^3 defects even at room temperature.

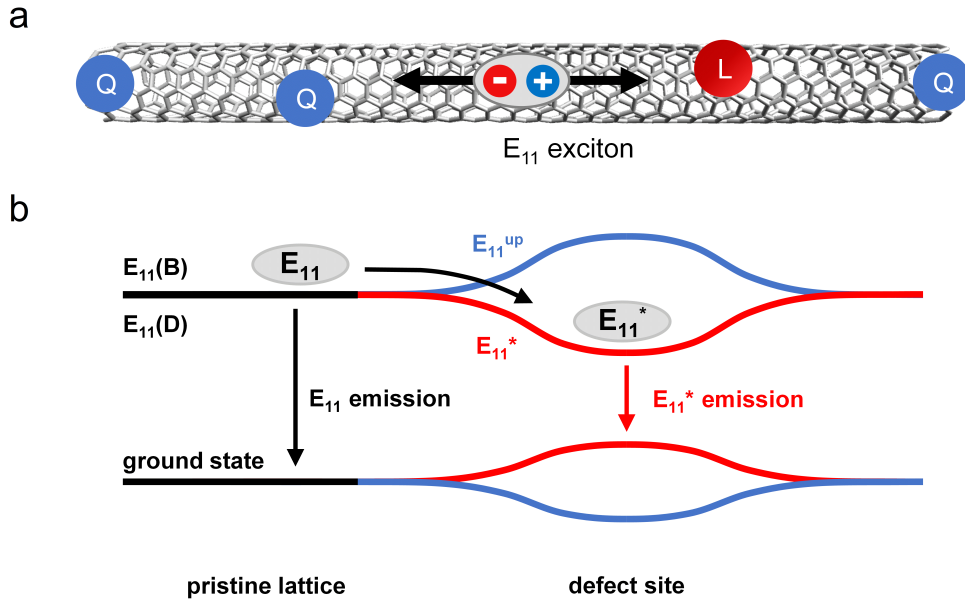


Figure 2.7: (a) Exciton diffusion along a (6,5) SWCNT with exciton-quenching (Q) and luminescent (L) defects. (b) Luminescent defects cause local symmetry-breaking and exciton-trapping in a bright, lower-lying state that gives rise to E_{11}^* emission. States marked in red (blue) colors possess the same parity.

Radiative relaxation from the energetically lower-lying E_{11}^* state gives rise to a red-shifted E_{11}^* defect emission feature at the expense of E_{11} emission intensity, as shown in Figure 2.8a. The difference between the energies of defect and E_{11} emission is referred to as optical trap depth ΔE_{opt} and exhibits an inverse correlation with the nanotube diameter.^{16,23,139} Since defect-localized excitons are no longer prone to diffusive quenching, their emission efficiency is exclusively determined by the rates of intrinsic radiative and non-radiative decay pathways (Figure 2.8b). For both pristine SWCNTs^{106,143} and emissive defects,¹⁴⁴ theory predicts radiative lifetimes of 1–10 ns. However, while diffusion-controlled quenching limits the lifetime of E_{11} excitons in solution-processed nanotubes at room temperature to ~ 10 ps, defect-localized excitons typically exhibit PL lifetimes on the order of a few 100 ps.^{139,145} The increase in exciton lifetime might lead to an overall increase in PLQY,^{16,145} but it was shown that this brightening strongly depends on the initial nanotube length and quenching site density.²² As such, high-quality, air-suspended SWCNTs grown *via* CVD across trenches and functionalized in the vapor phase even revealed a decrease in overall emission efficiency upon introduction of sp^3 defects.¹⁴⁶ It should be emphasized that defect emission is only observed for low concentrations of luminescent defects that are well-separated along the SWCNT. Due to the low number of defects in such samples, defect-state absorption is very weak and only observable for highly chirality-pure dispersions of functionalized nanotubes (*e.g.*, from polymer-wrapping).^{22,23,147} For high defect densities, the formation of extended electronic states, and thus excitons, is prevented since the lattice is too disrupted,²³ which results in a decreasing and ultimately vanishing luminescence.

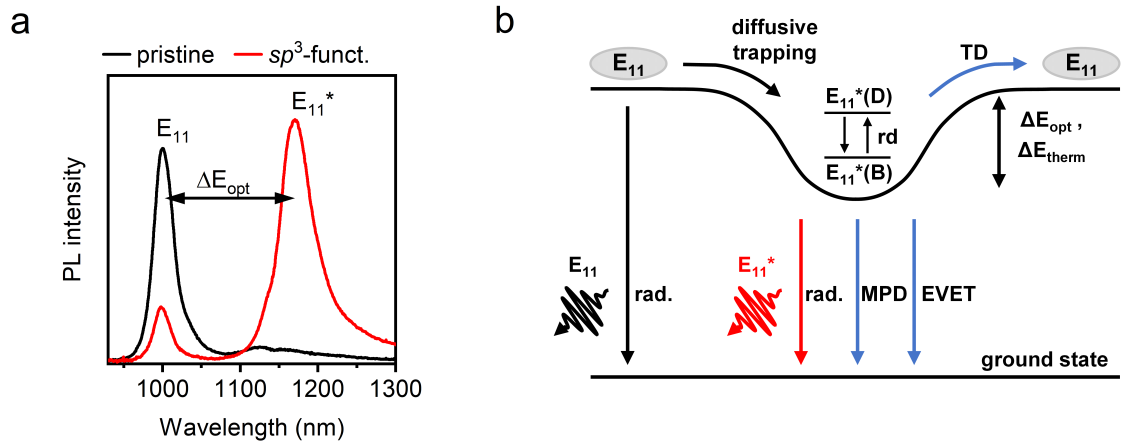


Figure 2.8: (a) PL spectra of pristine and sp^3 -functionalized (6,5) SWCNTs. (b) Schematic illustration of exciton dynamics at luminescent defects. Radiative and non-radiative decay pathways for E_{11}^* excitons are marked as red and blue lines, respectively.

Localization at defect sites effectively prevents diffusive exciton quenching, but at the same time enhances other non-radiative decay pathways (Figure 2.8b). Studies of the relaxation dynamics of luminescent defects introduced to different nanotube chiralities revealed that the main non-radiative decay pathway for trapped excitons is multi-phonon decay (MPD)¹³⁹ due to the enhanced exciton–phonon coupling upon localization.¹²⁹ As the optical gap decreases, less phonons are required for the relaxation process, which results in higher MPD rates.¹³⁹ Hence, larger-diameter SWCNTs functionalized with the same defect type exhibit shorter PL lifetimes^{23,139} and lower emission efficiencies.^{16,23}

In addition to MPD, Förster resonance energy transfer from the SWCNT to the environment (typically solvent) has been shown to deactivate defect-localized excitons.¹⁴⁴ The efficiency of this process is directly proportional to the absorption coefficient of the solvent in the energy range of defect emission (~ 1 eV), and since the latter typically corresponds to vibrational modes of solvent molecules, this relaxation pathway is also referred to as electronic-to-vibrational energy transfer (Evet).^{144,148,149} It was demonstrated that Evet strongly reduces the PL lifetime of functionalized SWCNTs dispersed in polar solvents (*e.g.*, H_2O) or coated with polar surfactants.^{144,150}

Furthermore, defect-localized excitons can be promoted back to the E_{11} level *via* thermal detrapping (TD). Notably, temperature-dependent PL measurements revealed a substantially lower thermal detrapping energy ΔE_{therm} (~ 100 meV for (6,5) SWCNTs with E_{11}^* defects) compared to the optical trap depth ($\Delta E_{opt} \sim 180$ meV).¹⁴² While the term $\Delta E_{opt} - \Delta E_{therm}$ has been attributed to the reorganization energy due to deformation of the nanotube lattice upon exciton trapping,¹⁴² the small measured Stokes shifts (~ 20 meV)²² indicate that this discrepancy is more likely the result of a significant energy splitting of the ground state at the defect site (see Figure 2.7b).¹³⁸ Moreover, ΔE_{therm} has been shown to strongly depend on the defect type.^{23,142}

As for the E_{11} level, each type of luminescent defects is associated with a manifold of different excitonic states, from which only one is bright and gives rise to radiative relaxation to the ground state, while the others are optically dark. Theoretical and experimental studies provided evidence that the ordering of bright and dark states depends on the defect type^{142,151,152} and that the lowest-energy singlet in aryl- and alkyl-functionalized SWCNTs is bright.¹⁵³ In contrast to that, the lowest state for oxygen defects is likely dark.¹⁴⁵ As a consequence, redistribution (rd) between bright and dark states within the defect manifold (Figure 2.8b) gives rise to a biexponential PL decay at room temperature.¹³⁹ Considering all the factors detailed above, the cumulative rate for exciton relaxation from sp^3 defects is given as the sum of individual rate constants for radiative and non-radiative decay pathways according to¹⁴⁴

$$\frac{1}{\tau_{\text{long}}} = \frac{1}{\tau_{\text{rad}}} + \frac{1}{\tau_{\text{MPD}}} + \frac{1}{\tau_{\text{EVET}}} + \frac{1}{\tau_{\text{TD}}} + k_{\text{other}} \quad (2.8)$$

where k_{other} includes all other irreversible relaxation processes. Since recombination can occur at any time, the short lifetime component is determined by the rate constants for exciton redistribution ($1/\tau_{\text{rd}}$) as well as exciton decay:¹⁴⁴

$$\frac{1}{\tau_{\text{short}}} = \frac{1}{\tau_{\text{rd}}} + \frac{1}{\tau_{\text{long}}} \quad (2.9)$$

It should be noted that at low temperatures, the thermal energy is not sufficient to allow for exciton redistribution among the bright and dark states, and so the decay becomes monoexponential with $1/\tau_{\text{long}}$.^{154,155} As proposed by He *et al.*, the relative amplitude of the long lifetime component (A_{long}) reflects the instantaneous exciton population in the bright defect state.¹⁴⁴

One of the most important features of emissive defects is the fact that they act as zero-dimensional states that can host only one exciton at any given time.¹⁵⁰ By virtue of this two-level character, luminescent defects give rise to high-purity single-photon emission at room temperature and in the NIR.^{18,19} Enhancing the radiative relaxation rate in functionalized SWCNTs coupled to plasmonic nanocavities *via* the Purcell effect even led to the demonstration of photon indistinguishability, which is a major requirement for emitters to enable their use in quantum information processing.²⁰ Another consequence of the two-level system is the saturation of defect emission at significantly lower exciton densities (*i.e.*, excitation powers) compared to E_{11} , which arises from state-filling due the much longer lifetime of defect-localized excitons (~ 100 ps) compared to the diffusion time to the defect sites (~ 10 ps).¹⁵⁶ Hence, the defect-to- E_{11} PL ratio is highly dependent on the measurement conditions, which hinders the direct comparison between different samples. Instead, the defect density can be reliably quantified *via* the Raman D/G⁺ ratio (see Chapter 3.5.2).¹⁴⁷

Thus far, the optical properties of luminescent defects were mainly investigated in solution or in single nanotubes deposited on a substrate, and only limited data on the impact of different environments is available in the literature. For functionalized SWCNTs dispersed in different solvents, no changes in defect emission wavelengths and oscillator strengths were observed,¹⁴⁴ which agrees with the theoretically predicted weak dipolar interactions with the environment owing to the relatively small dipole moment induced by defect formation.¹⁵¹ However, film deposition resulted in a broadening of the defect emission peak compared to the dispersion,¹⁵⁷ and removal of the polar surfactant from SWCNTs on polystyrene significantly prolonged the defect PL lifetimes by suppressing non-radiative decay *via* EVET.¹⁵⁰ Additional evidence for environmental effects on defect emission was provided by low-temperature PL spectroscopy of individual SWCNTs deposited on glass or embedded in a polymer matrix, which revealed variations in the relative emission intensities of different defect configurations possibly due to substrate quenching.¹⁵⁸ Finally, PL quenching through charge carriers in electrochemically doped SWCNT films (oxygen- and aryl-functionalized) was found to be more pronounced for defect-localized compared to mobile excitons.^{157,159}

2.2.2 Role of defect structure

While exciton localization at luminescent defects generally gives rise to red-shifted emission, there are several factors that determine the trapping potential, and thus the magnitude of the spectral red-shift. For aryl and alkyl sp^3 defects, it is commonly assumed that two fragments bind to the nanotube lattice to produce a closed-shell structure.¹⁶⁰ As predicted by theory and confirmed experimentally, the spectroscopic properties of the induced defect are predominantly dictated by the relative positions of these fragments on the nanotube lattice.^{17,151} Binding of the first defect group, which might occur *via* a radical or ionic mechanism, forms a reactive intermediate that contains an unpaired electron or charge which becomes delocalized over the *ortho* and *para* positions, as shown in Figure 2.9a. Subsequent binding of a second fragment saturates the intermediate and produces a stable, charge-neutral structure with a fixed binding configuration.

For chiral nanotubes such as (6,5) SWCNTs, this second binding event gives rise to six different possible defect structures, each associated with a different energy.¹⁵⁸ In fact, the resulting spectral diversity due to multiple defect configurations on the same SWCNT or in an ensemble is evident from PL spectra of individual functionalized nanotubes at cryogenic temperatures.^{147,158} As shown for achiral zigzag SWCNTs, the number of chemically distinct configurations, and thus the spectral variation, is reduced in nanotube hosts with higher symmetry.¹⁷ It should be noted that configurations where the fragments bind further apart are considered to be non-luminescent defect structures.^{140,158} As suggested by Saha *et al.*, nanotube functionalization with aryl defects inherits a selectivity for *ortho* configurations.¹⁷ Among them, the two most commonly encountered arrangements for chiral SWCNTs are

*ortho-L*₉₀ (also labelled as *ortho*⁺⁺) and *ortho-L*₃₀ (*ortho*⁺) that are associated with E_{11}^* and E_{11}^{*-} emission peaks, respectively (Figure 2.9b).

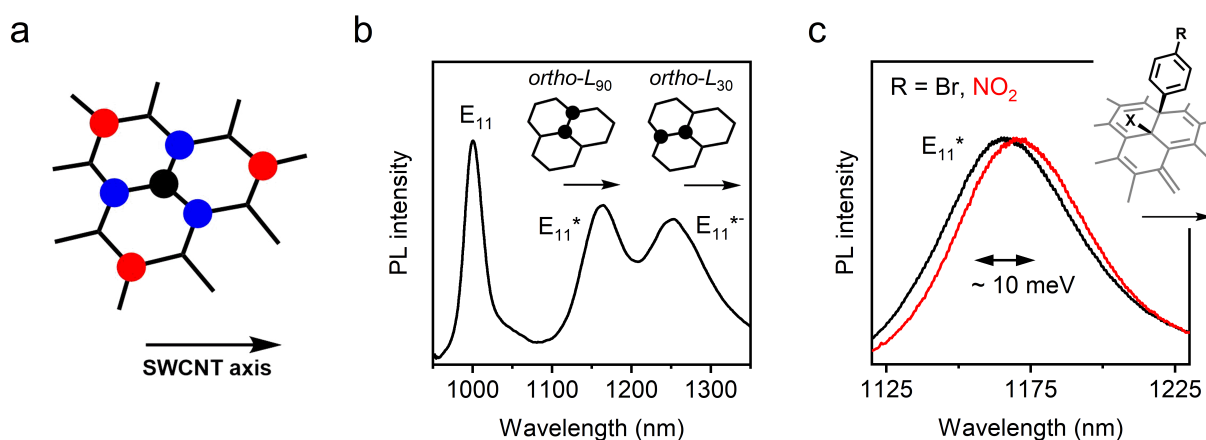


Figure 2.9: (a) Different binding configurations for sp^3 defect fragments on a (6,5) SWCNT lattice. The binding site of the first fragment is marked in black, and the possible *ortho* and *para* positions for binding of the second fragment are indicated in blue and red, respectively. The arrow corresponds to the orientation of the nanotube axis. (b) PL spectrum of a (6,5) SWCNT dispersion with both E_{11}^* and E_{11}^{*-} defects. Insets show the hypothesized molecular arrangements of the two defect fragments. (c) Defect emission from (6,5) SWCNTs with bromoaryl and nitroaryl E_{11}^* defects, respectively.

In addition to that, the localization potential and thus defect emission wavelength for a given binding configuration varies with the chemical nature of the attached fragment and the Hammett constant of its substituents. The optical trap depth increases with increasing electron-withdrawing character,^{16,22,161,162} as exemplified in Figure 2.9c for aryl-functionalized (6,5) SWCNTs with bromo- and nitrophenyl defects. Furthermore, a lower *s*-character of the defect carbon atom binding to the nanotube lattice shifts the emission to longer wavelengths.¹⁶² However, the impact of defect hybridization and electrostatic properties on exciton localization is substantially lower than the effect of the binding configuration.¹³

So far, the impact of the pairing group that saturates the reactive intermediate has been neglected. This fragment may either be a second aryl (alkyl) defect moiety, or a hydroxyl group or hydrogen atom that is abstracted from the solvent. Calculations corroborated that the electronic structure and optical properties of the defect remain largely unaffected by substitution of the pairing group.¹⁵¹ Nevertheless, a recent study found that steric interactions between the two fragments might favour the formation of a certain binding geometry.¹⁶⁰

While the discussion above focussed on aryl or alkyl sp^3 defects in SWCNTs, the case of oxygen functionalization is special in that only one atom binds to the nanotube lattice. However, oxygen-functionalized SWCNTs display a variety of different emission features as well. In this case, the main E_{11}^* and E_{11}^{*-} emission features are attributed to binding of the oxygen adduct in an ether and epoxide configuration (Figure 2.10a), respectively, and low-

temperature PL spectroscopy even revealed a splitting of the E_{11} transition into different states upon functionalization.¹⁵²

2.2.3 Covalent functionalization of SWCNTs

Over the past decade, a large variety of synthetic approaches to introduce luminescent defects to SWCNTs has been reported. The employed functionalization agents and reaction conditions depend strongly on the nanotube sample, *e.g.*, surfactant-dispersed in water,¹⁶ polymer-wrapped in organic solvents,²² or deposited on substrates.¹⁶³ Commonly, (6,5) SWCNTs are used, but functionalization of other chiralities with smaller or larger diameters was reported as well^{16,139} and revealed a decreasing reactivity with decreasing π -orbital misalignment (*i.e.*, strain) either due to a larger tube diameter or due to different orientations of the reactive bonds with respect to the tube axis.^{17,23} While Figure 2.10 and the following Section provide an overview over selected methods for covalent SWCNT functionalization, more details can be found in a recent review on this topic.¹⁶⁴

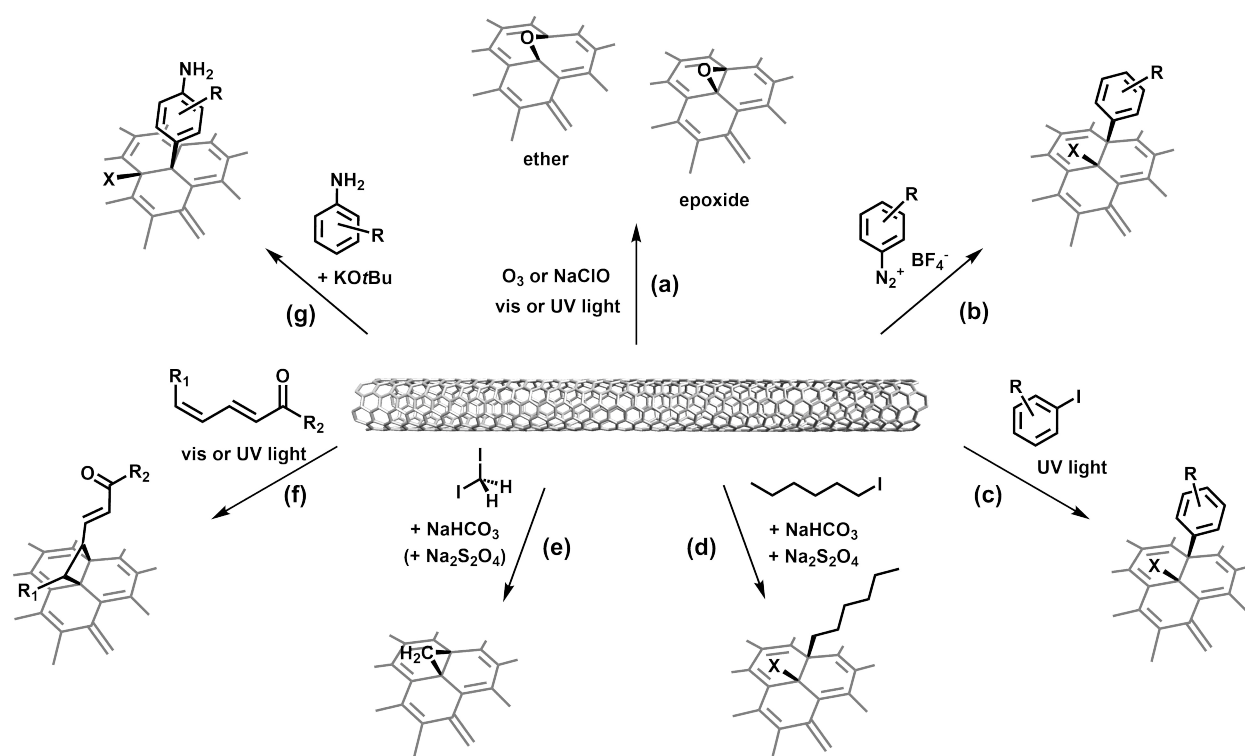


Figure 2.10: Selection of synthetic methods to introduce luminescent defects in SWCNTs. (a) Introduction of oxygen defects (ether, epoxide) with ozone^{138,145} or sodium hypochlorite;¹⁶⁵ creation of aryl defects from (b) pre-formed diazonium salts^{16,139} or (c) aryl iodides under UV irradiation;^{146,166} reductive coupling to introduce (d) monovalent alkyl defects¹⁶¹ or (e) divalent methylene defects;^{161,162} (f) photochemical [2+2] cycloaddition with enones;¹⁶⁷ and (g) nucleophilic addition of anilines.²³

The first intentional creation of emissive defects in aqueous SWCNT dispersions was achieved by ozone treatment, which is hypothesized to produce an ozonide species that subsequently

rearranges to a more stable ether or epoxide configuration (Figure 2.10a).¹³⁸ Aside from ozonolysis,^{138,145,152} oxygen defects were introduced using hypochlorite under UV light¹⁶⁵ or in the solid state *via* electron beam deposition of aluminum oxide or silicon oxide.^{18,163,168}

Due to their synthetic tunability and often higher emission efficiencies, however, luminescent aryl and alkyl sp^3 defects have attracted considerably more attention. In this regard, diazonium chemistry offers a particularly versatile approach and has frequently been used to attach aryl groups with different substituents, and thus functionalities, predominantly to water-dispersed SWCNTs (Figure 2.10b).^{16,139,169,170} Even though the reaction is relatively slow, it can be accelerated through light irradiation,¹⁷¹ or conducted on a large scale in a one-pot approach with *in situ* generated diazonium compounds from aniline derivatives and sodium nitrite in chlorosulfonic acid.¹⁷²

Likewise, the introduction of aryl defects can be accomplished through reaction with aryl halides under ultraviolet (UV) irradiation (Figure 2.10c).¹⁶⁶ Under these conditions, emissive defects can also be created from nitrobenzene or anilines.¹⁷³ Recently, photochemical functionalization of CVD-grown, air-suspended SWCNTs with iodobenzene in the gas phase was demonstrated. This controlled functionalization enabled the analysis of PL emission from the same nanotubes before and after defect introduction and without the influence of the solvent or surfactant environment.¹⁴⁶

Furthermore, functionalization with alkyl groups from the corresponding iodides can be achieved either in a Billups–Birch reaction^{174–176} or *via* reductive alkylation using sodium dithionite (Figure 2.10d).^{153,154,161} The latter process involves milder conditions and can also be extended to aryl iodides as well as divalent defects from diiodide precursors.¹⁶¹ Similarly, divalent alkyl defects can be attached solely in the presence of sodium bicarbonate (Figure 2.10e),¹⁶² and photochemical reaction with enones creates defects *via* [2+2] cycloaddition (Figure 2.10f).¹⁶⁷

As discussed in the previous Section, the optical properties of luminescent defects are mainly governed by their binding configuration on the nanotube lattice, which can lead to large spectral variations in functionalized SWCNT emission. Indeed, most of the abovementioned methods yield mixtures of E_{11}^* and E_{11}^{*-} defects at least for the commonly employed (6,5) SWCNTs. A preference for E_{11}^* defects is observed in functionalization reactions with diazonium salts,^{16,139} or with photoexcited aromatic compounds in the presence of dissolved oxygen (but not under inert conditions).¹⁷³ In contrast to that, *ortho*-substituted diazonium compounds¹⁷⁷ or the introduction of divalent methylene defects¹⁶² give rise to predominantly E_{11}^{*-} emission.

Thus far, the vast majority of functionalization methods uses aqueous SWCNT dispersions. However, the superior purity of polymer-wrapped nanotube samples and the beneficial properties of organic solvents (*e.g.*, higher viscosity and vapor pressure) make them better suited

for film deposition and device integration. To this end, two recently established protocols enable the controlled covalent functionalization of toluene-dispersed SWCNTs. As demonstrated by Berger *et al.*, E_{11}^* defects can be introduced to PFO-BPy-wrapped (6,5) SWCNTs using commercial diazonium salts that are solubilized in toluene with the aid of acetonitrile as polar co-solvent and an ether crown as phase-transfer agent.²² Moreover, Settele *et al.* reported that nucleophilic addition of aniline derivatives in the presence of the strong organic base potassium *tert*-butoxide (KO*t*Bu) selectively creates E_{11}^{*-} defects in polymer-wrapped, small- and large-diameter SWCNTs (Figure 2.10g).²³ These two approaches provide the basis for the experiments conducted in this thesis.

2.2.4 Impact on charge transport

As discussed in the previous Sections, the spectroscopic properties of luminescent defects in semiconducting SWCNTs have been intensely investigated and are already well-understood. Since covalent sidewall functionalization leads to a disruption in the electronic structure, they should also affect the nanotube's electrical properties. However, to date, little research efforts were directed at the impact of luminescent nanotube defects on charge transport. While the charge transport properties of individual SWCNTs and their networks will be reviewed in detail in Chapter 2.4, the following discussion is restricted to the limited number of studies involving electrical measurements of covalently functionalized SWCNTs.

Thus far, the impact of sp^3 defects on the nanotube conductivity or resistivity has been mainly studied using individual SWCNTs that were electrically contacted with two electrodes and exposed to an aqueous diazonium salt solution.^{178,179} In such experiments, Wilson *et al.* observed discrete upward and downward steps in the nanotube resistance, which they interpreted as signatures of the attachment and detachment of single defects.¹⁷⁸ Steps were ~ 6 k Ω ($\sim 20\%$ of the initial resistance), which was in good agreement with quantum theoretical calculations of short (metallic) nanotube segments¹⁸⁰ and significantly lower than for oxidative defects.^{181–183} Similar observations were made by Bouilly *et al.* who reported a change in nanotube conductance between $\sim 20\%$ and two orders of magnitude, depending on the number of attached defects which was controlled by exposing only parts of the SWCNT to the reactant solution through patterning of nanowells.¹⁷⁹ Electrically-controlled diazonium functionalization of two-terminal devices with metallic or semiconducting SWCNTs, however, revealed pronounced differences in the magnitude of resistance increase upon defect creation depending on the initial device resistance rather than electronic type of the nanotube.¹⁸⁴ It should be noted that divalent methylene adducts – as opposed to monovalent aryl defects – were found to preserve the conductance in single-nanotube devices based on either semiconducting or metallic SWCNTs.¹⁸⁵

Despite these advances, all previous reports had in common that they were lacking spectroscopic data to provide insights into the type of introduced defects, that is, whether they were

exciton-quenching or luminescent defects, and their binding configuration. On top of that, in some of these reports, the electronic type of nanotube was not specified. As a result, a comprehensive picture of the impact of low-level functionalization with luminescent defects on the charge transport properties of semiconducting SWCNTs is still missing. This includes the question whether sp^3 defects act as trapping sites for charge carriers in a similar fashion as they localize diffusing excitons, or rather as scattering centers. Moreover, fundamental aspects such as the impact of the defect binding configuration and nanotube chirality as well as the population of, and emission from, defect sites under electrical excitation remain unclear. Finally, no studies have been directed at networks of functionalized SWCNTs which are often used as charge transport and emission layers in thin film devices such as, *e.g.*, light-emitting field-effect transistors (see Chapter 2.3.3). The interaction of charge carriers with sp^3 defect sites and defect-localized excitons in active optoelectronic devices based on semiconducting SWCNT networks will be the main focus of this thesis.

2.3 Field-effect transistors

A thin film field-effect transistor (FET) is a three-terminal device in which the current flow through a semiconducting layer between two electrodes, called source and drain, can be controlled by the potential applied to a third electrode, the gate, which is separated from the semiconductor by an insulating layer, the gate dielectric (Figure 2.11). Upon application of a voltage between gate (V_g) and source, which is commonly set to ground potential ($V_s = 0$ V), mobile charge carriers are accumulated at the semiconductor/dielectric interface. Thereby, a conductive channel of length L and width W and a typical thickness of few nanometers is formed between the source and drain contacts. Applying a voltage between source and drain ($|V_d| > 0$ V) leads to a current flow (drain current, I_d), whereas the current between source and gate (gate current or leakage current, I_g) is limited to the nanoampere to picoampere range by the dielectric. As such, V_g can modulate the current flow over several orders of magnitude, which enables the use of FETs as electronic switches in circuits¹⁸⁶ and active-matrix displays.¹⁸⁷ Moreover, FETs are highly suitable tools to investigate the charge transport properties of the semiconducting material.¹⁸⁸

Figure 2.11 shows a schematic layout of a FET in a bottom-contact, top-gate configuration, as used in this thesis. The nomenclature indicates the relative positions of the source/drain contacts and the gate electrode with respect to the semiconducting layer. Other device architectures (*e.g.*, bottom-gate, top-contact FETs on a doped silicon wafer with thermally-grown SiO_2 that act as gate and dielectric, respectively) are also possible, but they differ in processing effort and resulting device performance.^{189,190} However, the basic working principle of FETs, as detailed in the following, does not depend on the device structure.

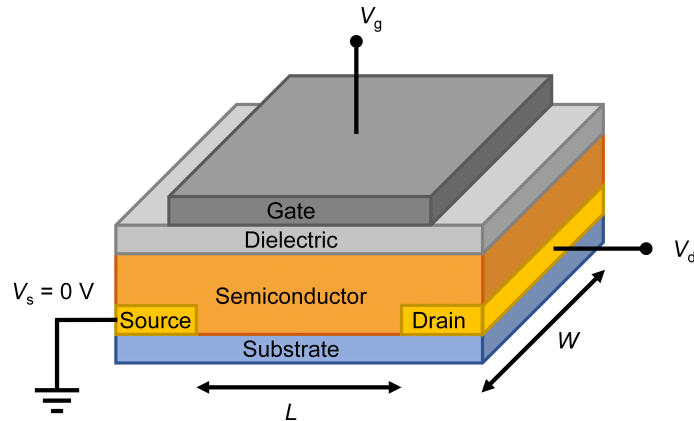


Figure 2.11: Schematic layout of a bottom-contact, top-gate FET with channel length L and width W . Under typical device operation conditions, the potential of the source electrode is set to ground ($V_s = 0$ V), and voltages are applied to the gate (V_g) and drain (V_d) electrodes, respectively.

2.3.1 Basic principle of unipolar FETs

Upon application of a gate voltage that exceeds the threshold voltage (V_{th}), mobile charge carriers are accumulated in the semiconducting layer at the interface to the gate dielectric. The threshold voltage is determined by the energetic positions of the band edges as well as additional trap states that are located within the bandgap of the semiconductor due to, *e.g.*, defects in the film, impurities, or disorder at the interface to the dielectric. For $V_g > V_{th}$, the density of accumulated mobile charge carriers per unit area (Q_{mob}) is given by

$$Q_{mob} = C_i(V_g - V_{th}) \quad (2.10)$$

with the areal capacitance $C_i = \frac{\epsilon_r \epsilon_i}{d_i}$ that is determined by the permittivities of free space (ϵ_r) and the dielectric material (ϵ_i), and the thickness of the dielectric layer (d_i). Assuming that source and drain electrodes are held at ground potential, the potential profile in the channel is constant and the carrier density distribution is homogeneous.

The application of a drain voltage V_d creates a lateral electric field and thus, the potential becomes dependent on the channel position, *i.e.*, the distance to the contact electrodes.¹⁹¹ Notably, the channel length needs to be significantly larger than the thickness of the dielectric layer ($L > 10d_i$),¹⁹² so that the charge distribution is determined by the gate field rather than the lateral field between source and drain (gradual channel approximation).¹⁸⁹ Considering only drift transport and neglecting diffusion currents, the drain current can be expressed as

$$I_d = \mu C_i \frac{W}{L} \left[(V_g - V_{th})V_d - \frac{1}{2}V_d^2 \right] \quad (2.11)$$

where the charge carrier mobility μ is assumed to be independent of the carrier density.¹⁸⁹ Depending on V_d , two regimes are commonly distinguished, as depicted in Figure 2.12a. In the linear regime, V_d is small compared to $(V_g - V_{th})$, which gives rise to a linear increase in I_d with V_g and simplifies Equation 2.11 to

$$I_{d,lin} = \mu_{lin} C_i \frac{W}{L} (V_g - V_{th}) V_d \quad (2.12)$$

When V_d is further increased and becomes larger than $(V_g - V_{th})$, a local depletion region is formed at the drain electrode, and the channel is pinched off. Consequently, the drain current cannot increase further, and the so-called saturation regime is entered. The linear and saturation regimes can be clearly identified in the output characteristics of a FET that show I_d versus V_d at a constant V_g (Figure 2.12b). Additionally, the transfer characteristics of a transistor (I_d versus V_g for a constant V_d ; see Figure 2.12c) allow for the direct extraction of various figures of merit for device operation (*e.g.*, on-voltage V_{on} and on/off current ratio I_{on}/I_{off}).¹⁸⁹

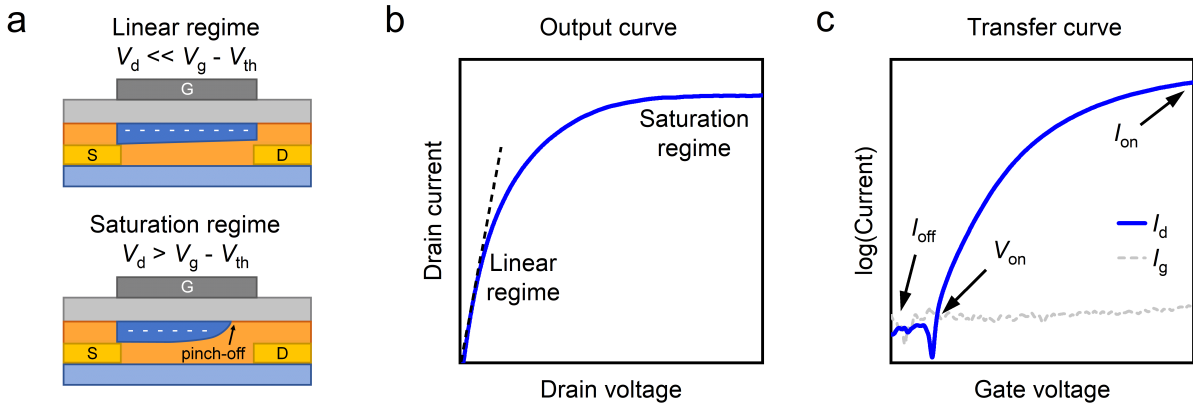


Figure 2.12: (a) Schematic illustration of linear (top) and saturation (bottom) regimes of device operation for a unipolar, n -type FET. (b) Corresponding output characteristics (at constant V_g) and (c) transfer characteristics (at constant V_d).

An important figure of merit for FET operation is the charge carrier mobility μ , which determines the maximum switching speed of the device and the current flow for a given gate and drain voltage.^{193,194} In the linear regime, the mobility can be calculated from the transconductance $\frac{\partial I_d}{\partial V_g}$ according to Equation 2.13.

$$\mu_{lin} = \frac{\partial I_d}{\partial V_g} \cdot \frac{L}{WC_i V_d} \quad (2.13)$$

Importantly, the charge carrier mobility is not a material constant, but depends strongly on the carrier density, device layout, film morphology, and measurement conditions. Furthermore, it should be emphasized that this expression is based on the gradual channel

approximation and neglects the effect of, *e.g.*, contact resistance for carrier injection that occurs in non-ideal devices.^{195,196} Moreover, the derivation of Equation 2.13 assumes a continuous and uniform semiconductor layer, which is neither the case for single SWCNTs nor for nanotube arrays and networks.¹⁹⁷ The additional problem of capacitance extraction in SWCNT FETs will be discussed in Chapter 2.4.1.

2.3.2 Ambipolar and light-emitting FETs

Thus far, the polarity of the charge carriers involved in current flow through the transistor was largely neglected, and the derived equations are applicable to unipolar *n*-type (electron conduction, $V_g > 0$) as well as *p*-type (hole conduction, $V_g < 0$) FETs. Various semiconducting materials including SWCNTs, however, support accumulation and transport of both holes and electrons (ambipolar charge transport).^{189,198} Depending on the applied gate and drain voltages with respect to the threshold voltages for hole ($V_{th,h}$) and electron ($V_{th,e}$) accumulation, either only one type of charge carriers, or both types at the same time, are present in the channel. Figure 2.13a schematically depicts a FET that is biased in the ambipolar regime.

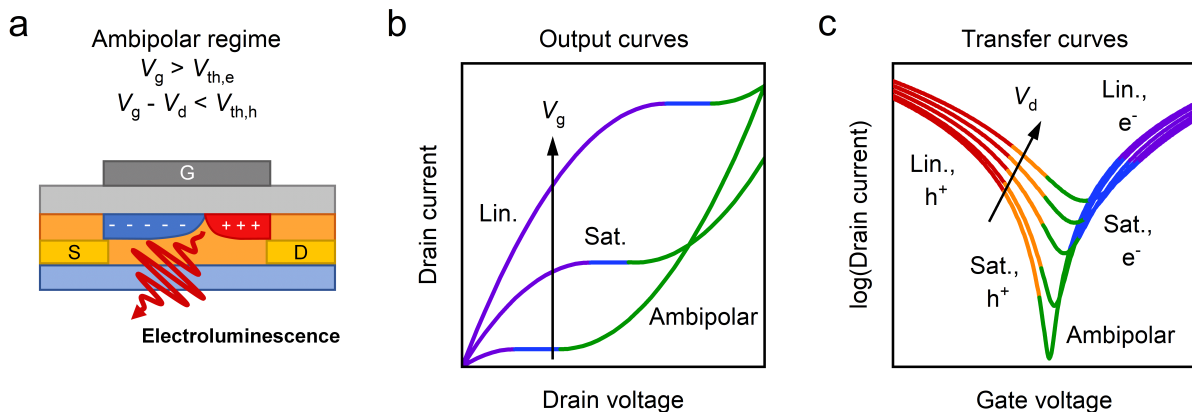


Figure 2.13: (a) Schematic illustration of a FET that is biased in the ambipolar regime. For $V_g > V_{th,e}$ and $V_g - V_d < V_{th,h}$, electrons are injected from the source, whereas holes are injected from the drain electrode. (b) Corresponding output characteristics (at constant V_g) and (c) transfer characteristics (at constant V_d). Colors indicate the different transport regimes. Output and transfer curves were calculated with a simplified model assuming equal hole and electron mobilities¹⁹¹ and show the evolution with increasing V_g and V_d , respectively.

For a unipolar *n*-type FET, the shape of the output characteristics was discussed in the previous Section. Starting in the linear regime, an increase in drain voltage results in a saturation of I_d and a pinch-off of the channel ($V_g - V_d < V_{th,e}$). In an ambipolar FET, even higher V_d gives rise to hole injection from the drain electrode, and the true ambipolar regime ($V_g - V_d < V_{th,h}$) is entered.^{191,199} This operating regime is characterized by a superlinear increase in drain current with drain voltage, as shown in Figure 2.13b.

Likewise, upon variation of V_g at a fixed V_d , the device switches between the different operating regimes as evident from the transfer curves in Figure 2.13c. The typical V-shape of the ambipolar transfer characteristics can be explained by a superposition of the branches of unipolar p - and n -type FETs.¹⁸⁹ In addition to the linear and saturation regimes for hole and electron transport, the ambipolar regime can be identified from the transfer curves in the region where the unipolar branches overlap. It should be noted that a positive increase in V_d at a given V_g facilitates hole injection from the drain, and therefore shifts the minimum of the transfer curve (V-point) to higher currents and higher values of V_g . Similarly, the V-point is shifted to lower V_g for a negative increase in V_d .¹⁹¹

In the ambipolar regime, electrons and holes are simultaneously accumulated, and the accumulation layers meet at a certain position in the channel. This region can be described as a pn -junction where the carrier density approaches zero and charge carriers of opposite polarity recombine.¹⁹⁹ Ambipolar carrier recombination gives rise to exciton formation and thus light emission from the transistor channel, which is referred to as electroluminescence (EL).²⁰⁰ The recombination zone is typically narrow ($< 1 \mu\text{m}$)²⁰¹ compared to the channel length (several μm), and its position between the contact electrodes is determined by the applied gate and drain voltages.²⁰² Through variation of V_d and V_g , the emission zone can be moved across the channel, thus enabling a visualization of current pathways.²⁰³ It should be noted that EL can also arise in unipolar FETs due to impact excitation from strongly accelerated charge carriers at the electrode edges.²⁰⁴

EL has been observed for light-emitting FETs (LEFETs) based on various semiconducting materials such as single-crystals,²⁰⁵ polymers,^{202,206} inorganic quantum dots,²⁰⁷ transition metal dichalcogenides,²⁰⁸ and semiconducting SWCNTs.^{109,110,209,210} By combining the switching properties of a FET with light emission of a light-emitting diode (LED),^{202,211} LEFETs are ideally suited to assess both the optical and electrical properties of the semiconducting layer within the same device.²⁰⁰

2.3.3 SWCNT network transistors

Thanks to the progress in sorting techniques, the application of semiconducting SWCNTs as active materials in FETs has reached a mature stage by now.^{7,188} However, the performance of SWCNT transistors can differ largely depending on the number of nanotubes that bridge the channel.²¹² Transistors based on individual semiconducting SWCNTs show extremely high charge carrier mobilities of 10^3 – $10^4 \text{ cm}^2(\text{Vs})^{-1}$ and even outperform monocrystalline silicon FETs,^{213,214} but are difficult to fabricate on a large scale and cannot tolerate any residual metallic nanotubes. These problems mostly persist for aligned SWCNT arrays that can be deposited from solution, *e.g.*, *via* the Langmuir–Schaefer method²¹⁵ or dielectrophoresis.⁷⁷ Notably, high-performance FETs and ring oscillators were recently demonstrated based on dense, highly aligned nanotube arrays prepared on a wafer scale by dip-coating.²¹⁶

In contrast to that, randomly oriented networks of semiconducting SWCNTs (for an atomic force micrograph, see Figure 2.14a) are easily and reproducibly obtained on a large scale using established deposition techniques such as spin-coating,⁷⁸ aerosol-jet printing,^{217,218} ink-jet printing,^{219,220} or gravure printing.²²¹ Due to the electron–hole symmetry of the nanotube DOS close to the Fermi level (compare Figure 2.4), SWCNT network FETs exhibit ambipolar transport characteristics (see the transfer curve in Figure 2.14b) at least with the typically employed high-work function metal contacts (*e.g.*, gold, palladium, platinum)²²² and when no intentional or unintentional doping (*e.g.*, electron trapping due to oxygen/water)²²³ is applied. As a result of inter-nanotube carrier hopping (see Chapter 2.4.2), such networks typically exhibit charge carrier mobilities of $1\text{--}100\text{ cm}^2(\text{Vs})^{-1}$ while maintaining on/off current ratios of $> 10^6$ (Figure 2.14b,c).^{78,224} These mobility values are comparable to those of amorphous or polycrystalline silicon, which makes SWCNT network FETs promising candidates for applications in flexible and stretchable electronics.^{7,212} In fact, ring-oscillators operating at gigahertz (GHz) frequencies²²⁵ and medium-scale integrated circuits²²⁶ based on semiconducting SWCNT networks have been demonstrated on flexible substrates.

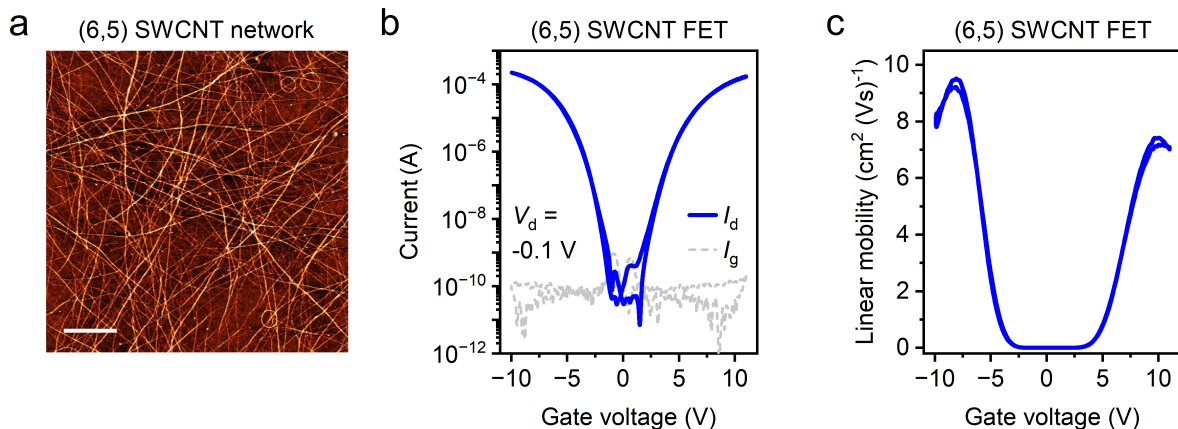


Figure 2.14: (a) Atomic force micrograph of a spin-coated (6,5) SWCNT network on SiO₂. The scale bar is 500 nm. (b) Linear transfer characteristics ($V_d = -0.1\text{ V}$) of an ambipolar (6,5) SWCNT network FET. (c) Gate voltage-dependent linear mobility calculated from (b) according to Equation 2.13.

Given the typically long channel lengths (tens of micrometers) and the high purity of available semiconducting SWCNT inks, the performance of SWCNT network FETs is not limited by residual metallic nanotubes as their concentrations are not sufficient to form percolating paths. However, beyond the semiconducting purity of the networks, the electrical characteristics of SWCNT network transistors are influenced by a large variety of different factors.⁷⁸ For example, the formation of Schottky barriers between semiconducting nanotubes and metal electrodes leads to contact resistance for carrier injection, as shown for SWCNTs with different metal contacts.^{227–229} Hence, the rational optimization of SWCNT FETs requires a fundamental understanding of charge transport mechanisms in purely semiconducting SWCNT networks, as discussed in detail in Chapter 2.4.

Furthermore, owing to their high ambipolar carrier mobilities and diameter-dependent emission features, SWCNT networks are ideally suited as charge transport and emission layers in LEFETs. Indeed, transistors based on SWCNT networks exhibit EL *via* electron–hole recombination upon application of appropriate gate and drain voltages.^{230–232} Even though external EL emission efficiencies for SWCNT LEFETs are very low ($\sim 0.01\%$),^{9,231} the advantage of light-emitting nanotube devices is their emission in the NIR spectral range close to application-relevant telecommunication wavelengths.²³³ For example, excitonic EL from electrolyte-gated (10,5) SWCNT network transistors at ~ 1300 nm is already within the telecommunication O-band (1260–1360 nm), and trion EL is even further red-shifted.¹³³ Moreover, spectrally and spatially resolved EL can be used to study the preferential current pathways in SWCNT networks (see Chapter 2.4.3).^{231,232}

2.4 Charge transport in semiconducting SWCNTs

In the early stages of nanotube research, investigations of their charge transport properties were complicated by the poorly controlled and varying sample compositions especially with respect to the presence of both semiconducting and metallic SWCNT species. The advances in sorting techniques (see Chapter 2.1.2) nowadays allow for the preparation of exclusively semiconducting or even chirality-pure nanotube samples and their device integration. As detailed in Chapter 2.3.3, random networks of SWCNTs are especially suitable as active layers in field-effect transistors and electronic circuits,^{78,225,234} as they are easily obtained on a large scale with typical solution-based processing techniques such as spin-coating or printing.²¹⁸ However, the superior purity of semiconducting SWCNTs has not only fuelled the progress in device optimization, but has also allowed researchers to study the many factors that influence both the microscopic and macroscopic charge transport in such networks.¹⁸⁸ This Section discusses the charge transport properties of semiconducting SWCNTs and their networks with a particular focus on intra- *versus* inter-nanotube transport, and gives a brief overview over the various experimental techniques that have been used to elucidate the underlying mechanisms.

2.4.1 Charge transport in individual nanotubes

The intrinsic transport properties of individual semiconducting SWCNTs are governed by their diameter, band structure, and DOS (see Chapter 2.1.3). Charge transport in short, defect-free SWCNTs is ballistic,²³⁵ but for nanotubes longer than the electron mean free path ($< 1 \mu\text{m}$),^{37,39} diffusive band transport is observed. Since elastic scattering in nanotubes is weak, charge transport in the diffusive regime is limited by inelastic carrier scattering with phonons or lattice defects.³⁵ Consequently, a decrease in temperature gives rise to an increase in maximum conductance and charge carrier mobility due to a lower phonon

scattering rate, as shown theoretically and experimentally.^{213,236} According to an empirical relation introduced by Perebeinos *et al.*, the impact of electron–phonon scattering on the intrinsic charge carrier mobility μ of a defect-free SWCNT can be described by²³⁶

$$\mu(T, d) = \mu_0 \frac{300 \text{ K}}{T} \left(\frac{d}{1 \text{ nm}} \right)^\alpha \quad (2.14)$$

where d is the nanotube diameter, T is the temperature, $\mu_0 = 12,000 \text{ cm}^2(\text{Vs})^{-1}$ and $\alpha = 2.26$. For a single (6,5) SWCNT ($d = 0.757 \text{ nm}$), Equation 2.14 yields an intrinsic carrier mobility of $\sim 6,400 \text{ cm}^2(\text{Vs})^{-1}$ at room temperature, whereas values well-above $10,000 \text{ cm}^2(\text{Vs})^{-1}$ are calculated for larger nanotube diameters. Measurements on transistors with single, CVD-grown nanotubes found lower effective mobilities that were still on the order of 10^3 to $10^4 \text{ cm}^2(\text{Vs})^{-1}$ and exhibited nearly the same temperature and diameter dependence.²¹³

Notably, the 1D DOS of SWCNTs leads to a strong dependence of the mobility on the charge carrier density (compare Figure 2.14c). As shown experimentally and theoretically for individual nanotubes and networks, the mobility initially increases with carrier density, until it reaches a maximum and subsequently decreases again.^{93,213,237,238} This observation can be rationalized by the reduction in the number of final states for scattered charge carriers upon filling of the first subband, but a sudden increase in scattering channels once the Fermi level reaches the higher subband.^{35,239} As shown for electrolyte-gated nanotubes, even higher carrier densities lead to filling of the second subband and thus a second mobility maximum.²³⁸

The intrinsic electronic structure of nanotubes also gives rise to a quantum capacitance which is proportional to the DOS at the Fermi level and possesses electron–hole symmetry.²³⁷ In a device, the total capacitance is a series combination of the electrostatic and the quantum capacitance, and since the latter is typically smaller ($\sim 4 \cdot 10^{-10} \text{ F m}^{-1}$), it needs to be taken into account.²⁴⁰ Additionally, nanotubes as 1D wires couple differently to a planar gate electrode.²³⁷ Together with the fact that SWCNT networks are discontinuous rather than dense films, this behaviour results in a device capacitance of a nanotube transistor that is significantly overestimated by a simple plate–plate model, especially for sparse networks or thin dielectrics.^{7,197,241} Experimentally, the capacitance of SWCNT network FETs was found to depend strongly on the network density, whereby saturation of the carrier mobility and on-conductance was observed for linear densities of $> 15 \mu\text{m}^{-1}$.¹⁹⁷

2.4.2 Charge transport in nanotube networks

While the intrinsic charge transport properties of an individual nanotube can be directly derived from their well-defined electronic structure, the case of SWCNT networks is arguably more complicated. The first, obvious parameter to influence the conductivity of a nanotube network is its density, *i.e.*, the degree of interconnectivity. For low-density, 2D networks

(below or around the percolation threshold²⁴²), charge transport has been described with percolation models, *e.g.*, to assess the impact of the degree of alignment or the content of residual metallic nanotubes on the overall conductance.^{243,244} SWCNT network densities for practical applications ($> 10 \mu\text{m}^{-1}$) are typically far above the percolation threshold and thus, these models do not apply anymore.¹⁹⁷ However, as discussed above, the capacitance of a SWCNT network, and thus carrier mobility, depend strongly on the network density.^{197,241}

Aside from the network density, a multitude of different factors exists that directly contribute to conductance or resistance in semiconducting SWCNT thin films, as visualized in Figure 2.15. The energetic landscape for charge transport is created by the distribution of different nanotube diameters (*i.e.*, bandgaps) as well as the surrounding dielectric and dipolar environment. For individual nanotubes, scattering with surface phonons reduces the intrinsic carrier mobility especially for polar substrates (*e.g.*, SiO_2) or gate dielectrics with a high dielectric constant ε (*e.g.*, HfO_2).²⁴⁵ In fact, large energetic disorder and charge trapping induced by the dielectric layer were found to limit the performance of SWCNT network transistors.^{8,246} To this end, bilayer polymer and metal oxide dielectrics combine the advantageous properties of a low trap density at the semiconductor/dielectric interface and a high capacitance to enable low-voltage device operation, as demonstrated for a range of semiconductors including SWCNT networks.^{247,248}

With respect to the dielectric environment, there is especially the question regarding the impact of residual surfactant or wrapping polymer from the sorting process (compare Chapter 2.1.2) that are commonly regarded as barriers to charge transport. For the latter, a further differentiation between excess, unbound polymer and polymer chains that are tightly wrapped around the nanotubes is necessary. Unbound polymer in solution can be easily removed by filtration and/or solvent rinsing of the SWCNT networks after deposition. However, while some studies showed that excess polymer can alter the temperature dependence of charge transport,²⁴⁹ others found that it does not significantly affect the carrier mobility.²⁵⁰ Removal of the strongly bound polymer is more challenging and requires more elaborate approaches. The use of supramolecular polymers that can be cleaved and washed off the as-deposited SWCNT films was demonstrated to enhance the performance of nanotube network transistors and thermoelectric devices.^{251,252} In contrast to that, removal of PFO-BPy in (6,5) SWCNT networks through metal complexation with a rhenium salt²⁵³ mainly gave rise to a higher degree of bundling.⁸⁵ Such nanotube bundles are associated with increased scattering²⁵⁴ and thus deterioration of the transport properties, hence further highlighting the complex interplay of different contributions to the overall conductivity and the difficulty to analyze the impact of one parameter alone. Aside from bundles, carrier scattering in nanotube networks might also occur at inter-nanotube junctions⁹⁴ as well as intentional (*e.g.*, luminescent sp^3 defects; see Chapter 2.2.4)¹⁷⁹ or unintentional lattice defects (*e.g.*, from processing).³⁵

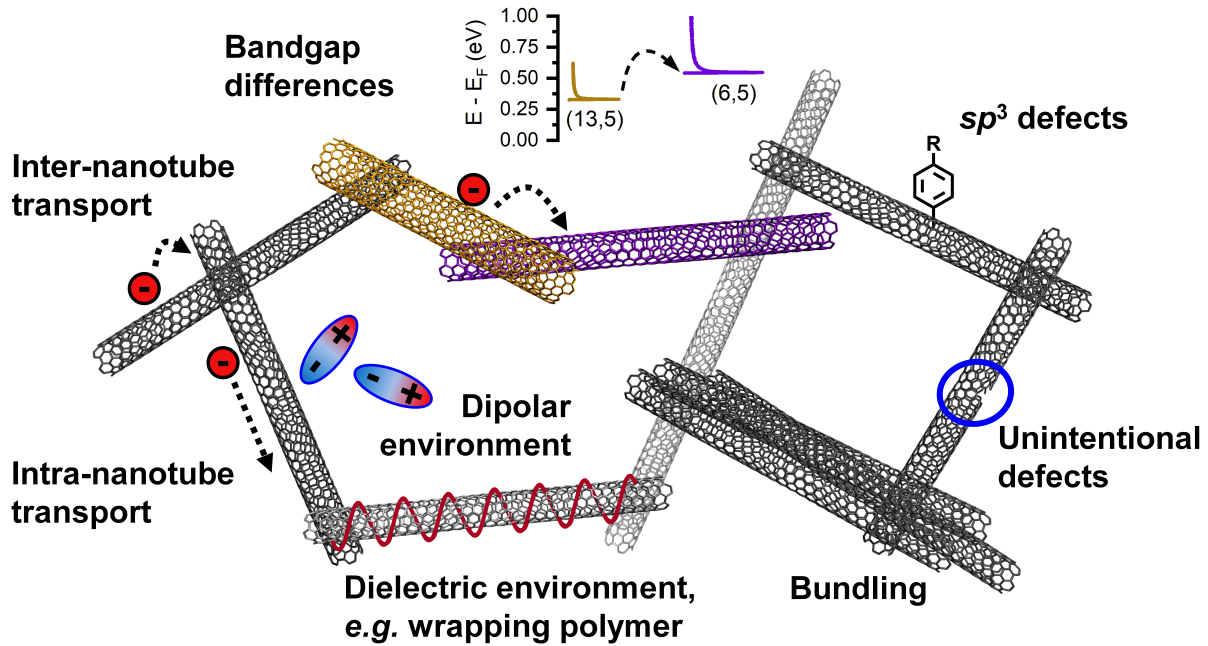


Figure 2.15: Illustration of different contributions to conductance or resistance in dense networks of purely semiconducting SWCNTs: Charge carrier transport along nanotube segments (intra-nanotube) and across nanotube–nanotube junctions (inter-nanotube), bandgap differences between different nanotube species, dipolar environment (*e.g.*, at the substrate–semiconductor or semiconductor–dielectric interface), dielectric environment (*e.g.*, due to residual wrapping polymer from the nanotube sorting process), presence of nanotube bundles, as well as scattering at unintentional defects (*e.g.*, from growth or processing) and intentional sp^3 defects. Reprinted from Zorn *et al.*, *Appl. Phys. Rev.* **2021**, *8*, 041318,¹⁸⁸ with the permission of AIP Publishing.

In addition to intra-nanotube transport as detailed in Chapter 2.4.1, charge carriers in SWCNT networks have to cross the junctions between different nanotubes (inter-nanotube transport; see Figure 2.15). These junctions are associated with resistances on the order of 10^2 – 10^5 k Ω ,^{254–256} which is significantly higher than the resistance of an individual nanotube segment (~ 10 k Ω μm^{-1}).^{213,256} Several studies established the strong dependence of the junction resistance on the diameter (proportional to $1/d$) and crossing angle of the nanotubes,^{257,258} their electronic type,²⁵⁵ as well as the presence of SWCNT bundles.^{254,256} Nanotubes on top of one another, *e.g.*, in a bundle or at a junction, also lead to a limited gating efficiency due to field screening.

The prevailing notion is that inter-nanotube junctions are the main bottleneck for charge transport in SWCNT networks.^{188,258,259} Hence, nanotube thin films are commonly regarded as disordered materials, in which the spatial and energetic disorder prevent band transport and the overall conductivity is limited by carrier hopping between the conductive regions. As such, several models that had been originally developed for disordered inorganic or organic semiconductors have been used to describe charge transport in SWCNT networks.²⁶⁰ Among

these models, the variable range hopping (VRH) describes the hopping transport between localized electronic states in the vicinity of the Fermi level.^{190,261} Here, the hopping rate between two states not only depends on their spatial but also their energetic separation. According to the VRH model, the temperature-dependent conductivity $\sigma(T)$ is given by

$$\sigma(T) = \sigma_0 \cdot \exp \left[- \left(\frac{T_0}{T} \right)^{1/n} \right] \quad (2.15)$$

where σ_0 is a temperature-independent prefactor, T_0 is a hopping parameter that depends on the density of states close to the Fermi level, and n is the dimensionality of the system.²⁶² As shown by Schiefl *et al.*, an advantage of this framework is that the characteristic DOS of SWCNTs can be included in a numerical model for charge transport in nanotube networks to capture the dependence of the mobility on charge carrier density.⁹³ The VRH model has been regularly applied to SWCNT networks,^{260,263–265} but several studies also found that it cannot accurately reproduce the temperature dependence of conductivity or carrier mobility over a wider temperature range.^{85,259,262,266}

Another commonly used approach to describe the temperature dependence of conductivity or carrier mobility in SWCNT networks is the fluctuation-induced tunneling (FIT) model, which reads²⁶⁷

$$\sigma(T) = \sigma_0 \cdot \exp \left(- \frac{T_1}{T + T_0} \right) \quad (2.16)$$

The FIT model was originally developed for conducting polymers²⁶⁸ and describes the tunneling of charge carriers through the energy barriers between conductive segments.^{262,267} In Equation 2.16, T_0 describes the lowest temperature that still allows for significant thermally activated transport, and thus marks the transition between the temperature-dependent transport regime at high temperatures, where the model approaches an Arrhenius-type behaviour, and a regime at low T that is characterized by temperature-independent tunneling.²⁶² T_1 is related to the activation energy that is required for a carrier to cross the insulating barrier, and σ_0 is a pre-factor that does not depend on temperature.²⁶² While the FIT model was found to yield better fits for SWCNT networks compared to the VRH model,^{85,246,259} the correlation of the fitting parameters with actual physical network properties remains ambiguous,²⁶⁶ and the nanotube DOS cannot easily be included within this framework.

Notably, carrier hopping across the inter-nanotube junctions is thermally activated and thus, the conductivity and carrier mobility decrease with decreasing temperature both in the VRH and in the FIT model, as evident from Equations 2.15 and 2.16. Indeed, temperature-dependent measurements commonly found thermally activated charge transport in SWCNT thin films.^{85,222,259,262,266} This observation is in stark contrast to single nanotubes, whose

intrinsic mobilities increase upon temperature reduction due to lower phonon scattering as detailed in Chapter 2.4.1. While the characteristic temperature and diameter dependence of individual SWCNTs (compare Equation 2.14) should still apply in a network, these results indicate that the role of nanotube–nanotube junctions might in fact be dominant. Despite this evidence, recent studies on purely semiconducting SWCNT networks with different compositions suggested that the contribution of intra-nanotube transport cannot simply be neglected,^{85,222,266} as discussed in detail in the following Section.

Clearly, the development of an analytical expression or a simulation model that includes intra- and inter-nanotube transport and can describe at least some of the many other influencing factors presents a formidable challenge. Monte Carlo simulations of the resistive properties of random SWCNT networks, containing both intra-nanotube and junction resistances, revealed a strong impact of the network density as well as the length and relative orientation of nanotubes.²⁶⁹ Very recently, Dash *et al.* theoretically investigated the electrical and thermoelectric properties of SWCNT networks by using a random resistor model and found that for an adequate description of the carrier mobility depending on the charge density, the intra-nanotube resistance needs to be taken into account.²⁷⁰

2.4.3 Experimental techniques

Beyond a purely theoretical approach, detailed insights into the underlying physics of charge transport in SWCNT networks can be obtained from a wide range of experimental techniques. To provide the basis for the interpretation of the results of this thesis, the particular focus of this Section is on temperature-dependent and spectroscopic measurements, and the insights gained with regard to the interplay of intra- and inter-nanotube conduction. A comprehensive overview of the experimental methods that have been used to investigate charge transport in networks consisting of purely semiconducting SWCNTs can be found in a recently published review on this topic.¹⁸⁸

Temperature-dependent measurements of carrier mobility and conductivity are a commonly used tool to study charge transport in semiconductors such as organic single crystals²⁷¹ and polymers,²⁷² as they enable a differentiation between different transport mechanisms (*e.g.*, band-like or thermally activated) and allow for testing of proposed analytical models. Indeed, a large number of such studies have been conducted on SWCNT network transistors.^{85,222,246,259,262–264} Importantly, a correction for the contact resistance (compare Chapter 2.3.3), which depends on temperature itself, is strictly required to extract the intrinsic network properties and can be achieved, *e.g.*, by using a gated four-point probe layout.¹⁹⁶ Employing such a device architecture, recent studies revealed higher carrier mobilities with a lower temperature dependence for large-diameter, polydisperse plasma torch SWCNT network FETs compared to purely (6,5) SWCNTs.^{85,222,266} Assuming that carrier hopping across the inter-nanotube junctions is the only limiting factor for transport, the opposite behaviour

would be expected due to the lower junction resistance in the monochiral compared to the multichiral networks. While a partial explanation might be provided by the inverse diameter dependence of the junction resistance,^{257,258} these results indicated that the overall charge transport can be described as a superposition of inter-nanotube hopping and intra-nanotube transport with its intrinsic diameter ($\mu \propto d^2$) and temperature ($\mu \propto 1/T$) dependence.²⁶⁶

While temperature-dependent measurements have provided detailed insights into charge transport mechanisms, they only yield information on the averaged, macroscopic network properties. Especially in SWCNT networks containing multiple species, a discrimination between different chiralities and their transport contributions would be desirable. To this end, the diameter-dependent optical transitions of nanotubes can be utilized as highly sensitive probes (see Chapter 2.1.4) for the distribution of charge carriers and current flow in SWCNT network devices.¹⁸⁸ For example, gate voltage-dependent PL quenching through carrier-mediated, non-radiative Auger recombination revealed the preferential charge accumulation on small-bandgap SWCNTs in multichiral nanotube network transistors.^{231,232}

Unfortunately, PL quenching can arise from either mobile or trapped charge carriers and thus, its correlation with charge transport remains ambiguous. To address this issue, dynamic techniques such as charge modulation spectroscopy in absorption (CMS) and in PL (CMPL; see Figure 2.16 for a schematic illustration) can be used to study charge transport in SWCNT networks.²⁷³ These experiments rely on the modulation of the optical transmission, or luminescence intensity, of the semiconducting layer in an operating FET upon application of a sinusoidal gate voltage (peak-to-peak voltage V_{pp} around an offset voltage V_{os}). The differential change in transmission or PL due to the periodically modulated charge density in the channel is recorded with a lock-in detection scheme and can be assigned exclusively to mobile carriers, since trapped carriers cannot follow the voltage modulation. While CMS has been widely used for FETs based on semiconducting polymers^{274–277} and small organic molecules,^{278,279} the introduction of CMPL spectroscopy might be useful for the study of materials with a low absorption but stronger emission, such as, *e.g.*, luminescent sp^3 defects in semiconducting SWCNTs. Notably, the combination of CMS with a confocal microscopy setup to perform charge modulation microscopy (CMM)²⁸⁰ was used very recently to investigate charge transport in SWCNT networks with micrometer spatial resolution.²⁸¹

Aside from optical excitation, excitons in SWCNTs can also be generated electrically by simultaneous accumulation of electrons and holes in the channel of a nanotube network FET, giving rise to EL *via* electron–hole recombination (see Chapter 2.3.2). As such, EL emission is directly related to the current density, and its spectral and spatial distribution enables the analysis of charge transport in SWCNT networks.^{231,232} For example, the EL shares of small-bandgap (large-diameter) nanotube species in multichiral SWCNT network FETs were significantly higher than observed in the corresponding PL spectra and expected from their relative concentration within the networks.²³² This observation indicated that the nanotubes

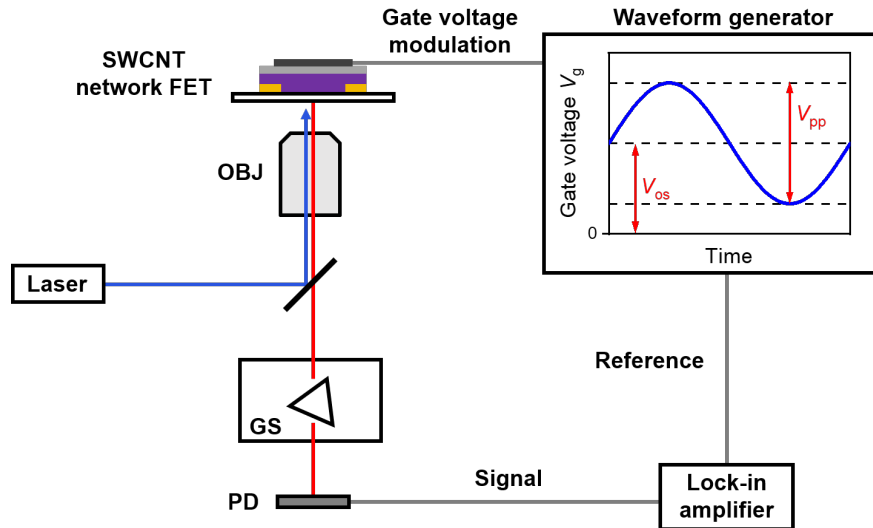


Figure 2.16: Schematic illustration of the setup for charge modulation PL (CMPL) spectroscopy. OBJ, objective; GS, grating spectrograph; PD, photodiode.

with smallest bandgaps contributed predominantly to the current, which was in agreement with the results from CMS and CMPL spectroscopy²⁷³ as well as numerical simulations.⁹³ Furthermore, the notion that the composite EL images reflect the preferential conduction pathways was recently confirmed for photoswitchable SWCNT network transistors with spatially defined regions of high and low carrier mobility that were patterned in the channel by local irradiation.²⁸²

The application of spectroscopic techniques is useful to study charge accumulation and transport depending on the nanotube species, but their diffraction-limited spatial resolution ($\sim 1 \mu\text{m}$) is not sufficient to offer information on the microscopic transport properties. Here, all-optical techniques such as microwave conductivity measurements (in the GHz frequency range) or terahertz (THz) spectroscopy are particularly suited, as they can probe the local carrier conductivity without the need for external electrodes.²⁸³ These experiments allow for a quantitative analysis of intrinsic charge transport properties, such as carrier mobility or scattering time, and can be conducted in a pump-probe scheme to provide access to the ultrafast carrier dynamics on picosecond time scales. For example, time-resolved microwave conductivity measurements were used to study the dynamics of photogenerated carriers in SWCNT dispersions and nanotube-fullerene heterojunctions,^{284,285} and to quantify the doping efficiency in nanotube thin films.²⁸³ THz spectroscopy, on the other hand, revealed significantly higher carrier mobilities and longer scattering times in (6,5) SWCNTs compared to semiconducting graphene nanoribbons²⁸⁶ as well as similar photoconductivity dynamics for semiconducting and metallic SWCNT films.²⁸⁷ Notably, the combination of local THz spectroscopy and macroscopic FET transport measurements has provided fundamental insights into charge transport in a variety of materials including graphene,²⁸⁸ conjugated polymers,²⁸⁹ and networks of transition metal dichalcogenides.²⁹⁰

Chapter 3

Experimental Details and Methods

This Chapter details the materials, sample fabrication procedures, and characterization techniques used in this thesis.

3.1 SWCNT dispersions

3.1.1 Selective dispersion of (6,5) SWCNTs in toluene

Nearly monochiral dispersions of (6,5) SWCNTs in toluene (Sigma Aldrich) were prepared *via* selective polymer-wrapping with the fluorene–bipyridine copolymer poly[(9,9-dioctylfluorenyl-2,7-diyl)-*alt*-(6,6'-2,2'-bipyridine)] (PFO-BPy, American Dye Source, $M_W = 40 \text{ kg mol}^{-1}$) in combination with shear force mixing as an exfoliation method.⁸⁷ CoMoCAT nanotube raw material (Chasm Advanced Materials, batches SG65i-L58 and SG65i-L63, and Sigma Aldrich, batch MKCJ7287) was dried at 130 °C over night and subsequently added at a concentration of 0.4 g L⁻¹ to a solution of PFO-BPy in toluene (0.5 g L⁻¹). The total volume was typically 250 mL. Then, shear force mixing (Silverson L2/Air) was applied at 10,230 rpm for 72–96 h while keeping the temperature at 20 °C with a water cooling bath. The resulting dispersion was centrifuged at 60,000g for 45 min (Beckman Coulter Avanti J-26XP centrifuge), and the supernatant was collected and subjected to another centrifugation step. The sediments were recycled, and the combined supernatants were filtered through a poly(tetrafluoroethylene) (PTFE) syringe filter (Whatman, 5 µm pore size) to remove large aggregates.

3.1.2 Selective dispersion of (7,5) SWCNTs in toluene

(7,5) SWCNTs were selectively dispersed with poly(9,9-dioctylfluorene) (PFO, Sigma Aldrich, $M_W > 20 \text{ kg mol}^{-1}$) from CoMoCAT nanotube raw material (Sigma Aldrich, batch MKCJ7287) under shear force mixing. The process was conducted as described above for the (6,5) SWCNTs except for the concentration of PFO in toluene, which was 0.9 g L⁻¹.

3.1.3 Aqueous dispersion of (6,5) SWCNTs

Aqueous dispersions of (6,5) SWCNTs were prepared by Dr. Han Li and Dr. Benjamin Flavel (Karlsruhe Institute of Technology) *via* the aqueous two-phase extraction (ATPE) method.⁷⁰ CoMoCAT SWCNT raw material (Chasm Advanced Materials, batch SG65i-L58) was sorted in an aqueous two-phase system composed of dextran ($M_W = 70 \text{ kDa}$, TCI) and poly(ethylene glycol) ($M_W = 6 \text{ kDa}$, Alfa Aesar) according to a diameter sorting protocol based on the surfactants sodium deoxycholate (DOC, BioXtra) and sodium dodecyl sulfate (SDS, Sigma Aldrich). First, the DOC concentration was fixed to 0.04% (w/v) and the concentration of SDS was increased to 1.1% (w/v) in order to push all species with diameters larger than (6,5) SWCNTs to the top phase for removal. Then, the SDS concentration was gradually increased from 1.2% to 1.5% (w/v) to collect the (6,5) SWCNT-enriched fractions. Metallic and semiconducting SWCNT species were separated by addition of sodium cholate (SC, Sigma Aldrich; total surfactant concentrations of 0.9% SC, 1% SDS and < 0.02% DOC) and sodium hypochlorite (NaClO, Sigma Aldrich) as an oxidant. The sorted (6,5) SWCNTs were

concentrated using a pressurized ultrafiltration stirred cell (Millipore) with a 300 kDa M_W cut-off membrane and subsequently adjusted to 2% (w/v) DOC for further processing.

3.2 Covalent functionalization of polymer-wrapped SWCNTs

3.2.1 Functionalization with aryldiazonium salts

Covalent functionalization of polymer-wrapped (6,5) SWCNTs with aryldiazonium salts to create $E_{11}^* sp^3$ defects was performed as described by Berger *et al.*²² As functionalization agents, 4-bromobenzenediazonium tetrafluoroborate (Sigma Aldrich, 96%) and 4-nitrobenzenediazonium tetrafluoroborate (Sigma Aldrich, 97%) were used. Due to the low solubility of the diazonium salts in toluene, acetonitrile (MeCN, Sigma Aldrich) was added as a co-solvent (volumetric fraction, 20 vol-%) and the crown ether 18-crown-6 (Sigma Aldrich, 99%) served as phase-transfer agent. (6,5) SWCNTs were functionalized at a concentration of $0.72 \mu\text{g mL}^{-1}$ (Chapter 4) or $0.54 \mu\text{g mL}^{-1}$ (Chapters 5 and 6), corresponding to an optical density of 0.4 cm^{-1} or 0.3 cm^{-1} at the E_{11} absorption peak, respectively. A solution of 18-crown-6 in toluene (concentration of 2 mg mL^{-1} in the final reaction mixture) and the diazonium salt dissolved in appropriate amounts of MeCN were added to the SWCNT dispersion. The degree of functionalization was controlled by the concentration of diazonium salt in the reaction mixture, which was typically between $50 \mu\text{g mL}^{-1}$ and $2000 \mu\text{g mL}^{-1}$. After thorough mixing, the reaction vessel was kept in the dark at room temperature for ~ 16 h. The reaction was stopped by filtration through a PTFE membrane filter (Merck Millipore JVWP, $0.1 \mu\text{m}$ pore size) and the filter cake was washed with MeCN and toluene (10 mL each) to remove unreacted diazonium salt, side-products, and excess wrapping polymer.

3.2.2 Functionalization with aniline derivatives

Luminescent $E_{11}^{*-} sp^3$ defects in polymer-wrapped (6,5) and (7,5) SWCNTs were created according to the protocol developed by Settele *et al.*²³ The functionalization procedure involved the use of SWCNT dispersions with a low content of unbound wrapping polymer, which were obtained from the shear force-mixed dispersions *via* filtration through a PTFE membrane filter (Merck Millipore JVWP, $0.1 \mu\text{m}$ pore size), washing with toluene (10 mL), and re-dispersion in fresh toluene by bath sonication. SWCNTs were functionalized with 2-iodoaniline (Sigma Aldrich, 98%) or 2-bromoaniline (Sigma Aldrich, 98%) in the presence of the strong organic base potassium *tert*-butoxide (KO*t*Bu, Sigma Aldrich, 98%). First, dimethyl sulfoxide (DMSO, Sigma Aldrich, anhydrous) and a solution of KO*t*Bu in tetrahydrofuran (THF, Sigma Aldrich, anhydrous) were added to a solution of the aniline compound in toluene. Then, the polymer-depleted SWCNT dispersion in toluene was added

to the reaction mixture to achieve an optical density of 0.3 cm^{-1} at the E_{11} absorption peak, corresponding to a concentration of $0.54 \text{ }\mu\text{g mL}^{-1}$ for (6,5) SWCNTs and $0.86 \text{ }\mu\text{g mL}^{-1}$ for (7,5) SWCNTs, respectively. The concentrations of the aniline derivative and $\text{KO}t\text{Bu}$ in the final reaction mixture were 29.3 mmol L^{-1} and 58.6 mmol L^{-1} , respectively, and the volumetric fractions were 83.3 : 8.3 : 8.3 vol-% toluene : DMSO : THF. The reaction proceeded under stirring and under the exclusion of light over 30–180 min before it was terminated by vacuum filtration through a PTFE membrane filter (Merck Millipore JVWP, $0.1 \text{ }\mu\text{m}$ pore size) and thorough washing with methanol and toluene (10 mL each) to remove unreacted compounds and by-products.

3.3 SWCNT thin film deposition and field-effect transistor fabrication

Prior to the deposition of SWCNT thin films, dispersions of pristine (6,5) and (7,5) SWCNTs obtained *via* shear force mixing were filtered through a PTFE membrane filter (Merck Millipore JVWP, $0.1 \text{ }\mu\text{m}$ pore size) and the collected nanotube material was washed with toluene to reduce the amount of excess, unbound wrapping polymer. Re-dispersion of the nanotubes by immersing a filter cake with pristine or functionalized SWCNTs in a small volume of fresh toluene and bath sonication (Branson 2510) for 30 min yielded concentrated SWCNT inks which were further processed as detailed below.

3.3.1 Spin-coating of SWCNT networks

Randomly oriented networks of semiconducting (6,5) SWCNTs with and without sp^3 defects on substrates were created through repeated spin-coating (2000 rpm, 30 s) from concentrated toluene dispersions (optical density of $8\text{--}10 \text{ cm}^{-1}$ at the E_{11} absorption peak, corresponding to a concentration of $14.4\text{--}18.0 \text{ }\mu\text{g mL}^{-1}$). After each spin-coating step, samples were annealed at $100 \text{ }^\circ\text{C}$ for 1–2 min. Finally, substrates were rinsed with THF and 2-propanol to remove residual unbound wrapping polymer, and blow-dried with nitrogen.

3.3.2 Aerosol-jet printing of SWCNT networks

Aerosol-jet printing of randomly oriented (7,5) SWCNT networks was accomplished with an Optomec AJ200 printer with a $200 \text{ }\mu\text{m}$ inner diameter nozzle and a movable, heated ($100 \text{ }^\circ\text{C}$) stage. Dispersions of (7,5) SWCNTs with and without sp^3 defects were diluted with toluene to an optical density of $1\text{--}2 \text{ cm}^{-1}$ at the E_{11} absorption peak, corresponding to a concentration of $2.9\text{--}5.7 \text{ }\mu\text{g mL}^{-1}$. To increase the viscosity for aerosol formation, 2 vol-% of terpineol (Sigma Aldrich, mixture of isomers) was added to form the final ink. During the printing process, the SWCNT ink was constantly sonicated and the aerosol was printed

onto the substrates at a carrier gas flow of 30 sccm and a sheath gas flow of 18–24 sccm (both nitrogen). SWCNT networks were created by printing single lines exclusively in the channel area of the transistors, which lowered the material consumption and removed the need for patterning of the semiconductor layer. Subsequent rinsing of the substrates with THF and 2-propanol removed residual terpineol and unbound wrapping polymer, and the samples were blow-dried with nitrogen.

3.3.3 Membrane transfer of SWCNT films

SWCNT films for optical-pump terahertz-probe spectroscopy (Chapter 5) were fabricated by a membrane-assisted transfer technique. Toluene dispersions of pristine and functionalized (6,5) SWCNT dispersions were diluted to an optical density of 0.1 cm^{-1} at the E_{11} absorption peak (concentration, $0.18 \text{ } \mu\text{g mL}^{-1}$). A volume of 10 mL of each dispersion was filtered through a mixed cellulose ester membrane (Merck Millipore VSWP, $0.025 \text{ } \mu\text{m}$ pore size), respectively. Fused silica substrates (PI-KEM) were cleaned by ultrasonication in acetone and 2-propanol, followed by UV/ozone treatment (Ossila E511). The filter membrane was cut to the size of the substrate by using a razor blade, placed on the substrate with the nanotube film facing down, and pressed against it while being wetted with 2-propanol. Then, the sample was immediately immersed in an acetone bath, which dissolved the filter membrane. The acetone was exchanged after 15 min and the washing process was repeated seven times to remove residues of the filter, leaving a SWCNT film on the substrates which was subsequently cleaned through rinsing with acetone and 2-propanol and blow-dried with nitrogen.

3.3.4 Fabrication of BCB-covered substrates

Alkali-free aluminum borosilicate glass substrates (Schott AF32eco, $300 \text{ } \mu\text{m}$ thickness) or pieces of silicon (Si) wafers (Siegert Wafer, $500 \text{ } \mu\text{m}$ thickness with 300 nm thermally-grown silicon dioxide (SiO_2)) were cleaned by ultrasonication in acetone and 2-propanol for 10 min each and subsequently transferred to a nitrogen-filled glovebox for the following steps. Under inert atmosphere, a resin of divinyltetramethylsiloxane-bis-benzocyclobutene (BCB, Cyclotene 3022-35, Lot: D191L7D007-070) was diluted with mesitylene. The dilution factor (typically between five- and ten-fold) was chosen as to give the desired final thickness of the BCB layer. The diluted solution was spin-coated onto the substrates (500 rpm for 3 s, then 8000 rpm for 60 s) and then cross-linked by thermal annealing at $290 \text{ } ^\circ\text{C}$ for 2 min, which rendered the BCB layer insoluble in organic solvents and water. Deposition of SWCNT thin films and device fabrication on BCB-covered substrates was carried out as detailed in the corresponding Sections in this Chapter, with the only difference being that substrates were cleaned only through rinsing with acetone and 2-propanol instead of ultrasonication in order to prevent damage to the BCB layer.

3.3.5 Fabrication of *h*-BN flakes on Si/SiO₂ substrates

Flakes of hexagonal boron nitride (*h*-BN) on Si/SiO₂ substrates were prepared by Tim Wedl under the supervision of Prof. Dr. Alexander Högele at the Ludwig Maximilian University of Munich. High-quality crystals of *h*-BN grown under high pressure were provided by Dr. Takashi Taniguchi and Dr. Kenji Watanabe at the National Institute for Materials Science (NIMS), Tsukuba, Japan.²⁹¹ From these crystals, flakes of different size and thickness were obtained by mechanical exfoliation using adhesive tape. The tape was brought into contact with a Si substrate (525 μm thickness with 80 nm thermally-grown SiO₂), heated to 110 °C for 3 min, and pulled off after cooling to room temperature, which left multiple flakes on the substrate surface. Typical dimensions of the flakes were several tens of micrometers in lateral size and several tens of nanometers in thickness. Substrates were cleaned by rinsing with acetone and 2-propanol prior to the deposition of SWCNT thin films.

3.3.6 Field-effect transistor fabrication

SWCNT network field-effect transistors (FETs) in a bottom-contact, top-gate device architecture were fabricated on alkali-free aluminum borosilicate glass substrates (Schott AF32eco, 300 μm thickness). Substrates were cleaned by ultrasonication in acetone and 2-propanol for 10 min each before spin-coating (4000 rpm, 30 s) of a double-layer photoresist, consisting of a bottom layer of non-photoactive LOR5B resist (micro resist technology, softbaked at 185 °C for 4 min) and a top layer of photoactive S1813 resist (micro resist technology, softbaked at 115 °C for 1 min). Then, the substrates were exposed to UV light ($\lambda = 365$ nm, i-line, 182 mJ cm⁻²) through photomasks (chrome-on-glass, Soda Lime, Compugraphics Jena) with a mask aligner (Suess MicroTec MA6), followed by development of the photoresist through immersion for 24–28 s in a tetramethylammonium hydroxide-based developer (Microposit MF-319). Bottom-contact electrodes were either patterned in an interdigitated electrode layout ($L = 20$ μm, $W = 10$ nm) for light-emitting field-effect transistors (LEFETs) or in a four-point probe layout ($L = 40$ μm, $W = 1$ μm), as shown in Figure 3.1.

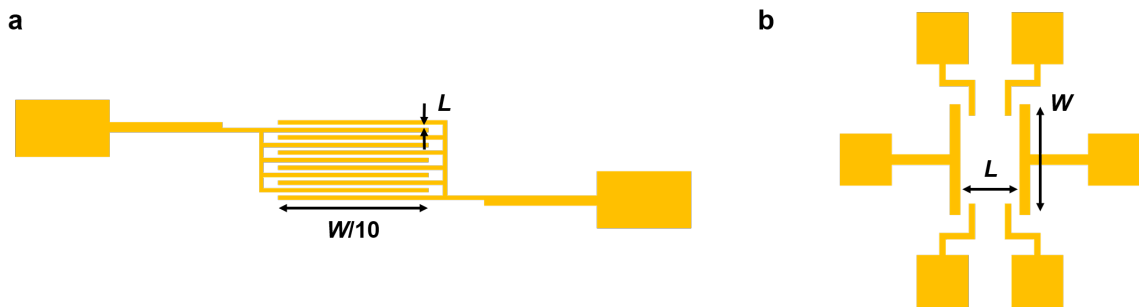


Figure 3.1: Bottom-contact electrode geometries. (a) Interdigitated electrodes ($L = 20$ μm, $W = 10$ nm) for light-emitting field-effect transistors. (b) Four-point probe structure ($L = 40$ μm, $W = 1$ μm) with two sets of voltage probes (width 4 μm, separated by 6 μm from source and drain, respectively). Note the different scales in (a,b).

After deposition of chromium (2–3 nm) as an adhesion layer and gold (30 nm) as the electrode material through electron-beam evaporation (Winter Vakuum Technik HVB 130), the residual photoresist was removed by lift-off in *N*-methyl-2-pyrrolidone (NMP) over night and substrates were cleaned by ultrasonication in acetone and 2-propanol. Then, random networks of SWCNTs were deposited *via* spin-coating or aerosol-jet printing as detailed above. Spin-coated SWCNT networks were subsequently patterned to remove all nanotubes outside the transistor channel area. This was accomplished by performing photolithography as described above to define photoresist structures covering only the channel area, oxygen plasma treatment (Nordson MARCH AP-600/30, 100 W, 2 min), and lift-off in NMP for 30–60 min. Samples were annealed in inert atmosphere at 150 °C for 30–45 min before the deposition of the gate dielectric layer, consisting of a ~ 11 nm poly(methyl methacrylate) (PMMA) layer and ~ 61 nm hafnium oxide (HfO_x). First, a solution of PMMA (Polymer Source, $M_W = 315 \text{ kg mol}^{-1}$, syndiotactic) in *n*-butylacetate (6 g L^{-1}) was spin-coated at 4000 rpm for 60 s, followed by annealing at 80 °C for 2 min. Then, the HfO_x layer was deposited *via* atomic layer deposition (ALD, Ultratech Savannah S100, 500 cycles) at a temperature of 100 °C from a tetrakis(dimethylamino)hafnium precursor (Strem Chemicals) and water as the oxidizing agent. Thermal evaporation (MB-ProVap 3G, M. Braun Inertgas-Systeme) of silver top-gate electrodes (30 nm) through a shadow mask completed the devices.

3.4 Spectroscopic characterization

3.4.1 Luminescence microscopy setup

All room-temperature PL and EL experiments, including charge modulation PL (CMPL) spectroscopy and time-correlated single-photon counting (TCSPC), were performed on a home-built laser setup as schematically depicted in Figure 3.2.

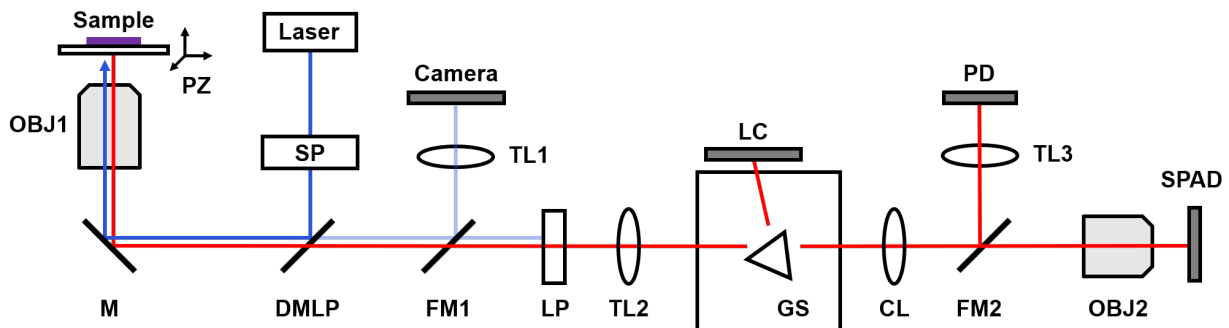


Figure 3.2: Schematic of the luminescence microscopy setup used in this thesis. The laser excitation and the different detection paths are indicated by blue and red lines, respectively.

The setup provided two different laser sources that were used for optical excitation. PL spectroscopy and TCSPC were performed using a picosecond-pulsed supercontinuum laser (Chapters 4 and 5: Fianium WhiteLase SC400, 20 MHz repetition rate; Chapters 6 and 7: NKT Photonics SuperK Extreme, 78.1 MHz maximum repetition rate, typically operated at a repetition rate of 19.5 MHz) coupled to a tunable bandpass filter (Photon etc. LLTF Contrast vis). A 785 nm laser diode (Alphas Lasers LD-785-50) operated in continuous wave (cw) mode served as excitation source for CMPL measurements and non-resonant PL spectroscopy under cw excitation. For both lasers, unwanted residual NIR light was blocked by suitable short-pass filters (**SP**). The laser light was guided to the sample *via* a dichroic long-pass filter (**DMLP**, cut-on 875 nm) and silver mirrors (**M**) and focussed with a NIR-optimized 50 \times objective (**OBJ1**, Olympus, N.A. 0.65).

Samples were placed on a three-dimensional piezo stage (**PZ**, Mad City Labs, Nano-LPS200). For measuring dispersions, a small volume was filled into a quartz cuvette (Hellma Analytics, QX material) that was sealed with a PTFE stopper, tipped to the side, and placed on the sample stage with a clear window facing down. SWCNTs on substrates were mounted with the film facing the objective, whereas spectroscopy on LEFETs was performed through the transparent glass substrate. Samples on glass substrates were imaged by illuminating from the top with the collimated beam of a lamp and projecting the light to a Si **camera** with a flippable mirror (**FM1**) and a tube lens (**TL1**). In all experiments, the sample was approached with the objective until the spectrally-integrated PL intensity on the detector reached its maximum value in order to focus the laser.

For the acquisition of spectra, scattered laser light was separated from the sample emission by the **DMLP** and an additional long-pass filter (**LP**, cut-on 830 nm). A tube lens (**TL2**) focussed the sample luminescence on the entrance slit of a grating spectrograph (**GS**, Princeton Instruments Acton SpectraPro SP2358) whose turret was equipped with two different gratings and a mirror. The emission was spectrally dispersed using a grating with 150 lines mm^{-1} (blaze wavelength 1200 nm) and spectra were detected with a liquid nitrogen-cooled InGaAs line camera (**LC**, Princeton Instruments OMA V:1024-1.7 LN). In a different configuration, the spectrally-selected emission exited the spectrograph and passed a collimation lens (**CL**) before it was either guided to an InGaAs photodiode (**PD**, Thorlabs FGA-10) *via* a flippable mirror (**FM2**) and a tube lens (**TL3**) to perform CMPL spectroscopy or focussed onto a gated InGaAs/InP single-photon avalanche diode (**SPAD**, Micro Photon Devices) with a NIR-optimized 20 \times objective (**OBJ2**, Mitutoyo, N.A. 0.40) for TCSPC measurements. The spectrometer was controlled either with the commercial WinSpec32 software or a custom-made LabVIEW script.

Spectral correction. Before each measurement, background spectra were acquired under dark conditions and subtracted from the sample spectra to account for thermal noise of the detector. All spectra were further corrected for the wavelength-dependent detector efficiency and absorption of optical components in the detection path. To this end, the broadband out-

put of a stabilized tungsten-halogen lamp (Thorlabs SLS201/M) with a known spectral power distribution $I_{theo,lamp}(\lambda)$ was transmitted through the detection path of the setup to measure a spectrum $I_{exp,lamp}(\lambda)$. Sample spectra were corrected according to $I_{corr}(\lambda) = I_{raw}(\lambda)/f(\lambda)$ with the transfer function $f(\lambda) = I_{theo,lamp}(\lambda)/I_{exp,lamp}(\lambda)$.

3.4.2 Voltage-dependent PL and EL spectroscopy

For the acquisition of gate voltage-dependent PL and EL spectra, SWCNT network LEFETs were mounted in the optical setup and the source, drain, and gate terminals were electrically contacted using micropositioners with electrical probe needles. Voltages were applied to the drain (V_d) and the gate (V_g) electrodes with a Keithley 2612A source meter, whereas the source terminal was held on ground potential. The source meter was controlled with a custom-made LabVIEW script. For gate voltage-dependent PL measurements, a small drain voltage of $V_d = -10$ mV was applied to monitor the doping level of the SWCNT film during the experiments by measuring the drain current (I_d). In EL measurements, samples were positioned so that the direction of current flow in the transistor channel was orthogonal to the optical axis of the detection path and consequently the 1D array of the InGaAs **LC**. Devices were illuminated from the top using the collimated output of a broadband lamp to align the center of the channel with the input slit of the spectrometer. The lamp was switched off, and V_d and V_g were adjusted to position the maximum EL signal in the center of the **LC** detector array. Then, the mirror in the **GS** was exchanged for a grating and a spectrum was recorded.

3.4.3 Charge modulation PL spectroscopy

CMPL spectroscopy records the differential change in PL upon modulation of the charge carrier density in a FET device.²⁷³ In CMPL experiments, devices were mounted in the setup and electrically contacted as described above. The source and drain electrodes were shorted and grounded, and V_g was modulated with a sinusoidal signal composed of a peak-to-peak voltage (V_{pp}) around a constant offset voltage (V_{os}) using a Keysight 33600A waveform generator. The modulation frequency f was 363 Hz unless otherwise specified. During this voltage modulation, SWCNT networks were optically excited with the output of the 785 nm cw laser diode. The spectrally-resolved emission was detected with an InGaAs photodiode (**PD**), and the signal was pre-amplified (Femto DLPCA-200 transimpedance amplifier) and fed to a lock-in amplifier (Stanford Research Systems SR830) that was phase-locked to the waveform generator signal. The lock-in detection scheme enabled recording of the periodically changing (with frequency f), differential PL signal (Δ PL). Static PL spectra with no applied bias were acquired in the same setup configuration by modulating the excitation beam with an optical chopper. The setup was controlled with a custom-made LabVIEW script.

3.4.4 Time-correlated single-photon counting

Time-resolved PL decays of SWCNT dispersions and thin films were measured in a TCSPC scheme. The pulsed supercontinuum laser served as excitation source and provided electrical trigger signals to a gated InGaAs/InP single-photon avalanche photodiode (**SPAD**) and a photon counting module (PicoQuant PicoHarp 300). The piezo controller was responsible for time-tagging of detected photons, and histograms of photon arrival times were created by the counting module and subsequently fitted with biexponential functions in a reconvolution procedure using the SymPhoTime64 software. As instrument response function (IRF), the fast, instrument-limited decay of the E_{11} PL of a drop-cast (6,5) SWCNT film at 1000 nm with a full width at half maximum (FWHM) of ~ 84 ps was recorded.

3.4.5 PL quantum yield determination

The PL quantum yield (PLQY), defined according to Equation 3.1 as the ratio of emitted (N_{em}) to absorbed (N_{abs}) photons, was determined *via* an absolute method using an integrating sphere.^{87,292}

$$\text{PLQY} = \frac{N_{em}}{N_{abs}} \quad (3.1)$$

SWCNT samples, which could be either dispersions in a quartz cuvette (Hellma Analytics, QX material) or thin films on glass substrates (Schott AF32eco, 300 μm thickness), were placed in an integrating sphere (Labsphere 4P-GPS-033-SL, Spectralon coating) using suitable holders. Samples were excited directly with the unfocussed output of the pulsed supercontinuum laser which was wavelength-filtered at 575 nm to be in resonance with the E_{22} absorption transition of (6,5) SWCNTs. Light was out-coupled from the integrating sphere with an optical fiber, focussed onto the entrance of the **GS** with the tube lens (**TL2**), and spectra were detected with the InGaAs **LC**. Each set of measurements was performed on the sample itself as well as a reference, which was the cuvette filled with pure solvent in the case of dispersions and the empty sphere in the case of film samples. The number of emitted photons N_{em} was determined *via* integration of the emission spectra that were recorded in the NIR (950–1400 nm) with additional long-pass filters (cut-on 715 nm and 900 nm) inserted in front of the **GS**. By detecting the intensity of the transmitted laser beam in the visible spectral range, the number of absorbed photons N_{abs} was calculated from the difference of the integrated laser signals at 575 nm. Note that the spectral intensity $I(\lambda)$ was recorded on a wavelength scale and therefore had to be multiplied with the wavelength, so that the integral of the resulting quantity $I(\lambda) \cdot \lambda$ was proportional to the number of photons. Spectral correction was performed as described in Chapter 3.4.1. In the case of liquid samples,

a cuvette with pure solvent was placed in the integrating sphere for the acquisition of the calibration lamp spectrum in the NIR to account for the strong absorption of toluene in this wavelength range. To avoid distortions of the spectra through re-absorption effects, liquid samples were diluted to an optical density of 0.1–0.2 cm^{-1} at the E_{11} absorption peak.²⁹³

3.4.6 EL imaging

The EL emission zone in operating SWCNT LEFETs during constant current sweeps was imaged using a NIR-optimized 50 \times objective (Olympus, N.A. 0.65) and a thermoelectrically-cooled InGaAs camera (Xenics XEVA-CL-TE3, 252 \times 320 pixels). Voltages were applied to the devices with a Keysight B1500A semiconductor parameter analyzer. The data was processed and EL images were created using the software ImageJ.

3.4.7 External quantum efficiency measurements

The external EL quantum efficiency (EQE) of SWCNT LEFETs was determined from measurements of the total light output of the devices during constant current sweeps (Agilent 4156C semiconductor parameter analyzer). The devices were placed on top of a calibrated InGaAs photodiode (Thorlabs FGA-21, active area 3.1 mm^2) which was held at 0 V. In this configuration, the silver top-gate acted as mirror to collect most of the emitted light. The EQE at a given drain current I_d was calculated from the maximum photodiode current I_{diode} according to Equation 3.2

$$\text{EQE} = \frac{I_{\text{diode}}}{I_d} \cdot \frac{\int \lambda \cdot EL_{\text{norm}}(\lambda) d\lambda}{\int S(\lambda) \cdot EL_{\text{norm}}(\lambda) d\lambda} \cdot \frac{e}{hc} \quad (3.2)$$

taking into account the spectral sensitivity of the photodiode $S(\lambda)$ weighted by the EL spectrum $EL_{\text{norm}}(\lambda)$ of the sample. As the spectral weight of the mobile E_{11} and defect-localized excitons changes with I_d , EL spectra recorded at similar drain currents as those used in the EQE measurements were utilized for the calculation of EQE values.

3.4.8 Low-temperature and temperature-dependent PL spectroscopy

Low-temperature and temperature-dependent PL spectra (5–300 K) of SWCNT films were measured in a home-built setup as schematically depicted in Figure 3.3. The output of a cw laser diode with 532 nm excitation wavelength (OBIS, Coherent) served as excitation source. The laser beam passed a neutral density filter (**ND**) and a short-pass filter (**SP**, cut-off 750 nm) and was sent to the objective *via* a dichroic long-pass filter (**DMLP**, cut-on 875 nm).

Samples were placed inside the sample chamber (**SC**) of a closed-cycle liquid helium-cooled cryostat (Montana Cryostation s50, base temperature 4.6 K) on an agile temperature sample mount (**ATSM**, with Lakeshore Model 335 temperature controller) and a three-dimensional piezo stage (**PZ**, attocube ANC350 piezo controller). During the measurements, the **SC** was kept under high-vacuum conditions ($< 10^{-5}$ mbar) using a turbopump (Pfeiffer Vacuum). The excitation laser was focussed through the window (uncoated fused silica) of the **SC** with a NIR-optimized $50\times$ objective (**OBJ**, Mitutoyo, N.A. 0.42) which was mounted outside the cryostat. Emitted photons were collected using the **OBJ** and guided to the spectrometer *via* gold mirrors (**M**). Laser light reflected off the sample surface was blocked by the **DMLP** and additional long-pass filters (**LP**). The emission signal was focussed with a tube lens (**TL**) onto the entrance of a Princeton Instruments IsoPlane SCT-320 grating spectrograph (**GS**). Spectra were acquired using a grating with blaze wavelength 1300 nm and 85 lines mm^{-1} and a thermoelectrically-cooled 2D InGaAs camera array (**2D CA**, NIRvana 640ST). To correct for the wavelength-dependent detector efficiency and the absorption of optics, spectral correction was performed as described in Chapter 3.4.1. Temperature-dependent spectra were recorded from the lowest to the highest temperature, waiting for complete thermal equilibration before each acquisition. Imaging of the PL signal from a larger area on the sample surface was achieved by using the mirror grating of the **GS** and expanding the excitation beam with a bi-concave or bi-convex lens that was mounted in front of the **DMLP**.

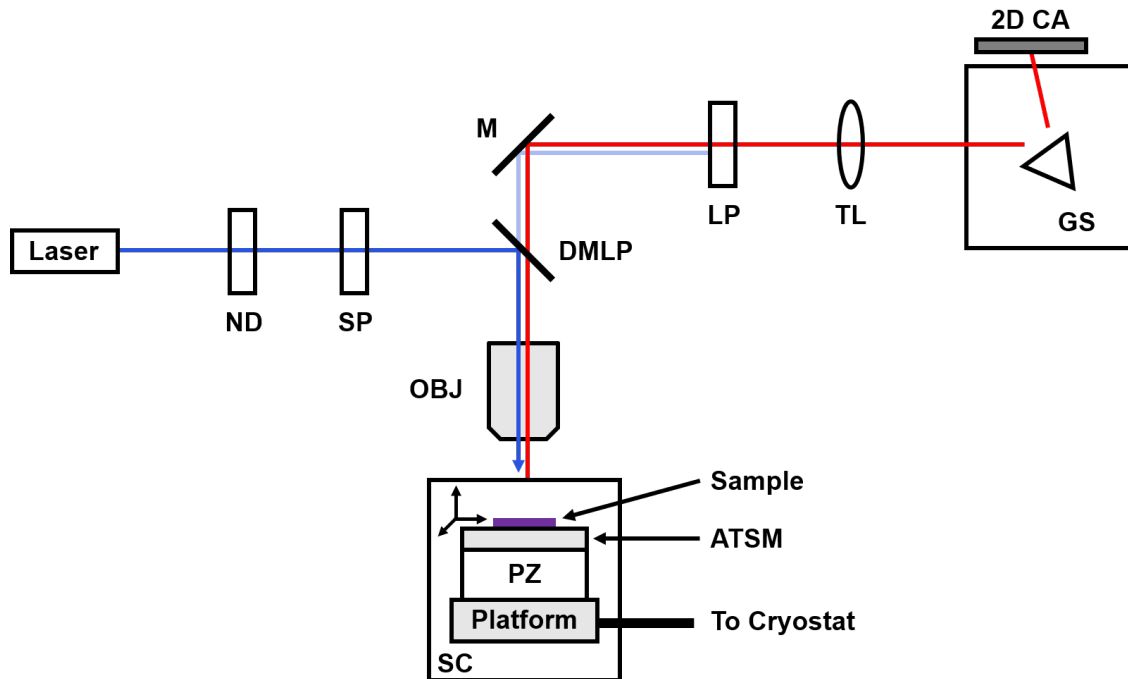


Figure 3.3: Schematic of the setup for low-temperature PL spectroscopy. The laser excitation and the detection path are indicated by blue and red lines, respectively.

3.4.9 Hyperspectral PL imaging on *h*-BN flakes

Hyperspectral PL imaging of spin-coated SWCNT networks on Si/SiO₂ substrates with *h*-BN flakes was performed by Dr. Shen Zhao under the supervision of Prof. Dr. Alexander Högele at the Ludwig Maximilian University of Munich. Samples were mounted in a home-built scanning confocal microscope on piezo-stepping units (ANPxyz101, attocube systems) for positioning with respect to the confocal spot of an apochromatic objective (LT-APO/IR/0.81, attocube systems). A Ti:sapphire laser (Mira900, Coherent) in cw mode was used for excitation around 750 nm with a power of 2 μ W. The PL was spectrally dispersed by a monochromator (Princeton Instruments Acton SP-2500) and detected with a liquid nitrogen-cooled InGaAs array (Princeton Instruments OMA V:1024-1.7 LN).

3.4.10 Optical-pump THz-probe and THz time-domain spectroscopy

Optical-pump terahertz (THz)-probe spectroscopy (OPTP) and THz time-domain spectroscopy (THz-TDS) experiments in Chapter 5 were performed by Wenhao Zheng under the supervision of Dr. Hai Wang and Prof. Dr. Mischa Bonn at the Max Planck Institute for Polymer Research in Mainz. Concentrated (6,5) SWCNT dispersions (optical density of 4–6 cm^{-1} at the E_{11} absorption peak, corresponding to a concentration of 7.2–10.8 $\mu\text{g mL}^{-1}$) stabilized with PFO-BPy (0.1 g L^{-1}) in toluene were measured in a fused silica cuvette (Hellma Analytics) with 1 mm path length. SWCNT films on fused silica substrates (PI-KEM) were prepared by membrane-assisted transfer as detailed above.

The THz spectroscopy setup was powered by a commercial, regenerative-amplified, mode-locked Ti:sapphire laser system (Spectra Physics Spitfire Ace) which provided laser pulses of ~ 50 fs duration with a central wavelength of 800 nm at a repetition rate of 1 kHz. The laser output was split into three different beam paths for the optical pump as well as the generation and detection of THz waves. To generate the optical pump pulses, incident 800 nm laser light was converted to ~ 1000 nm pulses (resonant with the E_{11} transition of (6,5) SWCNTs) with an optical parametric amplifier and mixing stages (Light Conversion, TOPAS). THz probe pulses were generated from the laser light *via* optical rectification in a zinc telluride (ZnTe) crystal along the $\langle 110 \rangle$ orientation and were guided to the SWCNT sample. The transmitted THz wave was sampled by another 800 nm pulse *via* the electro-optic effect in a second ZnTe crystal, and the signal was detected using balanced diodes. In OPTP measurements, the time-dependent photoconductivity was recorded by fixing the sampling beam to the peak of the THz field and varying the time delay between the pump and sampling beam with an optical delay stage. For THz-TDS experiments, the complete THz waveform without and with photoexcitation was sampled at a fixed pump–probe delay. The photoinduced change in THz transmission was calculated and converted from the time domain to the frequency

domain by Fourier transformation. To obtain the complex-valued frequency-dependent photoconductivity, the refractive indices of the solvent cuvette (for measurements in dispersion) or the substrate for film measurements were taken into account.²⁹⁴ During the measurements, the entire THz setup was kept under dry nitrogen atmosphere to avoid THz absorption by water, and samples were either purged with dry nitrogen in the case of nanotube dispersions or placed under vacuum conditions ($< 2 \cdot 10^{-4}$ mbar) in the case of SWCNT films.

3.5 Other characterization techniques

3.5.1 Absorption spectroscopy

Absorption spectra were recorded with a Varian Cary6000i UV-vis-NIR spectrometer. Liquid samples were measured in quartz glass cuvettes (Hellma Analytics, QS material) with 1 cm path length. All spectra were baseline-corrected by measuring the absorption of the cuvette with pure solvent. Film samples were placed in the light path using a custom sample holder.

3.5.2 Raman spectroscopy

Raman spectroscopy was performed with a Renishaw inVia Reflex confocal Raman microscope equipped with a $50\times$ long working distance objective (Olympus, N.A. 0.50) and three different lasers with excitation wavelengths of 532 nm, 633 nm, and 785 nm. Raman spectra of drop-cast or spin-coated SWCNT thin films were obtained by mapping an area of typically $100\times 100 \mu\text{m}^2$ (grating $2400 \text{ lines mm}^{-1}$) and computing the average of > 1000 individual measurements. High-resolution Raman maps were acquired in Streamline mode and peaks were fitted separately using a combination of a Lorentzian and a Gaussian line shape in the Wire 3.4 software. Figure 3.4 shows a representative Raman spectrum of (6,5) SWCNTs.

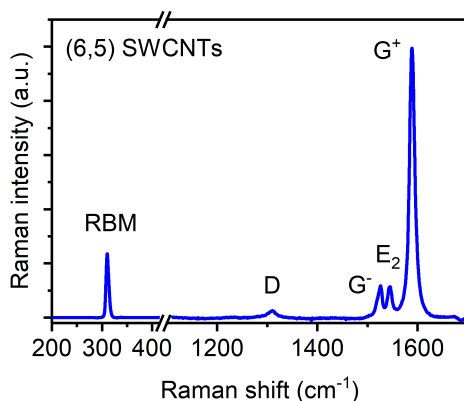


Figure 3.4: Representative Raman spectrum (532 nm excitation) of (6,5) SWCNTs.

The radial breathing mode (RBM, $100\text{--}350 \text{ cm}^{-1}$) depends inversely on the tube diameter and enables an assessment of the sample purity.²⁹⁵ In-plane vibrations of the sp^2 -hybridized

lattice give rise to the G modes (G^- , E_2 , G^+) whose relative intensities and peak positions are highly dependent on the doping level.²⁹⁶ The D mode ($1300\text{--}1350\text{ cm}^{-1}$) is associated with lattice defects and can be used to quantify the degree of disorder, typically *via* its intensity relative to the G^+ mode (D/ G^+ ratio).²⁹⁷ For small-diameter SWCNTs with luminescent defects, the differential change in Raman D/ G^+ area ratio upon covalent functionalization is proportional to the defect density, as shown by Sebastian *et al.*¹⁴⁷

3.5.3 Profilometry

Layer thicknesses of polymer films and metal oxide layers were determined with a Bruker DektakXT Stylus profilometer. For PMMA or BCB layers, films were spin-coated and processed under identical conditions as those in the sample fabrication, and the thicknesses were determined by scanning across grooves that were created by scratching the surface with the sharp tip of a pair of metal tweezers. For HfO_x layers, photolithographically-patterned substrates with parallel lines of photoresist were subjected to ALD together with the SWCNT FET substrates. The residual photoresist was removed *via* lift-off in NMP over night, and the substrates were rinsed with de-ionized water and blow-dried with nitrogen. The thickness was determined by scanning across the edge of the HfO_x film.

3.5.4 Atomic force microscopy

Atomic force microscopy (AFM) to characterize the topography of surfaces was performed under ambient conditions with a Bruker Dimension Icon atomic force microscope in ScanAsyst mode. Images were visualized, processed and analyzed using the open-source software Gwyddion. For the statistical analysis of the lengths of individual SWCNTs, dilute dispersions (optical density of $0.1\text{--}0.2\text{ cm}^{-1}$ at the E_{11} absorption transition) were spin-coated on pieces (approximately $1\times 1\text{ cm}^2$) of a Si wafer (Siegert Wafer, $500\text{ }\mu\text{m}$ thickness with 300 nm thermally-grown SiO_2). Excess polymer was removed through rinsing with THF and 2-propanol, and samples were subsequently blow-dried with nitrogen.

3.5.5 Electrical characterization

Current-voltage characteristics (transfer and output curves) of FETs were recorded with an Agilent 4156C semiconductor parameter analyzer in a nitrogen-filled glovebox. Temperature-dependent electrical measurements were carried out in a cryogenic probe station with a closed cooling cycle (CRX-6.5 K, Lake Shore Cryotronics) under vacuum conditions ($\leq 10^{-6}$ mbar). Experiments were conducted between $25\text{--}300\text{ K}$ starting from the lowest temperature, and for each temperature step (25 K), a 20 min waiting period was included before the actual measurement to ensure full thermal equilibration. Effective device capacitances were determined with an impedance analyzer (Solatron Analytical ModuLab XM MTS) from

capacitance–voltage sweeps. The devices were operated as plate capacitors with source and drain electrodes shorted and grounded, and the gate voltage was modulated with a peak-to-peak voltage of 200 mV and a frequency of 100 Hz. Capacitances were extracted in the on-state of the devices.

Chapter 4

Charge Transport in SWCNT Networks with Luminescent Defects

This Chapter discusses the impact of covalent functionalization on charge transport in SWCNT networks and on their emission spectra in light-emitting field-effect transistors.

The results presented in this Chapter were published in part in N.F. Zorn *et al.*, *ACS Nano* **2021**, *15*, 10451–10463.²⁹⁸ Modified versions of previously published Figures are presented with permission of the American Chemical Society. Light-emitting field-effect transistors with sp^3 -functionalized SWCNT networks were fabricated in collaboration with Felix J. Berger (Heidelberg University).

4.1 Introduction

As detailed in Chapter 2.2, covalent sp^3 functionalization presents a powerful approach to enhance the spectroscopic properties of semiconducting SWCNTs. Exciton localization at sp^3 defects prevents diffusive quenching and gives rise to red-shifted PL with improved ensemble quantum yields in dispersion^{16,22} and high-purity single-photon emission.¹⁹ The variation of the chemical nature of the attached moieties, or more importantly the selective introduction of defects with a specific binding configuration on the nanotube lattice, result in different optical trap depths and consequently spectral red-shifts.^{23,161} In combination with the diameter-dependent luminescence of SWCNTs, this enables tuning of their emission wavelengths across the NIR spectral range, which opens up avenues for the application of sp^3 -functionalized SWCNTs as quantum light sources at telecommunication wavelengths.²¹

While the spectroscopic properties of sp^3 defects have been investigated intensively, their impact on charge transport in SWCNTs remains poorly understood. Measurements on single-nanotube transistors exposed to an aqueous diazonium salt solution suggested that the introduction of isolated defects imparts only moderate changes to the electrical properties. An average resistance increase of $\sim 6\text{ k}\Omega$ was observed per binding event,¹⁷⁸ consistent with a decrease in conductance of roughly 20% that was reported in a different study using a similar approach.¹⁷⁹ These values are in good agreement with early quantum theoretical calculations and significantly lower than for oxidative point defects.^{180,181} In contrast to that, no change in electrical conductance was observed for both metallic and semiconducting SWCNTs upon introduction of divalent carbene defects.¹⁸⁵ However, the lack of information on the investigated nanotube species (chirality or even electronic type) in these previous reports prevented unambiguous conclusions. Additionally, in the absence of spectroscopic data, it remained unclear whether the observed changes were indeed due to luminescent sp^3 defects or rather due to other, exciton-quenching defect sites. Consequently, a comprehensive picture of the impact of sp^3 defects on charge transport as well as the interaction of charge carriers with such defects and with defect-localized excitons is still missing.

So far, no studies have been directed at random networks or arrays of functionalized SWCNTs, which possess high carrier mobilities and are therefore highly suitable for applications in FETs and electrically-driven light sources. Since the vast majority of functionalization methods has been restricted to aqueous nanotube dispersions,^{11,12,164} the device integration has

been hindered by their limited processability. Only with the recent progress in covalent functionalization of polymer-wrapped SWCNTs in organic solvents^{22,23} the scalable and reproducible deposition of homogeneous films to harness the optical properties of sp^3 defects in optoelectronic devices has come into reach.

In this Chapter, ambipolar and light-emitting FETs based on networks of sp^3 -functionalized SWCNTs are demonstrated for the first time. Such light-emitting field-effect transistors are ideally suited to assess the properties of sp^3 defects in active devices, as they permit the study of both charge transport and electroluminescence within the same device structure.²⁰⁰ The impact of covalent functionalization on charge transport through the networks and the interaction of charge carriers with the defect sites are investigated by using a combination of EL spectroscopy, static voltage-dependent and dynamic charge-modulated PL spectroscopy, and temperature-dependent current–voltage measurements.

4.2 Functionalization and characterization

Semiconducting (6,5) SWCNTs wrapped with the fluorene–bipyridine copolymer PFO-BPy were obtained by selective dispersion in toluene under shear force mixing (see Chapter 3.1.1) and served as the model system for this study.⁸⁷ The mild exfoliation method yields long nanotubes (average length $> 1 \mu\text{m}$) with a low number of exciton-quenching lattice defects that are also detrimental to charge transport. Absorption and Raman spectroscopy confirmed the high purity of the dispersions without significant amounts of other SWCNT species and metallic nanotubes. (6,5) SWCNTs were subjected to sp^3 functionalization according to the protocol developed by Berger *et al.*²² as detailed in Chapter 3.2.1. The reaction procedure involves the use of an aryldiazonium salt (here: 4-bromobenzenediazonium tetrafluoroborate, DzBr) as the functionalization agent, as schematically shown in Figure 4.1.

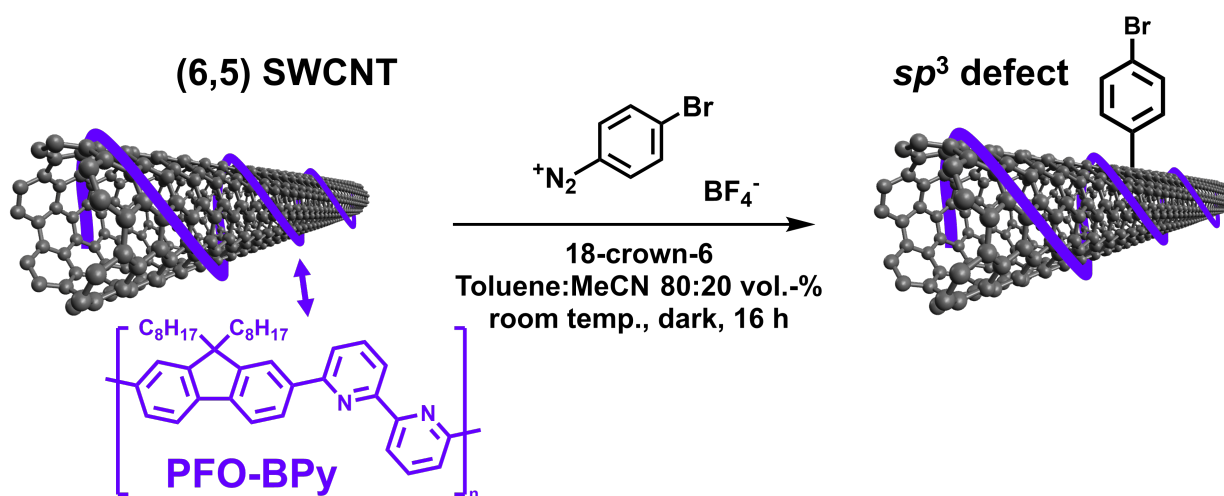


Figure 4.1: Reaction scheme for the covalent functionalization of PFO-BPy-wrapped (6,5) SWCNTs with 4-bromobenzenediazonium tetrafluoroborate in organic solvents.

To increase the solubility of the polar diazonium salt in the non-polar toluene, acetonitrile (MeCN) as co-solvent and a crown ether (18-crown-6) as phase-transfer agent were added to the mixture. After reaction for ~ 16 h under the exclusion of light, SWCNTs were collected through vacuum filtration, and unreacted DzBr and side-products as well as unbound wrapping polymer were washed off by thorough rinsing with MeCN and toluene. Crucially, the filtration and washing steps for the removal of excess polymer were similarly carried out for the pristine, untreated (6,5) SWCNT reference sample to ensure full comparability. Re-dispersion of the nanotubes in a small volume of fresh toluene gave highly concentrated inks (SWCNT concentration of $\sim 18.0 \mu\text{g mL}^{-1}$) that were suitable for thin film deposition *via* spin-coating.

Upon functionalization, a new emission feature (E_{11}^*) at 1166 nm corresponding to defect-localized excitons¹⁶ appeared in the PL spectra in dispersion, as shown in Figure 4.2a. Defect emission was red-shifted by approximately 174 meV from the mobile E_{11} exciton peak at 1002 nm. The density of induced defects and thus E_{11}^*/E_{11} PL ratio was controlled by the concentration of DzBr, with a PL area ratio of ~ 15 observed for the highest reactant concentration used here. Notably, for high reactant concentrations, a second emission peak emerged as a shoulder on the lower-energy side of the E_{11}^* PL feature in agreement with previous results.²² As detailed in Chapter 2.2.2, quantum mechanical calculations suggested that this additional peak, denoted as E_{11}^{*-} , corresponds to a different binding configuration of the attached groups on the SWCNT lattice which leads to a deeper optical trap depth.^{151,158}

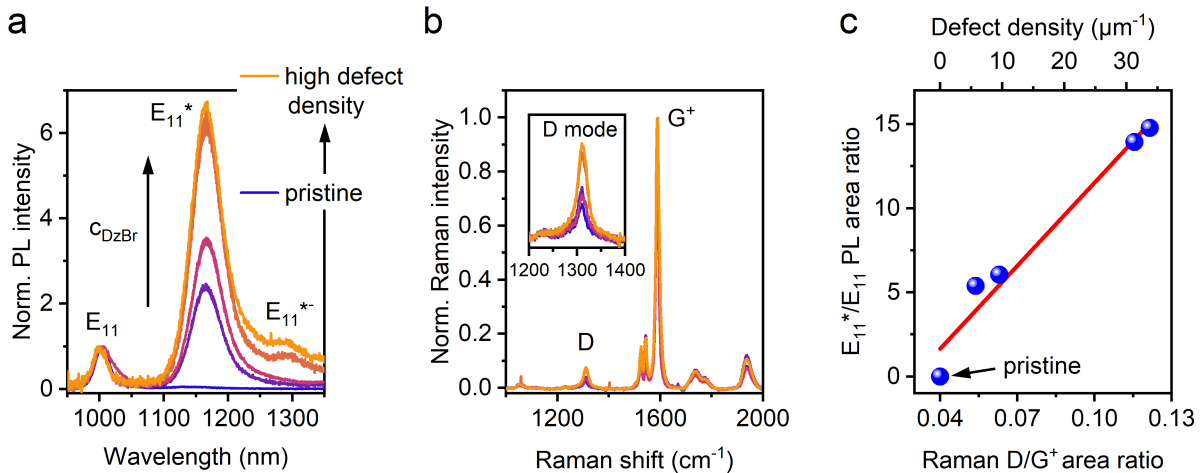


Figure 4.2: (a) Normalized PL spectra (pulsed E_{22} excitation at 575 nm) of (6,5) SWCNT dispersions functionalized with different concentrations of 4-bromobenzenediazonium tetrafluoroborate (c_{DzBr}). Emission peaks corresponding to mobile E_{11} excitons and defect-localized excitons (E_{11}^* , E_{11}^{*-}) are labelled. (b) Raman spectra (532 nm excitation) of pristine and functionalized (6,5) SWCNTs normalized to the G^+ mode. The inset shows a zoom-in on the defect-related D mode. (c) E_{11}^*/E_{11} PL area ratio *versus* Raman D/ G^+ area ratio and calculated sp^3 defect density. The red line is a linear fit to the data.

Resonant Raman spectroscopy (Figure 4.2b) further corroborated the controlled variation of sp^3 defect densities on the (6,5) SWCNTs. With increasing concentration of DzBr, the intensity of the D mode at $\sim 1310 \text{ cm}^{-1}$, which is proportional to the number of nanotube lattice defects, increased relative to the G^+ mode at $\sim 1590 \text{ cm}^{-1}$, which originates from a transverse in-plane phonon mode and is related to the number of sp^2 -hybridized carbon atoms.²⁹⁵ The integrated Raman D/ G^+ ratio can be used as a measure for the degree of functionalization and exhibits a linear correlation with the E_{11}^*/E_{11} PL ratio for the investigated range of defect densities (Figure 4.2c). According to a model that was recently developed by Sebastian *et al.*,¹⁴⁷ the number density of sp^3 defects in small-diameter semiconducting nanotubes can be calculated from the difference in Raman D/ G^+ area ratios of functionalized and pristine samples according to Equation 4.1:

$$n_d = 414 \text{ } \mu\text{m}^{-1} \cdot ((D/G^+)_{\text{funct}} - (D/G^+)_{\text{pris}}) \quad (4.1)$$

For the samples herein, this model yields values between ~ 6 and ~ 34 defects per μm of SWCNT. The Raman D/ G^+ area ratio and the calculated defect densities per unit length will be used equivalently in the following to quantify the impact of sp^3 defects on charge transport in (6,5) SWCNT network transistors.

4.3 Field-effect transistors with functionalized SWCNT networks

To investigate the charge transport and light emission properties of covalently functionalized (6,5) SWCNTs, they were integrated as dense networks in LEFETs with a bottom-contact, top-gate architecture (see Chapter 3.3.6). A schematic cross-section of the devices is shown in Figure 4.3a. Nanotube networks (pristine and different sp^3 defect densities) were deposited on glass substrates with photolithographically-patterned, interdigitated gold source/drain electrodes (channel length $L = 20 \text{ } \mu\text{m}$, channel width $W = 10 \text{ mm}$) *via* repeated spin-coating from concentrated dispersions. The double-layer dielectric, consisting of a thin layer of spin-coated poly(methyl methacrylate) (PMMA) and hafnium oxide (HfO_x) grown by atomic layer deposition on top, enabled low-voltage operation and encapsulated the devices to allow for measurements under ambient conditions.²⁴⁷ Devices were completed by thermal evaporation of silver top-gate electrodes.

Before the deposition of the dielectric layer, annealing of SWCNT networks was performed at $150 \text{ }^\circ\text{C}$ in inert atmosphere to remove most of the residual water and oxygen. At this annealing temperature, detachment of covalent aryl defects from the nanotube hosts should be negligible, since this effect has been shown to occur for temperatures above $\sim 200 \text{ }^\circ\text{C}$ using thermogravimetry coupled with mass spectrometry.²⁹⁹ Furthermore, higher annealing tem-

peratures were avoided as they were found to significantly enhance emission from unwanted sidebands in the spectral region between the E_{11} and E_{11}^* emission peaks (see Chapter 6). Figure 4.3a shows a representative atomic force micrograph of a network of sp^3 -functionalized SWCNTs. Nanotube networks for all devices were well-above the threshold for mobility saturation¹⁹⁷ with linear densities of >25 SWCNTs per μm , and the surface topography images did not show significant amounts of excess polymer or bundles that would have detrimental effects on the charge transport properties.^{85,254} Importantly, due to the relatively low defect density (average inter-defect distance between ~ 30 nm and ~ 170 nm, assuming a homogeneous distribution) and the small size of the covalently attached bromoaryl groups compared to the wrapping polymer with its octyl sidechains, the defects are unlikely to prevent intimate tube-tube contact and thus impede inter-nanotube carrier hopping.

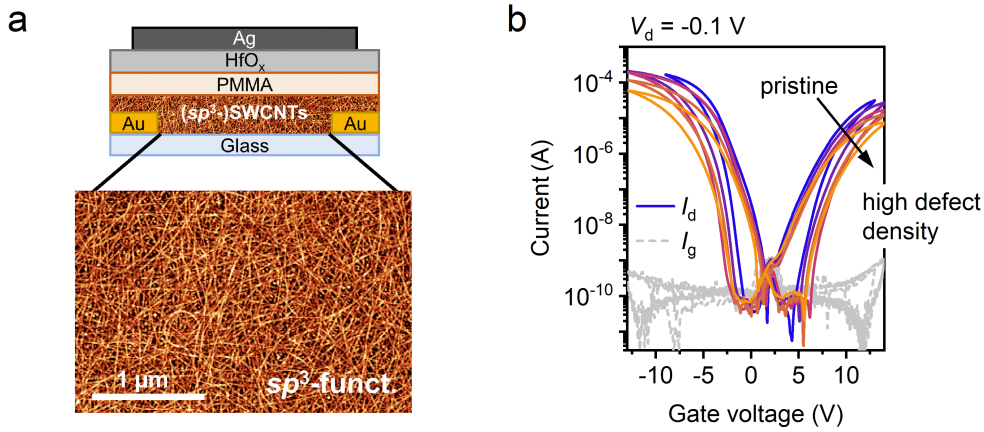


Figure 4.3: (a) Schematic cross-section of a bottom-contact, top-gate (6,5) SWCNT network FET (layer thicknesses not to scale) and representative atomic force micrograph of a dense network of sp^3 -functionalized SWCNTs with medium defect density ($n_d \sim 10 \mu\text{m}^{-1}$). The scale bar is $1 \mu\text{m}$. (b) Ambipolar transfer characteristics of pristine and functionalized SWCNT network FETs in the linear regime ($V_d = -0.1$ V). Solid lines are drain currents I_d , grey dashed lines are gate leakage currents I_g .

All devices exhibited ambipolar charge transport behaviour (*i.e.*, hole and electron conduction) as evident from the linear transfer characteristics in Figure 4.3b. High on/off current ratios of 10^5 – 10^6 and low gate leakage currents (< 1 nA) were obtained irrespective of the degree of functionalization. The residual current hysteresis between forward and reverse sweeps for all samples was likely caused by residual water and oxygen that was not completely removed due to the reduced annealing temperatures as discussed above.^{223,300} This observation agrees with the lower currents observed for electron conduction compared to the hole transport regime, which is also shown in the output characteristics in Figure 4.4. Nevertheless, the data indicate efficient charge injection with ohmic contacts even for SWCNT networks with the highest density of sp^3 defects and only minor non-idealities for electron injection in transistors with pristine nanotubes.

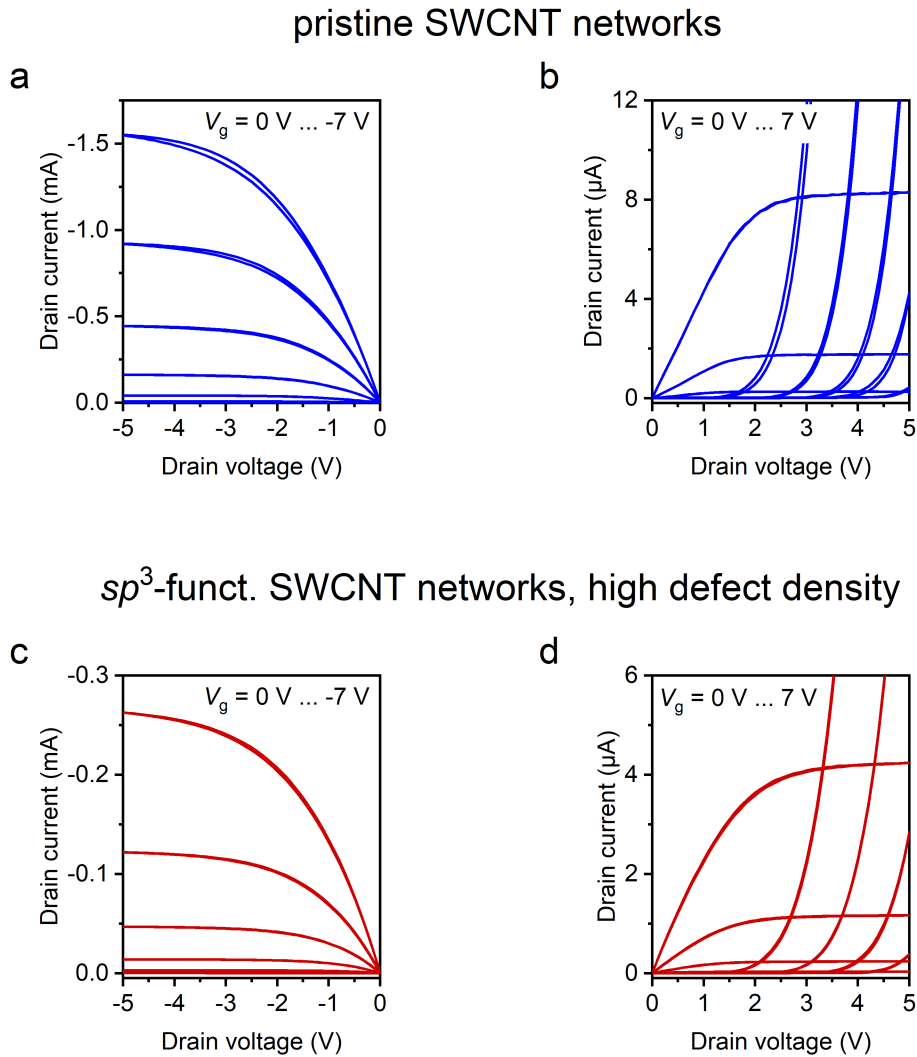


Figure 4.4: Representative output characteristics of ambipolar FETs with (a,b) pristine (6,5) SWCNT networks and (c,d) networks of highly functionalized (6,5) SWCNTs ($n_d \sim 34 \mu\text{m}^{-1}$) in hole and electron accumulation regimes, respectively. Gate voltage steps are 1 V.

As shown in the transfer characteristics (Figure 4.3b), an increase in sp^3 defect density led to a decrease in on-currents by a factor of 5–10 for the highest degree of functionalization with respect to the unfunctionalized reference transistors. Given the dense and homogeneous networks for all samples with very similar areal capacitances between 110–118 nF cm^{-2} , the differences in electrical characteristics can be directly assigned to the presence of sp^3 defects. To quantify the impact of luminescent defects on charge transport in SWCNT networks, maximum field-effect mobilities of holes and electrons were calculated from the linear transconductances (Table 4.1 and Figure 4.5a). Notably, the transconductance maximum, and thus maximum carrier mobility, was shifted to higher gate voltages for functionalized samples. Pristine nanotube networks exhibited charge carrier mobilities of $5.0 \pm 0.2 \text{ cm}^2(\text{Vs})^{-1}$ for holes and $1.2 \pm 0.2 \text{ cm}^2(\text{Vs})^{-1}$ for electrons, respectively. An increase in defect density

resulted in a gradual decrease in carrier mobilities for both holes and electrons. For the networks with the highest density of sp^3 defects, hole mobilities of $1.7 \pm 0.1 \text{ cm}^2(\text{Vs})^{-1}$ and electron mobilities of $0.4 \pm 0.04 \text{ cm}^2(\text{Vs})^{-1}$ were obtained, corresponding to approximately one third of the values for the pristine SWCNT FETs.

Table 4.1: Raman D/G⁺ area ratios, calculated sp^3 defect densities, and averaged linear hole and electron mobilities of pristine and functionalized SWCNT network FETs. Standard deviations were obtained from measurements of 8 different transistors for each network.

Raman D/G ⁺ area ratio	Defect density n_d (μm^{-1})	Hole mobility ($\text{cm}^2(\text{Vs})^{-1}$)	Electron mobility ($\text{cm}^2(\text{Vs})^{-1}$)
0.040	0	5.0 ± 0.2	1.2 ± 0.2
0.054	5.8	4.8 ± 0.2	1.2 ± 0.1
0.063	9.5	4.3 ± 0.4	0.8 ± 0.1
0.116	31.5	2.5 ± 0.1	0.6 ± 0.1
0.122	33.9	1.7 ± 0.1	0.4 ± 0.04

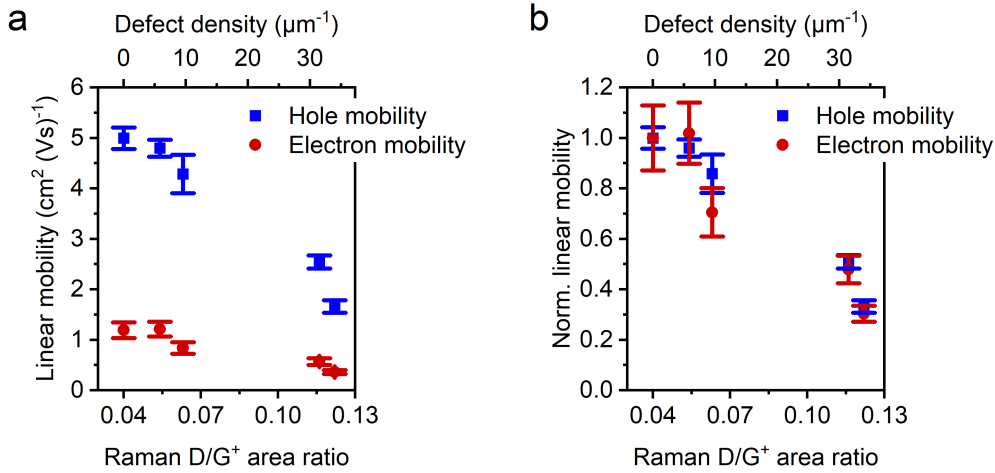


Figure 4.5: (a) Absolute and (b) normalized linear charge carrier mobilities of pristine and functionalized (6,5) SWCNT network FETs *versus* Raman D/G⁺ area ratio and calculated sp^3 defect density. Hole and electron mobilities are shown as blue squares and red circles, respectively. Error bars represent standard deviations for 8 different transistors measured for each network.

Figure 4.5b shows the linear mobilities normalized to the unfunctionalized reference transistors. Interestingly, the relative decrease of hole and electron mobilities is almost identical for all different defect densities. This similarity points towards comparable interactions of both charge carrier polarities with the bromoaryl defects investigated here. It also raises the question regarding the exact nature of the interaction between defect sites and charge carriers, that is, whether defects act as (shallow or deep) trap states for charge carriers in

a similar fashion as they localize diffusing excitons, or whether they are best described as scattering centers.

Notably, carrier mobilities of FETs with pristine networks and those with the lowest defect density ($n_d \sim 6 \mu\text{m}^{-1}$) were essentially the same. Even for the networks with $\sim 34 sp^3$ defects per μm , FETs were fully functional with good charge carrier mobilities and excellent switching behaviour. Previous studies on single-nanotube transistors reported an average conductance decrease of approximately 20% upon introduction of an isolated defect and up to two orders of magnitude for multiply functionalized SWCNTs.^{178,179} However, in devices with individual nanotubes, carriers are forced to pass the defect sites, whereas the presence of multiple conduction pathways in the dense networks would in principle allow the charges to travel predominantly on nanotube segments that contain no or only few sp^3 defects. While the latter would result in fewer available current paths and consequently lower carrier mobilities, a hypothetical circumvention of SWCNT segments hosting luminescent defects would also have direct implications for the possible emission of defect-state electroluminescence from sp^3 -functionalized SWCNT networks and thus their application potential in optoelectronic devices.

4.4 Electroluminescence from defect states

The emergence of new emission peaks in the NIR and the brightening of nanotube dispersions upon sp^3 functionalization are promising properties to be harnessed in SWCNT-based thin film devices, but thus far have been almost exclusively demonstrated in liquid systems and under optical rather than electrical excitation. To assess the light emission properties of functionalized SWCNT networks in operating devices, EL measurements were performed on the LEFETs described above. As detailed in Chapter 2.3.2, biasing a light-emitting transistor in the ambipolar regime leads to the simultaneous accumulation of holes and electrons in the channel and a narrow (1–2 μm) carrier recombination zone where the accumulation layers meet. Ambipolar recombination of thermalized charge carriers gives rise to excitons and consequently EL. The EL emission is directly related to the current density, and hence, its spatial and spectral distribution permit the analysis of charge transport in the SWCNT network or the semiconducting layer of a LEFET in general. EL imaging and spectroscopy were previously used to visualize preferential charge transport paths in photoswitchable SWCNT network FETs²⁸² and to identify the chirality-dependent current shares in nanotube networks composed of different semiconducting species.^{231,232} Furthermore, composite EL images of light-emitting polymer transistors showed a clear correlation with the microstructure of the semiconductor.²⁰³

Imaging of the emission zone in SWCNT network LEFETs was performed with a 2D InGaAs camera to record the integrated EL intensity across the NIR spectral range (800–1600 nm).

Devices were operated in the ambipolar regime at a constant drain current $I_d = -100 \mu\text{A}$ while simultaneously varying the gate and drain voltages. Figure 4.6a shows an EL emission zone that extends along the entire channel of a device with an sp^3 -functionalized network. Importantly, this recombination zone corresponds to a line of zero effective potential,³⁰¹ and the fact that it is not completely straight can be attributed to local potential variations due to contact resistance and local differences in gating efficiency.²⁸² Through variation of V_g and V_d , the emission zone could be moved across the channel from the source to the drain electrode and *vice versa*. A superposition of all individual EL images for an entire gate voltage sweep yields a composite EL image that reflects the current density distribution within the channel.^{203,282} The composite image in Figure 4.6b shows a homogeneous distribution of EL emission, and thus current density, from the entire channel area. No fragmentation of current pathways was observed within the diffraction-limited resolution of this method.

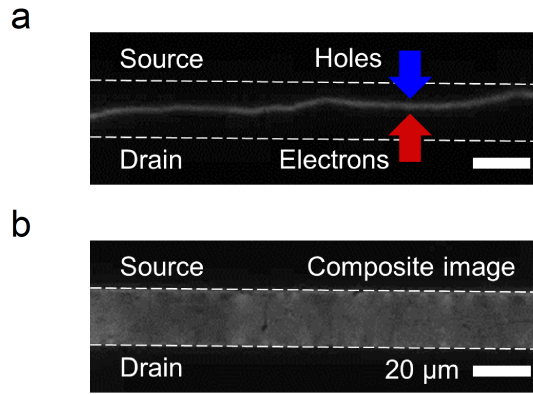


Figure 4.6: (a) Near-infrared EL image of the recombination and emission zone in the channel ($L = 20 \mu\text{m}$) of a functionalized (6,5) SWCNT network LEFET ($n_d \sim 10 \mu\text{m}^{-1}$). The device was biased in the ambipolar regime at a constant drain current $I_d = -100 \mu\text{A}$. Hole injection from the source and electron injection from the drain electrode are symbolized by blue and red arrows, respectively. (b) Composite EL image for a full gate voltage sweep ($I_d = -100 \mu\text{A}$) of the same device. Scale bars in (a,b) are $20 \mu\text{m}$.

For subsequent spectrally-resolved EL measurements, the emission zone was always positioned in the center of the channel (as in Figure 4.6a) to avoid potential effects of impact excitation or local differences in contact resistance at the electrode edges. Notably, no significant difference was observed in the spectral shapes of EL and PL spectra measured close to the contacts and in the center of the channel, respectively. However, it was recently shown that even minor differences in the current density distribution – and thus, position of the emission zone – can have a direct impact on the emission properties, such as the exciton-to-trion intensity ratio, of electrolyte-gated (6,5) SWCNT network FETs and short-channel transistors with individual nanotubes.^{134,302} Figure 4.7a shows a set of EL spectra of a pristine network transistor for different drain currents. Aside from E_{11} exciton emission at 1018 nm, emission from lower-energy sidebands¹¹² and a minor trion (charged exciton)

contribution at 1180 nm are visible in the spectra. Trion emission in electrostatically gated SWCNT FETs with solid dielectrics is low (see also the normalized spectra in Figure 4.8a) compared to electrolyte-gated nanotube networks^{133,134} in agreement with previous observations,²³² which is likely due to the significantly lower carrier densities. As expected, a higher drain current results in a higher carrier recombination rate and consequently EL intensity.

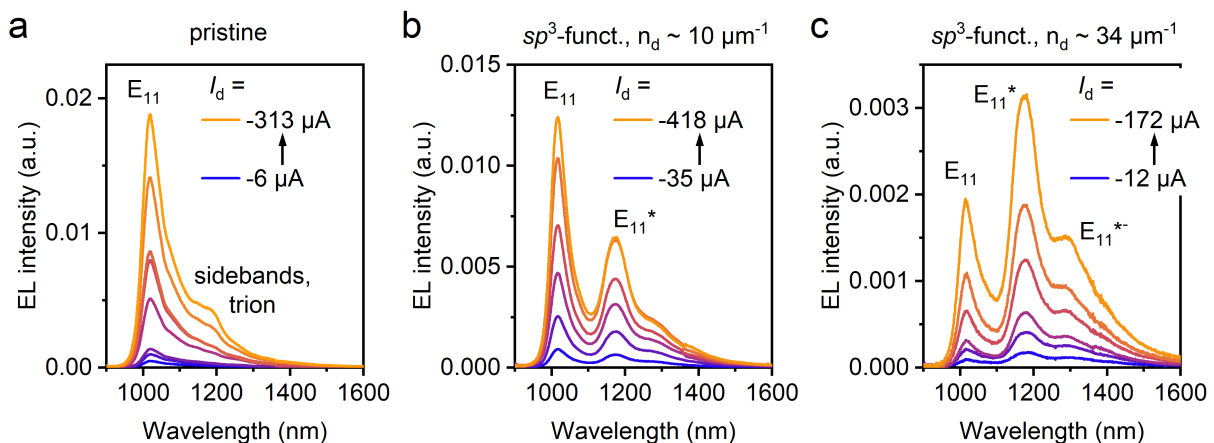


Figure 4.7: Representative EL spectra of (a) pristine and (b,c) sp^3 -functionalized (6,5) SWCNT network LEFETs in the ambipolar regime for different drain currents I_d .

The spectra of sp^3 -functionalized (6,5) SWCNT networks (Figure 4.7b,c) clearly show the emergence of new emission bands red-shifted from the E_{11} emission feature. Since trion emission is low and the new emission features are only visible for functionalized networks, they are unambiguously assigned to EL from the defect states. E_{11}^* emission at ~ 1175 nm was the dominant defect peak for all functionalized networks. For higher degrees of functionalization, emission from E_{11}^{*-} defects with a larger exciton trapping potential was observed at ~ 1285 nm in agreement with PL spectra of the dispersions (compare Figure 4.2a). EL from sp^3 defects was tunable in intensity *via* the defect concentration, with more than 80% of photons emitted through the defect channel for the highly functionalized networks with $n_d \sim 34 \mu\text{m}^{-1}$. Recently, emission from defect-localized trions was reported in low-temperature EL spectra of single-nanotube transistors with luminescent defects.³⁰³ It should be noted that neither in the LEFETs discussed here nor in EL from electrolyte-gated, functionalized SWCNT networks at much higher carrier densities (data not shown), spectral signs of such trapped trions could be identified. In a previous report by Xu *et al.*, defect EL *via* an impact excitation mechanism was observed in two-terminal devices with bundles of nitroaryl-functionalized nanotubes.³⁰⁴ The results presented here show that sp^3 -functionalized SWCNT networks can be fabricated into multifunctional devices, combining excellent charge transport and switching behaviour with light emission in the NIR. Very recently, controllable EL from sp^3 defects was also demonstrated for single-nanotube transistors,³⁰³ which is a major step towards their application as electrically-pumped, room-temperature quantum light sources.

As shown in the normalized spectra in Figure 4.8, EL from the defect states was stable over 1–2 orders of magnitude in current density. Only a slight decrease in defect emission intensity relative to the E_{11} peak was observed for higher drain currents, and thus gate voltages, for all sp^3 -functionalized networks. Notably, however, emission from defect-localized excitons was substantially lower with respect to the mobile E_{11} exciton peak than in the PL spectra of the dispersions (compare Figure 4.2a).

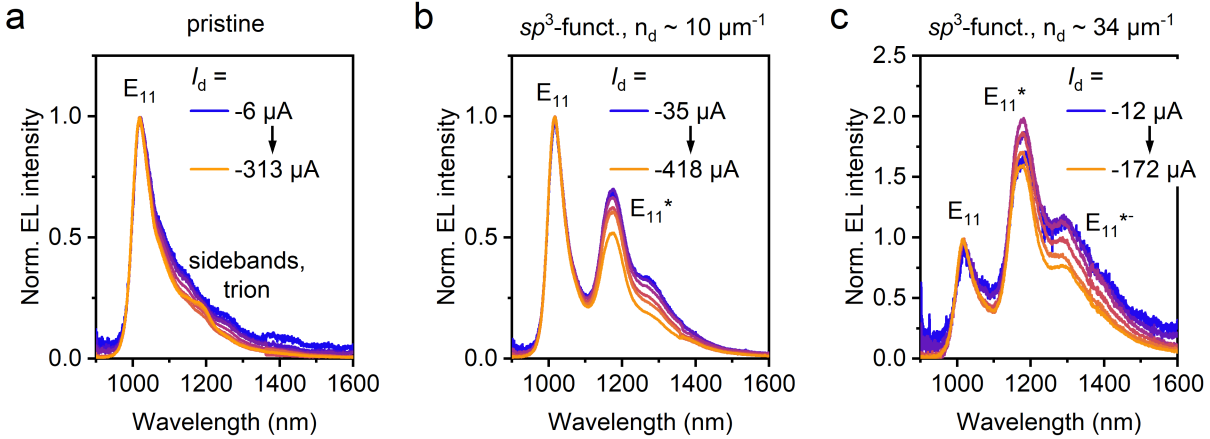


Figure 4.8: Normalized EL spectra of (a) pristine and (b,c) sp^3 -functionalized (6,5) SWCNT network LEFETs in the ambipolar regime for different drain currents I_d .

One possible cause could be state-filling of exciton traps, which leads to the saturation of defect emission at lower excitation densities compared to E_{11} in power-dependent PL measurements of functionalized SWCNT dispersions.^{22,156} However, double-logarithmic plots of integrated EL intensities *versus* I_d yielded linear correlations with slopes of ~ 1 for both pristine and functionalized network FETs (Figure 4.9), indicating that the measurements were conducted in the linear excitation regime. For a drain current of $-100 \mu\text{A}$, instantaneous exciton densities on the order of 0.1 excitons per SWCNT were calculated,³⁰⁵ assuming that every charge carrier recombines to form an exciton with an average lifetime of 100 ps. These estimated exciton densities are roughly two orders of magnitude lower than for the acquisition of PL spectra of the dispersions under pulsed laser excitation. Thus, state-filling cannot explain the lower defect emission intensities. Non-resonant PL spectra under continuous wave excitation, which exhibited very similar peak intensity ratios compared to the EL spectra (see Figure 4.11), corroborated this notion. Importantly, the similar spectral shapes of EL and PL spectra for low excitation densities suggest that there are no preferential current paths in sp^3 -functionalized SWCNT networks. The observation of E_{11}^* EL emission implies that carrier recombination takes place in close proximity to the defect sites, that is, within the exciton diffusion range. Hence, nanotube segments with luminescent defects must at least partially contribute to charge transport within the networks. The lower defect emission compared to the dispersions appears to be mainly associated with the SWCNT deposition as thin films on substrates, even though the exact reason is not entirely clear.

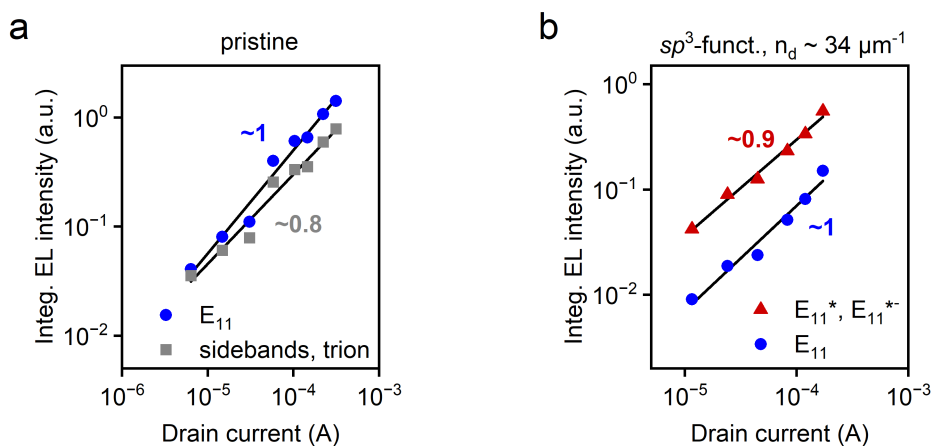


Figure 4.9: Double-logarithmic plots of the integrated EL intensity *versus* drain current for (a) pristine and (b) functionalized (6,5) SWCNT network LEFETs (high defect density, $n_d \sim 34 \mu\text{m}^{-1}$). Blue circles are E_{11} emission intensities, grey squares in (a) correspond to red-shifted sidebands and trion contributions, and red triangles in (b) are sp^3 defect emission intensities (E_{11}^* and E_{11}^{*-}). Black solid lines are linear fits to the data, and numbers indicate the corresponding slopes.

Interestingly, emission from E_{11}^{*-} defects was more pronounced in EL compared to PL spectra of the thin films. Ultrafast exciton transfer in SWCNT networks^{119,120} should play a similar role in both cases, since the majority of excitons is probably formed on pristine nanotube segments and subsequently funnelled to the defect sites, given the average distances between two defects of several tens of nanometers. Additionally, the further red-shifted defect exhibits a stronger decrease in emission intensity for higher I_d compared to the E_{11}^* peak (Figure 4.8c), which might point towards different interactions of defects with charge carriers depending on the binding configuration. While E_{11}^{*-} defects often appeared as an additional peak in the spectra of E_{11}^* -functionalized SWCNTs,^{22,173,306} their selective introduction has been recently accomplished in a base-mediated approach,²³ thus enabling further studies. LEFETs based on sp^3 -functionalized SWCNT networks with E_{11}^{*-} defects are discussed in Chapter 7.

4.5 EL efficiencies of light-emitting transistors with functionalized SWCNT networks

The brightening of semiconducting nanotubes in dispersion upon decoration with luminescent sp^3 defects^{16,22} has prompted hopes of higher EL yields in optoelectronic devices with SWCNT thin films. Light-emitting SWCNT network devices typically suffer from low quantum yields in films (PLQY $\sim 0.1\%$) and non-radiative Auger quenching of excitons with excess charge carriers, resulting in external EL quantum efficiencies (EQEs) on the order of 0.01%.^{9,10} EQEs of pristine and functionalized SWCNT network LEFETs, defined as the

number of emitted photons per injected charge carriers, were measured during constant drain current sweeps with the devices placed on top of a calibrated InGaAs photodiode and the silver top-gate acting as mirror to collect most of the EL emission (for experimental details, see Chapter 3.4.7). Figure 4.10a shows the EQE of an sp^3 -functionalized SWCNT network LEFET with a low defect concentration ($n_d \sim 6 \mu\text{m}^{-1}$) during a complete forward and reverse gate voltage sweep. Maximum EQE values of $\sim 0.02\%$ were reproducibly measured for different LEFETs with low sp^3 defect densities, which indeed exceeded the EL efficiencies measured for the pristine reference samples ($\sim 0.015\%$).

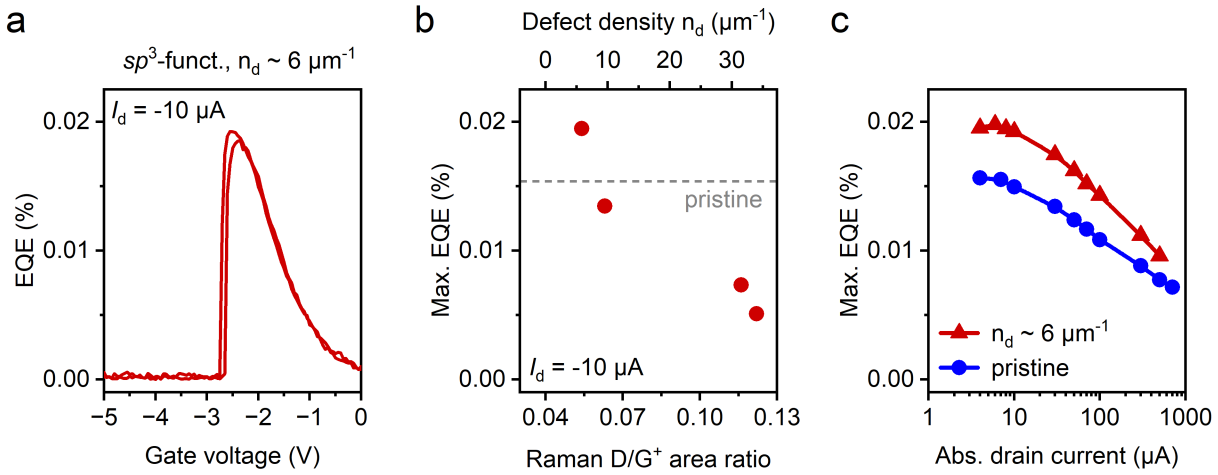


Figure 4.10: (a) EQE of an sp^3 -functionalized (6,5) SWCNT network LEFET ($n_d \sim 6 \mu\text{m}^{-1}$) during a gate voltage sweep at a constant drain current $I_d = -10 \mu\text{A}$. (b) Maximum EQEs ($I_d = -10 \mu\text{A}$) of sp^3 -functionalized LEFETs *versus* Raman D/G⁺ area ratio and calculated sp^3 defect density. The grey dashed line represents the EQE measured for pristine reference LEFETs. EQE values for the three lowest defect densities were averaged over 2 different devices. (c) Drain current-dependent EQE of pristine (blue circles) and functionalized ($n_d \sim 6 \mu\text{m}^{-1}$, red triangles) LEFETs. Lines are guides to the eye.

However, as shown in Figure 4.10b, EQEs decreased for LEFETs with even higher defect densities and were eventually even lower than for unfunctionalized SWCNTs. A similar trend was observed in PL measurements of functionalized SWCNT dispersions that exhibited a maximum in absolute quantum yields for low defect densities, followed by a decrease in luminescence efficiencies for higher degrees of functionalization.^{22,23} This effect was attributed to the formation of regions where the nanotube lattice is disrupted by too many defects, preventing the formation of extended electronic states and thus facilitating non-radiative exciton quenching.²³ Optimum defect densities to maximize the ensemble PL quantum yield are expected to be in the range of $\sim 5\text{--}10 \mu\text{m}^{-1}$, which corresponds to the average density of quenching sites according to the diffusion-limited contact quenching model.^{116,147} This expectation matches the trend for the maximum EQE values in Figure 4.10b. However, the decrease in EL efficiencies observed here is more pronounced than the drop in PL yields for higher defect densities, and thus can probably not be explained by this effect alone.

Instead, the decrease in charge carrier mobilities for highly functionalized SWCNT networks (see Figure 4.5) might also play a role. Even though the carrier density should be zero in the direct vicinity of the recombination zone, in reality there will be a certain number of excess charge carriers present, given that carrier recombination is not infinitely fast and the apparent width is 1–2 μm .^{307,308} For SWCNT network LEFETs, the presence of excess carriers in the emission zone has been shown through PL quenching and the observation of trion EL¹³⁴ as well as by Raman microscopy.³⁰⁹ The lower mobilities in the functionalized networks might lead to higher excess carrier densities and consequently increased quenching of electrically generated excitons with free charges.³⁰¹ This notion is further supported by a pronounced roll-off of maximum EQEs for increasing current densities observed for all samples, as exemplarily shown for LEFETs with unfunctionalized SWCNTs and with a low density of sp^3 defects in Fig. 4.10c. Annihilation of excitons through interaction with charge carriers is similarly known to be a source of efficiency roll-off in organic light-emitting diodes at high current densities.³¹⁰ Importantly, exciton–exciton annihilation can be excluded as a quenching source here, since the investigated range in drain currents should still be within the linear excitation regime (compare Figure 4.9). It should be noted that a similar roll-off of EL efficiencies at higher currents was recently observed for electrolyte-gated (6,5) SWCNT network LEFETs.¹³⁴

The observed trend in EQEs of sp^3 -functionalized SWCNT network LEFETs provides an interesting starting point for future studies. Furthermore, the discrepancy of defect emission intensities in dispersions and thin films calls for more detailed investigations of the interactions between covalently functionalized nanotubes within a network and with the substrate. While the remainder of this Chapter is concerned with the interaction of sp^3 defects with charge carriers, the influence of nanotube–substrate interactions and the effect of the optical trap depth of sp^3 defects on the EL spectra and efficiencies will be further discussed in Chapters 6 and 7.

4.6 Interaction of charge carriers with luminescent defects and defect-localized excitons

Excitons in SWCNTs are highly sensitive to the presence of charge carriers.⁹⁶ Consequently, doping-induced changes in the optical spectra (absorption and emission) of nanotubes can be analyzed to obtain insights into the carrier density distribution and charge transport.^{232,273,311,312} To this end, PL spectra of sp^3 -functionalized SWCNT network LEFETs were acquired under non-resonant continuous wave (cw) laser excitation at 785 nm while applying a static bias to the gate terminal of the devices. Figure 4.11a shows the spectra for a network with high defect density in hole accumulation. With increasing gate voltage and thus doping level, all peaks (E_{11} , E_{11}^* , and E_{11}^{*-}) are progressively quenched due to non-radiative Auger

recombination of excitons mediated by charge carriers.^{128,129} However, as seen from the spectra normalized to the E_{11} feature (Figure 4.11b), defect emission peaks are quenched more strongly compared to mobile excitons. This trend was also observed in PL spectra in electron accumulation (positive V_g) and is consistent with the decrease in E_{11}^* -to- E_{11} emission ratio in EL spectra for higher drain currents (compare Figure 4.8). At higher voltages, trion emission becomes visible in the normalized spectra at similar wavelengths to the E_{11}^* peak, thus preventing an unambiguous quantitative analysis of the relative peak intensities depending on the carrier density. Static gate voltage-dependent PL spectra under pulsed excitation at the E_{22} transition gave the same results, albeit with significantly lower defect emission intensities due to the higher excitation densities, leading to state-filling of exciton traps.¹⁵⁶

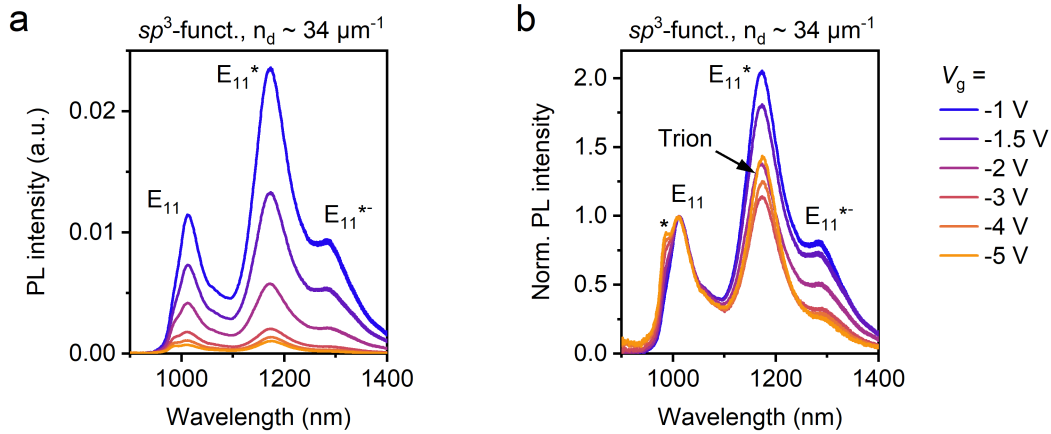


Figure 4.11: (a) Absolute and (b) normalized PL spectra (non-resonant cw excitation at 785 nm) of an sp^3 -functionalized (6,5) SWCNT network LEFET with high defect density ($n_d \sim 34 \mu\text{m}^{-1}$) at different gate voltages V_g in hole accumulation ($V_d = -10$ mV). At high voltages, trion emission becomes visible in the normalized spectra. The asterisk at ~ 985 nm marks the Raman 2D mode of (6,5) SWCNTs.

The relative decrease of the E_{11}^* defect PL with respect to the E_{11} exciton peak for increasing doping levels is in agreement with a previous report of *in situ* PL spectroscopy of electrochemically doped, aryl-functionalized (6,5) SWCNTs.¹⁵⁷ By recording the change in PL intensity upon application of positive and negative voltages, the oxidation and reduction potentials corresponding to the highest occupied molecular orbital (HOMO) and lowest unoccupied molecular orbital (LUMO) levels, respectively, were determined for E_{11} and E_{11}^* . For the bromoaryl defects as used here, the HOMO level was shifted by 31 meV to higher energies and the LUMO level was shifted by 22 meV to lower energies, which corresponds to an electrochemical bandgap that was 53 meV smaller for E_{11}^* compared to E_{11} . These results imply that the introduction of luminescent sp^3 defects creates lower-lying electronic states for charge carriers that might act as shallow trap states. Given the rather small energetic shifts on the order of the thermal energy at room temperature ($k_B T \sim 25$ meV), such traps would still allow for fast detrapping. Charge localization at the defect sites could also explain the

observed decrease in E_{11}^* -to- E_{11} emission ratio in EL and gated PL spectra with increasing carrier density due to predominant quenching of defect-localized excitons. Importantly, the similar shifts in the HOMO and LUMO levels for bromoaryl defects determined by Shiraishi *et al.*¹⁵⁷ suggest that sp^3 defects interact similarly with holes and electrons. This notion is in very good agreement with the observation that the relative decrease in linear hole and electron mobilities in the functionalized SWCNT networks with respect to the pristine reference was essentially identical for a given defect density (compare Figure 4.5b).

It should be noted that the electrochemical trap depth of bromoaryl defects (~ 25 meV)¹⁵⁷ significantly differs from the optical trap depth $\Delta E_{\text{opt}} \sim 174$ meV that is calculated from the difference in E_{11} and E_{11}^* PL emission energies. Similarly, temperature-dependent PL measurements have previously shown that the thermal detrapping energy ΔE_{therm} of excitons localized at an sp^3 defect is considerably lower than ΔE_{opt} .¹⁴² For the latter case, the difference has been attributed to the reorganization energy that reflects the distortion of the nanotube lattice upon defect creation,^{142,151} but its magnitude has been the subject of debate.²² While thermal trap depths of 75–150 meV were reported for E_{11}^* defects, values of only ~ 25 meV were found for E_{11}^{*-} defects with an even larger red-shift in defect PL and thus optical trap depth.^{23,142} In contrast to that, the electrochemical trap depths determined by PL spectroelectrochemistry measurements of oxygen-doped (6,5) SWCNTs were significantly larger for further red-shifted defect species.¹⁵⁹ These obvious discrepancies highlight the complex relationship between the optical, thermal, and electrochemical trap depths of luminescent defects in SWCNTs. To reconcile these observations and, more specifically, to clarify the similarities and differences in exciton and charge trapping mechanisms at sp^3 defect sites, further studies and input from theory are required.

To further elaborate on the notion of charge localization at sp^3 defects, PL spectra of a functionalized SWCNT network were acquired without and with applied gate voltage for different excitation powers. As expected, all emission peaks increased in intensity for higher pump powers. However, as detailed above, emission from sp^3 defects is known to saturate at lower excitation densities than E_{11} emission due to state-filling.^{22,156} This leads to a relative decrease in defect PL with respect to the E_{11} peak, as shown in the normalized pump power-dependent spectra in Figure 4.12a. Notably, only for the highest excitation powers used here, E_{11} emission also starts to saturate due to exciton–exciton annihilation.^{313,314} These measurements were repeated at a low, static gate voltage of $V_g = -2$ V to explore the effect of carrier doping while avoiding significant trion emission that could compromise the results (compare Figure 4.11b). As shown in Figure 4.12b, the initial E_{11}^* and E_{11}^{*-} emission intensities relative to the E_{11} peak were considerably lower due to predominant quenching of defect PL. However, the decrease in defect-to- E_{11} emission occurs at significantly higher excitation powers compared to those measurements in the undoped state. This trend is further shown by the integrated E_{11}^* -to- E_{11} PL ratios in Figure 4.12c. State-filling has been

attributed to the fast exciton diffusion to sp^3 defect sites compared to the relatively long lifetimes of defect-localized excitons.¹⁵⁶ On the other hand, the preferential accumulation of charge carriers in close proximity to the defects would lead to a shortening of E_{11}^* exciton lifetimes due to very efficient non-radiative quenching. Therefore, the effect of state-filling is reduced upon charge accumulation and only becomes significant at higher excitation densities. Consequently, these data suggest a certain degree of charge carrier localization at the sp^3 defects.

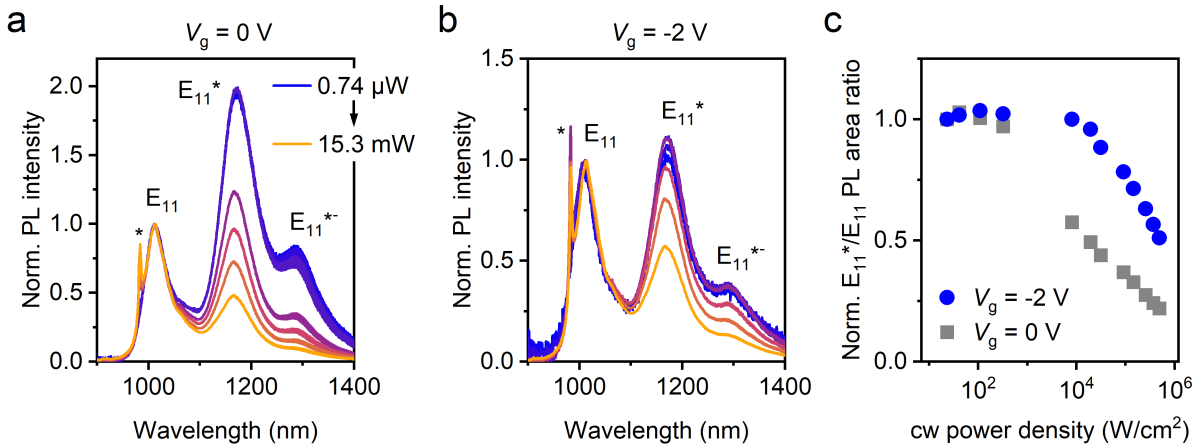


Figure 4.12: Normalized excitation power-dependent PL spectra (non-resonant cw excitation at 785 nm) of an sp^3 -functionalized (6,5) SWCNT network LEFET with high defect density ($n_d \sim 34 \mu m^{-1}$) (a) at zero gate voltage and (b) at $V_g = -2$ V. The asterisk at ~ 985 nm marks the Raman 2D mode of (6,5) SWCNTs. (c) E_{11}^* -to- E_{11} PL area ratio *versus* pump power density normalized to the values for the lowest excitation power. Data points for $V_g = 0$ V and $V_g = -2$ V are drawn as grey squares and blue circles, respectively.

While gate voltage-dependent PL spectra indicate the preferential accumulation of charge carriers at sp^3 defects, the magnitude of the trapping potential remains unclear. Due to the static nature of these measurements, the observed trends could be caused by deeply trapped carriers that do not contribute to charge transport in the networks. On the other hand, as suggested above, charge carriers could easily escape from shallow trapping potentials at room temperatures, which would render them sufficiently mobile to contribute to the current flow in the devices. To clarify whether or not charge carriers on sp^3 -functionalized SWCNT segments are indeed mobile, a dynamic measurement such as charge modulation PL (CMPL) spectroscopy is required.²⁷³ The working principle of CMPL spectroscopy is analogous to charge modulation spectroscopy (CMS) in absorption, which has provided detailed insights into charge transport mechanisms in polymers^{274–277} and small-molecule organic semiconductors.^{278,279} However, due to the low number of sp^3 defects introduced to the nanotube lattice and consequently their low absorption band,²² CMPL appears to be better suited to study their interaction with mobile charge carriers. In CMPL experiments, the gate voltage of a FET device is modulated around a constant offset potential V_{os} with a sinusoidal function

(peak-to-peak voltage V_{pp}) at a modulation frequency f while simultaneously exciting the semiconductor with a laser (see Chapter 3.4.3 and Figure 2.16). The gate voltage modulation causes a dynamic variation of accumulated carrier density in the SWCNT network, which in turn results in a modulation of the PL emission intensity with the same frequency. This differential change in PL intensity (ΔPL) is recorded in a lock-in detection scheme and can be unambiguously assigned to quenching by mobile carriers. In contrast, charge carriers in deep trap states cannot follow the modulation frequency and thus do not contribute to the spectra.

The CMPL spectra of a pristine SWCNT network transistor for different V_{os} with a constant V_{pp} of 0.2 V are shown in Figure 4.13a. Similar to the static PL spectra, a single peak was observed at 1025 nm, corresponding to modulation of the E_{11} exciton PL. In agreement with previous results, the ΔPL signal initially rises with increasing V_{os} due to an increase in capacitance as the device is switched from the off- to the on-state, leading to a higher modulated charge carrier density.²⁷³ After reaching a maximum at $V_{os} = -1.3$ V, a drop in CMPL signal intensity was observed. A higher offset potential is equivalent to a higher density of statically accumulated carriers in the channel on which the charge modulation is superimposed, so that static PL quenching becomes dominant at high V_{os} and the effect of the modulation vanishes. Since only the latter is recorded in CMPL experiments, the ΔPL signal decreases upon further increase in V_{os} . Irrespective of the offset voltage, the normalized spectra were essentially identical. It should be noted that at such low voltages, the transconductance and charge carrier mobility are low, and charges cannot fully follow higher modulation frequencies.²⁷³ Thus, an increase in f led to a decrease in CMPL signal. Despite this observation, CMPL spectra were obtained for frequencies up to ~ 10 kHz and displayed very similar spectral shapes, which confirms that exciton quenching with mobile carriers is the sole origin of the observed signal. No other physical processes should play a significant role, as they are expected to respond to the voltage modulation on different time scales.³¹⁵

Figure 4.13b shows the V_{os} -dependent CMPL spectra for an sp^3 -functionalized SWCNT network LEFET with a high defect density. In addition to the E_{11} peak at 1020 nm, CMPL signals corresponding to E_{11}^* and E_{11}^{*-} defects at 1175 nm and 1290 nm, respectively, can be clearly identified. Crucially, the observation of defect-state PL modulation manifests the interaction of sp^3 defects with mobile charge carriers in functionalized SWCNT networks. All peaks exhibited a similar trend with increasing V_{os} , that is, an initial increase followed by a decrease in signal intensity, as previously found for the pristine SWCNT network. However, the offset voltage corresponding to the maximum ΔPL signal was lower for the defect emission features compared to E_{11} , as can be seen by comparing the spectra at $V_{os} = -1.5$ V and -1.8 V in Figure 4.13b. This observation was further reflected in a relative decrease of the defect ΔPL features in the CMPL spectra normalized to the E_{11} signal

(Figure 4.13c). As discussed for the pristine sample, the ΔPL decrease for higher V_{os} is a result of static PL quenching. Static voltage-dependent PL spectra already established the predominant quenching of defect emission compared to E_{11} (Figure 4.11). Consequently, charge carrier localization in close proximity to the sp^3 defects reduces the magnitude of defect-state emission modulation, thus leading to the observed trends.

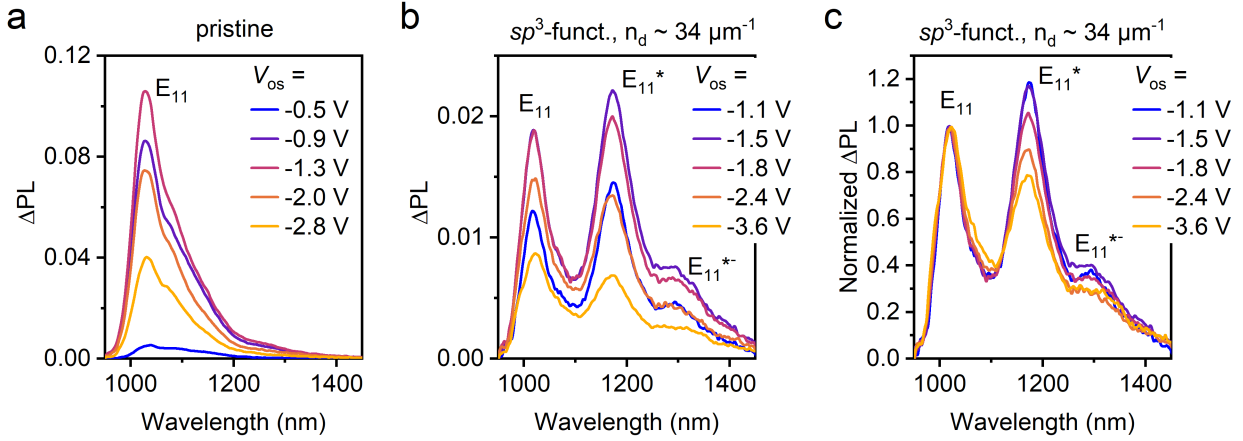


Figure 4.13: Charge-modulated PL spectra of (a) pristine and (b,c) sp^3 -functionalized (6,5) SWCNT network LEFETs for different offset voltages V_{os} . Spectra in (c) were normalized to the E_{11} ΔPL signal. All spectra were acquired with a peak-to-peak voltage $V_{\text{pp}} = 0.2$ V and a modulation frequency $f = 363$ Hz.

At first sight, charge trapping at the defect sites seemingly contradicts the observation of E_{11}^* and E_{11}^- signals in the CMPL spectra, which unambiguously confirm that sp^3 defects are sampled by mobile carriers. Importantly, however, modulation of optical transitions is possible even for shallow charge traps, provided that they can be filled and emptied on the time scale of carrier modulation.²⁷⁹ Frequency-dependent CMPL spectra of the highly functionalized networks up to ~ 8 kHz confirmed that carriers on nanotube segments with sp^3 defects are sufficiently mobile to follow such high modulation frequencies. No differences in the temporal response of E_{11} and defect PL modulation were observed. Following the argument by He *et al.*,¹⁴⁴ thermal detrapping from the defects – albeit in this case for charge carriers rather than excitons – was assumed to follow the Arrhenius equation $k = A \cdot \exp(-E_A/(k_B T))$ with k , E_A , k_B and T being the detrapping rate, activation energy, Boltzmann constant and temperature, respectively. According to transition state theory, the pre-exponential factor can be approximated as $A = k_B T/h$ with the Planck constant h .¹⁴⁴ Assuming an activation energy of ~ 25 meV in line with the electrochemical trap depth determined by Shiraishi *et al.*¹⁵⁷ and a temperature of 300 K, one obtains detrapping rates of $\sim 10^{12}$ s $^{-1}$ (detrapping times of ~ 1 ps), which exceed the carrier modulation frequency by orders of magnitude. CMPL experiments at lower temperatures and thus lower detrapping rates could offer further insights^{278,279} but were not possible with the current setup.

Nevertheless, the combination of dynamic CMPL and static voltage-dependent PL spectroscopy corroborated that sp^3 defects are energetically lower-lying electronic states that act as shallow charge traps but still allow for rapid detrapping of carriers at room temperature. The results provide evidence that sp^3 -functionalized SWCNT segments are sampled by mobile charge carriers and actively participate in carrier conduction through dense nanotube networks, which may ultimately enable their use as a charge transport and emission layer in thin film devices.

4.7 Temperature-dependent charge transport

Temperature-dependent current–voltage measurements are a commonly used tool to investigate charge transport in different types of semiconductors. By comparison of the extracted temperature dependence of conductivity or carrier mobility with theoretical models, detailed insights into the underlying charge transport mechanisms can be obtained. Indeed, such experiments have been previously utilized to study charge transport in semiconducting SWCNT networks, and all of them revealed an increase in carrier mobility with temperature, which was assigned to thermally activated hopping of charges across nanotube–nanotube junctions.^{85,246,259,262} In contrast to that, individual nanotubes exhibit band-like transport that is limited by electron-phonon scattering, and thus, carrier mobilities increase with decreasing temperature in a $\mu \propto 1/T$ proportionality.^{213,236}

As shown in Chapter 4.3, the introduction of sp^3 defects causes a moderate, yet noticeable, decrease in the maximum charge carrier mobilities in SWCNT network FETs (compare Figure 4.5) and hence should also affect their temperature dependence. For these measurements, transistors in a four-point probe layout (see Chapter 3.3.6) were fabricated from the dispersions with pristine and sp^3 -functionalized (low and high defect density, $n_d \sim 6 \mu\text{m}^{-1}$ and $\sim 34 \mu\text{m}^{-1}$) nanotubes in addition to the LEFET devices described above. This layout includes two voltage probes at fixed positions within the transistor channel ($L = 40 \mu\text{m}$, $W = 1 \text{mm}$) close to the source and drain electrodes, respectively. By linearly extrapolating the potential difference measured with the voltage probes, the voltage drops at the source and drain contacts, and thus contact resistance for charge carrier injection, can be calculated.³¹⁶ Because charge injection itself depends on temperature and charge carrier density, only the carrier mobilities after correction for the contact resistance can be unambiguously correlated with the charge transport properties of the SWCNT networks.^{85,196}

Temperature-dependent measurements of pristine and sp^3 -functionalized SWCNT network transistors were conducted between 25–300 K. For clarity, only every other curve is displayed in the transfer characteristics in Figure 4.14. All networks showed a decrease in on-currents for decreasing temperatures, corroborating overall thermally activated charge transport in agreement with previous results.^{85,262} Furthermore, the on-voltage (V_{on}) shifted

towards more positive values for electrons and more negative values for holes, respectively, when the temperature was lowered.

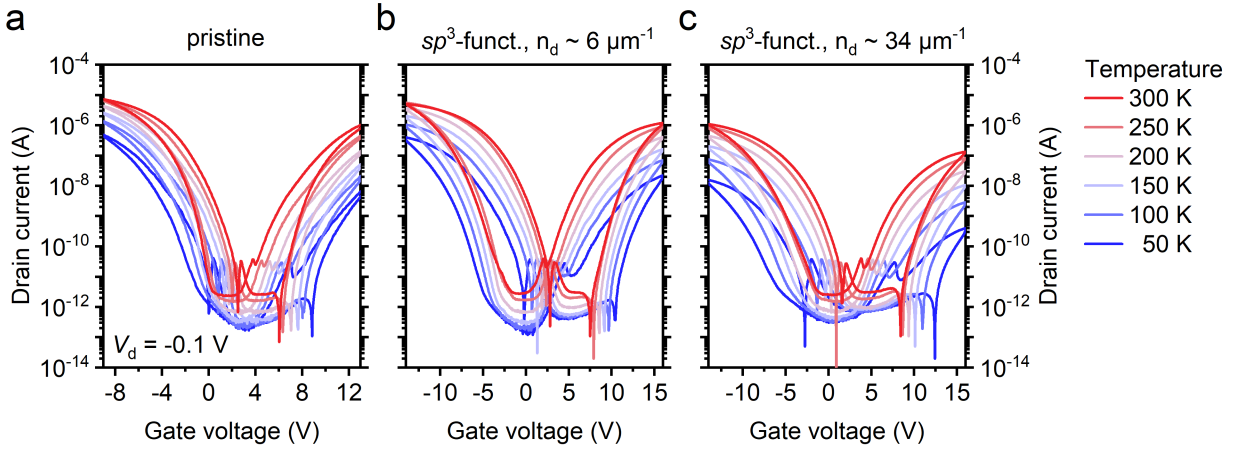


Figure 4.14: Temperature-dependent transfer characteristics of (a) pristine and (b,c) sp^3 -functionalized (6,5) SWCNT network FETs in the linear regime ($V_d = -0.1$ V).

As observed before, on-currents were lower for the sp^3 -functionalized SWCNT networks and higher gate voltages were required to reach the mobility maximum. These effects were more pronounced for the networks with a high degree of functionalization than for a low defect density. The impact of defects was also reflected in the subthreshold region of the transfer characteristics, which is typically dominated by shallow charge traps.²²² With increasing defect density, significantly lower subthreshold slopes and higher onset voltages were observed. According to Kalb *et al.*, the subthreshold swing S , *i.e.*, the inverse of the subthreshold slope, is related to the trap density N_{\square} at a given temperature T according to³¹⁷

$$S = \frac{\partial V_g}{\partial(\log(I_d))} = \frac{k_B T \ln(10)}{e} \left(1 + \frac{e^2}{C_i} N_{\square} \right) \quad (4.2)$$

In Equation 4.2, k_B is the Boltzmann constant, e denotes the elementary charge, and C_i is the areal capacitance. Calculated trap densities for holes and electrons at 300 K are listed in Table 4.2. An increase in trap densities by 50–60% for the highly functionalized sample compared to the pristine network confirms the moderate impact of sp^3 on charge transport at room temperature. As observed for the maximum charge carrier mobilities (compare Figure 4.5), the trend in trap densities was very similar for holes and electrons. Trap densities on the order of $10^{12} \text{ cm}^{-2} \text{ eV}^{-1}$ were in good agreement with previously reported values for (6,5) SWCNT networks,²²² and higher initial trap densities for electrons are likely due to the incomplete removal of oxygen and water as discussed above.

To analyze the temperature-dependent charge transport in networks of pristine and functionalized nanotubes, contact resistance-corrected charge carrier mobilities were calculated from the transfer curves between 25–300 K. Due to the temperature- and network-dependent

Table 4.2: Trap densities for holes and electrons at 300 K calculated from the subthreshold swings of pristine and sp^3 -functionalized (6,5) SWCNT network transistors according to Equation 4.2. Uncertainties are calculated by error propagation from the standard deviation of the linear fit of the subthreshold slope.

Defect density n_d (μm^{-1})	Trap density for holes $N_{\square}(\text{h}^+)$ ($10^{12} \text{ cm}^{-2} \text{ eV}^{-1}$)	Trap density for electrons $N_{\square}(\text{e}^-)$ ($10^{12} \text{ cm}^{-2} \text{ eV}^{-1}$)
0	5.9 ± 0.3	10.1 ± 0.1
5.8	8.3 ± 0.3	13.1 ± 0.1
33.9	9.4 ± 0.3	16.0 ± 0.1

shifts in the onset voltage and the gate voltage required to reach the transconductance maximum, mobilities were extracted at a fixed gate overpotential of 6 V above V_{on} , corresponding to a constant charge carrier density of approximately $4 \cdot 10^{12} \text{ cm}^{-2}$. While this value was chosen in order to allow mobility extraction for all samples even at the lowest temperatures where the mobility maximum in some instances was not reached due to the high V_{on} , it should be emphasized that similar trends were observed for values extracted at different overpotentials and, as far as analyzable, for maximum carrier mobilities. Notably, contact resistance-corrected network mobilities were 20–90% higher than apparent network mobilities before correction, which further highlights the importance of a suitable method to account for this effect.¹⁹⁶ Hole mobilities of SWCNT network FETs are plotted in Figure 4.15a on a logarithmic scale *versus* inverse temperature. Clearly, absolute mobilities were lower for sp^3 -functionalized networks compared to the pristine reference. The decrease in mobility upon functionalization at a given temperature was more pronounced for the values extracted at a certain gate overpotential compared to the maximum mobilities (compare Table 4.1) due to the shift of the transconductance maximum for the samples with sp^3 defects to higher gate voltages. For all samples, mobilities show a steep decrease from 300 K to 150 K and subsequently level off at lower temperatures.

As detailed in Chapter 2.4.2, two commonly used theoretical frameworks to describe the temperature dependence of charge transport in disordered semiconductors are the variable range hopping (VRH)²⁶¹ and the fluctuation-induced tunneling (FIT)²⁶⁷ models. Both models have also been applied to networks of nanotubes.^{188,260} In agreement with previous results for dense semiconducting SWCNT networks,⁸⁵ the VRH model did not provide a suitable fit to the data in Figure 4.15 especially in the low-temperature regime. While fits according to the FIT model yielded better results, the interpretation of the fitting parameters in terms of actual physical network parameters remains ambiguous.²⁶⁶ In addition, both models reduce charge transport through SWCNT networks exclusively to inter-tube carrier transport across nanotube–nanotube junctions, while neglecting the contribution of intra-nanotube transport along stretches of individual SWCNTs. Even though a defect that is directly located at an

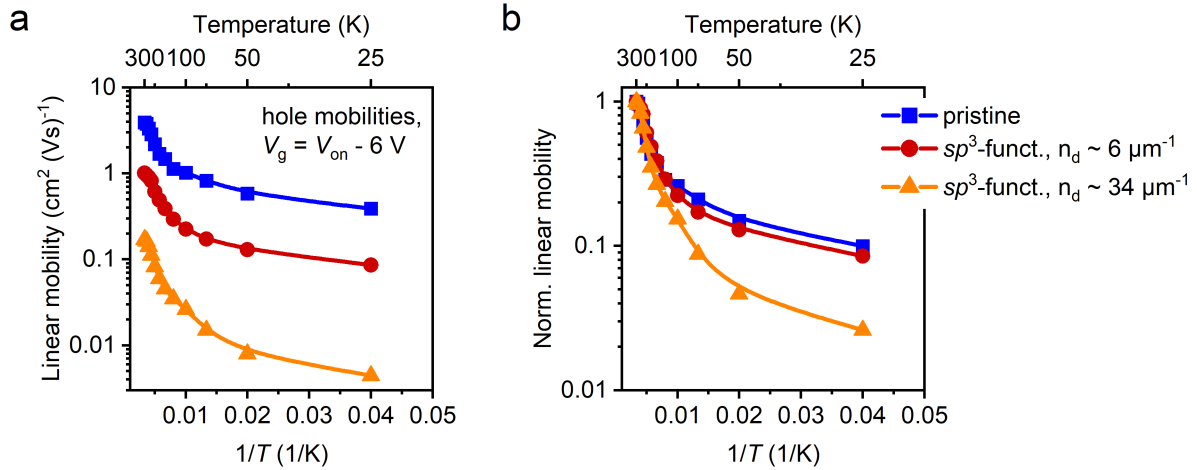


Figure 4.15: (a) Absolute and (b) normalized temperature-dependent hole mobilities of pristine and sp^3 -functionalized (6,5) SWCNT network FETs. Mobilities were extracted from linear transfer curves ($V_d = -0.1$ V) at a constant gate overpotential of $V_g = V_{on} - 6$ V and thus, constant charge carrier density of $\sim 4 \cdot 10^{12} \text{ cm}^{-2}$. Lines are guides to the eye.

inter-nanotube junction will presumably constitute an additional barrier to charge transport, it seems unlikely that the impact of a low number of covalently attached aryl groups on the junction resistance is the dominating effect for the dense SWCNT networks investigated here. Despite the large influence of sp^3 defects on the spectroscopic properties of SWCNTs due to the high exciton mobility in individual nanotubes and their networks,^{119,318} the average distance between two defects is still relatively large with several tens of nanometers even for the highest defect density of $n_d \sim 34 \mu\text{m}^{-1}$. Given the dense networks with >25 SWCNTs per μm and consequently many interconnecting junctions, the direct impact of sp^3 functionalization on the junctions and thus inter-nanotube charge transport is assumed to be limited. If this assumption is correct, changes in the intra-nanotube conductance upon functionalization must be the cause for the observed differences in mobilities, which would further support the idea that charge transport in semiconducting SWCNT networks is not only governed by the inter-nanotube junctions.²⁶⁶ Thus, in the following, the impact of luminescent defects on temperature-dependent charge transport will be assessed by qualitatively comparing the trends in carrier mobilities without applying an analytical model.

If the inter-nanotube junctions were the only limiting factor to charge transport through the networks, and assuming a minor impact of sp^3 functionalization on the junctions, the temperature dependence of charge carrier mobilities for pristine and functionalized SWCNT networks should be essentially the same. However, as shown from the mobilities normalized to the values at 300 K (Figure 4.15b), hole mobilities for the networks with sp^3 defects decreased even further with decreasing temperatures than for the unfunctionalized samples. In other words, carrier mobilities in SWCNT networks with a higher degree of functionalization exhibited a stronger temperature dependence. Identical trends were observed for electron

mobilities. The low impact of sp^3 defects on nanotube–nanotube junctions was corroborated by the very similar temperature dependencies of normalized carrier mobilities for all networks above 150 K, as shown by their similar slopes in Figure 4.15b. In this temperature range, charge transport is mainly governed by thermally activated carrier hopping across the junctions.

If sp^3 defects were to act as shallow charge traps, as suggested by spectroscopic experiments, their overall impact in the high-temperature regime should be low due to fast detrapping of carriers. Upon further decrease of the temperature, inter-tube carrier hopping is significantly slowed down, and inter-nanotube transport becomes dominated by tunneling processes of charges between conductive nanotube segments. Because tunneling is temperature-independent, the role of charge transport along these conductive segments (intra-nanotube transport) becomes more significant, and so does the impact of the defects. Slow detrapping from shallow charge traps at low temperatures results in a decrease in intra-nanotube conductivity and consequently lower carrier mobilities for functionalized compared to unfunctionalized SWCNTs.

To summarize, the temperature-dependent transport data support the hypothesis that both the contributions of inter-nanotube transport across the junctions and of intra-nanotube conduction play an important role for charge transport in SWCNT networks and their overall network mobilities. Importantly, the observation of defect-state EL and the results obtained by CMPL spectroscopy indicated that functionalized nanotube segments are sampled by mobile charge carriers and hence must at least partially contribute to charge transport. Therefore, the observed decrease in absolute carrier mobilities in networks with sp^3 defects and their stronger temperature dependence are attributed to an increase in intra-nanotube resistance rather than a reduction of conductive pathways through the networks.

It should be emphasized that while the spectroscopic data and the temperature-dependent transport measurements point towards the role of luminescent defects as shallow charge traps, additional experiments are necessary to fully understand the impact of sp^3 functionalization on charge transport in semiconducting SWCNTs. Because the experiments in this Chapter were conducted exclusively on dense nanotube networks, further insights into charge transport on a microscopic scale, *e.g.*, on a single-nanotube level, are required to obtain a comprehensive picture. This especially concerns the question whether defects are best described as charge traps or as scattering centers at room temperature. For individual nanotubes, charge transport is mainly limited by carrier–phonon scattering, with reported scattering lengths of several hundred nanometers up to $\sim 1 \mu\text{m}$.²¹³ In contrast to that, the scattering length in dense SWCNT networks is difficult to correlate with the estimated distances between two defects, because scattering can also occur, *e.g.*, at nanotube–nanotube junctions. From microwave conductivity measurements of (6,5) SWCNT networks with carrier mobilities of $\sim 4\text{--}8 \text{ cm}^2(\text{Vs})^{-1}$, Ferguson *et al.* estimated a transport length scale of $\sim 85\text{--}115 \text{ nm}$ by

using $L_d = \sqrt{6Dt}$ and $D = \mu k_B T / e$.²⁸³ Using the network mobilities in Table 4.1 yields estimated scattering lengths for the pristine samples of ~ 51 nm for electrons and ~ 88 nm for holes, whereas values of ~ 25 nm for electrons and ~ 43 nm for holes were obtained for the networks with the highest defect density. Assuming a homogeneous distribution of defects along the nanotubes without clustering, these estimated scattering lengths are considerably shorter than the inter-defect distances of several tens to hundreds of nanometers. To avoid the influence of the inter-nanotube junctions, measurements on short-channel transistors with individual functionalized nanotubes of a known chirality would be useful.^{179,319} In this device layout, charge carriers travelling through the transistor channel are forced to interact with the defects, thus enabling an unambiguous correlation of the observed changes with the impact of sp^3 functionalization on the intra-nanotube conductivity. A statistically significant number of measurements for such devices could even permit the analysis of the exact impact of functionalization depending on the SWCNT chirality and the defect binding configuration.²³ Additionally, contact-free all-optical techniques such as terahertz (THz) spectroscopy²⁸⁶ or microwave conductivity measurements²⁸³ could provide quantitative insights into the intrinsic charge transport properties of sp^3 -functionalized SWCNTs in dispersions and thin films.

4.8 Summary and conclusion

In this Chapter, fully functional light-emitting field-effect transistors based on dense networks of sp^3 -functionalized (6,5) SWCNTs were demonstrated. Despite a moderate decrease in charge carrier mobilities with increasing defect density, all devices exhibited good switching behaviour and ambipolar charge transport. These excellent electrical characteristics enabled the observation of electrically-pumped emission from the defect states that was red-shifted from the native E_{11} emission. Defect EL (mainly E_{11}^* but also E_{11}^{*-}) was tunable in intensity *via* the defect concentration and stable over a wide current range. Additionally, a brightening in external EL efficiencies was observed for SWCNT networks with low defect densities compared to the unfunctionalized reference transistors. Covalent functionalization of other nanotube chiralities and the selective introduction of E_{11}^{*-} defects, which possess an even deeper optical trap depth and thus spectral red-shift, should allow us to tune the emission spectrum of electroluminescent SWCNT devices across the NIR spectral range towards application-relevant wavelengths. This approach is further discussed in Chapter 7.

The combined data from various spectroscopic techniques and temperature-dependent current–voltage measurements suggested that sp^3 defects in the dense SWCNT networks may act as shallow charge traps that increase the resistance along individual nanotubes. Importantly, functionalized nanotube segments are still sampled by mobile carrier density and hence actively contribute to the charge transport through the networks. Charge carriers lo-

calized at the defect sites can be rapidly detrapped at room temperature, thus explaining the limited reduction in the overall network mobilities. However, the impact of defects becomes large at lower temperatures (< 150 K). Temperature-dependent carrier mobilities provide evidence that charge transport in SWCNT networks is not only governed by inter-nanotube hopping across the junction barriers, but the contribution of intra-nanotube resistance plays a significant role as well. Complementary experimental techniques are required to unambiguously elucidate the impact of luminescent defects on the intrinsic charge transport properties of covalently functionalized SWCNTs without the influence of nanotube junctions in a network. One such technique is optical-pump THz-probe (OPTP) spectroscopy, which can provide quantitative insights into microscopic charge transport in a direct and contact-free fashion. The use of OPTP spectroscopy to investigate the carrier dynamics in functionalized (6,5) SWCNT dispersions and films is described in the next Chapter.

Chapter 5

Carrier Dynamics in Functionalized SWCNTs Probed by Terahertz Spectroscopy

In this Chapter, the intrinsic charge transport and carrier dynamics in sp^3 -functionalized SWCNTs are studied with optical-pump terahertz-probe spectroscopy.

The results presented in this Chapter were published in W. Zheng, N.F. Zorn *et al.*, *ACS Nano* **2022**, *16*, 9401–9409.²⁹⁴ Wenhao Zheng and myself contributed equally to this publication and shared the first-authorship. Modified versions of previously published Figures are presented with permission of the American Chemical Society. Optical-pump terahertz-probe spectroscopy of SWCNT dispersions and films was conducted by Wenhao Zheng under the supervision of Dr. Hai Wang and Prof. Dr. Mischa Bonn at the Max Planck Institute for Polymer Research in Mainz.

5.1 Introduction

As detailed in Chapter 4, networks of covalently functionalized SWCNTs were successfully applied as charge transport and emission layers in LEFETs and exhibited EL from sp^3 defect states. Despite the excellent ambipolar transport characteristics even at high defect densities, a decrease in network mobilities with increasing degree of functionalization was observed. The multitude of different contributions to charge transport in SWCNT networks, and especially the apparent convolution of intra-nanotube band transport and inter-nanotube carrier hopping,¹⁸⁸ however complicated an assessment of the exact impact of the defects.

Charge transport in SWCNT networks is commonly hypothesized to be limited by transport across the inter-nanotube junctions.^{188,258,259} This notion is supported by the significantly lower carrier mobilities in SWCNT networks below $100 \text{ cm}^2(\text{Vs})^{-1}$ compared to individual nanotubes with diameter-dependent ($\mu \propto d^2$) mobilities of $> 1000 \text{ cm}^2(\text{Vs})^{-1}$.^{78,213,220,250} Indeed, previous temperature-dependent measurements of nanotube networks revealed overall thermally activated transport,^{85,246,259,262} which implied a dominant role of inter-nanotube hopping rather than intra-nanotube band transport with its characteristic $\mu \propto 1/T$ dependence. Measurements of SWCNT network FETs with varying nanotube bandgap distributions showed that the resistance of a junction was significantly higher than along the nanotubes,²⁵⁸ which is in agreement with results obtained by conductive AFM.^{254,256}

However, recent experimental studies on purely semiconducting SWCNT networks with different compositions have challenged this simplified picture.^{85,222,266} For FETs based on large-diameter, but polydisperse SWCNT networks, considerably higher carrier mobilities with a lower temperature dependence were found compared to monochiral, small-diameter (6,5) SWCNTs.²⁶⁶ From a model involving only the junctions, the opposite behaviour would be expected due to the lower hopping barriers in the monochiral networks, thus indicating that the influence of the diameter- and temperature-dependent intra-nanotube mobility cannot be neglected. Likewise, the observed differences in network mobilities and their temperature dependence for pristine and functionalized SWCNTs in Chapter 4 were attributed to changes in the intrinsic nanotube conductance caused by the defects^{178,179} and hence point in the same direction. While theoretical simulations of charge transport in SWCNT networks

could provide further insights, models that include intra-nanotube transport were reported only very recently.^{269,270}

Consequently, experimental methods that enable the study of charge transport in SWCNT networks on a microscopic level are required. In this regard, all-optical techniques in the gigahertz (GHz, *i.e.* microwave) and terahertz (THz) range are particularly suited, as they can probe the conductivity of charge carriers in semiconductors on very short length scales and without the need for external electrodes.²⁸³ Such techniques were also applied to SWCNT dispersions and films, albeit so far only with unfunctionalized nanotubes. One example are (time-resolved) microwave conductivity measurements, which were used to quantify the efficiency of chemical doping of semiconducting nanotube networks²⁸³ and the dynamics of photogenerated carriers in individually dispersed SWCNTs.²⁸⁴ On the other hand, time-resolved optical-pump THz-probe (OPTP) spectroscopy demonstrated very similar carrier dynamics in metallic and semiconducting SWCNT films²⁸⁷ and longer carrier scattering times in semiconducting nanotubes compared to graphene nanoribbons.²⁸⁶

OPTP spectroscopy is a direct and contact-free method in which an optical pump pulse creates free charge carriers in a semiconductor that are subsequently probed by a THz pulse.³²⁰ The THz pulse accelerates the charges over short distances on the order of tens of nanometers, resulting in a certain degree of energy dissipation of the THz field that can be directly related to local carrier transport on these length scales. Hence, OPTP spectroscopy has enabled a quantitative analysis of intrinsic charge transport properties, such as carrier mobilities and scattering times, in a variety of different nanomaterials.^{321–326} In this Chapter, local charge transport and carrier dynamics in covalently functionalized SWCNT dispersions and films are investigated with (temperature-dependent) OPTP spectroscopy. The comparison of the results to macroscopic transport measurements of functionalized SWCNT network FETs provides a clearer picture of the influence of sp^3 defects on charge transport in individual SWCNTs and their networks.

5.2 Functionalization and characterization

To investigate the impact of sp^3 defects on microscopic and macroscopic charge transport in SWCNTs, essentially monochiral dispersions of (6,5) nanotubes in toluene were prepared by shear force mixing and polymer-wrapping with PFO-BPy, as detailed in Chapter 3.1.1.⁸⁷ The high purity of the dispersions without residual metallic SWCNTs was confirmed by Raman and absorption spectroscopy. Covalent functionalization to introduce aryl sp^3 defects was performed with 4-nitrobenzenediazonium tetrafluoroborate ($DzNO_2$, see Figure 5.1a) in a solvent mixture of toluene and MeCN (80:20 vol-%) with the aid of 18-crown-6 as a phase-transfer agent (see Chapter 3.2.1 and the reaction scheme in Figure 4.1).²² After mixing of all components and reaction over night and in the dark, functionalized SWCNTs were

collected by vacuum filtration and thoroughly washed to remove unreacted diazonium salt that might remain on the nanotube surface. SWCNTs were re-dispersed in a dilute solution of PFO-BPy in toluene (0.1 g L^{-1}) to ensure colloidal stability and minimize aggregation at the high concentrations required for OPTP spectroscopy (optical density of $4\text{--}6 \text{ cm}^{-1}$ at the E_{11} absorption transition).

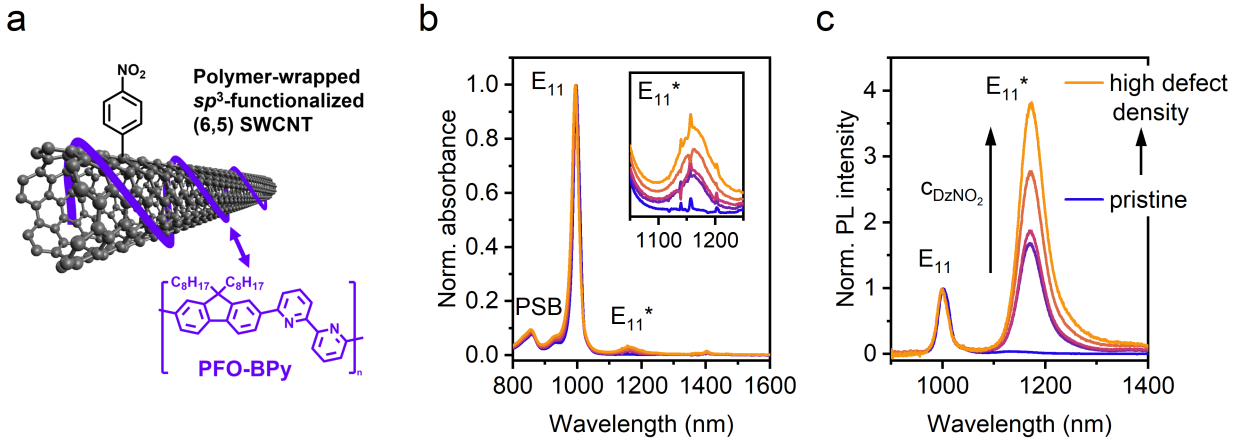


Figure 5.1: (a) Schematic illustration of a PFO-BPy-wrapped (6,5) SWCNT with a nitroaryl sp^3 defect. (b) Normalized absorption spectra and (c) normalized PL spectra (pulsed E_{22} excitation at 575 nm) of (6,5) SWCNT dispersions functionalized with different concentrations of 4-nitrobenzenediazonium tetrafluoroborate (C_{DzNO_2}). Labels indicate the main E_{11} and E_{11}^* transitions as well as the phonon sideband (PSB) in absorption. The inset in (b) shows a zoom-in on the E_{11}^* defect-state absorption feature.

The introduction of sp^3 defects to the SWCNTs was corroborated by the emergence of new E_{11}^* transitions in the absorption and PL spectra at 1160 nm and 1173 nm, respectively, as shown in Figure 5.1b,c. Calculated Stokes shifts of 12 meV for E_{11}^* and 6 meV for E_{11} were in good agreement with previously reported values.²² In emission, the dominant defect peak was red-shifted from the native E_{11} exciton by 185 meV. As expected, this red-shift was larger than for the bromoaryl defects (174 meV) used in Chapter 4 due to the more electron-withdrawing character of the nitroaryl group, and thus a deeper exciton trap depth.^{16,22} Through adjustment of the diazonium salt concentration (here, $50\text{--}1000 \mu\text{g mL}^{-1}$), different defect densities were created on the nanotubes, as shown by the variation in relative peak intensities in absorption and emission. Notably, no features corresponding to E_{11}^{*-} defects that can occur as a minority species in this functionalization scheme (compare Figure 4.2a) were observed in the PL spectra.

Resonant Raman spectroscopy further corroborated the controlled variation of the degree of SWCNT functionalization, as shown by the increase in the D mode at $\sim 1310 \text{ cm}^{-1}$ relative to the G^+ mode at $\sim 1590 \text{ cm}^{-1}$ with increasing reactant concentration (Figure 5.2a). From the difference in Raman D/ G^+ area ratios of functionalized and pristine SWCNTs, defect densities (n_{d}) between $6\text{--}21 \mu\text{m}^{-1}$ were calculated according to Equation 4.1.¹⁴⁷ Linear

correlations were found for the integrated E_{11}^*/E_{11} ratios in absorption and PL *versus* Raman D/G⁺ area ratio and calculated n_d (Figure 5.2b,c). While all these quantities may serve as metrics for the degree of functionalization, only the latter two will be used here.

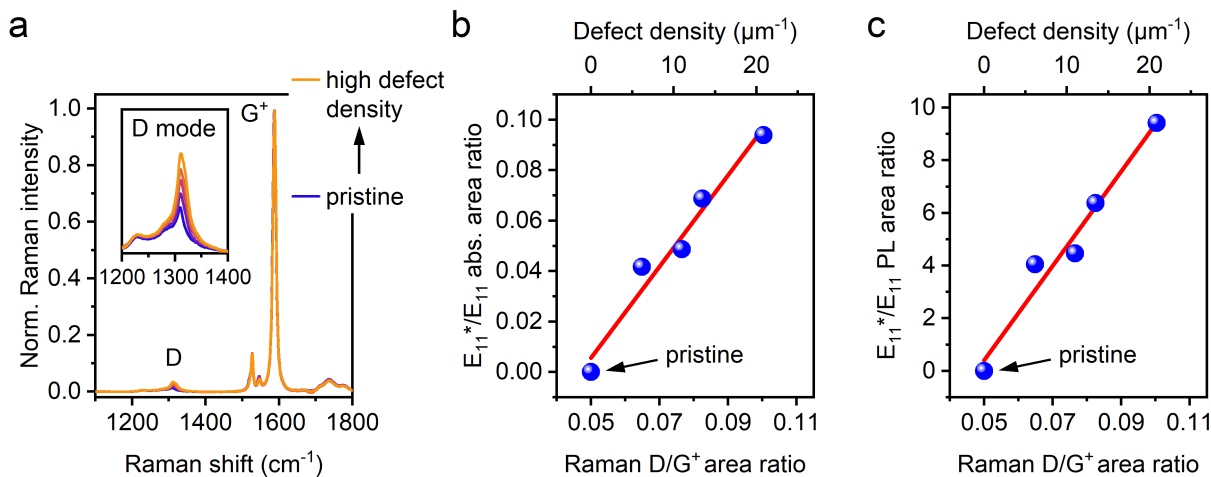


Figure 5.2: (a) Raman spectra (532 nm excitation) of pristine and functionalized (6,5) SWCNTs normalized to the G⁺ mode. The inset shows a zoom-in on the defect-related D mode. (b) E_{11}^*/E_{11} peak area ratio in absorption and (c) in PL *versus* Raman D/G⁺ area ratio and calculated sp^3 defect density. Red lines are linear fits to the data.

Importantly, the functionalization procedure did not significantly alter the length distribution of SWCNTs. Length statistics of more than 120 individual SWCNTs for each sample obtained by AFM revealed average nanotube lengths of $\sim 1.4 \mu\text{m}$. Figure 5.3 shows representative histograms for pristine SWCNTs and two different defect densities.

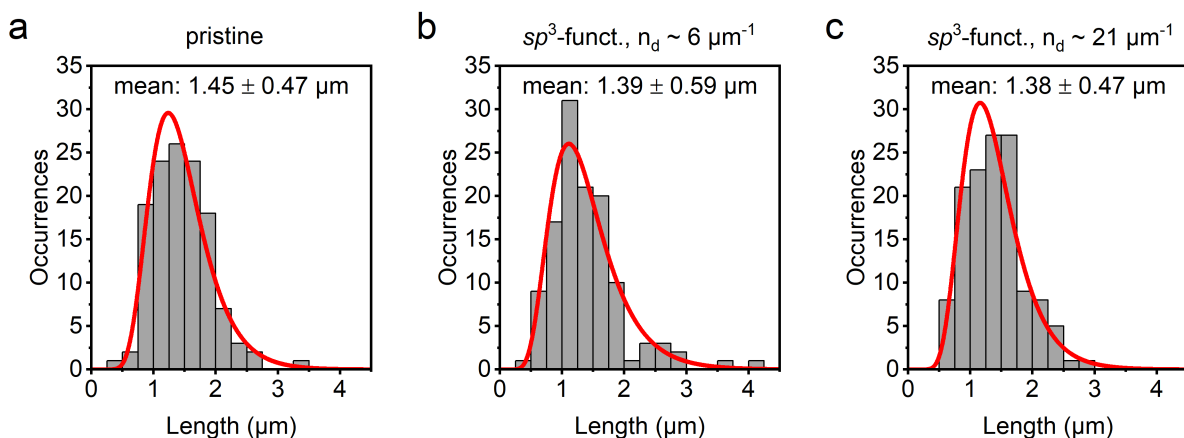


Figure 5.3: AFM statistics on individual nanotube lengths for (a) pristine and (b,c) functionalized (6,5) SWCNT dispersions. For each histogram, more than 120 individual SWCNTs were evaluated. Red lines are log-normal distributions.

5.3 OPTP spectroscopy of SWCNT dispersions

To investigate the impact of luminescent sp^3 defects on the local charge transport properties of (6,5) SWCNTs, OPTP spectroscopy was performed on concentrated nanotube dispersions as schematically illustrated in Figure 5.4 (see Chapter 3.4.10). Optical excitation at ~ 1000 nm (~ 1.25 eV, close to the E_{11} transition) generates a small population of free carriers that are subsequently probed by a single-cycle THz pulse (bandwidth ~ 0.4 – 2.5 THz, or 1.6 – 10 meV) of ~ 1 ps duration.³²⁰ Upon interaction with the charges, the THz field is attenuated, and the degree of energy dissipation is directly related to the local carrier mobility on the short length scales (tens of nanometers) probed by this technique. The transmitted THz pulses without and with photoexcitation are recorded in the time domain to measure the changes in amplitude and phase and calculate the complex-valued, photoinduced THz conductivity $\Delta\sigma$. Fixing the sampling beam to the peak of the THz field and monitoring the photoinduced absorption $\Delta E = E_{\text{pump}} - E$ as a function of pump–probe delay provides access to the ultrafast photoconductivity dynamics ($\Delta\sigma \propto -\Delta E/E$) with sub-picosecond resolution.³²⁰

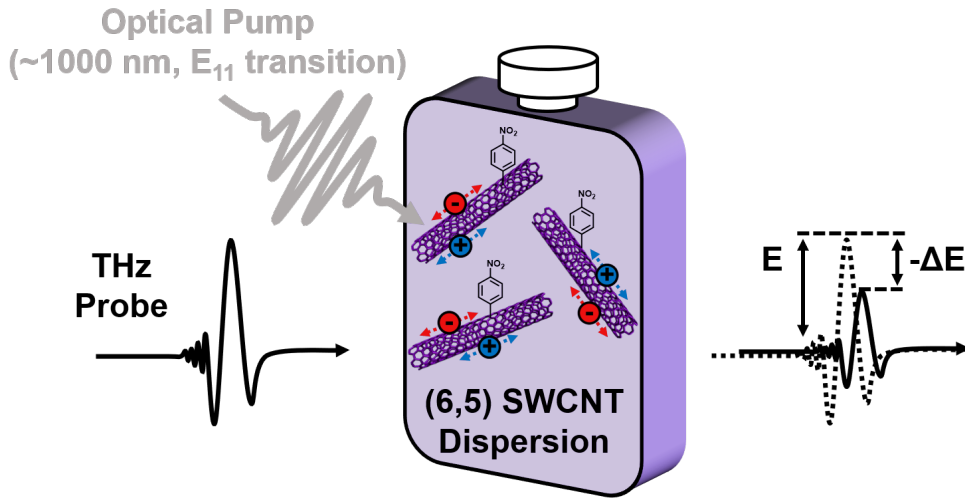


Figure 5.4: Schematic illustration of OPTP spectroscopy on nanotube dispersions.

Figure 5.5a shows the photoconductivity dynamics of pristine and functionalized SWCNT dispersions. To correct for the different optical densities of the dispersions, all transients were normalized to the absorbed photon density (N_{abs}). Before photoexcitation, no THz conductivity signal is observed, since the nanotubes are in the neutral state and no charge carriers are present. Upon excitation with optical pump pulses, the photogeneration of free carriers (holes and electrons) manifests itself in a steep sub-picosecond rise of the photoconductivity to its maximum value, followed by a subsequent decay. Note that only the magnitude of the real conductivity is shown here, as it reflects the THz response of free charge carriers. Importantly, free carriers contribute to both the real and imaginary conductivity. Uncharged photoexcitation products such as excitons do not absorb the THz field,

but they lead to a phase shift due to their polarizability and thus contribute exclusively to the imaginary part.²⁸⁶ For all samples, imaginary conductivities were low ($\sim 20\%$ of the real part), suggesting that the observed THz response was dominated by the photogenerated carriers on the nanotubes.³²² While the observation of free-carrier generation in SWCNTs upon photoexcitation has been reported previously,^{284,287,327} the underlying mechanism remains unclear. This aspect is further discussed in Chapter 5.4.

As shown in Figure 5.5a, the maximum photoconductivity shortly after optical excitation decreased monotonously with increasing degree of functionalization. It should be emphasized that OPTP spectroscopy probes the local charge transport properties of individual SWCNTs in dispersion and electronic coupling between different nanotubes can be neglected, as confirmed by the near-identical photoconductivities normalized to N_{abs} for dispersions with different SWCNT concentrations. Consequently, the observed trends can be directly attributed to the impact of sp^3 defects. The extracted maximum photoconductivities are displayed in Figure 5.5c. With respect to the pristine SWCNTs, a reduction by $\sim 13\%$ was observed for a defect density of $n_d \sim 6 \mu\text{m}^{-1}$, whereas the value was lowered by $\sim 30\%$ for the highest defect density ($n_d \sim 21 \mu\text{m}^{-1}$). Assuming a homogeneous distribution of sp^3 defects on the nanotubes, the range of defect densities corresponds to average inter-defect distances between ~ 170 nm and ~ 50 nm, respectively. The transport lengths probed by OPTP spectroscopy are on the order of few tens of nanometers (see below for an estimation of carrier diffusion lengths). Thus, it can be hypothesized that charge carriers in highly functionalized SWCNTs interact with one or few defect sites during their lifetime, whereas for the low defect densities, they might not interact with a defect at all. Overall, the values are in excellent agreement with the reported conductance decrease of 20% in single-nanotube transistors upon introduction of an isolated defect,^{178,179} and hence corroborate the small but noticeable impact of luminescent defects on intra-nanotube transport.

After reaching their maximum, THz conductivities exhibit a fast decay within few picoseconds, followed by a slow component as shown in the normalized photoconductivity transients in Figure 5.5b. The decay can be attributed to a decrease in charge carrier density due to carrier recombination and exciton formation.²⁸⁶ Excitons may subsequently diffuse along the nanotubes and become localized at the defects on picosecond time scales as shown by transient absorption spectroscopy.¹⁴¹ Clearly, the photoconductivity decay is faster for functionalized SWCNTs, and the relative amplitude of the fast decay component increases with increasing defect concentration. This decrease in photoconductivity lifetime might be associated with carrier trapping at sp^3 defect sites, which could facilitate charge recombination. The decrease in free-carrier lifetime with increasing number of defects is further shown by the extracted 1/e lifetimes (blue circles in Figure 5.5c). They exhibit a very similar trend compared to the maximum photoconductivities and decrease by approximately 20% from ~ 2.4 ps for the pristine nanotubes to ~ 1.9 ps for the highest defect density.

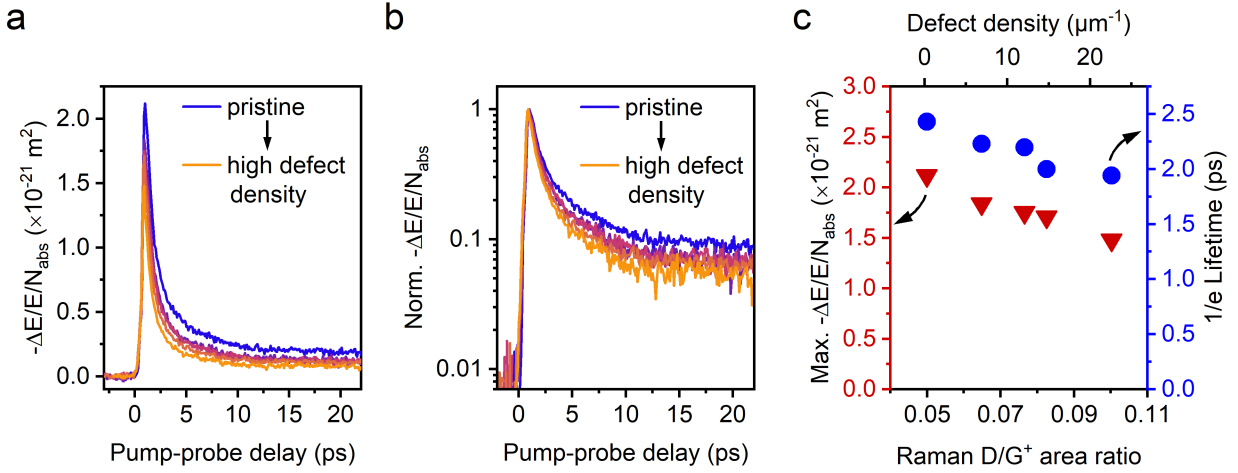


Figure 5.5: (a) Absolute and (b) normalized photoconductivity dynamics of pristine and functionalized SWCNT dispersions. The optical excitation energy was ~ 1.25 eV, and the absorbed photon density was $N_{\text{abs}} \sim 3 \cdot 10^{18} \text{ m}^{-2}$. Note, the data in (b) is plotted on a logarithmic scale. (c) Maximum THz photoconductivities normalized to the absorbed photon density (left axis, red triangles) and $1/e$ carrier lifetimes (right axis, blue circles) versus Raman D/G⁺ area ratio and calculated sp^3 defect density. Values were extracted from the data in (a) and (b), respectively. Data were measured by Wenhao Zheng (MPI for Polymer Research, Mainz).

To obtain more detailed insights into local charge transport, SWCNT dispersions were investigated by THz time-domain spectroscopy (THz-TDS). In this measurement scheme, the time delay between the optical pump and the THz probe pulses is kept constant to record the entire transmitted THz pulse in the time domain. Fourier transformation to the frequency domain provides access to the complex-valued, frequency-resolved photoconductivity spectra, as shown in Figure 5.6 for pristine and highly functionalized SWCNTs. It should be noted that while the data presented here was typically recorded at a pump-probe delay of 1.5 ps, similar trends were observed for different delays up to 6 ps.

The complex photoconductivity spectra exhibited a large real conductivity and a low contribution by the imaginary part for all pump-probe delays and samples. As already inferred from the maximum amplitude of the photoconductivity dynamics (compare Figure 5.5), the THz conductivity was lower for functionalized SWCNTs compared to the pristine reference. In agreement with previous results,^{286,328} the Drude-Smith model in Equation 5.1 provides a good fit to the data.^{329,330}

$$\sigma(\omega) = \frac{\epsilon_0 \omega_p^2 \tau_s}{1 - i\omega\tau_s} \cdot \left(1 + \frac{C}{1 - i\omega\tau_s} \right) \quad \text{with} \quad \omega_p^2 = \frac{e^2 N}{\epsilon_0 m^*} \quad (5.1)$$

The Drude-Smith model describes the motion of free charge carriers in a medium with preferential backscattering.³²⁹ In Equation 5.1, ϵ_0 is the vacuum permittivity, and τ_s is the

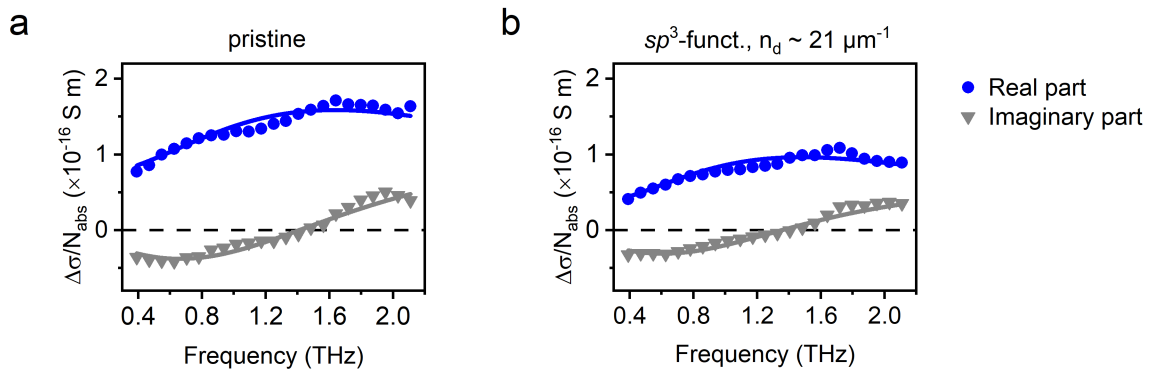


Figure 5.6: Complex photoconductivity spectra of (a) pristine and (b) functionalized ($n_d \sim 21 \mu\text{m}^{-1}$) SWCNT dispersions measured ~ 1.5 ps after photoexcitation. Blue circles are real parts of the conductivity, grey triangles are imaginary parts. Solid lines are fits according to the Drude-Smith model. Data were measured by Wenhao Zheng (MPI for Polymer Research, Mainz).

average charge scattering time. The plasma frequency ω_p is directly related to the charge carrier density N , with e and m^* being the elementary charge and the carrier effective mass, respectively. The backscattering parameter C essentially expresses the correlation between carrier momenta before and after a scattering event and can assume values between 0 and -1. For $C = 0$, scattering is fully isotropic, and Equation 5.1 reduces to the classical Drude model. The case of $C = -1$ on the other hand describes full preferential backscattering. It should be noted that for one-dimensional structures such as SWCNTs which are randomly oriented in three dimensions (*e.g.*, in a dispersion), an orientation-averaged value of $C = -\pi/4 \approx -0.79$ would be expected for complete backscattering.²⁸⁶ From the Drude-Smith fits to the frequency-resolved photoconductivity spectra, backscattering parameters between -0.78 and -0.85 were obtained for all dispersions. While an interpretation of the trends of only one of the three fitting parameters alone is not possible, the values for C indicate predominant backscattering for all samples including the pristine (6,5) SWCNTs, which agrees with a previous report.²⁸⁶ This preferential backscattering can be attributed to the nanoscale confinement of charge carriers along the one-dimensional SWCNTs.

The fitting results enabled the calculation of local carrier mobilities in the direct current (DC) limit by using Equation 5.2. Notably, the DC mobility is different from the microscopic mobility between two scattering events (given by $\mu = \frac{e \cdot \tau_s}{m^*}$), as it takes the backscattering effect into account. As such, it can be seen as a carrier transmission probability in the direction of an external electric field, and should be better suited for comparison, *e.g.*, with macroscopic mobilities determined from FET measurements.

$$\mu_{DC} = \frac{e \cdot \tau_s}{m^*} \cdot (1 + C) \quad (5.2)$$

Calculated DC mobilities were on the order of a few $100 \text{ cm}^2(\text{Vs})^{-1}$, as detailed in Table 5.1. These results are on the same order of magnitude as the diameter-dependent carrier mobilities in single-nanotube transistors.²¹³ It should, however, be emphasized that these mobilities were measured at low charge carrier densities (see below for an estimation) and reflect local charge transport in individually dispersed nanotubes on the short length scales probed by OPTP spectroscopy. Most importantly, the absolute mobility values may strongly depend on the applied fitting model. Even though the Drude-Smith model provides a good fit to the data and has been used previously to describe intrinsic charge transport in SWCNTs,^{286,328} it was not specifically developed for nanotubes and thus needs to be regarded as a purely phenomenological model.

In contrast to the absolute values, the relative trend in carrier mobilities does not depend on the fitting model and hence should enable a more robust comparison. For the SWCNT dispersion with the highest defect density, the decrease in DC mobility was $\sim 26\%$ with respect to the unfunctionalized reference, which is in excellent agreement with the observed decrease in maximum photoconductivity by $\sim 30\%$ upon functionalization (compare Figure 5.5a,c). Overall, the evolution of maximum photoconductivities and calculated DC mobilities with increasing defect density is very similar, as shown in Table 5.1 and Figure 5.7. This similarity provides further evidence that the observed trend in photoconductivities is indeed due to a decrease in intra-nanotube conductance with increasing degree of functionalization rather than due to differences in photogenerated charge carrier density.

Table 5.1: Raman D/G⁺ area ratios of pristine and functionalized SWCNTs, calculated sp^3 defect densities, maximum photoconductivities from OPTP measurements, and carrier mobilities in the DC limit determined from Drude-Smith fits of the complex photoconductivity spectra. Standard deviations were calculated from uncertainties of the fits.

Raman D/G ⁺ area ratio	Defect density n_d (μm^{-1})	Max. photoconductivity $-\Delta E/E/N_{abs}$ (10^{-21} m^2)	DC mobility $\mu(1 + C)$ ($\text{cm}^2(\text{Vs})^{-1}$)
0.050	0	2.12	325 ± 8
0.065	6.2	1.84	297 ± 7
0.077	11.0	1.75	285 ± 7
0.083	13.5	1.71	249 ± 6
0.100	20.8	1.48	240 ± 5

Using the calculated DC mobilities from the Drude-Smith fits and the $1/e$ carrier lifetimes extracted from the normalized photoconductivity dynamics (compare Figure 5.5b,c), the carrier diffusion lengths on the nanotubes can be estimated *via*

$$L_d = \sqrt{\frac{\mu \cdot \tau_{(1/e)} \cdot k_B \cdot T}{e}} \quad (5.3)$$

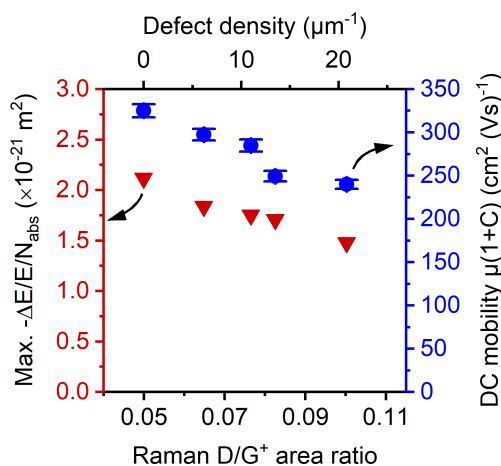


Figure 5.7: Maximum photoconductivities (left axis, red triangles) and photogenerated carrier mobilities in the DC limit (right axis, blue circles) *versus* Raman D/G⁺ area ratio and calculated sp^3 defect density. Error bars were determined from uncertainties of the fits. Data were measured by Wenhao Zheng (MPI for Polymer Research, Mainz).

For pristine SWCNTs, a diffusion length of 45 nm was obtained. The estimated carrier diffusion length decreased gradually with increasing defect density and was ~ 35 nm for the highly functionalized nanotubes. These values reflect the short length scales of charge transport that are probed in OTP measurements and corroborate the notion that the majority of photogenerated carriers interact with one or only few defects during their lifetime. Consequently, the observed decrease in maximum photoconductivity and carrier mobility can be attributed to the decrease in intra-nanotube conductance upon covalent functionalization, and the magnitude of their reduction confirms that the impact of sp^3 defects on the intrinsic charge transport properties of semiconducting (6,5) SWCNTs is only moderate especially at low defect densities.

5.4 Mechanism of photoinduced free-carrier generation

Due to their low dimensionality and consequently poor screening of Coulomb interactions, the spectroscopic properties of SWCNTs are dominated by strongly bound excitons.^{96,101} Given their large binding energies of ~ 360 meV for (6,5) SWCNTs,¹⁰² these excitons should be the primary species that is produced upon photoexcitation. Several studies reported the dissociation of excitons at heterojunctions to produce a photocurrent.^{331–336} In addition, even without an energetic driving force for exciton dissociation, the generation of free charges following optical excitation has been widely observed in the literature for individual SWCNTs and films.^{284,287,327,334,337–341} While nanotube–nanotube or nanotube–electrode contacts may promote exciton dissociation in films,²⁸⁴ the mechanism of optical free-carrier generation especially in nanotube dispersions has remained unclear.

The nature of the primary product of photoexcitation in OPTP measurements of SWCNTs has been debated previously. Some studies suggested that the THz response of SWCNTs originated from excitons³⁴² or from intra-excitonic transitions,³⁴³ while others attributed the photoresponse in OPTP experiments on mixed metallic/semiconducting SWCNT films and monochiral nanotube dispersions to free charge carriers.^{286,287} A different report highlighted the importance of the nanotube length on the frequency-dependent response and concluded that photoexcitation leads to plasmonic resonances.³²⁸

The optical generation of free charge carriers in SWCNT dispersions upon excitation at the lowest excitonic transitions was previously reported in flash-photolysis time-resolved microwave conductivity experiments on chirality-enriched (7,5) SWCNTs²⁸⁴ as well as transient absorption spectroscopy³³⁷ and OPTP spectroscopy²⁸⁶ of (6,5) SWCNTs. Likewise, the THz response in the measurements described here is attributed to free charge carriers based on the large magnitude of the real conductivity and small contribution by the imaginary conductivity for all samples with and without sp^3 defects. The very similar photoconductivity dynamics for pristine and functionalized SWCNT dispersions – especially on the very short time scales after photoexcitation including the build-up of the photoconductivity – suggest that the defects have no significant impact on the generation of free carriers. Furthermore, the linear dependence of the photoconductivity amplitude on the photon fluence within the range used in the experiments rules out carrier generation *via* exciton–exciton annihilation, which is a two-body process and should therefore exhibit a non-linear response. Due to the free-carrier-dominated THz response for all time delays as indicated by the minor imaginary conductivity, hot exciton dissociation as free-carrier generation mechanism appears unlikely.^{322,344} This notion is further supported by the fact that the excitonic transition is excited resonantly. Neither the thermal energy nor the energy in the THz pulse (< 10 meV) are sufficiently high to cause exciton dissociation.

An alternative explanation for the generation of free carriers could involve the thermodynamic equilibrium between bound excitons and dissociated electron–hole pairs. Exciton dissociation leads to an increase in entropy and hence reduction of the free energy of the system. On the other hand, the enthalpy and thus free energy is also reduced upon formation of excitons due to the strong Coulomb interactions between hole and electron. Consequently, an equilibrium between exciton formation and dissociation can result in a coexistence of excitons and free charge carriers, as previously discussed in the context of photoexcitation of a variety of different materials.^{344–346} According to the one-dimensional Saha equation, the fraction of free charge carriers (x) can be expressed as follows:³⁴⁷

$$\frac{x^2}{1-x} = \frac{1}{n} \left(\frac{2\pi m k_B T}{h^2} \right)^{1/2} e^{-\frac{E_B}{k_B T}} \quad (5.4)$$

Equation 5.4 includes the total excitation density n , the effective exciton mass m , the Boltzmann constant k_B , the temperature T , the Planck constant h , and the exciton binding energy E_B . With the experimentally determined photoexcitation density and assuming an exciton binding energy of ~ 360 meV for (6,5) SWCNTs,¹⁰² the yield for free-carrier generation is calculated to be $\sim 0.8\%$. Similarly, dividing the charge carrier density N inferred from the Drude-Smith fits of the frequency-resolved photoconductivity spectra (compare Equation 5.1) by the excitation density yields $\sim 0.1\%$ for the fraction of free carriers, which is in good agreement with the result from the Saha equation. This result is also consistent with previous reports of free-carrier quantum yields that ranged between few percent in transient absorption spectroscopy³³⁷ and an estimated lower limit of 0.04% in microwave conductivity measurements.²⁸⁴ Interestingly, higher yields for free-carrier generation were found for excitation at the E_{22} and E_{33} resonances compared to E_{11} excitation, which were attributed to the electronic coupling of these higher-energy excitonic states to unbound states of lower-energy excitons.^{284,337} While a strong THz response for both pristine and functionalized SWCNT dispersions was also observed in OPTP experiments under E_{22} excitation in this thesis, no detailed analysis was performed in this regard.

Even though the estimated free-carrier quantum yield is low in the OPTP experiments described herein, the high mobilities of charge carriers in SWCNTs and consequently their strong THz absorption coefficient result in a THz signal that is dominated by free charges, whereas excitons only show a minor contribution. While the presented thermodynamic model could rationalize the observation of photogenerated carriers in individually dispersed SWCNTs,^{284,286,337} further experiments are needed to explore their origin in greater detail.

5.5 Macroscopic charge transport in SWCNT network FETs

Previously, the combination of transistor measurements with OPTP spectroscopy has provided detailed insights into charge transport in a wide range of materials including conjugated polymers, graphene, and networks of transition metal dichalcogenides.^{288–290,348} As shown above, OPTP spectroscopy of individual SWCNTs in dispersion unambiguously confirmed the impact of sp^3 defects on the intra-nanotube conductance. To directly compare the results to macroscopic charge transport in SWCNT thin films, nanotube network FETs were fabricated with nitroaryl-functionalized (6,5) SWCNTs. Due to the requirement of highly concentrated SWCNT dispersions for both OPTP measurements and FET fabrication, and thus high material consumption, different but very similar sample series were used. Normalized absorption and Raman spectra of pristine and functionalized SWCNTs for device fabrication are shown in Figure 5.8a,b. As discussed above, the variation in sp^3 defect densities with increasing reactant concentration was reflected in an increase in E_{11}^* defect-state

absorption as well as a higher Raman D/G⁺ area ratio. Both the E_{11}^*/E_{11} area ratios in absorption and the calculated defect densities (6–29 μm^{-1}) compared very well to those of the dispersions measured by OPTP spectroscopy (Figure 5.8c).

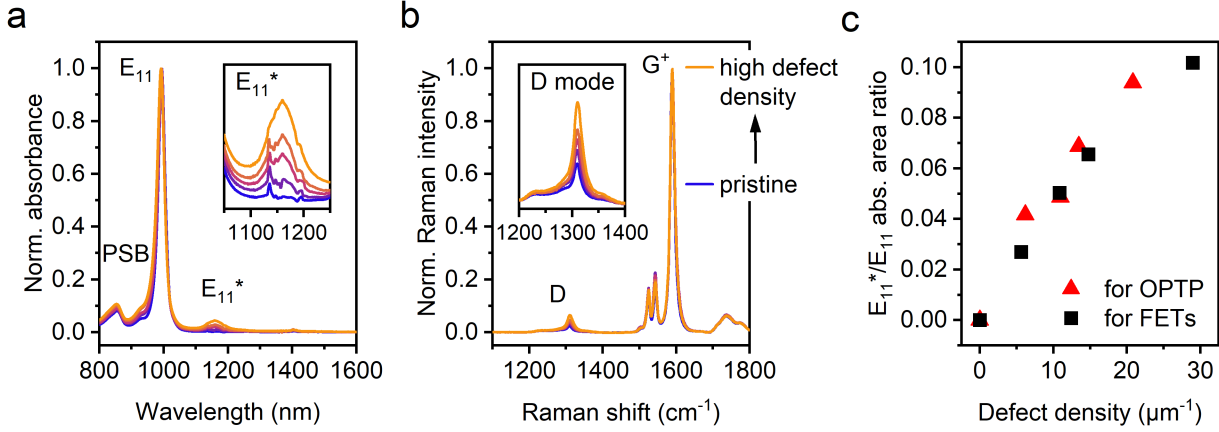


Figure 5.8: Characterization of SWCNT dispersions for FET fabrication. (a) Normalized absorption spectra of pristine and functionalized (6,5) SWCNTs and zoom-in on the E_{11}^* defect-state absorption. (b) Raman spectra (532 nm excitation) normalized to the G⁺ mode and zoom-in on the defect-related D mode. (c) E_{11}^*/E_{11} area ratio in absorption *versus* calculated sp^3 defect density for the two sample series used for FET fabrication (black squares) and OPTP measurements (red triangles), respectively.

FETs were fabricated with interdigitated gold source/drain contacts ($L = 20 \mu\text{m}$, $W = 10 \text{nm}$), dense, spin-coated SWCNT networks, a double-layer PMMA/HfO_x gate dielectric, and a silver top-gate electrode, as described in Chapter 3.3.6. A schematic cross-section of the devices and a representative AFM image of a functionalized nanotube network are shown in Figure 5.9a. All networks exhibited similar areal capacitances (104–123 nF cm⁻²) and SWCNT densities ($> 30 \mu\text{m}^{-1}$), and hence were well-above the threshold for mobility saturation.¹⁹⁷

Representative linear transfer characteristics (Figure 5.9b) confirmed ambipolar charge transport with low gate leakage currents and high on/off current ratios for all networks. Again, the hysteresis was likely due to incomplete removal of oxygen and moisture at the relatively low annealing temperature of 150 °C to avoid defect cleavage,²⁹⁹ which was also reflected in the lower electron *versus* hole currents.^{223,300} As previously observed for bromoaryl E_{11}^* defects, on-currents of the devices and linear network mobilities decreased with increasing degree of functionalization (compare Chapter 4.3). For hole mobilities, a drop from $4.8 \pm 0.2 \text{ cm}^2(\text{Vs})^{-1}$ for the pristine transistors to $2.3 \pm 0.1 \text{ cm}^2(\text{Vs})^{-1}$ for the networks with the highest defect density was observed. Electron mobilities decreased from $1.2 \pm 0.1 \text{ cm}^2(\text{Vs})^{-1}$ (pristine) to $0.4 \pm 0.1 \text{ cm}^2(\text{Vs})^{-1}$ for the highly functionalized networks. Averaged mobilities for at least 16 devices for each network are given in Table 5.2.

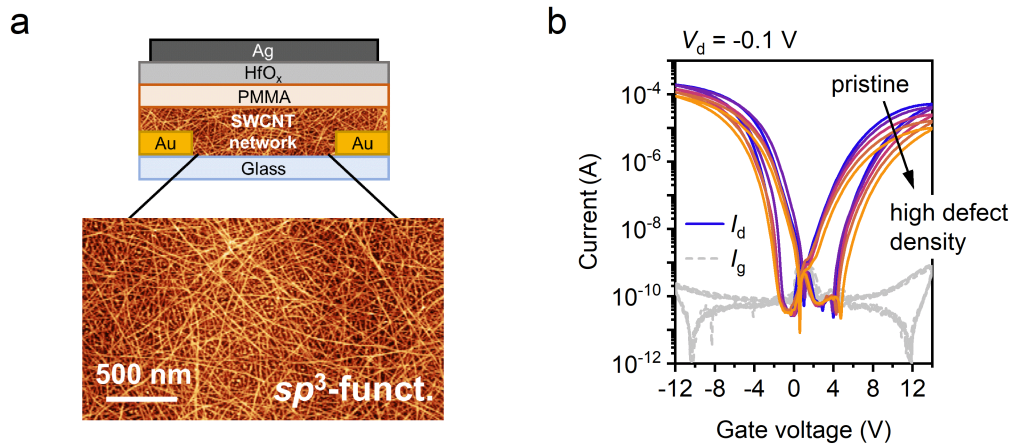


Figure 5.9: (a) Schematic cross-section of a bottom-contact, top-gate (6,5) SWCNT network FET (layer thicknesses not to scale) and representative atomic force micrograph of a dense network of sp^3 -functionalized SWCNTs with medium defect density ($n_d \sim 15 \mu\text{m}^{-1}$). The scale bar is 500 nm. (b) Ambipolar transfer characteristics of pristine and functionalized SWCNT network FETs in the linear regime ($V_d = -0.1 \text{ V}$). Solid lines are drain currents I_d , grey dashed lines are gate leakage currents I_g .

Table 5.2: Raman D/G⁺ area ratios, calculated sp^3 defect densities, and averaged linear hole and electron mobilities of pristine and functionalized SWCNT network FETs. Standard deviations were obtained by averaging over at least 16 transistors for each network.

Raman D/G ⁺ area ratio	Defect density n_d (μm^{-1})	Hole mobility ($\text{cm}^2(\text{Vs})^{-1}$)	Electron mobility ($\text{cm}^2(\text{Vs})^{-1}$)
0.058	0	4.8 ± 0.2	1.2 ± 0.1
0.072	5.6	3.7 ± 0.1	1.1 ± 0.1
0.085	10.8	3.4 ± 0.1	1.1 ± 0.1
0.094	14.7	3.1 ± 0.1	0.6 ± 0.1
0.128	29.0	2.3 ± 0.1	0.4 ± 0.1

The gradual decrease in carrier mobilities with increasing density of sp^3 defects is further shown in Figure 5.10a,b. Overall, the mobility reduction by $\sim 50\text{--}70\%$ for the highest defect density of nitroaryl defects ($n_d \sim 29 \mu\text{m}^{-1}$) with respect to the pristine reference transistors is in very good agreement with the observed decrease by 50% for the bromoaryl defects at a defect density of $n_d \sim 31.5 \mu\text{m}^{-1}$ (compare Chapter 4.3). This result is consistent with the very similar HOMO and LUMO levels of nitro- and bromo-substituted aryl E_{11}^* defects, as determined by Shiraishi *et al.* via PL spectroelectrochemistry.¹⁵⁷ In their study, a slight decrease in the HOMO level energy was found with increasing Hammett constant of the substituent (increasing electron-withdrawing character), whereas the LUMO energy remained largely unaltered. However, the differences in electrochemical bandgaps (58 meV and 53 meV smaller compared to E_{11} for nitroaryl and bromoaryl defects, respectively) were

only minor. A similar report on oxygen-functionalized SWCNTs suggested that differences in the defect structure might have a larger impact,¹⁵⁹ which will be further assessed in Chapter 7 using aryl-functionalized (6,5) SWCNTs with E_{11}^{*-} defects. It should be noted that for the bromoaryl defects in Chapter 4, the reduction in network mobilities was essentially identical for holes and electrons. In contrast to that, the normalized hole and electron mobilities for the nitroaryl defects in Figure 5.10b exhibit some differences. However, no clear trend of the deviations was observed, which rendered it difficult to draw conclusions on the origin of this effect.

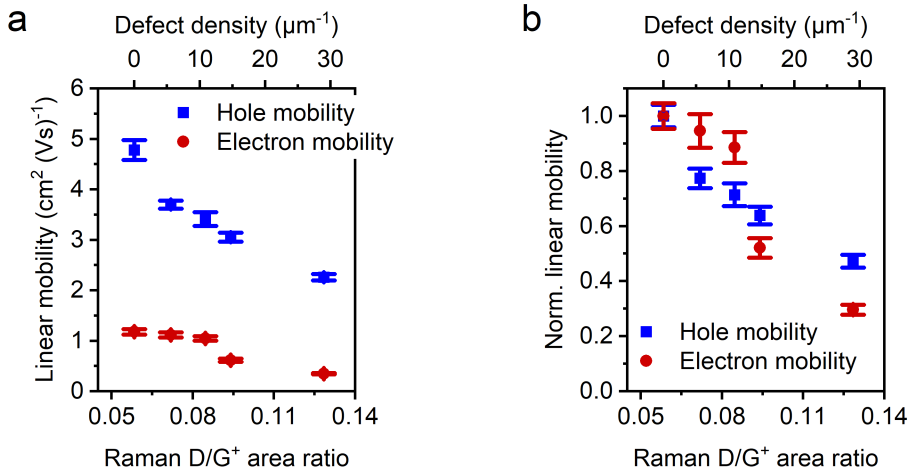


Figure 5.10: (a) Absolute and (b) normalized linear charge carrier mobilities of pristine and functionalized (6,5) SWCNT network FETs *versus* Raman D/G⁺ area ratio and calculated sp^3 defect density. Hole and electron mobilities are shown as blue squares and red circles, respectively. Error bars represent standard deviations for at least 16 different transistors measured for each network.

Importantly, the charge carrier densities under typical device operation conditions and at the mobility maximum are considerably higher than those in THz measurements. From the areal network capacitance, a charge density depending on the applied gate voltage can be calculated according to $N_{\text{areal}} = \frac{C_{\text{areal}} |V_g|}{e}$. At the mobility maximum ($|V_g| \sim 8$ V), this corresponds to roughly $5 \cdot 10^{12}$ charges per cm^2 . With the areal nanotube density calculated from the average nanotube length (1.4 μm) and the linear network density ($30 \mu\text{m}^{-1}$),⁹⁴ this gives an estimated ~ 1500 carriers per SWCNT. Gate voltages in the subthreshold regime correspond to an estimated charge density of tens to a few hundreds of carriers per SWCNT. These charge carrier densities are similar to those previously reported for electrochemical doping and redox-doping of (6,5) SWCNTs ($\sim 5\text{--}500$ carriers per μm SWCNT).³¹²

Photoexcitation of SWCNT dispersions in OPTP measurements generates only a small population of free charge carriers. From Drude-Smith fits to the frequency-resolved photoconductivity spectra, a carrier density of $N \sim 3 \cdot 10^{18} \text{ m}^{-3}$ was calculated *via* the plasma frequency (compare Equation 5.1). For a SWCNT dispersion with an optical density of 5 cm^{-1} at the

E_{11} absorption transition, a concentration of $\sim 4 \cdot 10^{18}$ SWCNTs per m^3 can be estimated by taking the molar absorptivity of (6,5) SWCNTs,³⁴⁹ their geometrical factor of 88,000 carbon atoms per μm tube length, and their average length into account. Consequently, experiments were conducted at low charge densities of approximately one carrier per SWCNT, which is 2–3 orders of magnitude lower compared to FET measurements.

Bearing these discrepancies in mind, the results from FET measurements can now be compared to those from OPTP spectroscopy. Figure 5.11 shows the trends in linear hole mobilities and maximum THz photoconductivity *versus* calculated defect density. As discussed above, the defect densities were slightly different in both measurement series, but still covered the same range. The decrease in maximum photoconductivity ($\sim 30\%$ for $n_d \sim 21 \mu\text{m}^{-1}$) and hole mobility ($\sim 50\%$ for $n_d \sim 29 \mu\text{m}^{-1}$) for the highest degree of functionalization with respect to the unfunctionalized reference was very similar. The same results were obtained when considering the calculated mobilities from fits to the frequency-resolved photoconductivities ($\sim 26\%$ reduction) or the linear electron instead of hole mobilities in SWCNT network FETs ($\sim 70\%$ reduction; compare Figure 5.7 and 5.10b).

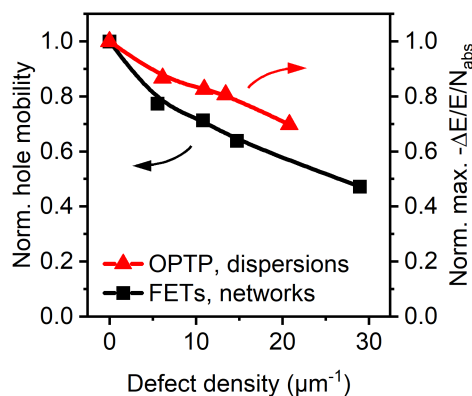


Figure 5.11: Normalized linear hole mobilities from FET measurements (left axis, black squares) and normalized maximum photoconductivities from OPTP measurements (right axis, red triangles) of pristine and functionalized (6,5) SWCNTs *versus* calculated sp^3 defect density. Lines are guides to the eye.

It should be emphasized again that OPTP spectroscopy probes the short-range, intra-nanotube transport over distances of tens of nanometers, where charge carriers interact with one or few defects during their lifetime. In contrast to that, FET measurements reflect the long-range transport in dense SWCNT networks over tens of micrometers (channel length $L = 20 \mu\text{m}$), which involves the interaction of charges with many defect sites as well as both intra-nanotube conduction and inter-nanotube hopping. Furthermore, the interaction of nanotubes within a network and with the substrate influences the carrier mobilities in the FETs,²⁴⁵ and charge densities in OPTP measurements are considerably lower than those in an operating transistor (see above). Taking these differences into account, the trends

observed in both measurements compare reasonably well. The comparable impact of sp^3 defects on the microscopic and macroscopic carrier mobilities corroborates the significance of intra-nanotube conduction for the overall charge transport in SWCNT networks.²⁶⁶

5.6 Temperature-dependent OPTP spectroscopy of SWCNT films

To gain further insights into microscopic charge transport in nanotube networks with and without luminescent defects, temperature-dependent OPTP measurements were performed on dense (6,5) SWCNT films. Films of several tens of nanometers in thickness and an optical density of ~ 0.3 – 0.4 cm^{-1} at the E_{11} transition were fabricated from pristine and nitroaryl-functionalized ($n_d \sim 32 \text{ } \mu\text{m}^{-1}$) SWCNT dispersions *via* filtration followed by membrane transfer onto fused silica substrates (see Chapter 3.3.3). Both films showed a strong THz response after optical excitation and considerably higher maximum photoconductivities than the dispersions, which can be attributed to enhanced electronic coupling and facilitated exciton dissociation, *e.g.*, at nanotube–nanotube contacts in films.^{284,350} However, the re-scaled photoconductivity dynamics were very similar, as shown for the pristine SWCNTs in Figure 5.12a. The faster conductivity decay observed for the films agrees with results from time-resolved microwave conductivity measurements^{284,334} and is possibly due to inter-nanotube junctions or traps in the films that can act as recombination centers.²⁸⁵

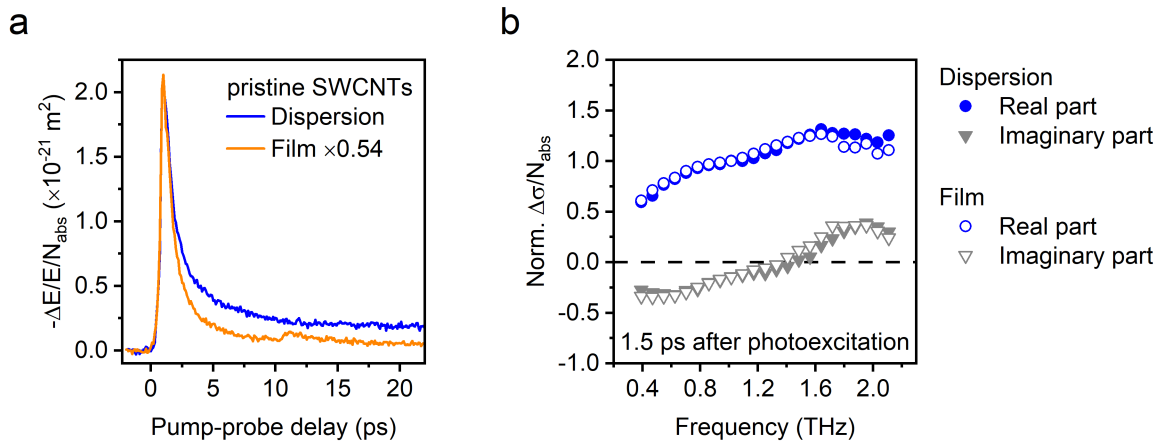


Figure 5.12: (a) Photoconductivity dynamics of a pristine (6,5) SWCNT dispersion and film (scaled by a factor of 0.54). The optical excitation energy was $\sim 1.25 \text{ eV}$, and the absorbed photon density was $N_{\text{abs}} \sim 2 \cdot 10^{18} \text{ m}^{-2}$. Note that the small feature at $\sim 11 \text{ ps}$ is due to a back-reflection. (b) Complex photoconductivity spectra of a pristine SWCNT dispersion (filled symbols) and film (empty symbols) measured $\sim 1.5 \text{ ps}$ after photoexcitation and normalized to the values at 1 THz. Blue circles are real parts of the conductivity, grey triangles are imaginary parts. Data were measured by Wenhao Zheng (MPI for Polymer Research, Mainz).

Furthermore, both real and imaginary parts of the normalized frequency-resolved photoconductivities were almost identical (Figure 5.12b). Overall, the similarities in the THz response of SWCNT dispersions and films confirm that OPTP spectroscopy probes the local charge transport properties even in nanotube networks.

Figure 5.13a,b shows the temperature-dependent photoconductivity dynamics of pristine and functionalized SWCNT films between 288 K and 78 K. Similar to the measurements in dispersion (compare Figure 5.5), optical excitation at ~ 1000 nm generates free carriers on the nanotubes that give rise to a transient THz conductivity on the time scale of few picoseconds. At 288 K, the maximum photoconductivity of the functionalized SWCNT film was reduced by approximately 25% with respect to the pristine nanotube sample, which is in very good agreement with the results for the dispersion and can be attributed to the impact of sp^3 defects on intra-nanotube carrier transport. A decrease in temperature resulted in an increase in maximum THz photoconductivity for both samples. However, the increase was quite pronounced for the pristine film ($\sim 15\%$ at 78 K), whereas only a minor change ($< 5\%$) was observed for the functionalized SWCNTs. The temperature-dependent conductivity maxima normalized to the values at room temperature are displayed in Figure 5.13c. For individual SWCNTs, charge transport is band-like and limited by carrier-phonon scattering, hence an increase in carrier mobility with decreasing temperature is expected.^{213,236} The results from OPTP spectroscopy indicate that covalent SWCNT functionalization not only changes the magnitude of local carrier conductivity by increasing the nanotube resistance,¹⁷⁸ but also affects the temperature dependence of intra-nanotube charge transport.

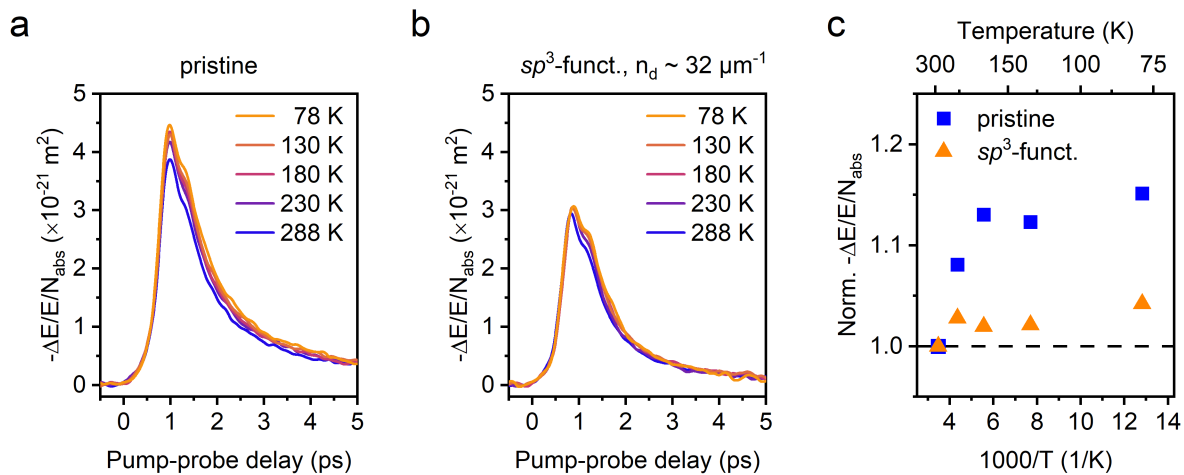


Figure 5.13: Temperature-dependent photoconductivity dynamics of (a) pristine and (b) functionalized ($n_d \sim 32 \mu\text{m}^{-1}$) SWCNT films. The optical excitation energy was ~ 1.25 eV, and the absorbed photon density was $N_{abs} \sim 2 \cdot 10^{18} \text{ m}^{-2}$. (c) Maximum photoconductivity (blue squares, pristine SWCNTs; orange triangles, functionalized SWCNTs) extracted from the data in (a,b) *versus* inverse temperature. Values were normalized to the data points at 288 K, as indicated by the dashed line. Data were measured by Wenhao Zheng (MPI for Polymer Research, Mainz).

This hypothesis was further tested in THz-TDS measurements, which provided access to the frequency-resolved photoconductivity spectra (Figure 5.14). For all different temperatures, the spectra were well-described by the Drude-Smith model (compare Equation 5.1).

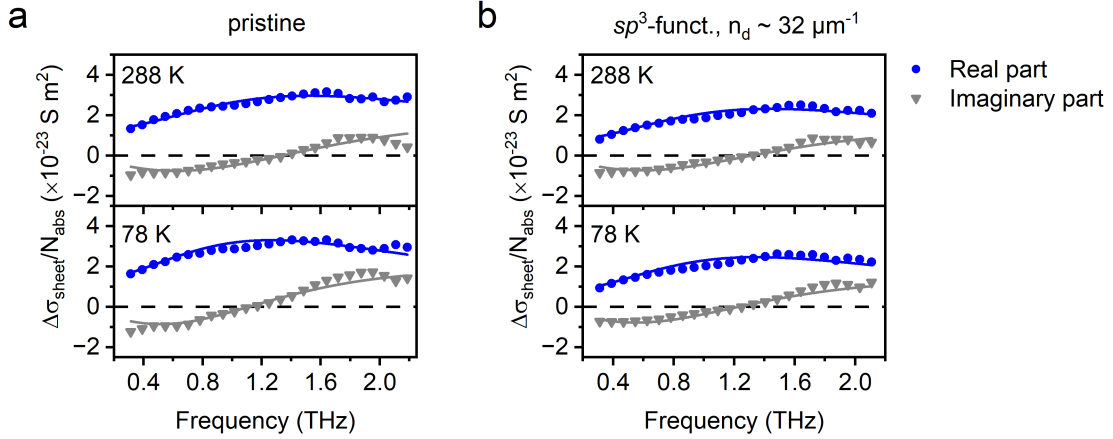


Figure 5.14: Complex photoconductivity spectra of (a) pristine and (b) functionalized ($n_d \sim 32 \mu\text{m}^{-1}$) SWCNT films measured ~ 1.5 ps after photoexcitation at 288 K (top) and 78 K (bottom), respectively. Blue circles are real parts of the conductivity, grey triangles are imaginary parts. Solid lines are fits according to the Drude-Smith model. Data were measured by Wenhao Zheng (MPI for Polymer Research, Mainz).

From the fitting results, the temperature-dependent local carrier mobilities were calculated according to Equation 5.2. As shown in Figure 5.15a, DC mobilities were on the order of a few $100 \text{ cm}^2(\text{Vs})^{-1}$ and lower for the functionalized compared to the pristine SWCNT film, similar to the results for dispersions (compare Table 5.1). The mobilities for the pristine nanotubes increased substantially with decreasing temperature and followed the expected $\mu \propto 1/T$ relationship,^{213,236} corroborating that OPTP spectroscopy effectively probes the intra-nanotube band-like transport in SWCNT films. However, the mobilities of the functionalized SWCNTs were almost temperature-independent and increased only slightly with decreasing temperature. The mobility increase due to reduced phonon scattering should be similar for pristine and functionalized SWCNTs. It appears that the impact of sp^3 defects becomes more pronounced at lower temperatures and effectively counteracts the mobility increase from reduced phonon scattering. This observation suggests that the interaction time of a carrier with a defect site becomes longer when the temperature is reduced, thus supporting the hypothesis that the defects are not only carrier scattering centers but might also act as charge carrier traps.

As opposed to transport along segments of individual nanotubes, charge transport in interconnected SWCNT networks is thermally activated due to inter-nanotube carrier hopping, which means that the carrier mobilities decrease with decreasing temperature.^{85,262} Previous measurements of SWCNT network FETs with pristine and bromoaryl-functionalized

nanotubes revealed pronounced differences in their temperature-dependent mobilities (compare Chapter 4.7). To compare the results to the OPTP spectroscopy data, temperature-dependent SWCNT network mobilities of this previous device generation are displayed in Figure 5.15b. Even though this data was acquired for nanotube networks with bromoaryl defects instead of the nitroaryl defects utilized in the THz studies, the very similar defect densities ($n_d \sim 34 \mu\text{m}^{-1}$ and $\sim 32 \mu\text{m}^{-1}$, respectively) and comparable impact on the mobilities in SWCNT network FETs should permit a direct comparison of the results.

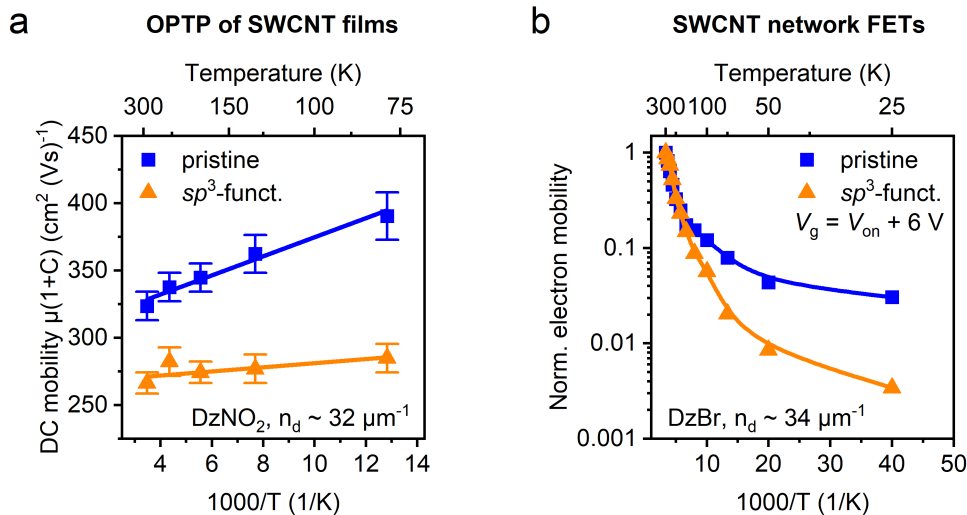


Figure 5.15: (a) Temperature-dependent carrier mobilities in the DC limit extracted from Drude-Smith fits to the complex photoconductivity spectra of pristine and functionalized (nitroaryl E_{11}^* defects, $n_d \sim 32 \mu\text{m}^{-1}$) SWCNT films. Solid lines are linear fits. Blue squares are pristine SWCNT samples, orange triangles correspond to sp^3 -functionalized SWCNTs. (b) Temperature-dependent linear electron mobilities of pristine and functionalized (bromoaryl E_{11}^* defects, $n_d \sim 34 \mu\text{m}^{-1}$) SWCNT network FETs normalized to the values at 300 K. The data was taken from Chapter 4.7 for comparison. Solid lines are guides to the eye. Mobilities were extracted at a constant gate overpotential of $V_g = V_{on} + 6 \text{ V}$ (constant carrier density of $\sim 4 \cdot 10^{12} \text{ cm}^{-2}$) and corrected for contact resistance.

For the networks (Figure 5.15b), the impact of sp^3 defects on the temperature dependence of the mobilities was low at higher temperatures. At lower temperatures ($< 100 \text{ K}$), the impact of defects became larger and led to a stronger mobility decrease compared to the pristine networks. Based on the results from temperature-dependent THz spectroscopy, these observations can now be attributed to the convolution of inter- and intra-nanotube charge transport with their respective temperature dependencies. In the high-temperature regime ($> 150 \text{ K}$), charge transport through the networks is dominated by thermally activated hopping across the junctions, with little impact of the sp^3 defects that predominantly affect the intra-nanotube conductance. The latter becomes more significant at lower temperatures, when hopping is slowed down.

For pristine SWCNT networks, the decrease in inter-nanotube carrier hopping at lower temperatures is counteracted by the increase in intra-nanotube mobilities due to reduced

phonon scattering. Hence, the network mobilities level off in the low-temperature regime. For functionalized SWCNTs, however, intra-nanotube transport is nearly independent of the temperature due to the impact of the defects. Consequently, it cannot counteract the reduction in inter-nanotube hopping and as a result, the decrease in overall network mobilities at low temperatures is larger compared to the pristine nanotube networks. In summary, the combination of temperature-dependent OPTP spectroscopy of SWCNT films and transport measurements of SWCNT network FETs suggest that a superposition of intra-nanotube (affected by sp^3 defects) and inter-nanotube contributions is required to adequately describe the overall charge transport in SWCNT networks.²⁶⁶

Importantly, the reduction in photoconductivity for the functionalized SWCNTs compared to the pristine films persisted even for photoexcitation densities that were an order of magnitude higher. Similar to the discussion in Chapter 5.5, the excitation densities can be converted into estimated charge carrier densities in OPTP measurements at lower (Figure 5.13) and higher fluence, which were ~ 1 and ~ 10 carriers per SWCNT, respectively. It should be emphasized that the charge densities in OPTP measurements at high fluence come close to those in FET measurements at low gate voltages. Consequently, the combination of OPTP and FET measurements indicates that the observed mobility trends are consistent over 2–3 orders of magnitude in charge densities, corroborating the notion that the results obtained from both methods are directly comparable. It also highlights the complementary nature of both techniques, which enable an in-depth study of the impact of sp^3 defects on charge transport in individual SWCNTs and nanotube networks.

5.7 Summary and conclusion

In this Chapter, time-resolved OPTP spectroscopy was established as a highly suitable technique to investigate the intrinsic charge transport properties of covalently functionalized SWCNTs in dispersions and films. Measurements on individually dispersed SWCNTs revealed that the introduction of sp^3 defects leads to a moderate reduction in local nanotube conductivity, charge carrier mobility, and carrier lifetime. The defects also diminish the increase in carrier mobility for decreasing temperatures, corroborating their direct influence on intra-nanotube transport. Importantly, however, the impact of the defects at room temperature – especially at application-relevant defect densities – is limited. For example, the decrease in local conductivity and carrier mobility for defect concentrations that are associated with maximum ensemble PL quantum yields ($n_d < 10 \mu\text{m}^{-1}$)¹⁴⁷ was only $\sim 15\%$. The comparable impact of functionalization on the local photoconductivity of single nanotubes in dispersion and the network mobilities in FETs further supports the idea that charge transport in random SWCNT networks is not solely limited by the inter-nanotube junctions, but the contribution of intra-nanotube transport is significant as well.²⁶⁶

The frequency-dependent THz conductivity was generally well-described by the Drude-Smith model involving preferential backscattering of charge carriers for both pristine and functionalized SWCNTs. However, the faster decay of the photoconductivity with increasing degree of functionalization and the effect on the temperature dependence of intrinsic carrier mobilities in functionalized SWCNTs suggest that the impact of sp^3 defects might go beyond a simple scattering contribution. In agreement with spectroscopic experiments and temperature-dependent transport measurements of functionalized SWCNT networks as described in Chapter 4, these observations indicate a certain degree of charge trapping at the defect sites. Figure 5.16 illustrates the impact of sp^3 defects on charge transport in individual (6,5) SWCNTs and randomly oriented nanotube networks. As corroborated by OPTP spectroscopy, luminescent defects directly affect the intrinsic charge transport properties of SWCNTs, and they may act as shallow charge traps from which carriers can readily detrapp at room temperature. The increase in nanotube resistance upon functionalization also leads to reduced carrier mobilities in dense SWCNT networks due to the significance of both intra-nanotube transport and inter-nanotube hopping for the overall charge transport properties. On the other hand, the influence of defects on the nanotube–nanotube junctions is not significant. Overall, the moderate impact of luminescent defects on carrier transport in single nanotubes and their networks may enable electrically-pumped light-emitting devices and single-photon sources with covalently functionalized SWCNTs.

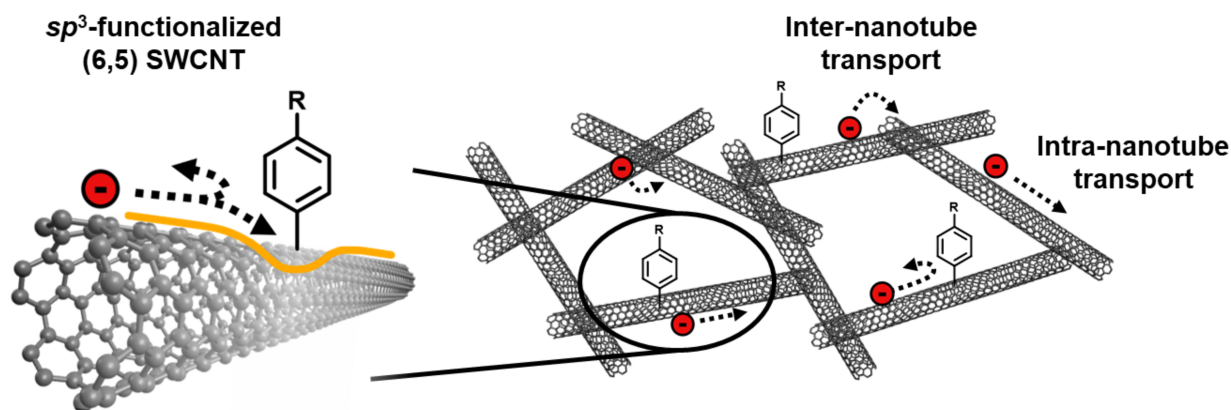


Figure 5.16: Schematic illustration of the impact of luminescent defects on charge transport in SWCNTs and their networks.

As demonstrated in this Chapter, time-resolved THz spectroscopy combined with FET measurements provided detailed insights into the charge transport properties of SWCNTs on a microscopic and macroscopic level and over a wide range of charge carrier densities. Using this complementary approach, further studies on functionalized nanotubes of various chiralities and with different sp^3 defect structures should help to gain a unified picture of the impact of covalent functionalization on carrier transport in SWCNTs.

Chapter 6

Near-Intrinsic Emission Spectra from SWCNT Thin Films on BCB-Passivated Substrates

This Chapter introduces substrate passivation with the cross-linked polymer BCB to enhance the emission spectra of SWCNT thin films and light-emitting devices.

The results presented in this Chapter were published in part in N.F. Zorn *et al.*, *Adv. Opt. Mater.* **2023**, DOI: 10.1002/adom.202300236.³⁵¹ Modified versions of previously published Figures are presented with permission of Wiley-VCH. High-quality crystals of hexagonal boron nitride (*h*-BN) grown under high pressure were provided by Dr. Takashi Taniguchi and Dr. Kenji Watanabe (National Institute for Materials Science (NIMS), Tsukuba, Japan). Flakes of *h*-BN on Si/SiO₂ substrates were prepared by Tim Wedl and hyperspectral mapping of SWCNTs on these substrates was performed by Dr. Shen Zhao under the supervision of Prof. Dr. Alexander Högele (Ludwig Maximilian University of Munich). Aqueous (6,5) SWCNTs were provided by Dr. Han Li and Dr. Benjamin Flavel (Karlsruhe Institute of Technology). (7,5) SWCNTs were provided by Sebastian Lindenthal, and functionalized (6,5) SWCNTs were prepared by Simon Settele (both Heidelberg University).

6.1 Introduction

The application of SWCNTs in light-emitting devices requires well-defined, narrowband emission spectra not only in nanotube dispersions but also in thin films on substrates. However, as detailed in Chapter 2.1.4, excitons in SWCNTs are highly sensitive to their environment, as the electric field lines defining the Coulomb interaction between electron and hole largely pass through the exterior of the nanotube.^{96,352} Compared to air-suspended SWCNTs, optical transitions of solution-dispersed nanotubes are typically shifted to lower energies,³⁵³ and this red-shift becomes stronger with increasing dielectric constant ϵ of the solvent or surfactant.^{121,122,354,355} For SWCNTs deposited on substrates, interactions between different nanotubes in a network and with the substrate facilitate exciton quenching and thus result in low emission efficiencies.^{9,87} Nanotube–substrate interactions are especially strong with the polar surfaces of commonly used glass or Si/SiO₂ substrates. This notion is reflected in the vanishing PL emission from SWCNTs grown on SiO₂, which was attributed to strong and possibly covalent interactions with the substrate induced during the growth process as well as mechanical strain.^{124,356} Furthermore, the initially bright emission from air-suspended SWCNTs is efficiently quenched at the contacts with the SiO₂ support.^{123,357,358} To enable detailed spectroscopic investigations in a homogeneous dielectric environment, SWCNTs are commonly embedded in a non-polar polymer matrix,^{23,158,359,360} but even this approach leads to a pronounced PL lifetime shortening compared to air-suspended nanotubes.¹²⁵ Moreover, isolated SWCNTs in a polymer layer do not form a percolating network and thus are not suitable for application in light-emitting devices.

Aside from environmental effects, the excitonic emission peak in the spectra of SWCNTs, especially in thin films, features a series of red-shifted emissive sidebands, with the most prominent ones being denoted as Y₁, X₁, and G₁ (Figure 6.1a).^{105,112,113} Through measurements of isotope-labelled SWCNTs, the X₁ band was assigned to brightening of the

K-momentum dark exciton under emission of a D phonon, whereas the G_1 band was assigned to emission from the bright E_{11} exciton coupled to a G phonon.¹⁰⁵ As detailed in Chapter 2.1.4, the exact origin of the Y_1 sideband is not entirely clear yet, but it has been attributed to defect-related emission either from a brightened triplet state or due to extrinsic effects.¹¹² Notably, the intensity of the Y_1 band was shown to vary largely between different nanotube samples and even between different spots on the same SWCNT.¹¹² Clearly, these sidebands lead to undesired spectral broadening and complicate the analysis of nanotube emission spectra, as recently shown for SWCNT network LEFETs.⁸

Consequently, strategies to enhance the luminescence spectra of SWCNT thin films and suppress or ideally eliminate sideband emission are required. In this regard, passivation of substrates presents a powerful approach. For example, the PL of as-grown SWCNTs was recovered through transfer onto SiO_2 substrates treated with an alkylsiloxane self-assembled monolayer, which was attributed to breaking of chemical bonds between SWCNTs and the growth substrate as well as blocking of electron transfer from the nanotubes to SiO_2 .³⁵⁶ Similarly, reduced PL quenching and narrower emission linewidths were observed for individual SWCNTs on h -BN flakes compared to SiO_2 .^{126,127} Flakes of h -BN have been widely used as encapsulation layers to reduce the PL linewidth and enhance the carrier mobility in 2D materials and layered van der Waals heterostructures.^{361–365} However, this approach suffers from the limited accessibility of h -BN with the required quality, and its limited scalability prevents large-area substrate passivation and device fabrication. A compelling alternative are polymeric buffer layers that can be easily applied over large areas *via* spin-coating, as demonstrated very recently for high-performance MoS_2 FETs on SiO_2 passivated with a cyclic olefin copolymer.³⁶⁶

This Chapter introduces substrate surface passivation with the polymer BCB (cross-linked, B-staged divinyltetramethylsiloxane-bis-benzocyclobutene) as a means to enhance the emission spectra of pristine and sp^3 -functionalized SWCNT thin films. The compatibility of this approach with semiconductor device fabrication is demonstrated for light-emitting (6,5) SWCNT network FETs on BCB-passivated glass substrates, which exhibit excellent charge transport properties and near-intrinsic EL spectra with increased EQEs.

6.2 PL spectra of SWCNT films on BCB-passivated substrates

Nearly monochiral dispersions of (6,5) SWCNTs wrapped with PFO-BPy in toluene were prepared by shear force mixing (see Chapter 3.1.1)⁸⁷ and served as the model system to investigate the impact of nanotube–substrate interactions on the emission spectra of SWCNT thin films. The high purity of the dispersions with a low content of excess, unbound wrapping polymer and no other SWCNT species was confirmed by absorption and Raman spectroscopy.

From these dispersions, SWCNT thin films on alkali-free aluminum borosilicate glass (Schott AF32eco) or Si/SiO₂ substrates were created through repeated spin-coating. As shown in Figure 6.1a, the E_{11} exciton emission in the PL spectrum of a thin film on glass at 1018 nm was substantially red-shifted with respect to the peak in a toluene dispersion at 999 nm. This shift can be explained by the higher dielectric constant of the environment.¹²² Furthermore, peak broadening and emission from lower-energy sidebands (Y_1 , X_1 , G_1) were more pronounced in the film.

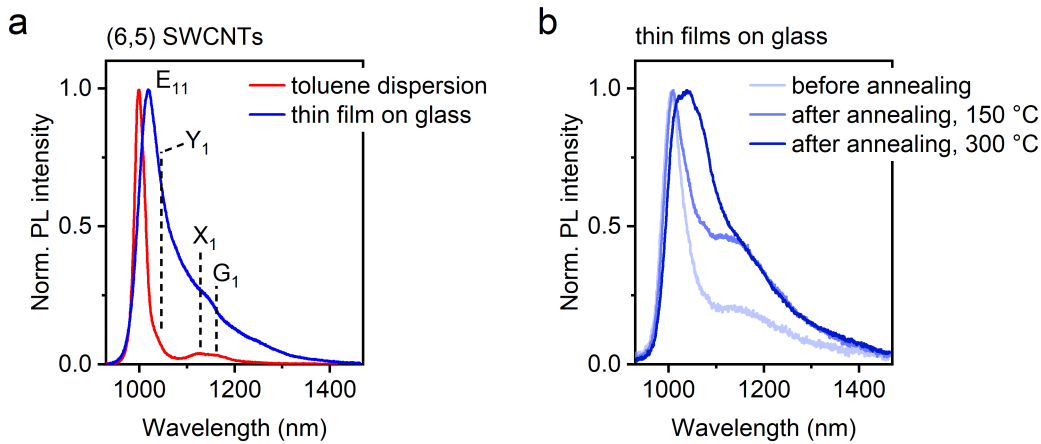


Figure 6.1: (a) Normalized PL spectra of PFO-BPy-wrapped (6,5) SWCNTs in a toluene dispersion and a spin-coated thin film on glass. Labels indicate the E_{11} exciton peak and commonly observed emissive sidebands (Y_1 , X_1 , G_1). (b) Normalized PL spectra of (6,5) SWCNT thin films on glass before and after annealing in inert atmosphere for 30 min at 150 °C and 300 °C, respectively.

The fabrication of SWCNT thin film devices typically involves one or several annealing steps, for example to remove residual moisture and oxygen that cause undesired doping and charge trapping.^{223,300} As previously shown by thermogravimetric analysis, decomposition of small-diameter (6,5) SWCNTs occurs at temperatures above 400 °C.³⁶⁷ Thus, annealing under typical conditions (≤ 300 °C) should neither damage the SWCNT films nor have any detrimental effect on their emission spectra. However, PL spectra under resonant E_{22} excitation showed a significant increase in sideband emission from SWCNT thin films on glass already after 30 minutes of annealing at 150 °C in inert atmosphere (Figure 6.1b). This effect became even more pronounced at a higher annealing temperature of 300 °C. For the latter, the strong increase in Y_1 sideband emission led to a shift of the apparent peak maximum to ~ 1040 nm, and the spectrum after annealing exhibited a broad, featureless tail that extended beyond 1400 nm. Note that the spectra shown here were normalized to the E_{11} peak due to the impact of sample-to-sample variations and even slight differences in the excitation laser focus on the absolute intensities. Importantly, the PL spectra in Figure 6.1b and in this Chapter in general were averaged over more than 100 individual measurements from a $50 \times 50 \mu\text{m}^2$ map of the films. As confirmed by AFM, spin-coating

created homogeneous SWCNT networks on the substrates. Hence, the PL data should be representative for the entire film, and local spot-to-spot variations should not play a significant role. Since annealing was performed in a dry nitrogen atmosphere, oxygen and moisture from ambient air can be ruled out as a cause for the increase in sideband emission. Instead, it is hypothesized that the detrimental effects on the emission spectra of SWCNT thin films are due to nanotube–substrate interactions.

To test this hypothesis, glass substrates were passivated with a layer of the cross-linked polymer BCB as detailed in Chapter 3.3.4. BCB is a commercially available material (as Cyclotene™ resin) that is used in semiconductor industry as an interlayer dielectric in the fabrication of multichip modules and integrated circuits.³⁶⁸ It can be readily applied over large areas by spin-coating the precursor solution to yield a homogeneous film with high transparency and low surface roughness.¹⁹² Subsequent thermal annealing (typically at 290 °C for 2 minutes in this thesis) leads to cross-linking *via* electrocyclic ring opening of the benzocyclobutene units followed by Diels-Alder reaction. Under these conditions, the degree of cross-linking should be > 95%.¹⁹² Figure 6.2 shows the molecular structures of the precursor and the cross-linked BCB polymer, which possesses a low static dielectric constant ($\epsilon(\text{BCB}) = 2.65$),³⁶⁸ no dangling bonds or polar side groups, and is generally very apolar and hydrophobic. The cured, B-staged films are essentially insoluble in organic solvents or water with only minimal swelling. These properties present a clear advantage over other polymeric buffer layers (*e.g.*, polystyrene) and allow for the deposition of SWCNT thin films under identical processing conditions compared to the non-passivated substrates.

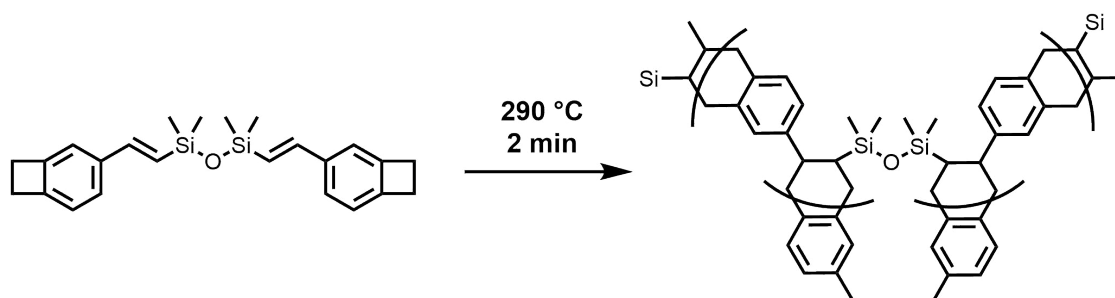


Figure 6.2: Molecular structures of the divinyltetramethylsiloxane-bis-benzocyclobutene precursor (left) and the cross-linked, B-staged BCB polymer (right). Cross-linking was typically achieved by thermal annealing at 290 °C for 2 minutes.

SWCNT thin films were spin-coated from the same dispersion onto glass substrates without and with a BCB layer (~ 75 nm). Nanotube networks on both substrates were equally dense, as confirmed by AFM. As shown in Figure 6.3, substrate surface passivation with BCB significantly enhanced the SWCNT emission spectra and suppressed sideband emission irrespective of the annealing temperature. The spectra of SWCNT films on BCB-passivated glass before and after annealing at 150 °C were essentially identical (Figure 6.3a,b). Only after annealing at 300 °C, emission from the Y_1 sideband appeared as a shoulder to the

E_{11} peak, but its intensity was substantially reduced compared to the spectrum on the non-passivated substrate (Figure 6.3c). PL measurements under low excitation power in an integrating sphere (compare Chapter 3.4.5) corroborated the lower sideband emission intensity and indicated a slight improvement of the absolute E_{11} PLQY (950–1050 nm). However, absolute emission efficiencies were still low ($\sim 0.1\%$). It should be emphasized that BCB passivation led to lower E_{11} peak widths and sideband emission even in the spectra of SWCNT films before any annealing step (Figure 6.3a).

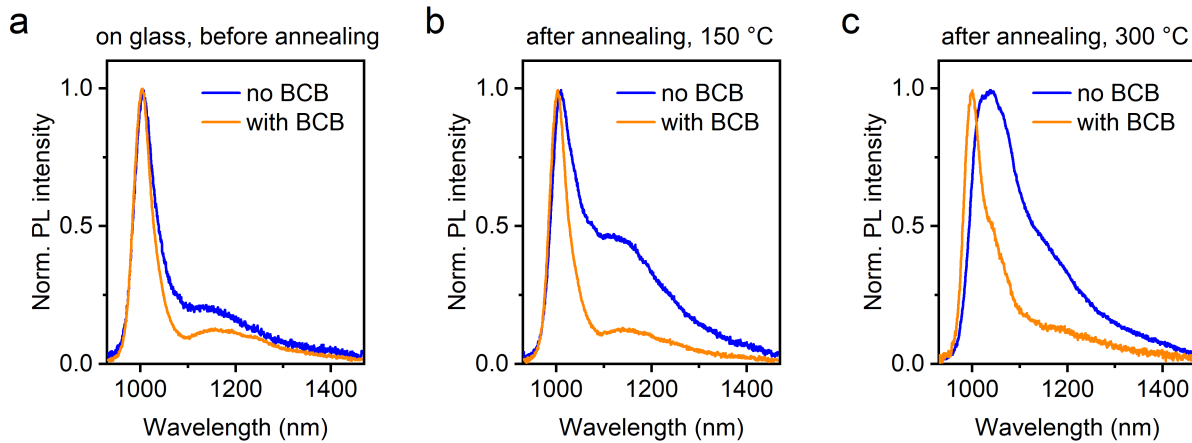


Figure 6.3: Normalized PL spectra of (6,5) SWCNT thin films on glass without and with a ~ 75 nm BCB layer (a) before annealing and (b,c) after annealing in inert atmosphere for 30 min at 150 °C and 300 °C, respectively.

Figure 6.4a shows the PL spectra of SWCNT films on glass substrates with different thicknesses of the BCB passivation layer after annealing at 150 °C. While the E_{11} emission peak was slightly sharper for the ~ 75 nm BCB layer compared to the layer with ~ 35 nm thickness, both substrates showed a comparable improvement of the luminescence spectrum with respect to the bare glass. As demonstrated previously, BCB layers as thin as 10 nm still exhibit high dielectric breakdown strengths¹⁹² and thus should also be sufficient to enhance the SWCNT emission spectra. The favourable effect of BCB passivation persisted irrespective of the SWCNT network density (dense or sparse networks; see Figure 6.4b). Interestingly, the films with higher SWCNT density on glass exhibited more pronounced emission from the phonon-related sidebands (X_1 , G_1), which might be due to stronger tube–tube interactions and consequently enhanced exciton-phonon coupling in dense networks. In contrast to that, no differences were observed in the PL spectra of dense and sparse SWCNT films on BCB.

These observations were not restricted to glass substrates, as corroborated by measurements of SWCNT films on Si/SiO₂. The spectra on non-passivated substrates (Figure 6.5a) exhibited substantial E_{11} peak broadening and increased Y_1 sideband emission after annealing at 300 °C, which could again be circumvented through passivation with BCB (Figure 6.5b). In agreement with the spectra on BCB-covered glass, the emission intensity of the Y_1 band was strongly reduced on passivated Si/SiO₂ even at such high annealing temperatures. In-

terestingly, emission from the phonon-related X_1 and G_1 sidebands was virtually absent in the spectra on BCB before and after annealing.

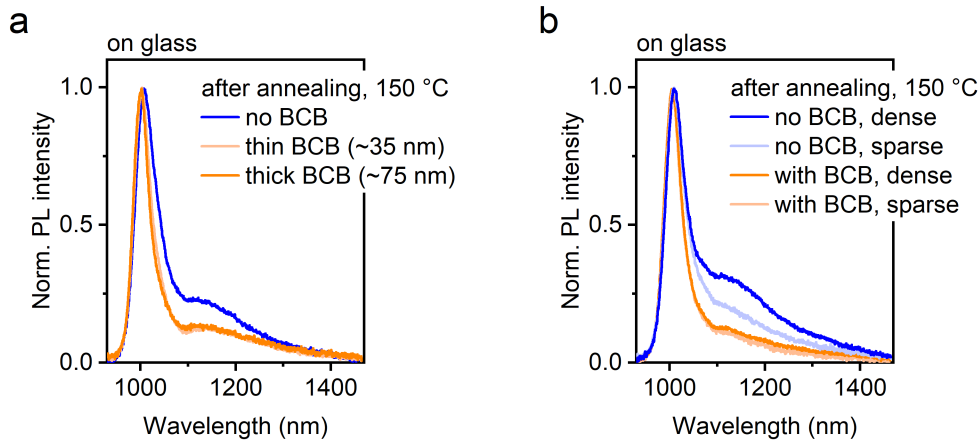


Figure 6.4: (a) Normalized PL spectra of (6,5) SWCNT thin films on glass without BCB, with a ~ 35 nm BCB layer, and with a ~ 75 nm BCB layer. (b) Normalized PL spectra of dense and sparse (6,5) SWCNT thin films on glass without and with a ~ 75 nm BCB layer. Samples were annealed in inert atmosphere at 150°C for 30 min (a) and 45 min (b).

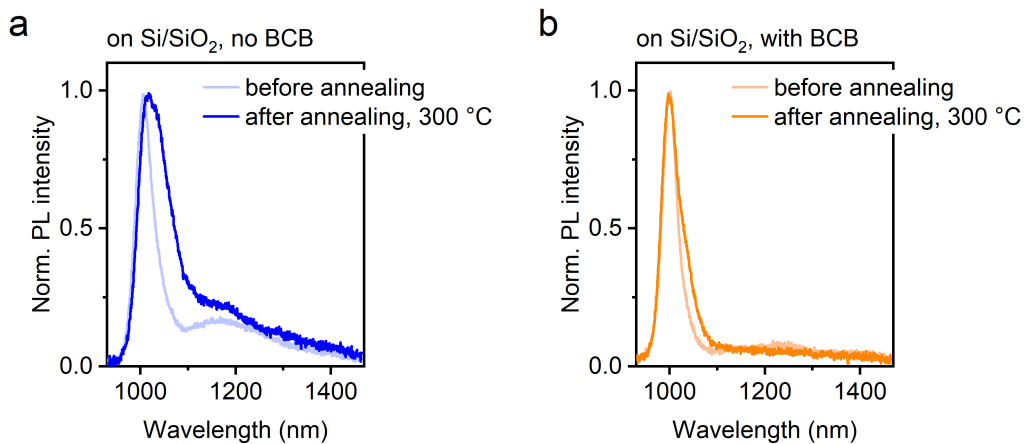


Figure 6.5: Normalized PL spectra of (6,5) SWCNT thin films on Si/SiO₂ (a) without and (b) with ~ 65 nm BCB before and after annealing in inert atmosphere at 300°C for 30 min.

Throughout all these samples, the optical transition energy of the E_{11} exciton emission was consistently blue-shifted by ~ 5 – 10 meV for the SWCNT films on BCB compared to the bare substrates. This observation might be attributed to the lower dielectric constant of BCB compared to glass and SiO₂ ($\epsilon(\text{AF32eco glass}) = 5.1$, $\epsilon(\text{SiO}_2) = 3.9$). It should be emphasized that BCB exhibits no absorption bands in the NIR spectral region that could compromise the measured emission spectra. Instead, the elimination of direct interactions between SWCNTs and the substrate surface must play a key role in the enhancement of their optical properties.

6.3 Origin of the Y_1 sideband

Initial PL spectroscopy experiments corroborated that substrate passivation with BCB strongly suppresses emission from lower-energy sidebands and especially from the Y_1 band that emerged upon annealing of (6,5) SWCNT thin films. To obtain further insights into the underlying mechanism, resonant Raman spectroscopy was performed on SWCNT films on glass without and with BCB. Similar to the PL data, the Raman spectra shown here represent averaged data from > 2500 individual measurements obtained by mapping a $100 \times 100 \mu\text{m}^2$ area of the films. As shown in Figure 6.6a, annealing of the SWCNT films on glass at 150°C was accompanied by a relative increase of the D mode with respect to the G^+ mode. The Raman D mode is related to the number of sp^3 -hybridized carbon atoms, whereas the G^+ mode is proportional to the number of sp^2 carbons in the SWCNT lattice.²⁹⁷ Thus, the increase in Raman D/ G^+ area ratio suggests that the annealing step caused the introduction of nanotube lattice defects. Strikingly, the Raman D/ G^+ ratio remained nearly constant upon annealing of SWCNTs on BCB (Figure 6.6b). It should be noted that the relative D mode intensity for the films without and with BCB before annealing was essentially identical, as shown in Figure 6.6c. The extracted D/ G^+ area ratios are listed in Table 6.1. Importantly, similar trends were observed for SWCNT films on Si/SiO₂.

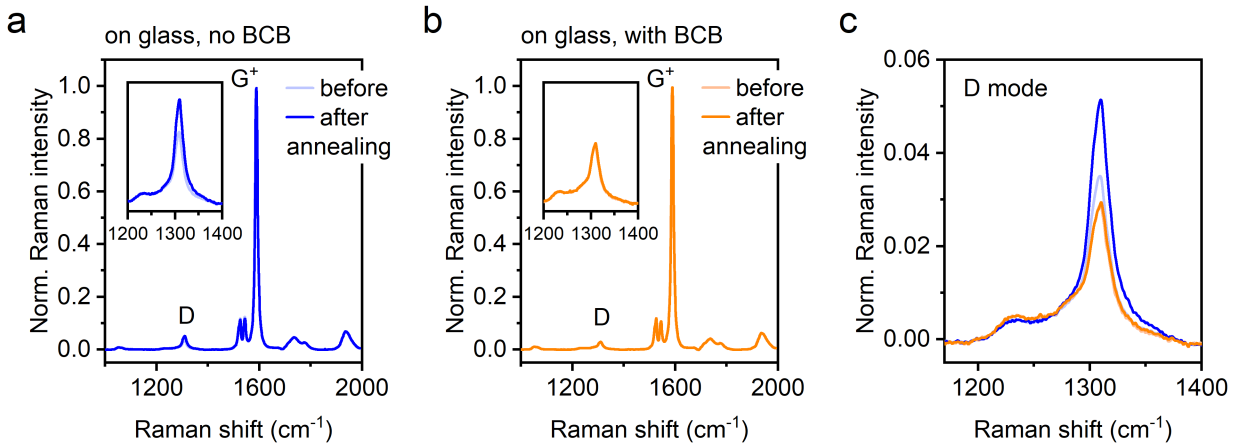


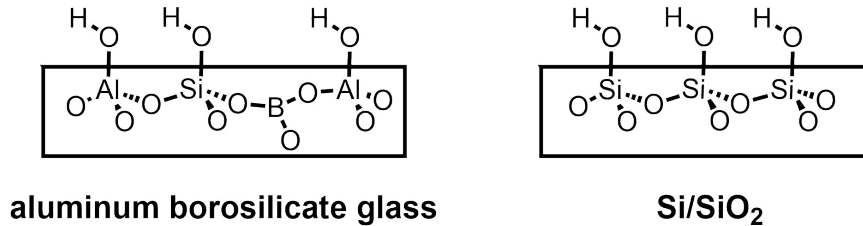
Figure 6.6: Normalized Raman spectra of (6,5) SWCNT thin films on glass (a) without and (b) with a ~ 75 nm BCB layer before and after annealing at 150°C for 30 min. Insets (same y-axis scale in (a,b)) show a zoom-in on the defect-related D mode. (c) Raman D mode normalized to the G^+ mode for all spectra shown in (a,b). Note that the relative D mode intensity for the films on BCB before and after annealing was essentially identical.

The results described here are consistent with a recent study that reported an increase in Raman D/ G^+ area ratio as well as peak broadening of the E_{11} PL emission during oxygen-mediated photodegradation of (6,5) SWCNTs in a polymer matrix and in a film.³⁶⁹ In addition, the photochemical introduction of guanine defects in DNA-wrapped (6,5) SWCNTs was shown to red-shift and broaden the E_{11} emission peak and activate the D mode.^{370–372}

Table 6.1: Raman D/G⁺ area ratios of (6,5) SWCNT thin films on glass substrates without and with a ~ 75 nm BCB layer before and after annealing at 150 °C for 30 min.

Sample	Raman D/G ⁺ area ratio before annealing	Raman D/G ⁺ area ratio after annealing (150 °C, 30 min)
No BCB	0.079	0.109
With BCB	0.077	0.079

Based on these observations, the Y_1 sideband, whose origin has remained elusive thus far,¹¹² can be associated with the introduction of defects in the nanotube lattice. These defects might originate from interactions of the SWCNTs with the oxygen-containing terminal groups on the glass or SiO₂ substrates, as schematically illustrated in Figure 6.7. Hence, passivation of the substrate surfaces with BCB effectively prevents defect formation. Based on the model for luminescent defects in small-diameter semiconducting SWCNTs (compare Equation 4.1),¹⁴⁷ the increase in Raman D/G⁺ area ratio for the sample without BCB upon annealing corresponds to ~ 12 defects that were induced per μm of nanotube.

**Figure 6.7:** Schematic drawings of the polar surfaces of aluminum borosilicate glass (left) and thermally-grown SiO₂ on Si (right) as used in this thesis.

Thus far, several studies reported on the covalent functionalization of SWCNTs with reactive oxygen species (*e.g.*, ozone, hypochlorite) in dispersion.^{138,145,165} These exciton-trapping defects give rise to multiple red-shifted emission peaks that were attributed to different binding configurations of the induced ether and epoxide groups.¹⁵² Low-temperature PL spectroscopy showed that oxygen functionalization also led to a splitting of the E_{11} peak into different emission features.¹⁵² Notably, one of these features (termed E_{11}^-) was red-shifted by only ~ 26 meV with respect to the E_{11} peak and behaved very similarly to the E_{11}^* emission (ether defect, optical trap depth ~ 135 meV). The resemblance between this E_{11}^- defect and the Y_1 sideband suggests that the latter might be of similar origin. Interestingly, emission peaks in the spectral region of the Y_1 band were also observed in low-temperature PL spectra of individual, aryl-functionalized SWCNTs.^{23,158} Moreover, untreated single SWCNTs deposited on Si/SiO₂ substrates exhibited E_{11} peak splitting and lower-energy satellite peaks (shifted by tens of meV) that were attributed to unintentional covalent sidewall defects.³⁷³ It should be emphasized that the inferred role of defects as a possible origin of the Y_1 sideband is not

to be confused with recent reports on the population of the K-momentum dark excitonic state through exciton scattering at lattice defects, which gives rise to emission from the X_1 band.^{114,115}

In addition to solution-based methods, the creation of luminescent oxygen defects in individual SWCNTs was similarly achieved in the solid state through electron-beam deposition of aluminum oxide (AlO_x) and SiO_2 .^{163,168} These defects even behaved as room-temperature single-photon emitters.¹⁸ Likewise, Raman spectroscopy revealed the introduction of sp^3 -hybridized defects in graphene-based transistors upon deposition of AlO_x *via* electron-beam evaporation.³⁷⁴ Thus, the observation of on-substrate defect introduction as described here might open up possibilities for the controlled functionalization of SWCNTs with luminescent oxygen defects on reactive oxidic surfaces through annealing or under light irradiation with spatial precision.³⁷⁵

To corroborate the notion that the Y_1 sideband originates from exciton-trapping defects, temperature-dependent PL spectroscopy between 5–300 K was performed on SWCNT films that were deposited on glass without and with BCB. Consistent with the data shown above, the PL spectrum on glass at 300 K featured a broad, red-shifted tail adjacent to the E_{11} emission (orange curve in Figure 6.8a). A decrease in temperature to 100 K resulted in a relative increase in emission from the Y_1 band that eventually exceeded the emission intensity of the E_{11} peak. In the E_{11} -normalized SWCNT spectra on BCB (Figure 6.8b), the shoulder corresponding to Y_1 sideband emission similarly increased in intensity with decreasing temperature, but remained significantly diminished. For both samples, no additional changes in spectral shapes were observed upon further cooling to 5 K.

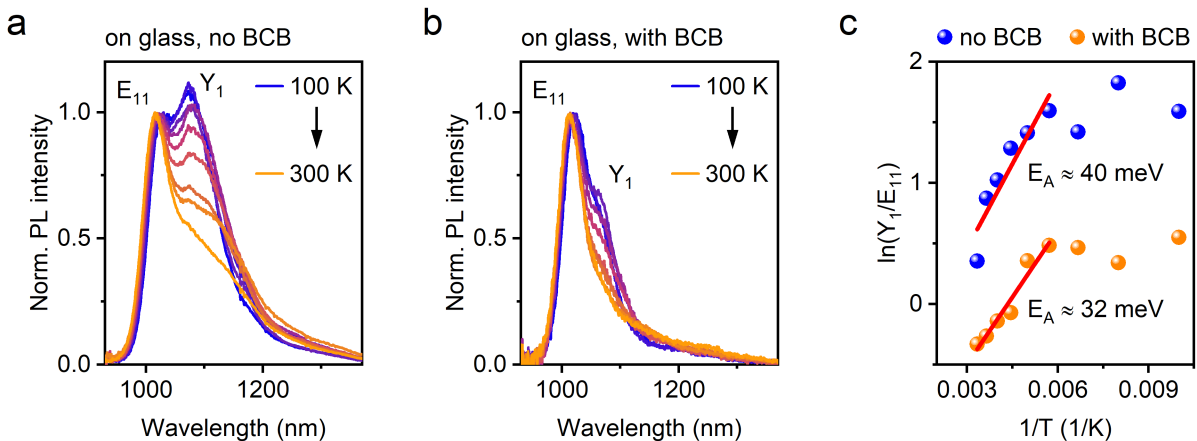


Figure 6.8: Normalized temperature-dependent PL spectra of (6,5) SWCNT thin films on glass (a) without and (b) with a ~ 80 nm BCB layer between 100 K and 300 K in steps of 25 K. Samples were annealed in inert atmosphere at 150 °C for 45 min. (c) Logarithmic peak area ratios of Y_1 and E_{11} peaks determined from fits of the spectra in (a,b) *versus* inverse temperature. Red lines are linear fits to the data between 175 K and 300 K.

The spectra in Figure 6.8a,b were fitted with three Gauss peaks to account for the contributions of E_{11} , Y_1 , and a further red-shifted tail including the X_1 and G_1 bands. Figure 6.8c shows the logarithmic Y_1 -to- E_{11} peak area ratio *versus* inverse temperature for the films on glass and on BCB. For both samples, the integrated PL area ratios initially increased upon cooling down from room temperature, and then remained roughly constant for temperatures lower than 175 K. From linear fits to the data between 175 K and 300 K, activation energies of ~ 40 meV and ~ 32 meV were extracted for the SWCNTs on glass and on BCB, respectively. These thermal trap depths are on the order of the thermal energy at room temperature ($k_B T \sim 25$ meV) and hence would allow for fast detrapping of excitons. Moreover, the values are in very good agreement with those reported for shallow traps in pristine (6,5) SWCNTs, which lead to spontaneous exciton localization at cryogenic temperatures.³⁷³ Thus, these results corroborate the notion that the Y_1 sideband originates from shallow excitonic trap states. It should be noted that the values are also consistent with previously measured thermal trap depths of intentionally introduced aryl or alkyl sp^3 defects (~ 75 – 150 meV for E_{11}^* , ~ 25 meV for E_{11}^-) and oxygen ether defects (~ 24 meV).^{23,142}

Additional evidence for the hypothesis of shallow excitonic traps as the origin of Y_1 emission was provided by pump power-dependent PL spectroscopy under pulsed excitation at the E_{22} transition and under off-resonant cw excitation. In both experiments, Y_1 emission saturated at lower excitation powers compared to the E_{11} peak (Figure 6.9), which points towards a state-filling effect.^{22,156} Very recently, PL spectra of SWCNT network FETs under applied gate voltage showed that the Y_1 band quenched faster with increasing charge density.⁸ A similar behaviour was observed for intentionally introduced aryl sp^3 defects in Chapter 4.6.

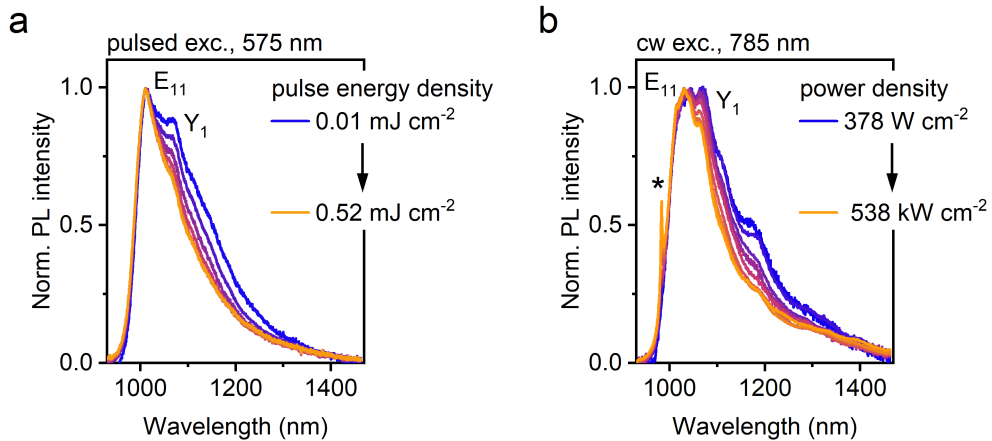


Figure 6.9: Normalized, excitation power-dependent PL spectra of a (6,5) SWCNT thin film on glass after annealing in inert atmosphere at 300 °C for 30 min (a) under pulsed excitation at 575 nm and (b) under cw excitation at 875 nm. The asterisk marks the Raman 2D band of (6,5) SWCNTs.

6.4 Polymer-wrapped (7,5) and surfactant-coated (6,5) SWCNT films

So far, it was shown that films of (6,5) SWCNTs wrapped with PFO-BPy exhibit near-intrinsic emission spectra when deposited on BCB-passivated substrates. To explore whether or not this effect is generalizable to other nanotube species, (7,5) SWCNTs were selectively dispersed in toluene *via* polymer-wrapping with poly(9,9-dioctylfluorene) (PFO; see Chapter 3.1.2) and spin-coated on glass substrates. Figure 6.10a shows the PL spectra of (7,5) SWCNT films on glass without and with a BCB layer before annealing, which were essentially identical. Due to the larger diameter and consequently smaller bandgap of (7,5) SWCNTs compared to (6,5) SWCNTs, their E_{11} emission peak was red-shifted and appeared at ~ 1047 nm. Interestingly, even after annealing at 300 °C for 60 minutes, the PL spectra on glass and on BCB exhibited only minor differences (Figure 6.10b). For the film on BCB, the E_{11} peak was slightly sharper and blue-shifted. However, the impact of BCB was significantly lower compared to (6,5) SWCNT films. This observation is consistent with a previous report of EL spectra from SWCNT network LEFETs on glass substrates, which showed pronounced sideband emission for (6,5) SWCNTs but not for (7,5) SWCNTs.¹³³

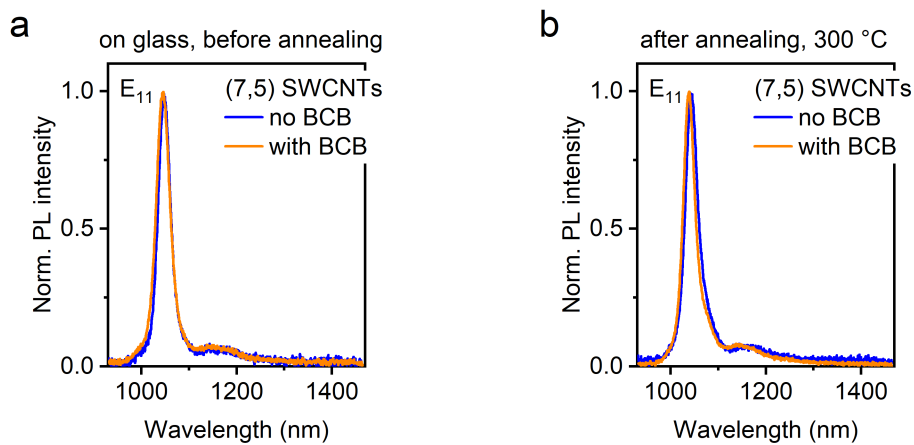


Figure 6.10: Normalized PL spectra of (7,5) SWCNT thin films on glass without and with a ~ 75 nm BCB layer (a) before and (b) after annealing in inert atmosphere at 300 °C for 60 min.

Prolonged annealing of (7,5) SWCNT films on Si/SiO₂ substrates at 300 °C, however, gave rise to Y₁ sideband emission in the PL spectra (Figure 6.11a). In contrast to that, nearly identical luminescence spectra before and after annealing were measured for the (7,5) SWCNT film on BCB, as shown in Figure 6.11b. The direct comparison of PL spectra on Si/SiO₂ without and with BCB layer after annealing (Figure 6.11c) corroborates the notion that BCB passivation suppresses sideband emission and Y₁ defect formation also for other SWCNT species, even though the effect of annealing was less pronounced for (7,5) SWCNTs than for (6,5) SWCNTs.

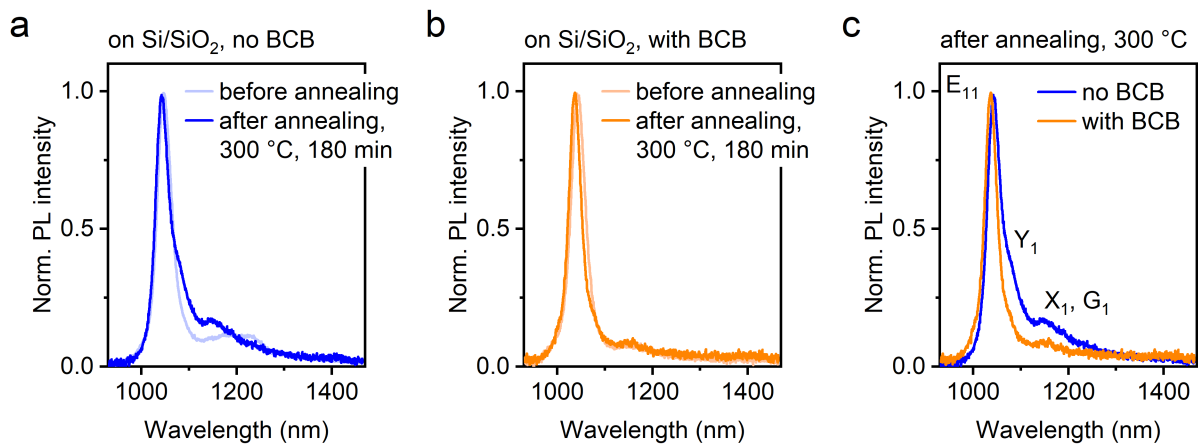


Figure 6.11: Normalized PL spectra of (7,5) SWCNT thin films on Si/SiO₂ (a) without and (b) with a ~ 75 nm BCB layer before and after annealing in inert atmosphere at 300 °C for 180 min. (c) Comparison of normalized PL spectra after annealing. The E_{11} exciton peak and emissive sidebands (Y_1 , X_1 , G_1) are labelled.

Moreover, these results provide further insights into the parameters that are relevant to defect formation in SWCNTs on substrates upon annealing. Sideband emission in (7,5) SWCNTs was significantly reduced compared to (6,5) SWCNTs, which points towards an influence of the nanotube geometry. Due to their larger diameter, (7,5) SWCNTs ($d \sim 0.83$ nm) are less strained and therefore less reactive than (6,5) SWCNTs ($d \sim 0.76$ nm). Similar observations were made in the covalent functionalization of both species with aryl sp^3 defects.^{23,147} Hence, films of large-diameter SWCNTs might be less prone to defect introduction due to nanotube–substrate interactions, which should be tested in future experiments.

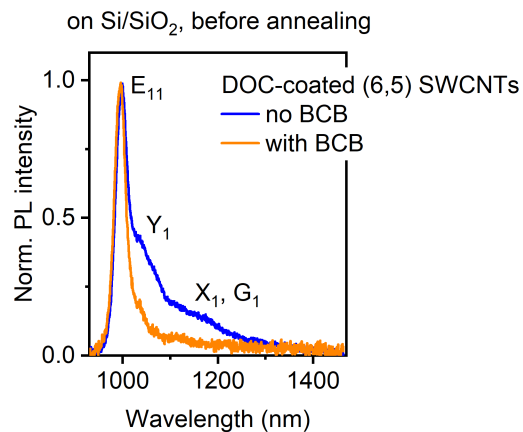


Figure 6.12: Normalized PL spectra of (6,5) SWCNT thin films deposited from an aqueous dispersion with sodium deoxycholate (DOC) on Si/SiO₂ without and with a ~ 75 nm BCB layer. The E_{11} exciton peak and emissive sidebands (Y_1 , X_1 , G_1) are labelled.

To rule out that defect formation and sideband emission are related to polymer-specific interactions and, more specifically, to the presence of the bipyridine units in PFO-BPy, dispersions of (6,5) SWCNTs stabilized with sodium deoxycholate (DOC) in water were prepared *via* the aqueous two-phase extraction (ATPE) method (see Chapter 3.1.3 for details).^{66,70} As displayed in Figure 6.12, PL spectra of DOC-coated nanotube films (excess surfactant washed off) on Si/SiO₂ exhibited a pronounced Y₁ band even before annealing, which could be circumvented by applying a BCB passivation layer. Hence, the observed effects are indeed due to nanotube–substrate interactions and independent of the polymer or surfactant. Similarly, cryogenic PL spectra of both as-grown and micelle-encapsulated individual nanotubes on Si/SiO₂ revealed shallow excitonic traps that were attributed to sidewall defects,³⁷³ and photodegradation of (6,5) SWCNTs due to oxygen defect formation was found to be largely unaffected by the polymer content.³⁶⁹

6.5 SWCNT films on *h*-BN flakes

A prominent material for substrate passivation are flakes of *h*-BN that have found widespread application as atomically-flat encapsulation layers for 2D materials.^{362,364} Likewise, *h*-BN has recently been used to enhance the optical properties of individual SWCNTs,^{126,127} but was not applied to nanotube networks yet. To this end, flakes of *h*-BN were prepared *via* mechanical exfoliation from high-quality crystals²⁹¹ and subsequently transferred onto Si/SiO₂ substrates. A detailed description of the sample preparation is given in Chapter 3.3.5. Typical dimensions of the *h*-BN flakes (ϵ (in-plane, bulk) = 4.98, ϵ (out-of-plane, bulk) = 6.93)³⁷⁶ were tens of micrometers in lateral size and tens of nanometers in thickness, respectively. Figure 6.13a shows a microscope image of a representative *h*-BN flake. Dense SWCNT network on substrates containing multiple such flakes were created by spin-coating. AFM confirmed that the nanotube densities on *h*-BN and on the substrate were essentially identical.

A hyperspectral PL map of the integrated E_{11} -to-sideband emission ratio of a (6,5) SWCNT film on a *h*-BN flake is shown in Figure 6.13b. In detail, a higher ratio corresponds to less sideband emission relative to the E_{11} exciton peak (red color), whereas a lower ratio indicates more emission from sidebands (blue color). Clearly, the PL map resembles the outline of the *h*-BN flake in Figure 6.13a and shows that sideband emission was substantially lower on *h*-BN compared to Si/SiO₂. This notion was further corroborated by the significantly sharper E_{11} emission in the PL spectrum on *h*-BN *versus* Si/SiO₂ (Figure 6.13c, spots indicated by circles in Figure 6.13b). It should be emphasized that SWCNTs on *h*-BN also exhibited higher absolute PL emission intensities in agreement with previous results for individual nanotubes.¹²⁷ Overall, the PL spectra of (6,5) SWCNT thin films on *h*-BN and on BCB were very similar, which suggests that both materials are equally effective in preventing defect formation by eliminating nanotube–substrate interactions.

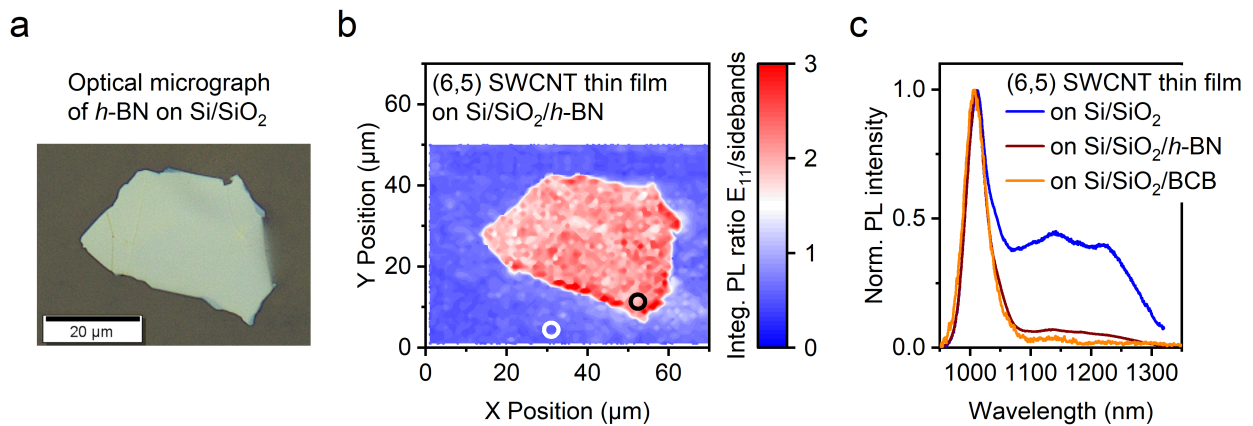


Figure 6.13: (a) Optical micrograph of a *h*-BN flake on Si/SiO₂. (b) Hyperspectral PL map of the ratio of E_{11} emission (integration from 950–1050 nm) to sideband emission (integration from 1100–1300 nm) of a (6,5) SWCNT film on Si/SiO₂/*h*-BN (same flake as in (a)). (c) Normalized PL spectra of (6,5) SWCNTs on Si/SiO₂ (blue line, white circle in (b)) and on *h*-BN (brown line, black circle in (b)). The orange line shows a normalized PL spectrum of a (6,5) SWCNT film on Si/SiO₂/BCB for comparison. SWCNTs on Si/SiO₂/*h*-BN were measured by Dr. Shen Zhao (Ludwig Maximilian University of Munich).

Furthermore, Raman mapping was performed for (6,5) SWCNT films on a ~ 80 nm *h*-BN flake (Figure 6.14a). The map of the integrated Raman D/G⁺ ratio in Figure 6.14b and the spectra in Figure 6.14c show a significantly lower intensity of the D mode relative to the G⁺ mode on *h*-BN compared to Si/SiO₂ already before annealing. Annealing at 300 °C resulted in a substantial increase in D/G⁺ area ratio on the substrate and, to a lower extent, on the *h*-BN flake (see Figure 6.14d,e).

Overall, PL and Raman spectroscopy of SWCNT thin films on *h*-BN flakes corroborated a comparable effect of substrate passivation with *h*-BN and BCB. The suppression of sideband emission in the PL spectra was very similar, and the Raman D/G⁺ ratio indicated a lower number of surface-induced nanotube lattice defects. This observation points towards substrate surface passivation as a general concept to achieve near-intrinsic emission from SWCNT films and single nanotubes^{126,127} in the solid state. Nevertheless, passivation using *h*-BN flakes offers only limited scalability when it comes to large-area device fabrication, and bulk crystals with the required quality are not easily accessible. In contrast to that, BCB is commercially available and can be reproducibly processed into highly planar films over large areas by spin-coating. These advantages are further demonstrated in the fabrication of SWCNT thin film devices on BCB-passivated substrates as detailed in the following.

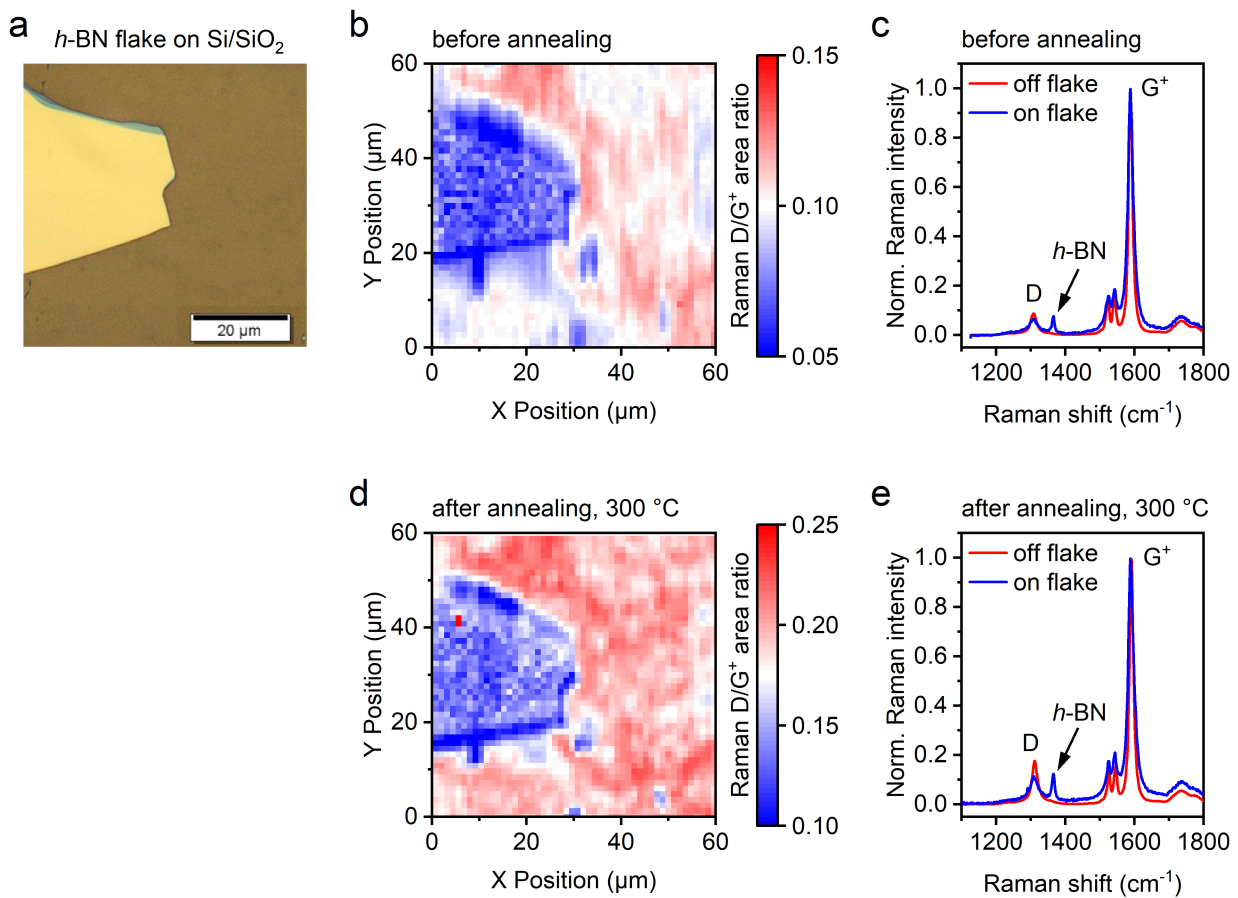


Figure 6.14: (a) Optical micrograph of a ~ 80 nm thick h -BN flake on Si/SiO₂ (scale bar, 20 μ m). (b) Map of the Raman D/G⁺ area ratio (532 nm excitation) of a (6,5) SWCNT film on the flake from (a) before annealing and (c) normalized, averaged Raman spectra on the flake (blue line) and on the substrate (red line). (d) Map of the Raman D/G⁺ area ratio of a (6,5) SWCNT film on the same flake after annealing at 300 °C for 30 min and (e) normalized, averaged Raman spectra on the flake (blue line) and on the substrate (red line). Note the different color scales in (b,d). The data in (b-e) was processed by Sebastian Lindenthal (Heidelberg University).

6.6 SWCNT LEFETs on BCB-passivated substrates

In order to demonstrate the compatibility of BCB passivation with typical processing steps used in the fabrication of optoelectronic semiconductor devices,³⁷⁷ bottom-contact, top-gate (6,5) SWCNT network LEFETs were fabricated on glass substrates with and without an additional BCB layer (for details, see Chapter 3.3.6). A schematic cross-section of a device on a BCB-covered substrate is shown in Figure 6.15a. On top of the passivation layer, interdigitated gold source/drain electrodes ($L = 20$ μ m, $W = 10$ nm) were patterned *via* photolithography and electron-beam evaporation. Spin-coating of concentrated SWCNT dispersions created dense nanotube networks with similar network densities irrespective of the substrate (without or with BCB), as confirmed by AFM. Devices were completed by

deposition of a double-layer PMMA/HfO_x gate dielectric and thermal evaporation of a silver top-gate electrode. Owing to its excellent chemical stability, no detrimental effects on the BCB layer were observed during device fabrication including, *e.g.*, lift-off in NMP and patterning of SWCNT networks through oxygen plasma etching.

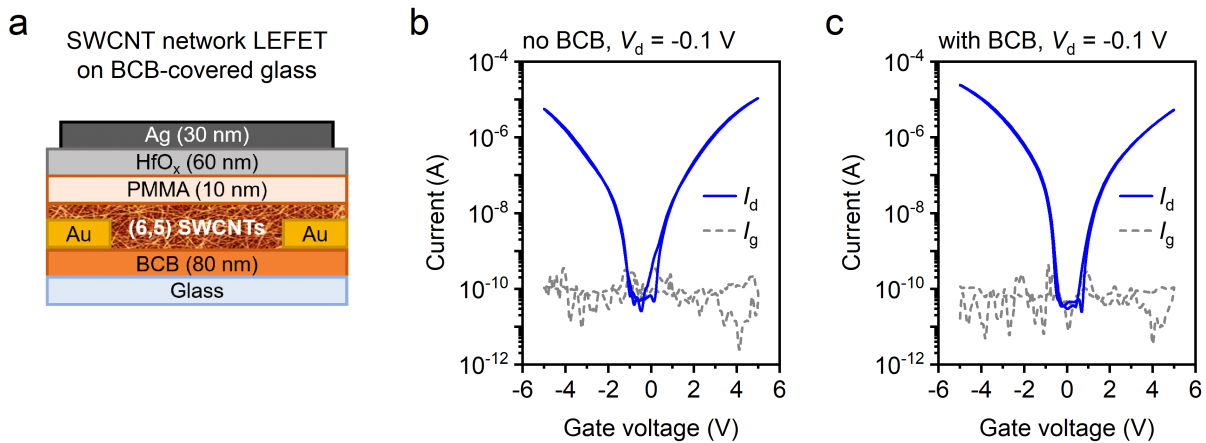


Figure 6.15: (a) Schematic cross-section of a (6,5) SWCNT network LEFET (layer thicknesses not to scale) on a BCB-covered glass substrate, and ambipolar transfer characteristics of LEFETs on glass substrates (b) without and (c) with a ~ 80 nm BCB layer in the linear regime ($V_d = -0.1$ V). Solid lines are drain currents I_d , grey dashed lines are gate leakage currents I_g .

As evident from the linear transfer characteristics in Figure 6.15b,c, LEFETs exhibited balanced ambipolar charge transport and low gate leakage currents irrespective of the presence or absence of the BCB layer. This observation was further reflected in the linear hole and electron mobilities that remained largely unaffected by substrate passivation (Table 6.2). Notably, the use of BCB as an additional gate dielectric has previously enabled the observation of *n*-type transport in semiconducting polymer FETs on Si/SiO₂ by preventing electron trapping at the hydrophilic SiO₂ interface.¹⁹⁸ Likewise, passivation of Si/SiO₂ substrates with a cyclic olefin copolymer was found to improve the electrical characteristics of transistors based on monolayer MoS₂.³⁶⁶ However, it should be emphasized that the gate field confines charge accumulation and transport in FETs to a thin layer at the semiconductor/dielectric interface. Both previous reports employed a bottom-gate device architecture, in which the Si and SiO₂ layers of the substrate act as back-gate and gate dielectric, respectively. Consequently, the direct interaction of charge carriers with the polar substrate surface resulted in charge trapping and detrimental effects on the electrical performance.³⁰⁰ As opposed to these examples, charge transport in the top-gate LEFETs used here occurs at the interface between SWCNT network and the non-polar PMMA layer. Therefore, no significant impact of BCB passivation on charge transport can be expected.

The operation of a LEFET in the ambipolar transport regime gives rise to carrier recombination in the transistor channel and EL emission, as detailed in Chapter 2.3.2. EL spectra of

Table 6.2: Averaged linear hole and electron mobilities of pristine (6,5) SWCNT network LEFETs on glass substrates without and with a ~ 80 nm BCB layer. Standard deviations were obtained from measurements of 7 different transistors for each network.

Sample	Hole mobility ($\text{cm}^2(\text{Vs})^{-1}$)	Electron mobility ($\text{cm}^2(\text{Vs})^{-1}$)
No BCB	3.5 ± 0.2	2.4 ± 0.1
With BCB	3.9 ± 0.3	2.1 ± 0.3

(6,5) SWCNT network LEFETs on glass and on BCB are shown in Figure 6.16a,b for different drain currents I_d . Strikingly, substrate passivation with BCB gives rise to near-intrinsic EL from the SWCNT film and drastically suppresses emission from lower-energy sidebands which is rather pronounced for the device on glass (Figure 6.16a). BCB passivation also permits the analysis of the trion emission feature (~ 1165 nm) that emerges at higher I_d .¹³³

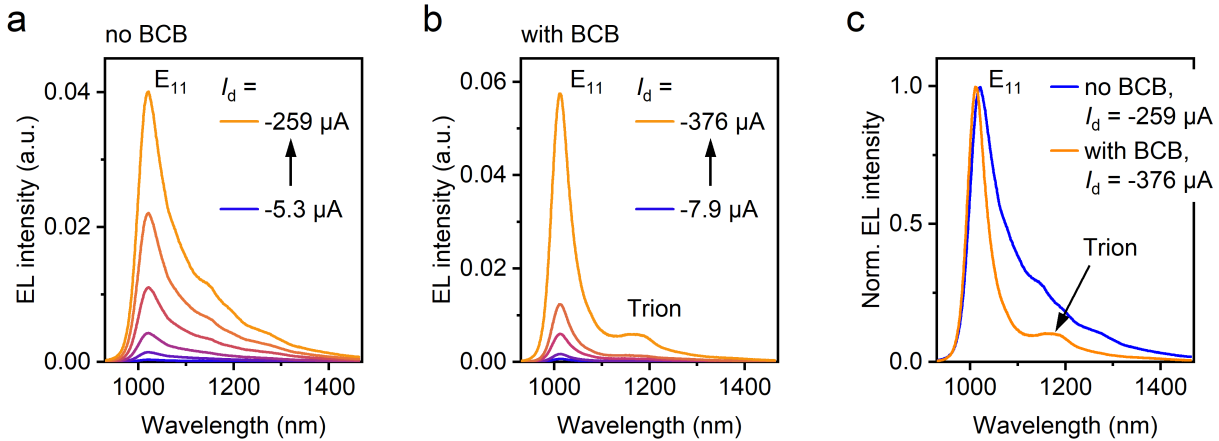


Figure 6.16: EL spectra of (6,5) SWCNT network LEFETs on glass substrates (a) without and (b) with a ~ 80 nm BCB layer for different drain currents I_d . SWCNT films were annealed at 150 °C for 45 min before deposition of the PMMA/ HfO_x dielectric. (c) EL spectra on glass and on BCB at similar drain currents normalized to the E_{11} emission.

The direct comparison of normalized EL spectra for LEFETs without and with BCB at similar I_d in Figure 6.16c highlights the positive effect of substrate passivation on the optical properties of the SWCNT films. This observation is in contrast to the charge transport properties that were not affected significantly by the BCB layer. However, unlike the charge carriers, excitons are not confined to the SWCNT/dielectric interface by the electric field. Due to their high mobility in SWCNT networks,^{119,120,318} excitons are much more sensitive to even few nanotube lattice defects that might be introduced at the substrate interface.

In agreement with previous reports²³² and as shown in Chapters 4.4 and 4.6, trion emission was low in the EL spectra of LEFETs, but became more pronounced in PL spectra of doped SWCNT films at a constant gate voltage V_g . Figure 6.17a shows the normalized

PL spectra of (6,5) SWCNTs on glass in electron accumulation. Absolute PL intensities monotonously decreased with increasing charge density (*i.e.*, V_g) due to Auger quenching of excitons with charge carriers.^{128,129} With increasing V_g , the trion emission intensity increased with respect to the E_{11} exciton peak, but the underlying sideband emission clearly complicated its analysis.⁸ In contrast to that, the spectra on BCB (Figure 6.17b) featured two narrow and symmetric peaks corresponding to exciton (~ 1010 nm) and trion emission (~ 1183 nm), respectively. The same observations were made for PL spectra in hole accumulation (negative V_g ; data not shown). Consistent with previous data for electrolyte-gated (6,5) SWCNT LEFETs,¹³³ the energy separation between trion and exciton emission peaks was slightly higher for negative trions (electron accumulation, $\Delta E \sim 180$ meV) than for positive trions (hole accumulation, $\Delta E \sim 173$ meV). As evident from the direct comparison of gated PL spectra at $V_g = 3$ V (Figure 6.17c), substrate passivation with BCB allows for the unambiguous extraction of the trion-to-exciton emission ratio and thus facilitates the correlation, *e.g.*, with carrier density and dielectric environment.^{8,134}

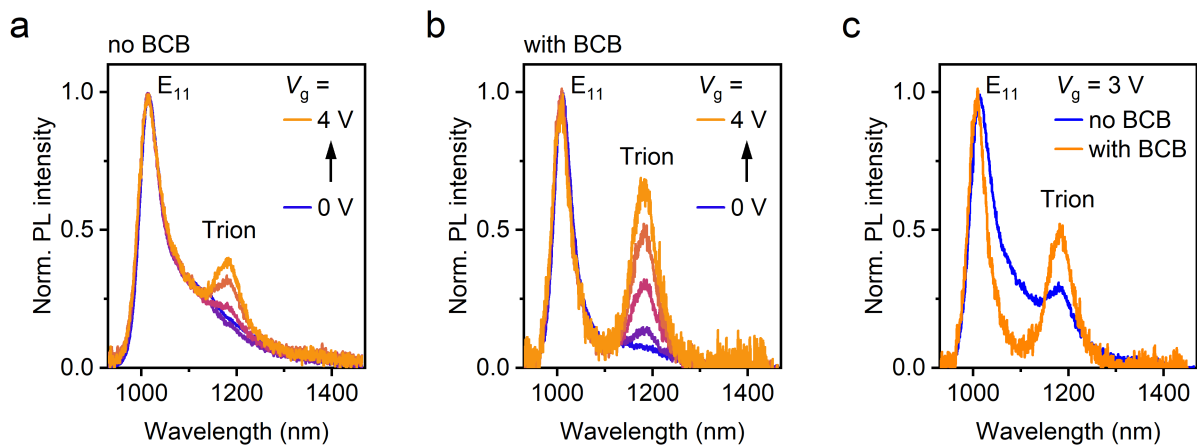


Figure 6.17: Normalized, gate voltage-dependent PL spectra of (6,5) SWCNT network LEFETs on glass substrates (a) without and (b) with a ~ 80 nm BCB layer in electron accumulation ($V_d = -10$ mV; gate voltage steps were 1 V). SWCNT films were annealed at 150 °C for 45 min before deposition of the PMMA/HfO_x dielectric. (c) Comparison of spectra on glass and on BCB at $V_g = 3$ V.

Absolute EL efficiencies of LEFETs on glass without and with BCB layer were determined from EQE measurements during constant current sweeps (see Chapter 3.4.7). As shown in Figure 6.18, an increase in EQE from $\sim 0.012\%$ to $\sim 0.017\%$ was observed for the device on BCB with respect to the LEFET without passivation. While these minor differences were observed for two different devices of each type, a larger dataset would be required to obtain statistically significant values and standard deviations. The slightly lower EQE for devices without passivation could be attributed to quenching of excitons at the nanotube–substrate interface.³¹⁸ In summary, substrate passivation with BCB enhances the shape of PL and EL spectra of SWCNT thin films and optoelectronic devices and, to a lesser degree, also the absolute emission efficiencies.

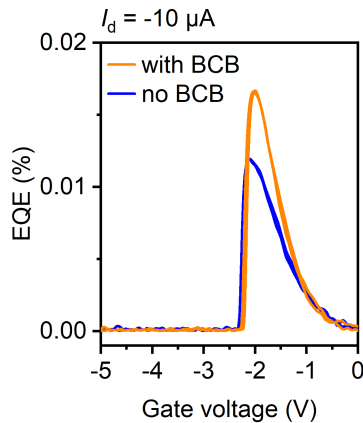


Figure 6.18: EQE of (6,5) SWCNT network LEFETs on glass substrates without and with a ~ 80 nm BCB layer during a gate voltage sweep at a constant drain current $I_d = -10 \mu\text{A}$. SWCNT films were annealed at 150°C for 45 min before deposition of the PMMA/ HfO_x dielectric.

6.7 Covalently functionalized SWCNT films on BCB

So far, the different spectroscopic data corroborated that substrate passivation with BCB prevents the unintentional introduction of lattice defects to pristine SWCNT films, which are detrimental to their emission spectra. In contrast to that, the controlled covalent functionalization of SWCNTs with luminescent sp^3 defects has emerged as a powerful approach to tune their spectroscopic properties.^{11,12,14} While Chapter 4 showcased the suitability of functionalized SWCNT networks as charge transport and emission layers in light-emitting devices, their EL spectra were broadened compared to the respective dispersions and exhibited undesired sideband emission just as the pristine nanotube films.

To assess whether substrate passivation with BCB similarly enhances the luminescence spectra of intentionally functionalized nanotubes on substrates, nitroaryl E_{11}^* defects were introduced to (6,5) SWCNTs through reaction with DzNO_2 (see Chapter 3.2.1 and Figure 4.1).²² Figure 6.19a shows the PL spectra of functionalized SWCNT films on glass without and with BCB after annealing at 150°C . Spectra collected from SWCNT networks on BCB showed significantly sharper E_{11} and E_{11}^* emission peaks, and unwanted sideband emission was suppressed. No change in relative intensities of emission from mobile and defect-localized excitons was observed. Previously, defect emission wavelengths and oscillator strengths of functionalized SWCNTs were found to be nearly independent of the dispersing solvent,¹⁴⁴ which was attributed to the relatively small dipole moment induced by defect formation and consequently small effects of dipole–dipole interactions with the environment on the optical properties.¹⁵¹ On the other hand, low-temperature PL spectra of single SWCNTs deposited on glass or embedded in a polymer matrix exhibited variations in relative emission intensities of different defect configurations which were associated with substrate quenching.¹⁵⁸

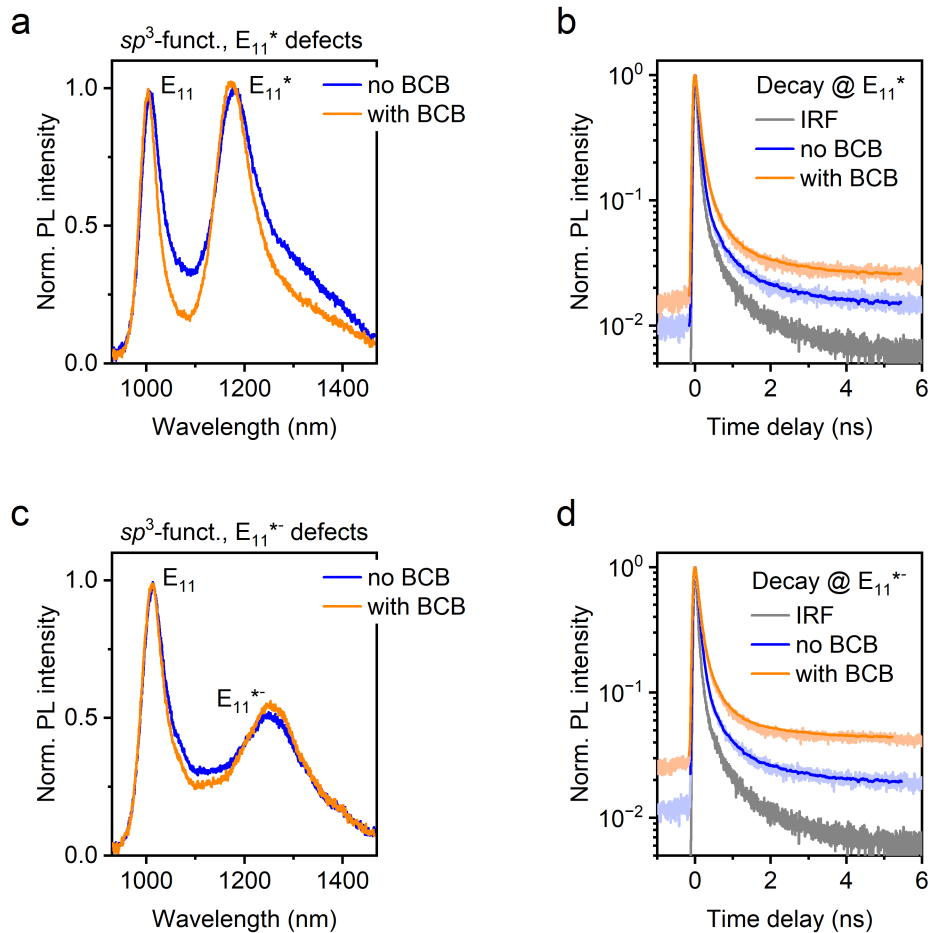


Figure 6.19: (a) Normalized PL spectra of (6,5) SWCNT thin films with nitroaryl E_{11}^* defects on glass substrates without and with a ~ 75 nm BCB layer, and (b) time-resolved PL decays at the E_{11}^* emission wavelength (1170 nm) with biexponential fits to the data. (c) Normalized PL spectra of (6,5) SWCNT thin films with aniline E_{11}^{*-} defects on glass substrates without and with a ~ 75 nm BCB layer, and (d) time-resolved PL decay at the E_{11}^{*-} emission wavelength (1250 nm) with biexponential fits to the data. All films were annealed at 150 °C for 45 min. In (b,d), the instrument response function (IRF) is shown in grey.

Time-resolved PL measurements in a TCSPC scheme (see Chapter 3.4.4) are a direct way to study the effect of BCB passivation on the exciton dynamics. PL decays at the E_{11}^* emission wavelength are shown in Figure 6.19b. Extracted lifetime components and relative amplitudes from biexponential fits are listed in Table 6.3 together with those obtained from measurements in a toluene dispersion. Clearly, SWCNT thin film deposition results in a strong reduction in PL lifetimes, which indicates enhanced non-radiative decay. This observation might be ascribed to more efficient phonon-induced decay through nanotube–nanotube and nanotube–substrate interactions in films compared to dispersions.¹²⁹ Furthermore, increased dielectric screening in films might favor non-radiative free-carrier recombination over radiative exciton recombination,^{122,352} which should especially apply to nanotubes that are

in direct contact with the substrate surface.^{124,356} Similarly, shorter E_{11} PL lifetimes were observed previously for pristine SWCNTs embedded in a polymer matrix compared to air-suspended nanotubes,¹²⁵ and PL lifetimes of isolated nanotubes in dispersion were found to depend on the surfactant and solvent.^{378,379}

The amplitude-averaged lifetime of E_{11}^* emission in the SWCNT film on BCB was higher by approximately a factor of 2 compared to the film on glass. As discussed above, the longer PL lifetime on BCB *versus* on the bare substrate might be attributed to the lower dielectric constant of the environment and possibly less phonon-induced decay. BCB might also suppress p -doping of nanotubes at the polar substrate surface,³⁵⁶ which results in efficient non-radiative Auger quenching.^{128,129} For functionalized (6,5) SWCNTs deposited on polystyrene, a previous report found a significant increase in defect-state PL lifetime upon removal of DOC from the nanotube surface.¹⁵⁰ This observation was explained by non-radiative EVET¹⁴⁴ from the SWCNT to the surfactant, which might similarly occur between SWCNTs and the substrate and is suppressed by the BCB layer. Unfortunately, it was not possible to resolve the decay of E_{11} exciton emission with the available setup, thus preventing a comparison of the effect of BCB passivation on mobile and defect-localized excitons.

Table 6.3: Long (τ_{long}) and short (τ_{short}) lifetime components, normalized amplitudes (A_{long} , A_{short}), and amplitude-averaged lifetimes ($\tau_{\text{ampl.-avg.}}$) obtained from biexponential fits to the PL decays of sp^3 -functionalized (6,5) SWCNT dispersions and thin films at the E_{11}^* (1170 nm) and E_{11}^{*-} (1250 nm) emission wavelength, respectively.

Defect type	Sample type	τ_{long} (ps)	A_{long}	τ_{short} (ps)	A_{short}	$\tau_{\text{ampl.-avg.}}$ (ps)
E_{11}^*	Toluene dispersion	433	0.24	156	0.76	222
	Thin film, no BCB	56	0.21	26	0.79	32
	Thin film, with BCB	131	0.14	48	0.86	60
E_{11}^{*-}	Toluene dispersion	562	0.47	173	0.53	355
	Thin film, no BCB	89	0.12	33	0.88	40
	Thin film, with BCB	189	0.09	55	0.91	67

As shown in Figure 6.19c,d, substrate passivation with BCB similarly results in enhanced emission spectra and prolonged PL lifetimes in films of (6,5) SWCNTs that were selectively functionalized with further red-shifted E_{11}^{*-} defects (emission at ~ 1250 nm; for experimental details, see Chapter 3.2.2).²³ Table 6.3 displays the fitting parameters obtained from biexponential fits to the PL decays at the wavelength of defect emission. Again, thin film deposition led to a strong PL lifetime shortening of the E_{11}^{*-} defect emission. Consistent with previous reports,^{23,144} the lifetime of E_{11}^{*-} PL was longer compared to E_{11}^* emission for all sample types due to the deeper exciton trapping potential. The magnitude of PL lifetime increase for the films on BCB with respect to the non-passivated substrate was very similar for both defect types.

As demonstrated above, BCB passivation proved to be fully compatible with the fabrication of SWCNT network LEFETs and led to enhanced EL spectra of pristine nanotube films as well as higher EQEs. The improved PL spectra of SWCNT films with luminescent sp^3 defects on BCB-covered substrates already indicated that this concept should be transferrable to light-emitting devices with intentionally functionalized SWCNTs. To this end, LEFETs based on nanotube networks with E_{11}^{*-} defects were fabricated on glass without and with BCB layer (see Chapter 3.3.6). The device layout was identical to the one displayed in Figure 6.15a. Again, EL spectra of LEFETs on BCB exhibited less emission from unwanted sidebands in the wavelength range between the E_{11} and E_{11}^{*-} emission peaks (Figure 6.20a). Both peaks were slightly blue-shifted compared to the samples without BCB. Note that different functionalized SWCNT dispersions were used to fabricate the films in Figure 6.19c and 6.20a and thus, the relative peak intensities cannot be directly compared.

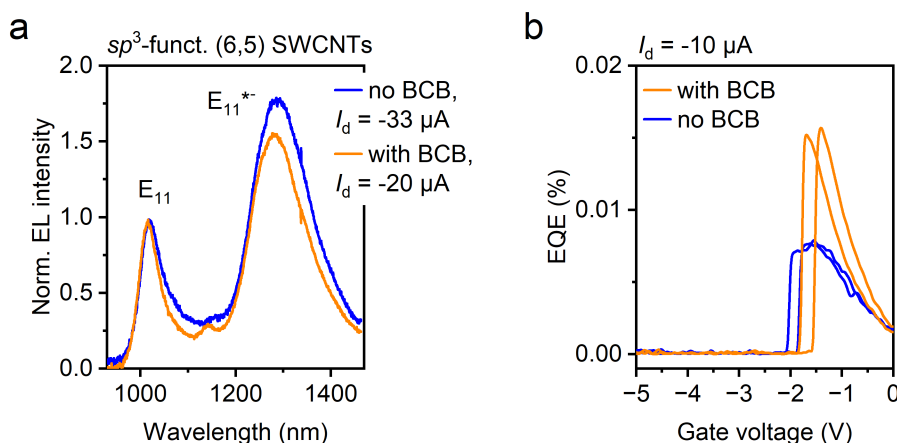


Figure 6.20: (a) Normalized EL spectra of functionalized (6,5) SWCNT network LEFETs with E_{11}^{*-} defects on glass substrates without and with a ~ 80 nm BCB layer, and (b) EQE of such LEFETs during a gate voltage sweep at a constant drain current $I_d = -10 \mu A$. SWCNT films were annealed at $150^\circ C$ for 45 min before deposition of the PMMA/HfO_x dielectric.

EQE measurements of E_{11}^{*-} -functionalized SWCNT LEFETs on BCB revealed significantly higher EL efficiencies compared to those on glass substrates (Figure 6.20b). The increase in EQE from $\sim 0.008\%$ (no BCB) to $\sim 0.016\%$ (with BCB) was consistent with the roughly two-fold increase in PL lifetime (see Table 6.3) and hence can be attributed to reduced non-radiative exciton quenching achieved by substrate passivation. Notably, the effect of BCB on the EQE was even more pronounced than for the pristine SWCNT network LEFETs (compare Figure 6.18). Even though an increase in EQE by substrate passivation was reproducibly observed for different devices, more measurements are required for a statistically significant quantification of the brightening effect. Overall, the beneficial impact of BCB passivation on the optical properties of covalently functionalized SWCNTs in thin films opens up new avenues for their application as tunable solid-state NIR emitters and single-photon sources.^{18,19}

6.8 Summary and conclusion

In this Chapter, surface passivation with the cross-linked, low dielectric constant polymer BCB was introduced as a powerful approach to enhance the luminescence spectra of SWCNT thin films on commonly used glass and Si/SiO₂ substrates. PL spectra of (6,5) SWCNT networks on BCB exhibited significantly lower emission from red-shifted sidebands, especially from the so-called Y₁ band whose origin had been elusive thus far. Corroborated by Raman and temperature-dependent PL spectroscopy, the Y₁ sideband can now be attributed to nanotube sidewall defects that act as shallow excitonic trapping potentials. These defects are most likely introduced through interactions between SWCNTs and the polar, oxygen-containing terminal groups on the substrate surface, independent of the coverage of the nanotube sidewalls by a wrapping polymer or a surfactant. While similar observations were made for (7,5) SWCNTs, the degree of defect introduction, and thus Y₁ sideband emission intensity, appears to be related to the nanotube geometry and reactivity as previously observed in covalent functionalization reactions. Thus, films of SWCNTs with larger diameters might be more stable towards lattice defect introduction on substrates. Extending on this initial observation, luminescent oxygen defects might be introduced to small-diameter SWCNTs in the solid state using reactive oxidic surfaces to tune their emission wavelengths for applications.

For SWCNT films on *h*-BN flakes, a similar enhancement of their emission spectra was observed compared to BCB. However, the commercial availability of BCB combined with its facile and reproducible deposition as thin films over large areas *via* spin-coating make it ideally suited as a high-quality passivation layer in the fabrication of optoelectronic devices. The outstanding stability of BCB towards most chemicals and solvents as well as its compatibility with typical semiconductor processing steps used in device fabrication was demonstrated in the realization of SWCNT network LEFETs on BCB-covered glass with excellent charge transport properties, improved EL spectra, and higher EQEs. BCB passivation was also shown to facilitate the analysis of trion peaks in EL and gated PL spectra.

Moreover, substrate surface passivation with BCB resulted in enhanced luminescence spectra and longer PL lifetimes from thin films of *sp*³-functionalized SWCNTs and thus lays the foundation for their application as narrowband, tunable solid-state NIR emitters, as will be further discussed in Chapter 7. Future studies should investigate whether BCB passivation can be generalized to other low-dimensional excitonic semiconductors to provide access to their intrinsic emission properties and enhance device performance. For example, substrate interactions were found to cause non-idealities in the electrical characteristics of devices based on graphene,³⁶¹ graphene nanoribbons,³⁸⁰ and transition metal dichalcogenides,^{366,381} and they obstructed investigations of the intrinsic photophysics of 2D materials.³⁶² Overall, BCB emerges as an ideal substrate passivation layer for spectroscopic investigations of, and light-emitting devices with, SWCNTs and possibly other low-dimensional emitters.

Chapter 7

Further Red-Shifted Electroluminescence from Functionalized SWCNT Networks

In this Chapter, luminescent defects with a deeper optical trap depth are introduced to different nanotube species to adjust the emission wavelength of SWCNT network LEFETs.

Light-emitting field-effect transistors based on SWCNT networks with E_{11}^{*-} defects were fabricated in collaboration with Simon Settele and Finn L. Sebastian. (7,5) SWCNT dispersions were provided by Sebastian Lindenthal (all Heidelberg University).

7.1 Introduction

As detailed in Chapter 4, (6,5) SWCNT network LEFETs with E_{11}^* sp^3 defects exhibited high charge carrier mobilities and red-shifted EL emission at ~ 1175 nm, which might enable their use as electrically-driven, solid-state NIR emitters. To boost their potential for practical applications, however, the defect emission should ideally be centered within one of the standard telecommunication bands (O-band, 1260–1360 nm, or C-band, 1530–1565 nm).^{18–20} Furthermore, spectral variations that arise, *e.g.*, from different defect species or other emissive sidebands (see Chapter 6) must be reduced as far as possible.

The emission wavelength of luminescent defects in SWCNTs is assumed to be predominantly governed by their specific binding configuration on the nanotube lattice.^{17,152,158} Following the attachment of a defect group to the SWCNT, the resulting reactive intermediate imparts a delocalized charge or unpaired electron that is subsequently saturated through binding of a second fragment.¹⁶⁰ For chiral nanotubes such as (6,5) SWCNTs, this second binding event gives rise to six geometrically distinct species that might be produced upon covalent functionalization.¹⁵⁸ As corroborated by density functional theory calculations, each of these different defect configurations is associated with a different exciton trap depth and thus emission wavelength.^{13,151} The most commonly observed defect emission bands in (6,5) SWCNTs, denoted as E_{11}^* (~ 1160 nm) and E_{11}^{*-} (~ 1250 nm),^{23,144,173,306} are hypothesized to originate from binding of the two fragments to adjacent (*ortho*) carbon atoms around the circumference (*ortho-L*₉₀) and along the nanotube axis (*ortho-L*₃₀), respectively.^{17,151,158}

Due to the deeper exciton trapping potential, the E_{11}^{*-} defect configuration gives rise to further red-shifted emission with higher single-photon purity compared to E_{11}^* defects and is therefore better suited for applications.²³ Hence, different strategies for the controlled introduction of E_{11}^{*-} defects to aqueous nanotube dispersions have been explored, including the use of achiral zigzag SWCNTs¹⁷ or pre-arranged bisdiazonium reactants with methylene linkers,³⁰⁶ the creation of divalent defects,¹⁶² and very recently by exploiting intermolecular interactions between reagents and nanotube sidewalls.¹⁷⁷ However, only with the recently reported E_{11}^{*-} -selective functionalization of polymer-wrapped SWCNTs in organic solvents,²³ the scalable and reproducible deposition of SWCNT networks with further red-shifted defects for thin film device fabrication has come into reach. In combination with the diameter-dependent optical transition energies of different semiconducting nanotube species, this approach should facilitate tuning of the emission spectrum of light-emitting SWCNT devices across the NIR spectral range.^{17,19}

Aside from a high degree of control over the spectroscopic properties, the realization of optoelectronic devices with E_{11}^{*-} -functionalized SWCNTs requires a detailed understanding of their charge transport characteristics. For single-nanotube transistors, the electrical conductance remained unaltered upon introduction of divalent methylene defects,¹⁸⁵ but it was reduced through attachment of monovalent aryldiazonium defects.^{178,179} In the latter reports, however, the exact nature of defects (*i.e.*, luminescent or exciton-quenching, and their binding configuration) remained unknown due to the lack of spectroscopic data. Consequently, further studies are necessary to assess the impact of SWCNT functionalization on charge transport depending on the defect structure.

In this Chapter, networks of small-diameter (6,5) and (7,5) SWCNTs with E_{11}^{*-} defects are integrated in LEFETs to shift the EL emission further towards telecommunication wavelengths. Electrical characterization and spectroscopic experiments under electrostatic doping provide initial insights into the impact of the defect binding configuration on charge transport in covalently functionalized SWCNT thin films.

7.2 (6,5) SWCNT network LEFETs with further red-shifted defects

Nearly monochiral dispersions of (6,5) SWCNTs were prepared from nanotube raw material by selective polymer-wrapping with PFO-BPy as described in Chapter 3.1.1, followed by removal of excess, unbound polymer *via* filtration and re-dispersion in toluene before the functionalization step. Raman and absorption spectroscopy confirmed the high purity of the dispersions with negligible amounts of other SWCNT species and no metallic nanotubes. The selective introduction of E_{11}^{*-} defects to these (6,5) SWCNTs was performed according to the procedure developed by Settele *et al.* (see Chapter 3.2.2) as schematically illustrated in Figure 7.1.²³ Defects were created with 2-iodoaniline in the presence of the strong organic base potassium *tert*-butoxide (KOTBu). Dimethylsulfoxide (DMSO) and tetrahydrofuran (THF) were added as co-solvents, and the reaction proceeded under stirring and in the dark within 30 minutes. After quenching of the reaction through vacuum filtration and washing with toluene and methanol, functionalized SWCNTs were re-dispersed in toluene for characterization and device fabrication.

As shown in the PL spectra in Figure 7.2a, this functionalization gave rise to a new emission feature at ~ 1250 nm that corresponds to E_{11}^{*-} defects.²³ These defects are attributed to binding of the two fragments in the axial direction of the SWCNT,^{151,158} resulting in a deeper optical trap depth compared to E_{11}^* defects (see, *e.g.*, Chapters 4 and 5). The stronger exciton localization was reflected in a large red-shift of the E_{11}^{*-} emission by 248 meV with respect to the E_{11} peak and a long amplitude-averaged defect PL lifetime of 362 ps as determined by TCSPC measurements. No features corresponding to E_{11}^* defects were observed in the PL

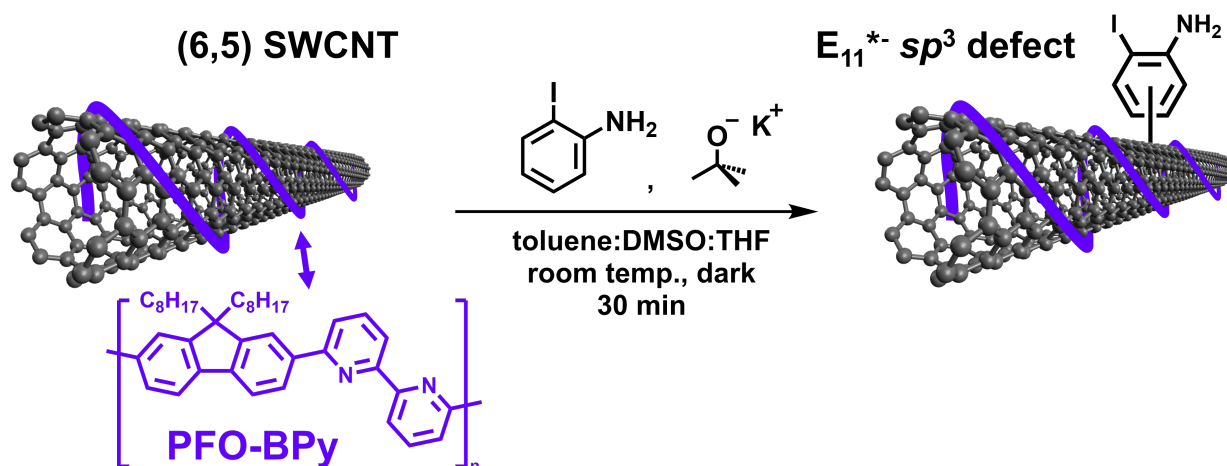


Figure 7.1: Reaction scheme for the covalent functionalization of PFO-BPy-wrapped (6,5) SWCNTs with 2-iodoaniline and potassium *tert*-butoxide (KO*t*Bu) in organic solvents. Note that bond formation between the aromatic fragment and the SWCNT might occur in different positions, as discussed in the text.

spectra, which underlines the high selectivity of this functionalization method towards one specific defect structure. Note that the reaction is hypothesized to occur *via* nucleophilic attack from a deprotonated aniline species, in which the negative charge is delocalized.²³ Hence, bond formation to the SWCNT might occur in different positions of the aromatic fragment, depending on the charge distribution in the delocalized system. As the defect emission wavelength is predominantly governed by the binding configuration rather than the chemical structure of the attached group,^{17,158} differences in the exact binding position are expected to have only a minor impact on the optical properties.

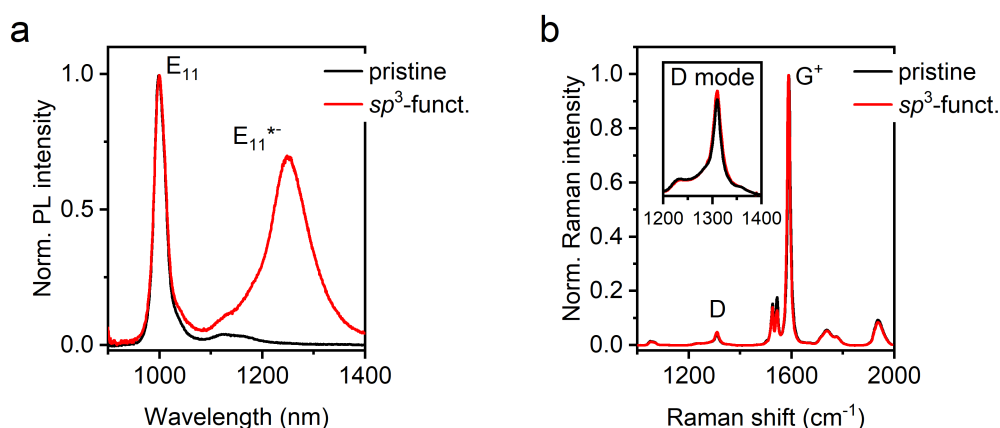


Figure 7.2: (a) Normalized PL spectra of a pristine (6,5) SWCNT dispersion and a dispersion after functionalization with 2-iodoaniline. Emission peaks corresponding to mobile E_{11} excitons and defect-localized E_{11}^{*-} excitons are labelled. (b) Raman spectra (532 nm excitation) of pristine and functionalized (6,5) SWCNTs normalized to the G^+ mode. The inset shows a zoom-in on the defect-related D mode. Data were measured by Simon Settele (Heidelberg University).

A slight, yet noticeable increase in the defect-related Raman D mode intensity with respect to the G^+ mode further corroborated the covalent attachment of defect groups to the SWCNTs (Figure 7.2b). The Raman D/ G^+ area ratio, which is indicative for the number of nanotube lattice defects,²⁹⁷ increased from ~ 0.09 for pristine SWCNTs to ~ 0.10 for functionalized SWCNTs. An estimation based on the recently reported model that links the number of sp^3 defects induced in small-diameter SWCNTs to the differential Raman D/ G^+ area ratio (compare Equation 4.1) yielded a density of approximately 3.5 defects per μm of nanotube.¹⁴⁷

From concentrated dispersions (optical density of 8 cm^{-1} at the E_{11} absorption peak, corresponding to a SWCNT concentration of $\sim 14.4\text{ }\mu\text{g mL}^{-1}$),³⁴⁹ dense networks of pristine and functionalized SWCNTs were deposited *via* spin-coating on BCB-passivated glass substrates (compare Chapter 6) with photolithographically-patterned, interdigitated gold source/drain electrodes ($L = 20\text{ }\mu\text{m}$, $W = 10\text{ }\mu\text{m}$). Similar to the procedure for SWCNTs with E_{11}^* defects, nanotube networks were annealed at $150\text{ }^\circ\text{C}$ to remove residual oxygen and water while preventing thermally-induced defect cleavage.²⁹⁹ On top of the SWCNTs, a double-layer PMMA/ HfO_x dielectric was deposited, followed by thermal evaporation of a silver top-gate electrode (for details, see Chapter 3.3.6). Figure 7.3a shows a schematic cross-section of a LEFET and a representative AFM image of a dense, sp^3 -functionalized SWCNT network. Pristine and functionalized SWCNT networks exhibited high areal capacitances of 130 nF cm^{-2} and 137 nF cm^{-2} , respectively, and comparable network densities that were well-above the mobility saturation threshold.¹⁹⁷

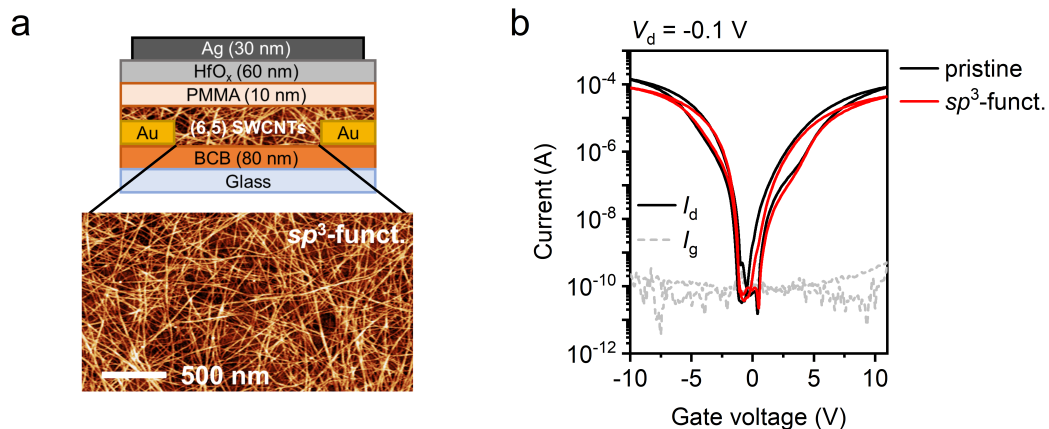


Figure 7.3: (a) Schematic cross-section of a bottom-contact, top-gate (6,5) SWCNT network LEFET (layer thicknesses not to scale) and representative atomic force micrograph of a dense network of sp^3 -functionalized SWCNTs with E_{11}^* defects. The scale bar is 500 nm. (b) Ambipolar transfer characteristics of pristine and functionalized SWCNT network LEFETs in the linear regime ($V_d = -0.1\text{ V}$). Solid lines are drain currents I_d , grey dashed lines are gate leakage currents I_g .

Representative transfer characteristics of pristine and functionalized SWCNT network transistors are shown in Figure 7.3b. All devices exhibited ambipolar charge transport (*i.e.*, hole and electron conduction) and high on/off current ratios. The current hysteresis was rela-

tively low, which suggests that most of residual water and oxygen were removed even at the low annealing temperature of 150 °C.^{223,300} Despite the low defect density ($n_d \sim 3.5 \mu\text{m}^{-1}$), however, on-currents were significantly reduced by a factor of ~ 2 for devices based on functionalized *versus* pristine SWCNT networks. The impact of sp^3 defects was further reflected in a pronounced decrease in maximum charge carrier mobilities (Table 7.1). Hole mobilities decreased by $\sim 44\%$ from $3.9 \pm 0.3 \text{ cm}^2(\text{Vs})^{-1}$ (pristine) to $2.2 \pm 0.1 \text{ cm}^2(\text{Vs})^{-1}$ (functionalized), whereas electron mobilities were reduced by $\sim 48\%$ from $2.1 \pm 0.3 \text{ cm}^2(\text{Vs})^{-1}$ to $1.1 \pm 0.1 \text{ cm}^2(\text{Vs})^{-1}$ upon functionalization.

Table 7.1: Averaged linear hole and electron mobilities of pristine and E_{11}^{*-} -functionalized (6,5) SWCNT network LEFETs. Standard deviations were obtained from measurements of at least 7 different transistors for each network.

Sample	Defect density n_d (μm^{-1})	Hole mobility ($\text{cm}^2(\text{Vs})^{-1}$)	Electron mobility ($\text{cm}^2(\text{Vs})^{-1}$)
pristine	0	3.9 ± 0.3	2.1 ± 0.3
sp^3 -funct.	3.5	2.2 ± 0.1	1.1 ± 0.1

Consistent with the observations for E_{11}^* defects (compare Chapters 4.3 and 5.5), the comparable drop in hole and electron mobilities points towards similar interactions of both charge carrier polarities with the defect sites, irrespective of the defect binding configuration on the SWCNT lattice. However, the relative carrier mobility reduction was much stronger for E_{11}^{*-} compared to E_{11}^* defects. The introduction of a low number of nitroaryl E_{11}^* defects ($n_d \sim 6 \mu\text{m}^{-1}$) in Chapter 5.5 resulted in a decrease in network mobilities of 10–20%. For a low density of bromoaryl E_{11}^* defects ($n_d \sim 6 \mu\text{m}^{-1}$; compare Chapter 4.3), hole and electron mobilities were even found to be essentially identical to those measured in LEFETs with pristine SWCNT networks. These results are in stark contrast to the mobility reduction by almost 50% for the aniline defects given the low degree of functionalization with $n_d \sim 3.5 \mu\text{m}^{-1}$. Clearly, the defect binding configuration appears to have a significant impact on charge transport in functionalized SWCNTs, which was previously indicated by measurements of single-nanotube transistors with monovalent *versus* divalent defects.¹⁸⁵ To obtain more detailed insights into the interaction of charge carriers with E_{11}^{*-} defects and defect-localized excitons, (time-resolved) PL spectroscopy under static charge accumulation was performed, as described in the following.

7.3 Impact of binding configuration on defect-carrier interaction

The observation of substantially reduced carrier mobilities in SWCNT networks with further red-shifted defects, despite the relatively low degree of functionalization, prompted a more detailed investigation of the interaction between charge carriers and E_{11}^{*-} defect sites. Due to the high sensitivity of SWCNT excitons to the presence of charge carriers,⁹⁶ changes in the emission spectra of nanotube networks upon doping can be correlated with the distribution of carrier density and charge transport.^{134,232,273} To investigate the effect of static, gate field-induced doping on the luminescence properties of (6,5) SWCNT network LEFETs with E_{11}^{*-} defects, PL spectra under pulsed E_{22} excitation were acquired at different gate voltages. Absolute emission intensities of both E_{11} and E_{11}^{*-} peaks decreased strongly with increasing V_g due to highly efficient Auger quenching of excitons with charge carriers.^{128,129} Figure 7.4a shows the E_{11} -normalized PL spectra in hole accumulation. In agreement with the results for E_{11}^* defects (compare Chapter 4.6), however, the E_{11}^{*-} defect peak was more strongly quenched than emission from mobile E_{11} excitons. Again, this observation suggests that charge carriers might preferentially reside in the vicinity of sp^3 defects, thus indicating a certain degree of carrier localization at the defect sites. The relatively low defect peak intensity under pulsed excitation, presumably due to state-filling,^{22,156} complicated a quantitative analysis of the E_{11}^{*-} -to- E_{11} PL ratio depending on the carrier density, especially at higher voltages where defect emission was almost completely quenched. To circumvent this issue, V_g -dependent PL spectra were also measured under non-resonant cw excitation, as discussed below.

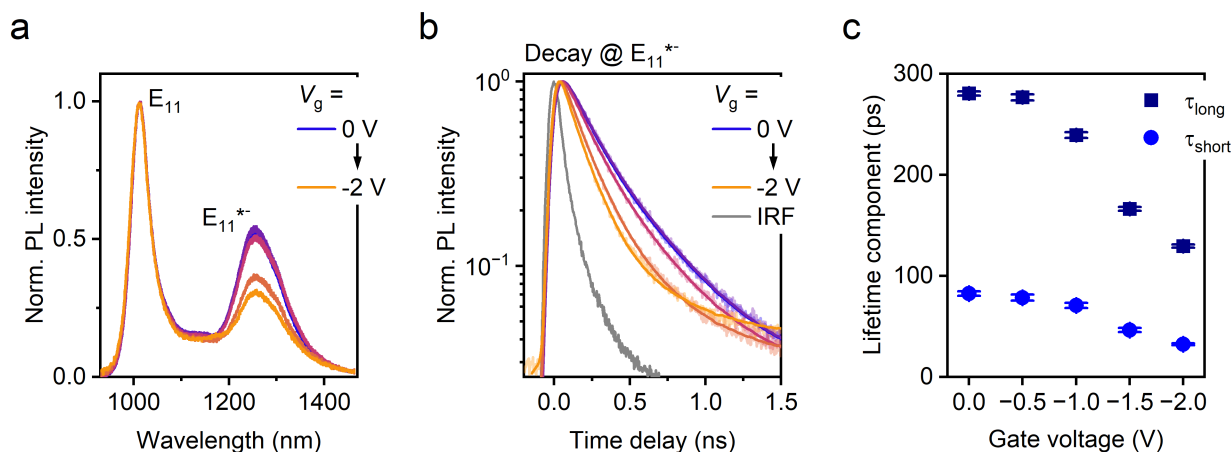


Figure 7.4: (a) Normalized PL spectra (pulsed E_{22} excitation at 575 nm) of a (6,5) SWCNT network LEFET with E_{11}^{*-} defects at different gate voltages V_g (voltage steps, 0.5 V) in hole accumulation ($V_d = -10$ mV). (b) Time-resolved PL decays at the E_{11}^{*-} defect emission wavelength (1260 nm) at different V_g corresponding to the spectra in (a). Measured data are shown in light colors, biexponential fits to the data are shown in darker colors. The instrument response function (IRF) is shown in grey. (c) Extracted lifetime components (τ_{long} , τ_{short}) obtained from biexponential fits in (b) *versus* applied gate voltage.

Further insights into the interaction of charge carriers and defect-localized excitons were obtained from PL lifetime measurements that were conducted by TCSPC (see Chapter 3.4.4). In contrast to the E_{11} emission, the PL lifetime of the defects was sufficiently long to be resolved with the available setup despite the strong lifetime shortening upon SWCNT film deposition (compare Chapter 6.7). PL decay traces were acquired in the undoped state and at different gate voltages (Figure 7.4b), and all curves exhibited biexponential decays as commonly found for sp^3 defects at room temperature.¹³⁹ However, PL lifetimes progressively decreased with increasing doping level, thus indicating that carrier-mediated Auger quenching poses an efficient non-radiative decay pathway for excitons localized at E_{11}^{*-} defects.

Extracted lifetime components are shown in Figure 7.4c *versus* applied gate voltage, and all fitting results are given in Table 7.2. For sp^3 defects, τ_{short} has previously been assigned to the redistribution of exciton population over the defect-state manifold, whereas τ_{long} reflects all radiative and non-radiative decay pathways of defect-localized excitons (see Chapter 2.2.1).¹³⁹ According to He *et al.*, the long lifetime component can be expressed as

$$\frac{1}{\tau_{\text{long}}} = \frac{1}{\tau_{\text{rad}}} + \frac{1}{\tau_{\text{MPD}}} + \frac{1}{\tau_{\text{EVET}}} + \frac{1}{\tau_{\text{TD}}} + k_{\text{other}} \quad (7.1)$$

with the radiative lifetime τ_{rad} as well as contributions from non-radiative decay *via* multiphonon decay (MPD), electronic-to-vibrational energy transfer (EVET), and thermal detrapping (TD).¹⁴⁴ The non-radiative decay channel through Auger quenching with charge carriers can be seen as an additional term to the cumulative rate of all other contributing processes (k_{other}). This rate constant is low for SWCNTs in the undoped state¹⁴⁴ but becomes significant upon gate-induced charge accumulation, as Auger quenching is a highly efficient process.^{128,129} Consequently, τ_{long} decreases with increasing gate voltage. The short lifetime component, on the other hand, is given by

$$\frac{1}{\tau_{\text{short}}} = \frac{1}{\tau_{\text{rd}}} + \frac{1}{\tau_{\text{long}}} \quad (7.2)$$

with τ_{rd} being the time constant for exciton redistribution.¹⁴⁴ Thus, the reduction in τ_{long} leads to a decrease in τ_{short} as well (see Table 7.2). It should be noted that for higher voltages, a moderate reduction in amplitude A_{long} (increase in A_{short}) was observed. Previously, He *et al.* attributed a small A_{long} in the defect PL lifetime of water-dispersed SWCNTs to a small instantaneous population of the bright defect state due to highly efficient non-radiative decay *via* EVET.¹⁴⁴ Likewise, for (6,5) SWCNTs with covalently attached organic radicals, the reduced defect PL lifetime and lower weight of the long lifetime component were associated with radical-enhanced exciton quenching.³⁶⁰ In agreement with these results, the decrease in A_{long} with increasing charge density could be due efficient non-radiative decay through carrier-mediated Auger quenching of trapped excitons.

Table 7.2: Gate voltage-dependent E_{11}^{*-} PL decay in an sp^3 -functionalized (6,5) SWCNT network LEFET. Long (τ_{long}) and short (τ_{short}) lifetime components, normalized amplitudes (A_{long} , A_{short}), and amplitude-averaged lifetimes ($\tau_{\text{ampl.-avg.}}$) were obtained from biexponential fits to the PL decays at the E_{11}^{*-} emission wavelength (1260 nm).

Gate voltage (V)	τ_{long} (ps)	A_{long}	τ_{short} (ps)	A_{short}	$\tau_{\text{ampl.-avg.}}$ (ps)
0.0	281	0.35	83	0.65	152
-0.5	277	0.38	79	0.62	153
-1.0	239	0.36	71	0.64	132
-1.5	166	0.32	47	0.68	84
-2.0	129	0.29	32	0.71	61

For a more detailed evaluation of the carrier density-dependent E_{11}^{*-} exciton quenching, PL spectra at a constant gate voltage were acquired under non-resonant cw excitation at 785 nm. The pump power in this measurement scheme was lower compared to the spectra measured under pulsed excitation (compare Figure 7.4a), which resulted in a higher defect-to- E_{11} emission ratio (less state-filling)^{22,156} and thus facilitated the quantitative analysis of spectral changes. Figure 7.5a shows the gate voltage-dependent PL spectra of a (6,5) SWCNT network LEFET with E_{11}^{*-} defects in hole accumulation. With increasing gate voltage, and thus accumulated charge density, both the E_{11} exciton peak at ~ 1012 nm and the E_{11}^{*-} defect emission at ~ 1268 nm were progressively quenched due to carrier-mediated non-radiative Auger decay.^{128,129} As evident from the normalized spectra in Figure 7.5b, the defect emission feature was more strongly quenched than the E_{11} peak, in agreement with the results from PL spectroscopy under pulsed excitation (compare Figure 7.4a). For higher gate voltages, emission from trions at ~ 1177 nm became visible. Spectra in electron accumulation revealed the same trends.

PL intensities of E_{11} and E_{11}^{*-} obtained from fits to the spectra are displayed in Figure 7.5c together with a transfer curve of the LEFET in the linear regime. For pristine SWCNTs, quenching of the E_{11} PL is typically observed in both hole and electron accumulation, and the maximum emission intensity of the network is observed in the undoped state.^{382,383} Obviously, the E_{11}^{*-} PL intensity followed the same trend and was quenched with increasing charge carrier density to an even higher degree than the E_{11} emission. It should be noted that the observation of E_{11}^{*-} PL quenching upon doping with holes and electrons confirms that this emission feature arises from charge-neutral, defect-localized excitons, and that E_{11}^{*-} defects are not charged species that originate from defect-localized trions, as was suggested by few previous reports.^{153,384} Hence, it can be concluded that emission from E_{11}^{*-} defects is excitonic in nature and is associated with a deeper exciton trap due to a different binding configuration of the attached fragments on the SWCNT lattice, in agreement with theoretical calculations.^{13,151,158}

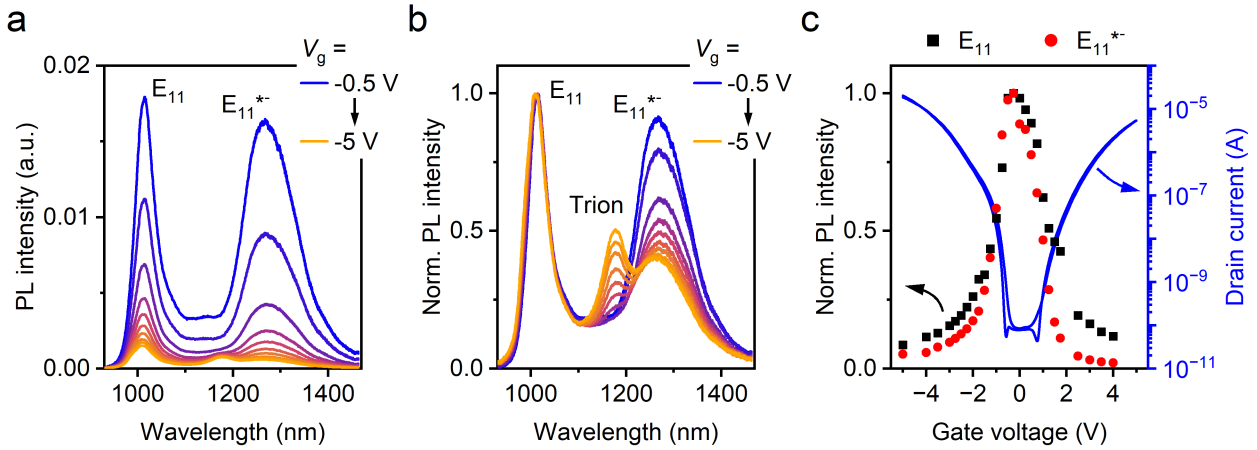


Figure 7.5: (a) Absolute and (b) normalized PL spectra (non-resonant cw excitation at 785 nm) of a (6,5) SWCNT network LEFET with E_{11}^{*-} defects at different gate voltages V_g in hole accumulation ($V_d = -10$ mV). At high voltages, trion emission becomes visible in the normalized spectra. (c) PL intensities of E_{11} (black squares) and E_{11}^{*-} (red circles) obtained from peak fits and normalized to their maxima. A transfer curve (linear regime, $V_d = -0.1$ V) of the LEFET measured at the same time is shown in blue (right axis).

The predominant quenching of defect emission with respect to the E_{11} PL was similarly observed for (6,5) SWCNT networks with bromoaryl E_{11}^* defects in Chapter 4.6. These results were in agreement with a report by Shiraishi *et al.* on PL spectroscopy of electrochemically doped (6,5) SWCNTs with E_{11}^* aryl defects.¹⁵⁷ In their study, the oxidation and reduction potentials corresponding to the HOMO and LUMO levels, respectively, were determined from the potentials corresponding to half the initial PL intensity. For E_{11}^* , the HOMO level was shifted to higher energies and the LUMO level was shifted to lower energies with respect to E_{11} , thus resulting in a smaller electrochemical bandgap for the defect compared to the E_{11} state. With increasing electron-withdrawing nature (*i.e.*, Hammett constant) of the aryl defect substituent, the shift in HOMO energy increased only slightly from ~ 23 meV to ~ 38 meV, whereas the shift in LUMO energy remained essentially the same (~ 20 meV).¹⁵⁷ These results indicated that luminescent defects in SWCNTs might act as shallow charge traps, as discussed in detail in Chapter 4.6. Notably, the similar impact of bromoaryl and nitroaryl E_{11}^* defects on the carrier mobilities in (6,5) SWCNT network LEFETs (compare Chapters 4.3 and 5.5) corroborated the notion that charge transport in functionalized SWCNTs might be largely unaffected by the chemical nature of attached groups.

However, a different study by Shiraishi *et al.* using *in situ* PL spectroelectrochemistry on oxygen-doped (6,5) SWCNTs indicated that the defect binding configuration – as opposed to the attached group – might have a larger impact on the electronic levels.¹⁵⁹ According to Ma *et al.*, the two main peaks in the emission spectra of oxygen-functionalized (6,5) SWCNTs are associated with binding of the oxygen atom in an ether (E_{11}^*) or epoxide (E_{11}^{*-}) configuration, respectively.¹⁵² For E_{11}^* defects (optical trap depth, 168 meV), the determined

electrochemical bandgap was 14 meV smaller compared to E_{11} , whereas the difference in electrochemical bandgaps of E_{11} and E_{11}^{*-} (optical trap depth, 264 meV) was 163 meV.¹⁵⁹

Owing to the further red-shift of E_{11}^{*-} emission compared to the E_{11}^* peak, the quantitative analysis of the V_g -dependent PL intensities was possible despite the emergence of the trion emission feature for higher carrier densities. To this end, gate voltage-dependent PL spectra were fitted with a superposition of Gauss peaks to account for the contributions of E_{11} , Y_1 (~ 1070 nm) and E_{11}^{*-} as well as trion emission (only for $|V_g| > 2$ V). Figure 7.6a,b shows the normalized PL intensities of E_{11} and E_{11}^{*-} in hole and electron accumulation, respectively. Note that the x-axis was adjusted in order to shift the PL maximum (*i.e.*, undoped state) to zero voltage. As introduced by Tanaka *et al.* for PL spectroelectrochemistry of pristine nanotubes³⁸⁵ and analogous to the reports for functionalized SWCNTs,^{157,159} the data were described with Nernst-type equations according to

$$\left(\frac{\text{PL}(V_g)}{\text{PL}_{\text{max}}}\right)_{\text{holes}} = \frac{1}{1 + \exp\left(A \cdot (V_{g,1/2}^h - V_g)\right)} \quad (7.3)$$

for negative V_g (hole accumulation) and

$$\left(\frac{\text{PL}(V_g)}{\text{PL}_{\text{max}}}\right)_{\text{electrons}} = \frac{1}{1 + \exp\left(A \cdot (V_g - V_{g,1/2}^e)\right)} \quad (7.4)$$

for the positive V_g (electron accumulation), respectively. In Equations 7.3 and 7.4, $\left(\frac{\text{PL}(V_g)}{\text{PL}_{\text{max}}}\right)$ is the gate voltage-dependent PL intensity normalized to the maximum value in the undoped state. A is a fitting parameter, and $V_{g,1/2}^h$ and $V_{g,1/2}^e$ correspond to the gate voltages in hole and electron accumulation, respectively, at which the initial PL intensity of the SWCNTs has decreased by 50%.

Fits to the data and fitting results for the potentials at half the initial PL intensity are shown in Figure 7.6 and Table 7.3. Note that the extracted voltages cannot directly be converted into an electronic bandgap due to the lack of a reference potential. However, it can be stated that the difference between the voltages at half PL intensity in hole and electron accumulation ($\Delta V_{g,1/2} = V_{g,1/2}^e - V_{g,1/2}^h$) – similar to the electrochemical bandgap defined as the difference between oxidation and reduction potentials in the studies by Shiraishi *et al.*^{157,159} – was substantially lower for E_{11}^{*-} compared to E_{11} . This voltage difference $\Delta V_{g,1/2}$ was 2.87 V for E_{11} and 2.17 V for E_{11}^{*-} (see Table 7.3), corresponding to a reduction by $\sim 24\%$ for the defect state. In the previous study on oxygen-doped (6,5) SWCNTs, the electrochemical bandgap of E_{11}^{*-} was $\sim 14\%$ lower than of E_{11} (1.032 eV *versus* 0.862 eV),¹⁵⁹ which compares very well to the data shown here. Consequently, the data corroborate that E_{11}^{*-} defects in (6,5) SWCNTs are energetically lower-lying states for charge carriers.

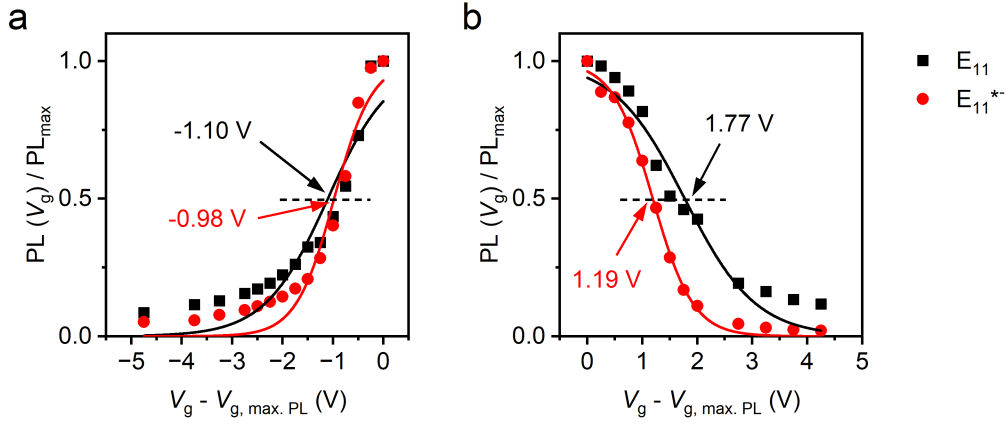


Figure 7.6: PL intensities of E_{11} (black squares) and E_{11}^{*-} (red circles) in (a) hole accumulation and (b) electron accumulation obtained from fits to the PL spectra (non-resonant cw excitation at 785 nm) of a (6,5) SWCNT network LEFET with E_{11}^{*-} defects and normalized to their maxima. Note that the x-axis was adjusted in order to shift the PL maximum (*i.e.*, undoped state) to zero voltage. Solid lines are fits according to Equations 7.3 and 7.4. Gate voltages corresponding to half the initial PL intensity are indicated.

Table 7.3: Gate voltage-dependent PL quenching of E_{11} and E_{11}^{*-} in a (6,5) SWCNT network LEFET. Voltages corresponding to half the initial PL intensity in hole ($V_{g,1/2}^h$) and electron ($V_{g,1/2}^e$) accumulation and voltage differences $\Delta V_{g,1/2} = V_{g,1/2}^e - V_{g,1/2}^h$ were obtained from fits to the data in Figure 7.6 according to Equations 7.3 and 7.4.

State	$V_{g,1/2}^h$ (V)	$V_{g,1/2}^e$ (V)	$\Delta V_{g,1/2}$ (V)
E_{11}	-1.10	1.77	2.87
E_{11}^{*-}	-0.98	1.19	2.17

As discussed in Chapter 4.6, the lower-lying electronic states created upon introduction of E_{11}^{*-} defects might lead to carrier localization at the defect sites, thus explaining the predominant quenching of defect PL and the lower network mobilities for functionalized SWCNT transistors compared to the unfunctionalized reference LEFETs. Charge trapping at E_{11}^{*-} defects might be stronger than at E_{11}^* defects, as indicated by the larger reduction in network mobilities and the more pronounced decrease in defect emission with respect to E_{11} upon doping. To determine the electrochemical bandgap of E_{11}^{*-} for a quantitative analysis of the trapping potential, PL measurements on electrochemical transistors with functionalized SWCNT networks under application of a gate voltage *versus* a reference electrode would be useful.³⁸⁶

7.4 Functionalized (7,5) SWCNT network LEFETs

The data presented so far indicated that the impact of covalent functionalization on charge transport in (6,5) SWCNTs strongly depends on the binding configuration of the sp^3 defects introduced to the nanotube lattice. E_{11}^{*-} defects with a larger optical red-shift caused a substantially larger reduction in SWCNT network mobilities compared to E_{11}^* defects. This observation raises the question whether the impact of luminescent defects on the charge transport properties also depends on the SWCNT chirality, and if so, to what extent.

To this end, E_{11}^{*-} defects were introduced to (7,5) SWCNTs (for a schematic illustration, see Figure 7.7a) that were selectively dispersed in toluene *via* polymer-wrapping with PFO under shear force mixing as described in Chapter 3.1.2. Despite the high selectivity of PFO for the (7,5) SWCNT chirality, the absorption spectrum of a pristine toluene dispersion exhibited minor peaks corresponding to residual (6,5) and (7,6) SWCNTs, respectively (Figure 7.7b). Raman spectroscopy confirmed the absence of metallic SWCNTs as well as the high quality of pristine nanotubes with a low degree of lattice disorder, as indicated by the low Raman D/G⁺ area ratio of ~ 0.04 (see Figure 7.7c).

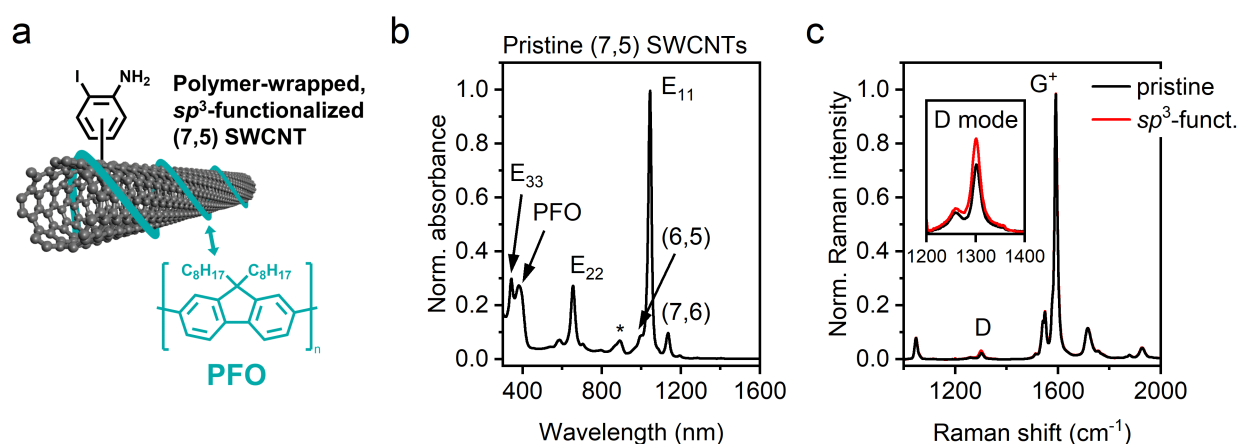


Figure 7.7: (a) Schematic illustration of a PFO-wrapped (7,5) SWCNT with an E_{11}^{*-} defect. (b) Absorption spectrum of a (7,5) SWCNT dispersion in toluene. The main excitonic transitions of (7,5) SWCNTs (E_{11}^* , E_{22} , E_{33}), the polymer absorption band, and peaks corresponding to the E_{11}^* transitions of residual (6,5) and (7,6) SWCNTs are labelled. The asterisk marks the E_{11}^* phonon sideband of (7,5) SWCNTs. (c) Raman spectra (633 nm excitation) of pristine and functionalized (7,5) SWCNTs normalized to the G⁺ mode. The inset shows a zoom-in on the defect-related D mode.

Covalent functionalization of (7,5) SWCNTs in organic solvents was accomplished by reaction with 2-iodoaniline and KO t Bu as detailed above for (6,5) SWCNTs (compare Figure 7.1 and Chapter 3.2.2). Due to the lower reactivity of (7,5) SWCNTs, the reaction time was 180 minutes. After collection of functionalized nanotubes by vacuum filtration followed by thorough washing with toluene and methanol to remove reaction side-products, SWCNTs were re-dispersed in toluene *via* bath sonication. The resulting concentrated dispersions

(optical density of $1\text{--}2\text{ cm}^{-1}$ at the E_{11} absorption peak, corresponding to a concentration of $2.9\text{--}5.7\text{ }\mu\text{g mL}^{-1}$)³⁴⁹ were suitable for subsequent characterization and device fabrication (see below). As shown in Figure 7.7c, the covalent attachment of sp^3 defects was reflected in a higher intensity of the defect-related Raman D mode relative to the G^+ mode, and thus Raman D/ G^+ area ratio, for the functionalized nanotubes. From the difference in Raman D/ G^+ area ratio of functionalized and pristine (7,5) SWCNTs, the degree of functionalization was estimated to approximately 8 sp^3 defects per μm SWCNT according to Equation 4.1.¹⁴⁷ Only a weak defect emission feature at $\sim 1272\text{ nm}$ was observed in the PL spectra of the functionalized (7,5) SWCNT dispersion.

(7,5) SWCNT LEFETs were fabricated on BCB-passivated glass substrates ($\sim 55\text{ nm}$ BCB layer; compare Chapter 6) with photolithographically-patterned gold source/drain contacts in an interdigitated electrode layout ($L = 20\text{ }\mu\text{m}$, $W = 10\text{ nm}$). Here, aerosol-jet printing was used for the deposition of homogeneous SWCNT thin films.²¹⁸ To increase viscosity, terpineol was added to the SWCNT dispersions, and the nanotube inks were printed exclusively in the channel area of the devices to lower the material consumption (see Chapter 3.3.2). A representative AFM image of a printed, random network of sp^3 -functionalized (7,5) SWCNTs with E_{11}^{*-} defects is shown in Figure 7.8a. SWCNT networks were annealed at $150\text{ }^\circ\text{C}$ for 45 minutes to remove residual oxygen and moisture from ambient air before deposition of PMMA ($\sim 14\text{ nm}$) and HfO_x ($\sim 65\text{ nm}$) as the double-layer gate dielectric. Devices were completed by thermal evaporation of 30 nm silver top-gate electrodes. Except for the slightly different layer thicknesses, the overall device layout was identical to the one displayed in Figure 7.3a.

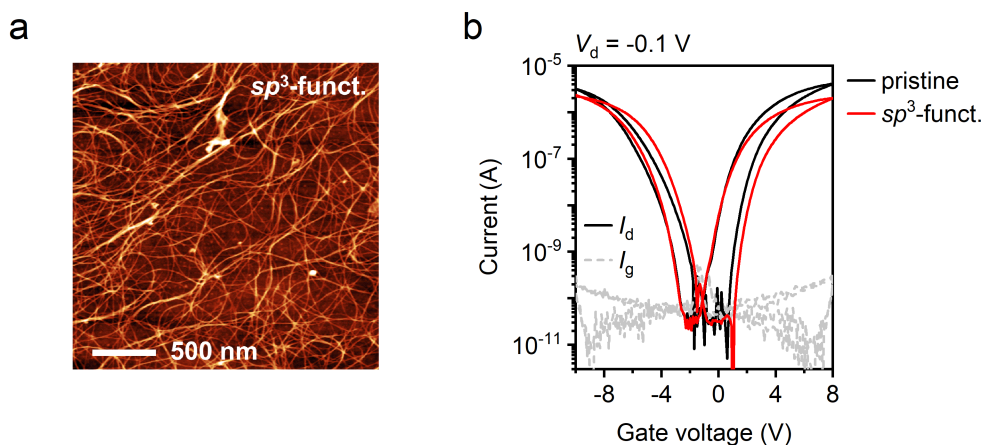


Figure 7.8: (a) Representative atomic force micrograph of an aerosol-jet-printed network of sp^3 -functionalized (7,5) SWCNTs with E_{11}^{*-} defects. The scale bar is 500 nm . (b) Ambipolar transfer characteristics of pristine and functionalized (7,5) SWCNT network LEFETs in the linear regime ($V_d = -0.1\text{ V}$). Solid lines are drain currents I_d , grey dashed lines are gate leakage currents I_g .

As shown in the representative transfer characteristics in the linear regime in Figure 7.8b, all LEFETs exhibited balanced ambipolar charge transport with low gate leakage currents and minor current hysteresis. Very similar areal capacitances of $\sim 87\text{--}88 \text{ nF cm}^{-2}$ were measured for pristine and functionalized networks, which highlights the comparability of the devices. Surprisingly, on-currents of these FETs were significantly lower compared to (6,5) SWCNT network transistors (compare, *e.g.*, Figure 7.3b). This observation was also reflected in relatively low mobilities of $0.14 \pm 0.01 \text{ cm}^2(\text{Vs})^{-1}$ for both holes and electrons that were obtained by averaging over 8 different LEFETs (Table 7.4). Due to the diameter-dependent mobilities in SWCNTs ($\mu \propto d^2$)²¹³ and the slightly larger diameter of (7,5) *versus* (6,5) SWCNTs ($d \sim 0.83 \text{ nm}$ and $\sim 0.76 \text{ nm}$, respectively), higher network mobilities would be expected for (7,5) SWCNT LEFETs. The minor differences in network densities cannot account for these pronounced differences. Instead, it is hypothesized that the presence of minority species with smaller bandgaps, especially the (7,6) SWCNTs (see the absorption spectrum in Figure 7.7b), is detrimental to charge transport. As previously established by EL and charge modulation spectroscopy of semiconducting SWCNT networks with different species, charge transport in such networks predominantly occurs through small-bandgap (large-diameter) nanotubes.^{232,273} If their abundance is low, such as for the (7,6) SWCNTs here, they might ultimately act as charge traps.²³² Additionally, the AFM image of the printed (7,5) SWCNT network (Figure 7.8a) revealed a higher degree of bundling compared to the spin-coated (6,5) SWCNTs (Figure 7.3a), thus further lowering the effective conductivity along the nanotubes through charge carrier scattering.^{85,254}

Table 7.4: Averaged linear hole and electron mobilities of pristine and E_{11}^{*-} -functionalized (7,5) SWCNT network LEFETs. Standard deviations were obtained from measurements of 8 different transistors for each network.

Sample	Defect density $n_d \text{ (}\mu\text{m}^{-1}\text{)}$	Hole mobility $(\text{cm}^2(\text{Vs})^{-1})$	Electron mobility $(\text{cm}^2(\text{Vs})^{-1})$
pristine	0	0.14 ± 0.01	0.14 ± 0.01
sp^3 -funct.	7.6	0.07 ± 0.01	0.06 ± 0.01

In agreement with previous results for (6,5) SWCNT network LEFETs with E_{11}^* and E_{11}^{*-} defects, functionalized (7,5) SWCNTs exhibited lower on-currents compared to the pristine reference transistors (Figure 7.8b). Averaged mobilities of $0.07 \pm 0.01 \text{ cm}^2(\text{Vs})^{-1}$ for holes and $0.06 \pm 0.01 \text{ cm}^2(\text{Vs})^{-1}$ for electrons were extracted from the linear transfer characteristics of functionalized (7,5) SWCNT network LEFETs, as listed in Table 7.4. These values correspond to a reduction by $\sim 50\%$ for holes and $\sim 57\%$ for electrons with respect to the unfunctionalized networks. Again, the very similar decrease in hole and electron mobilities upon functionalization suggests similar interactions of luminescent defects with both types of charge carriers as previously observed for E_{11}^* and E_{11}^{*-} defects in (6,5) SWCNTs.

Even though the functionalized (7,5) SWCNT LEFETs remained fully operational, the reduction in network mobilities by approximately $\sim 50\%$ was relatively strong, given the moderate defect density of $n_d \sim 8 \mu\text{m}^{-1}$. Notably, these results are in good agreement with the mobility decrease by almost 50% for E_{11}^{*-} defects in (6,5) SWCNTs for a low degree of functionalization ($n_d \sim 3.5 \mu\text{m}^{-1}$) as discussed in Chapter 7.2 above. In contrast to that, low densities of bromoaryl and nitroaryl E_{11}^* defects ($n_d \sim 6 \mu\text{m}^{-1}$) introduced to (6,5) SWCNTs only led to a minor drop in network mobilities of less than 20% with respect to the unfunctionalized LEFETs (compare Chapters 4.3 and 5.5). To assess whether this low carrier mobility reduction upon E_{11}^* functionalization can be observed for other SWCNT species as well, future studies should be directed at (7,5) SWCNT network LEFETs with E_{11}^* defects. Overall, the data indicate that the impact of covalent functionalization on charge transport in small-diameter semiconducting SWCNTs might strongly depend on the defect binding configuration.

7.5 Impact of SWCNT chirality on defect–carrier interaction

Similar to the (6,5) SWCNT LEFETs in Chapter 7.3, the interaction of E_{11}^{*-} defects and charge carriers in functionalized (7,5) SWCNT transistors was studied by gate voltage-dependent PL spectroscopy under low-power, non-resonant cw excitation at 785 nm. Note that due to the weak defect emission from the functionalized (7,5) SWCNT networks described above, the LEFETs discussed here were fabricated from a dispersion with 2-bromoaniline E_{11}^{*-} defects with a higher degree of functionalization (defect density $n_d \sim 13.5 \mu\text{m}^{-1}$ as estimated by Raman spectroscopy).¹⁴⁷

Gate voltage-dependent PL spectra in electron accumulation are shown in Figure 7.9a. Two main peaks were observed in the spectra, corresponding to E_{11} and E_{11}^{*-} emission at ~ 1055 nm and ~ 1288 nm, respectively. The feature at ~ 1150 nm was assigned to residual (7,6) SWCNTs. All emission peaks decreased in intensity with increasing charge density in the network. Consistent with the results for (6,5) SWCNT networks, quenching of the defect emission was more pronounced than for mobile excitons, as evident from the normalized PL spectra in Figure 7.9b. It should be noted that E_{11} emission from (7,6) SWCNTs was more strongly quenched with respect to the (7,5) SWCNTs as well, thus indicating the predominant accumulation of charges in smaller-bandgap nanotube species in agreement with previous reports.^{232,273} At higher gate voltages, trion emission at ~ 1223 nm became significant. All trends were also reproduced for spectra acquired in hole accumulation.

The large red-shift of E_{11}^{*-} defects enabled a quantitative analysis of the spectra through fitting with several Gauss peaks to account for E_{11} , Y_1 (~ 1095 nm) and E_{11}^{*-} emission from (7,5) SWCNTs. At low gate voltages, the E_{11} PL from (7,6) SWCNTs was fitted as well,

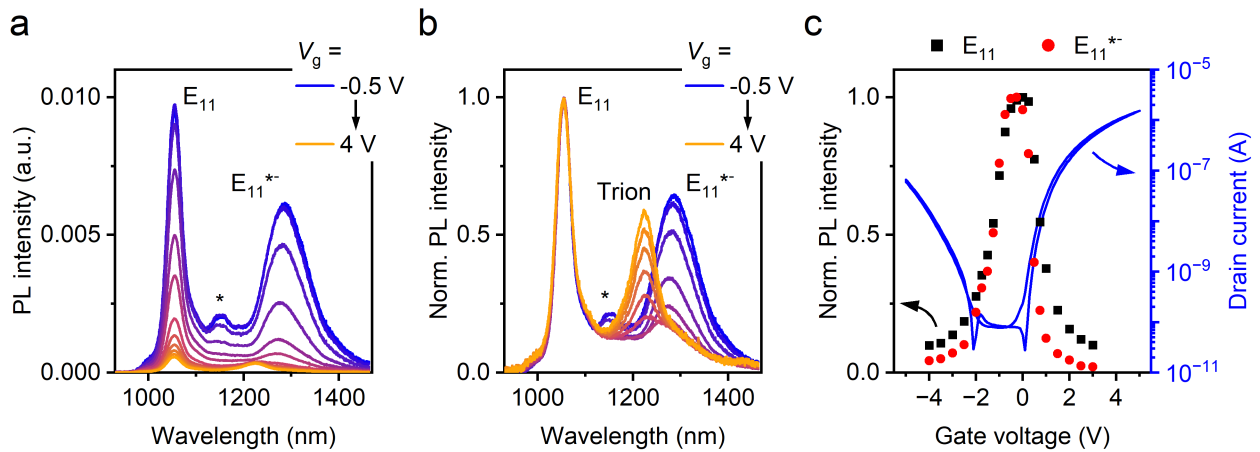


Figure 7.9: (a) Absolute and (b) normalized PL spectra (non-resonant cw excitation at 785 nm) of a (7,5) SWCNT network LEFET with E_{11}^{*-} defects at different gate voltages V_g in electron accumulation ($V_d = -10$ mV). At high voltages, trion emission becomes visible in the normalized spectra. The asterisk marks the E_{11} emission peak of residual (7,6) SWCNTs. (c) PL intensities of E_{11} (black squares) and E_{11}^{*-} (red circles) obtained from peak fits and normalized to their maxima. A transfer curve (linear regime, $V_d = -0.1$ V) of the LEFET measured at the same time is shown in blue (right axis).

whereas a peak fit for trion emission was included for higher voltages ($V_g > 1$ V and < -2 V). Extracted PL intensities of E_{11} and E_{11}^{*-} versus gate voltage are displayed in Figure 7.9c alongside a linear transfer curve of the LEFET. The minor shift of the transfer curve can be attributed to residual doping. As expected, maximum PL intensities were observed in the undoped state, and both emission features were progressively quenched upon accumulation of holes and electrons. Moreover, carrier-induced quenching was stronger for defect-localized compared to mobile excitons.

To further quantify this effect, the voltage-dependent PL intensities were fitted according to Equations 7.3 and 7.4 as shown in Figure 7.10. Clearly, the voltages at which the initial PL intensity had decreased by 50% ($V_{g,1/2}^h$ and $V_{g,1/2}^e$ for hole and electron accumulation, respectively) were lower for E_{11}^{*-} compared to E_{11} . As detailed above, the extraction of an energy difference in electronic levels from this data was not possible due to the lack of a reference potential. However, the relative difference in $\Delta V_{g,1/2}$ (*i.e.*, $V_{g,1/2}^e - V_{g,1/2}^h$) for E_{11} and E_{11}^{*-} may serve as an indicator for the impact of defects. As listed in Table 7.5, this voltage difference was 1.86 V for E_{11}^{*-} and 2.42 V for E_{11} . The $\sim 23\%$ reduction (0.56 V) in $\Delta V_{g,1/2}$ for the defect state versus E_{11} is very similar to the result obtained for E_{11}^{*-} -functionalized (6,5) SWCNTs (reduction by $\sim 24\%$ or 0.7 V, compare Chapter 7.3) and in good agreement with the $\sim 15\%$ reduction in electrochemical bandgap of E_{11}^{*-} with respect to E_{11} (0.850 eV versus 1.003 eV) reported for oxygen-doped (7,5) SWCNTs.¹⁵⁹

The comparable results for E_{11}^{*-} -functionalized (6,5) and (7,5) SWCNT networks are in agreement with the previous study by Shiraishi *et al.* on oxygen-functionalized SWCNTs

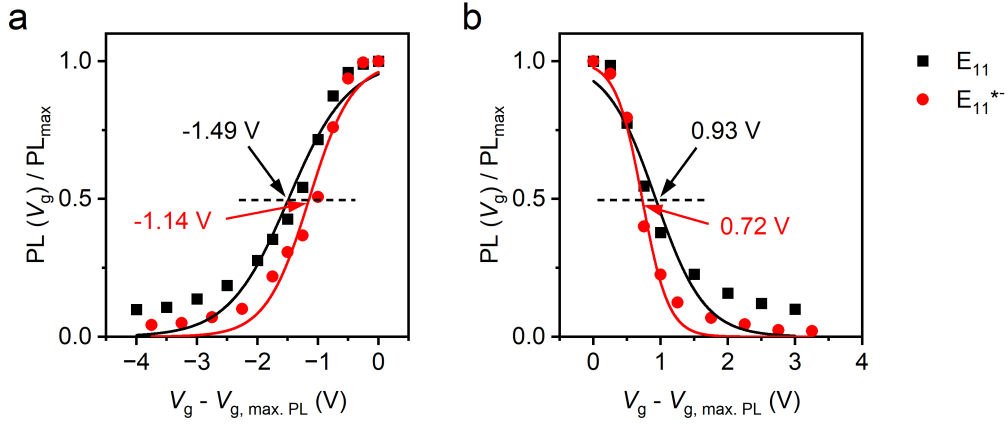


Figure 7.10: PL intensities of E_{11} (black squares) and E_{11}^{*-} (red circles) in (a) hole accumulation and (b) electron accumulation obtained from fits to the PL spectra (non-resonant cw excitation at 785 nm) of a (7,5) SWCNT network LEFET with E_{11}^{*-} defects and normalized to their maxima. Note that the x-axis was adjusted in order to shift the PL maximum to zero voltage. Solid lines are fits according to Equations 7.3 and 7.4. Gate voltages corresponding to half the initial PL intensity are indicated.

Table 7.5: Gate voltage-dependent PL quenching of E_{11} and E_{11}^{*-} in a (7,5) SWCNT network LEFET. Voltages corresponding to half the initial PL intensity in hole ($V_{g,1/2}^h$) and electron ($V_{g,1/2}^e$) accumulation and voltage differences $\Delta V_{g,1/2} = V_{g,1/2}^e - V_{g,1/2}^h$ were obtained from fits to the data in Figure 7.10 according to Equations 7.3 and 7.4.

State	$V_{g,1/2}^h$ (V)	$V_{g,1/2}^e$ (V)	$\Delta V_{g,1/2}$ (V)
E_{11}	-1.49	0.93	2.42
E_{11}^{*-}	-1.14	0.72	1.86

with different defect configurations (E_{11}^* ether defects and E_{11}^{*-} epoxide defects).¹⁵⁹ Their PL measurements of different small-diameter, functionalized SWCNTs under electrochemical doping indicated that for both defect types, the nanotube chirality dependence of HOMO and LUMO level energy shifts with respect to E_{11} was not significant. Likewise, a very similar reduction in electrochemical bandgap of E_{11}^* versus E_{11} was observed for different SWCNT species that were functionalized with aryldiazonium salts.¹⁵⁷

In summary, gate voltage-dependent PL spectroscopy of E_{11}^{*-} -functionalized (6,5) and (7,5) SWCNT networks indicated a comparable impact of luminescent defects on charge transport in different nanotube chiralities at least for these small-diameter species. The comparison with the results obtained for E_{11}^* defects (Chapters 4 and 5), however, suggested a strong effect of the defect binding configuration, in analogy to their very different exciton trapping potentials. As the optical trap depth for a given defect binding configuration decreases with increasing SWCNT diameter,^{16,23,139} differences in the impact of covalent functionalization on the nanotube charge transport properties might be observed for large-diameter SWCNTs.

7.6 Defect-state EL at telecommunication wavelengths

While the experiments described in this Chapter so far revealed the pronounced impact of E_{11}^* defects on charge transport in (6,5) and (7,5) SWCNT network transistors, it should be emphasized again that all devices remained fully functional and exhibited good ambipolar charge transport characteristics. As such, they should also allow for the investigation of defect population and emission under electrical excitation. To this end, SWCNT network LEFETs were operated in the ambipolar regime to simultaneously accumulate holes and electrons in the channel and generate a narrow carrier recombination and emission zone (see Chapter 2.3.2). Through variation of V_g and V_d , the emission zone was always positioned in the center of the channel for spectrally-resolved EL measurements in order to avoid potential effects of contact resistance or impact excitation at the electrodes. Furthermore, full comparability between spectra recorded for different currents, *e.g.*, with respect to their trion-to-exciton intensity ratio, was ensured by keeping the carrier density distribution in the channel balanced.¹³⁴

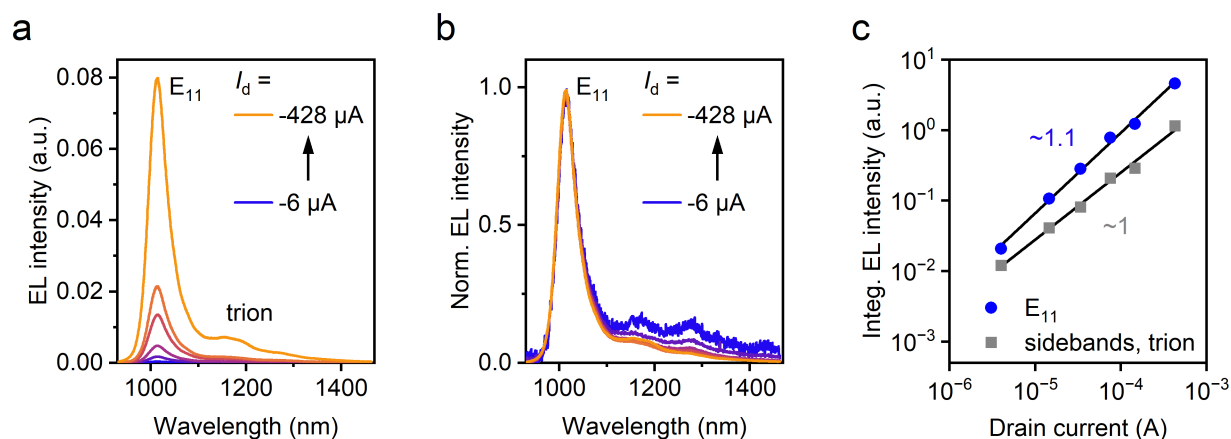


Figure 7.11: (a) Absolute and (b) normalized EL spectra of a pristine (6,5) SWCNT network LEFET in the ambipolar regime for different drain currents I_d . (c) Double-logarithmic plot of the integrated EL intensity *versus* drain current. Blue circles are E_{11} emission intensities, grey squares correspond to red-shifted sidebands and trion contributions (integration from 950–1100 nm and 1100–1400 nm, respectively). Black solid lines are linear fits to the data, and numbers indicate the corresponding slopes.

Figure 7.11a shows the EL spectra of a pristine (6,5) SWCNT network LEFET for different drain currents I_d . The E_{11} exciton emission was visible as a narrow peak at ~ 1015 nm with only very little unwanted emission from lower-energy sidebands thanks to substrate passivation with BCB (compare Chapter 6.6). An increase in I_d , and thus carrier recombination, led to an increase in EL intensity and the emergence of the trion emission peak at ~ 1165 nm in agreement with previous results.¹³³ The normalized spectra, however, were very similar over 2–3 orders of magnitude in current density, as shown in Figure 7.11b. A double-logarithmic plot of the integrated EL intensity of E_{11} emission as well as contributions from sidebands

and trion (integration between 950–1100 nm and 1100–1400 nm, respectively) *versus* drain current revealed linear correlations with slopes of ~ 1 , thus indicating that the measurements were conducted in the linear excitation regime (Figure 7.11c).

EL spectra of sp^3 -functionalized (6,5) SWCNT network LEFETs in the ambipolar regime exhibited two emission peaks at ~ 1015 nm and ~ 1280 nm, corresponding to emission from mobile E_{11} excitons and excitons localized at E_{11}^{*-} defects, respectively (Figure 7.12a). Importantly, the maximum of the defect emission peak was already located within the telecommunication O-band (1260–1360 nm). At low drain currents, more than 85% of photons were emitted through the defect channel. These results highlight the spectral tunability of defect emission that was made possible by controlling the binding configuration.²³ They further demonstrate the applicability of covalently functionalized SWCNT networks with E_{11}^{*-} defects in electrically-driven, NIR-emitting thin film devices.

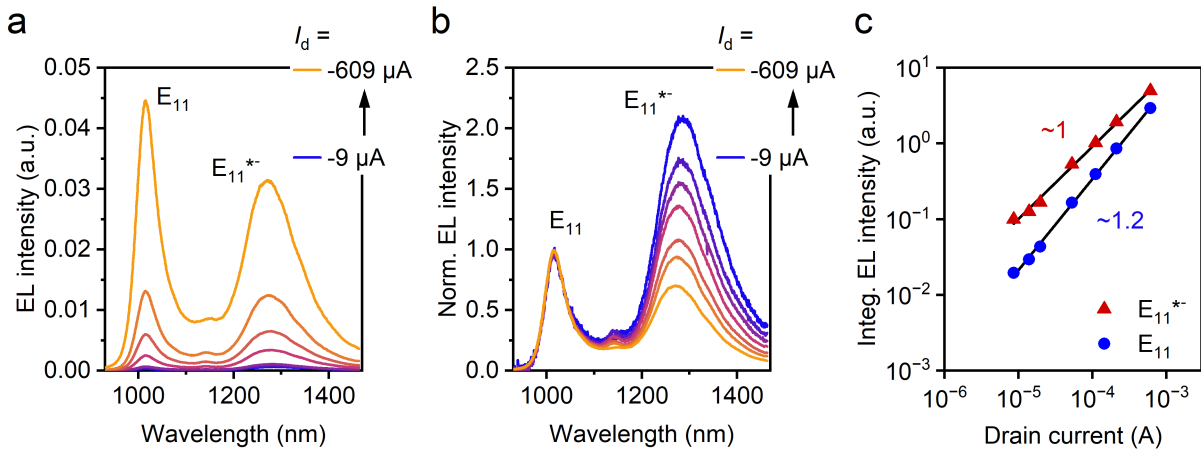


Figure 7.12: (a) Absolute and (b) normalized EL spectra of a (6,5) SWCNT network LEFET with E_{11}^{*-} defects in the ambipolar regime for different drain currents I_d . (c) Double-logarithmic plot of the integrated EL intensity *versus* drain current. Blue circles correspond to E_{11} emission, red triangles denote E_{11}^{*-} defect emission (integration from 950–1100 nm and 1150–1450 nm, respectively). Black solid lines are linear fits to the data, and numbers indicate the corresponding slopes.

Defect emission was observed over a wide current range, as shown in the E_{11} -normalized EL spectra in Figure 7.12b. It should be noted that the relative E_{11}^{*-} emission for low drain currents was substantially higher than in the PL spectrum in dispersion (compare Figure 7.2a). While this observation could be explained by the higher excitation density in pulsed PL experiments, and thus state-filling of deep E_{11}^{*-} exciton traps,¹⁵⁶ it is in striking contrast to the results obtained from EL spectroscopy of (6,5) SWCNT network FETs with E_{11}^{*-} defects (see Chapter 4.4). For the latter, E_{11}^{*-} defect emission in SWCNT thin films was significantly reduced compared to the dispersions.

However, in the emission spectra of diazonium-functionalized SWCNT networks, emission from E_{11}^{*-} defects – that were introduced in the functionalization reaction as a minority species – was quite prominent as well (compare, *e.g.*, Figure 4.7). Thus, it might be speculated whether the defect binding configuration (*i.e.*, optical trap depth) can account for the differences in defect emission intensities in dispersions *versus* thin films. Previously, discrepancies in relative E_{11}^* and E_{11}^{*-} emission intensities were observed in low-temperature PL spectra of individual SWCNTs that were deposited on glass or embedded in a polymer matrix, which was associated with substrate quenching.¹⁵⁸ It should be noted that the SWCNT network LEFETs with E_{11}^{*-} defects described here were fabricated on BCB-passivated glass substrates, whereas transistors with E_{11}^* in Chapter 4 were built on non-passivated glass. Overall, more detailed investigations are required to assess the spectral changes upon nanotube thin film deposition from dispersions, as well as the various external factors (*e.g.*, defect type, film morphology, nanotube–substrate interactions) governing the relative sp^3 defect and E_{11} emission intensities in functionalized SWCNT thin films.

In the normalized EL spectra in Figure 7.12b, a pronounced decrease in E_{11}^{*-} emission intensity with respect to E_{11} was observed with increasing I_d . A similar trend was found for the E_{11}^* EL peak in the spectra of bromoaryl-functionalized (6,5) SWCNT network FETs in Chapter 4.4 (compare Figure 4.8), albeit to a much lesser extent. Notably, linear correlations were found between the integrated EL emission of both E_{11} and E_{11}^{*-} features (integration 950–1100 nm and 1150–1450 nm, respectively) and the drain current in a double-logarithmic plot, as shown in Figure 7.12c. Thereby, state-filling of exciton traps can be ruled out as a possible cause.¹⁵⁶ This notion was further corroborated by the low instantaneous exciton densities on the order of 0.1 excitons per SWCNT for $I_d = -100 \mu\text{A}$, which were estimated analogous to Naber *et al.*³⁰⁵ assuming recombination of every injected carrier under exciton formation and an average exciton lifetime of 100 ps. An alternative explanation for the decrease in E_{11}^{*-} -to- E_{11} EL intensity with increasing drain currents could involve the predominant charge-induced quenching of defect-localized compared to mobile excitons, as already shown by gate voltage-dependent PL spectroscopy in Chapter 7.3. In agreement with the results from Chapters 4 and 5, this observation was ascribed to preferential accumulation of carriers at the defect sites. Interestingly, despite the defect EL quenching at higher currents being apparent from the spectra, no clear deviation from the linear relationship between integrated intensity and I_d (Figure 7.12c) was observed.

Even though defect EL from (6,5) SWCNT network LEFETs with E_{11}^{*-} defects was already located in the first telecommunication band, a further red-shift of the emission peak towards even longer wavelengths would be desired. To this end, EL spectroscopy was performed on LEFETs based on pristine and E_{11}^{*-} -functionalized (7,5) SWCNTs. Figure 7.13a shows the drain current-dependent EL spectra of pristine (7,5) SWCNT network LEFETs. Aside from the main E_{11} exciton peak of (7,5) SWCNTs at ~ 1055 nm, an additional peak corresponding

to emission from residual (7,6) SWCNTs was observed at ~ 1150 nm. Furthermore, trion emission from (7,5) SWCNTs (~ 1225 nm) was visible in the spectra for high current densities.¹³³ As expected, all peaks increased in intensity with increasing I_d , *i.e.*, higher carrier recombination. Normalized EL spectra are shown in Figure 7.13b. The slight decrease of the (7,6) SWCNT feature with respect to the E_{11} EL of (7,5) SWCNTs for increasing currents is in agreement with previous results that revealed carrier density-dependent current shares in polydisperse nanotube networks.^{232,273} At low carrier densities, charge transport predominantly occurs through small-bandgap species, which is reflected in a higher share of EL intensity.²³² For higher currents, the trion emission increased relatively to the E_{11} peak, which indicated the presence of excess charge carriers in the emission zone.^{133,134}

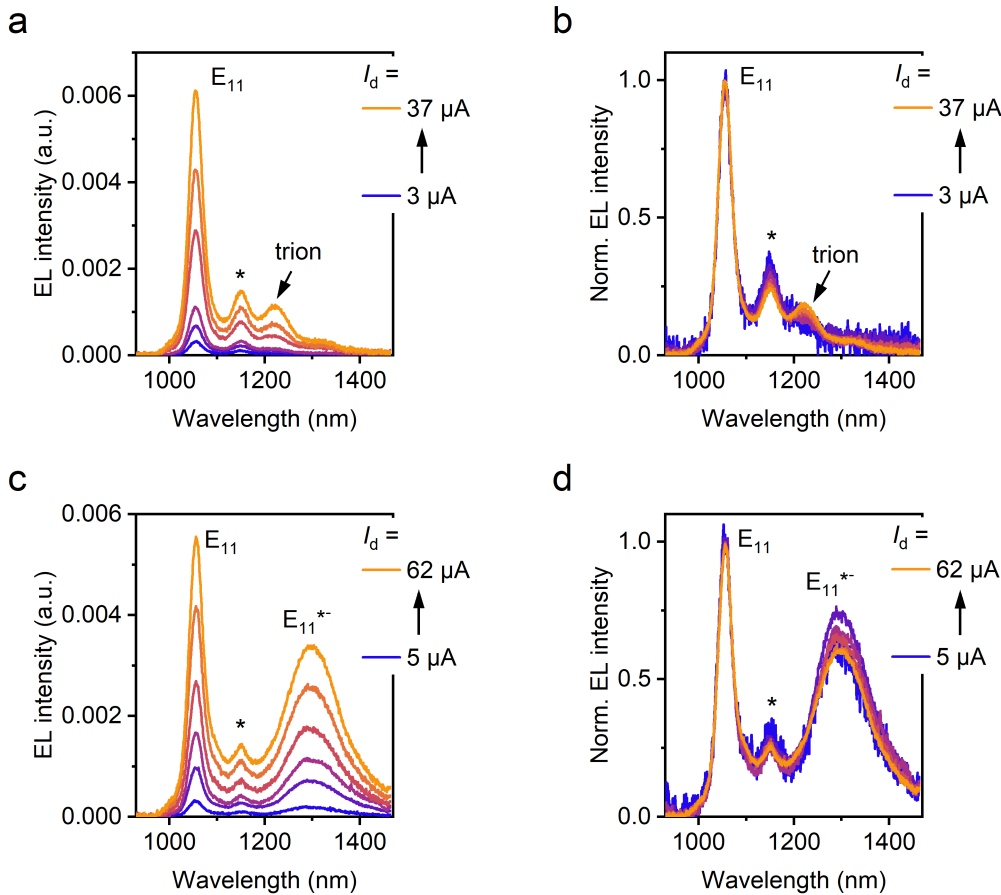


Figure 7.13: Absolute and normalized EL spectra of (a,b) a pristine (7,5) SWCNT network LEFET and (c,d) a (7,5) SWCNT network LEFET with E_{11}^{*-} defects in the ambipolar regime for different drain currents I_d . The asterisk marks the E_{11} peak of residual (7,6) SWCNTs.

The EL spectra of functionalized (7,5) SWCNT LEFETs displayed in Figure 7.13c showed two distinct emission features that are assigned to emission from E_{11} excitons (~ 1055 nm) and E_{11}^{*-} defects (~ 1300 nm). Again, a minor feature corresponding to EL from residual (7,6) SWCNTs was observed as well. The E_{11}^{*-} defect emission peak was red-shifted by another ~ 20 nm (~ 15 meV) with respect to the peak in the EL spectra of functionalized (6,5) SWCNT LEFETs (compare Figure 7.12). As confirmed by the normalized EL spectra

in Figure 7.13d, defect emission was stable for different drain currents and decreased only slightly for higher I_d relative to the E_{11} peak intensity. Even though the reduction in E_{11}^{*-} -to- E_{11} EL ratio with increasing drain current appears to be less pronounced than for the E_{11}^{*-} -functionalized (6,5) SWCNTs (compare Figure 7.12b), the direct comparison is hampered by the limited current range due to the lower mobilities.

Notably, defect-state EL with high spectral purity at ~ 1320 nm was reported very recently for transistors with individual functionalized (7,5) SWCNTs, which presents a major advancement towards the realization of electrically-pumped single-photon sources at telecommunication wavelengths based on nanotubes with luminescent defects.³⁰³ Overall, these results showcase the spectral tunability of sp^3 defect emission achieved by choice of SWCNT species and control over the defect binding configuration, which might enable the application of covalently functionalized SWCNTs in NIR-emitting devices.

7.7 Summary and conclusion

This Chapter demonstrated the realization of monochiral (6,5) and (7,5) SWCNT network LEFETs with E_{11}^{*-} defects that were introduced to toluene-dispersed nanotubes by employing a recently established, highly selective functionalization approach.²³ These E_{11}^{*-} defects are associated with a different binding configuration on the SWCNT lattice, which gives rise to a deeper exciton trap depth and consequently larger spectral red-shift compared to E_{11}^* defects. The excellent solution-processability of E_{11}^{*-} -functionalized SWCNTs allowed for the reproducible deposition of homogeneous SWCNT thin films on substrates *via* spin-coating and aerosol-jet printing, and thus device integration.

Electrical device characterization revealed a reduction in the carrier mobilities of SWCNT networks upon functionalization even for low defect densities that was more pronounced than previously observed for E_{11}^* defects (compare Chapters 4 and 5). These results point towards a strong impact of the defect binding configuration on charge transport in functionalized nanotubes. Charge density-dependent (time-resolved) PL spectroscopy corroborated efficient Auger quenching of defect-localized excitons mediated by charge carriers and indicated that E_{11}^{*-} states may act as shallow charge traps with a deeper trapping potential compared to E_{11}^* defects. This hypothesis should be tested in future studies on covalently functionalized SWCNT network transistors with different nanotube species. To unambiguously evaluate the impact of luminescent defects on charge transport in individual SWCNTs and thin films depending on the binding configuration and nanotube diameter, complementary experimental techniques such as time-resolved THz spectroscopy^{286,287} (compare Chapter 5) or microwave conductivity measurements^{283,284} are required. Furthermore, input from theory might contribute to a fundamental understanding of the optoelectronic properties of sp^3 -functionalized SWCNTs.

Despite the impact of sp^3 defects on charge transport, all devices exhibited high charge carrier mobilities, which enabled the observation of EL from E_{11}^{*-} defect states *via* ambipolar carrier recombination. Defect EL peaks were centered at ~ 1280 nm and ~ 1300 nm for LEFETs based on functionalized (6,5) and (7,5) SWCNT networks, respectively, which corresponds to emission within the first telecommunication wavelength band (O-band). Figure 7.14 gives an overview of the tailored emission spectra of sp^3 -functionalized SWCNT thin films in LEFETs under electrical excitation as demonstrated in this thesis.

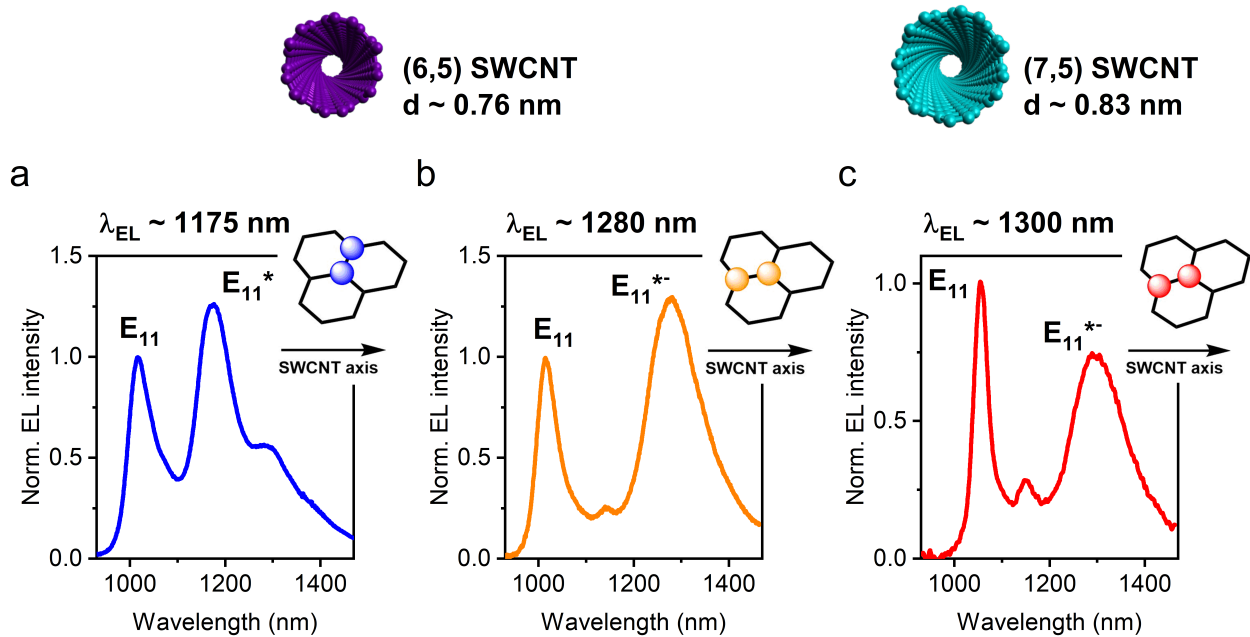


Figure 7.14: Wavelength-tunable EL from sp^3 defects in LEFETs with small-diameter, semiconducting SWCNT networks through choice of the nanotube species and control over the defect binding configuration. Representative normalized EL spectra of LEFETs with (a) aryldiazonium-functionalized (6,5) SWCNTs with E_{11}^* defects (data taken from Chapter 4 for comparison), (b) aniline-functionalized (6,5) SWCNTs with E_{11}^{*-} defects, and (c) aniline-functionalized (7,5) SWCNTs with E_{11}^{*-} defects. Insets show the hypothesized binding configurations of (a) E_{11}^* defects (*ortho-L*₉₀) and (b,c) E_{11}^{*-} defects (*ortho-L*₃₀).

The selective dispersion of (6,5) SWCNTs *via* polymer-wrapping with PFO-BPy and subsequent functionalization with an aromatic diazonium salt gave rise to E_{11}^* defect EL at ~ 1175 nm (Figure 7.14a), whereas the selective introduction of E_{11}^{*-} defects through functionalization with an aniline derivative resulted in defect EL at ~ 1280 nm (Figure 7.14b). As shown in the insets, these defects are hypothesized to differ by the arrangement of molecular fragments on the SWCNT lattice, which is the main factor governing their emission wavelength. Through E_{11}^{*-} -selective functionalization of (7,5) SWCNTs, which have a slightly larger diameter and were sorted *via* polymer-wrapping with PFO, a further emission red-shift and defect EL at ~ 1300 nm were accomplished (Figure 7.14c).

The results presented here highlight the tunability of the emission spectrum of covalently functionalized SWCNTs. Through combination of the diameter-dependent SWCNT optical transition energies and the defect binding configuration on the nanotube lattice, emission from SWCNTs with luminescent defects can in principle be shifted across the NIR spectral range.¹⁶⁰ By using larger-diameter SWCNT species, it should be possible to shift the defect emission wavelength into the C-band to enhance their application potential. Unfortunately, however, the monotonous decrease in optical trap depth of luminescent defects with increasing SWCNT diameter as well as the lower reactivity of large-diameter nanotubes due to lower strain make it increasingly difficult to achieve even more red-shifted defect emission.^{16,23,139} Overall, the demonstration of efficient defect-state luminescence in the telecommunication O-band under electrical excitation opens up new avenues for the application of covalently functionalized SWCNTs in light-emitting devices and as quantum emitters in the NIR.²¹

Chapter 8

Conclusion and Outlook

At the beginning of this thesis, the spectroscopic properties of luminescent sp^3 defects in semiconducting SWCNTs had been investigated substantially and were already well-understood. Several reports demonstrated the brightening of the total photoluminescence (PL) emission upon functionalization,^{16,22} the attachment of defect groups with various functionalities,^{169,170} and high-purity single-photon emission from defect-localized excitons in the near-infrared (NIR) at room temperature.¹⁹ Despite these advances, most studies exclusively focussed on SWCNT dispersions and defect-state emission following optical excitation. The application of functionalized SWCNTs in optoelectronic devices, however, requires a detailed understanding of defect population and emission under electrical excitation (electroluminescence, EL), which had yet to be demonstrated, and of their optical properties in thin films on substrates. Even though few initial studies were directed at the impact of nanotube functionalization on charge transport,^{178,179,185} a comprehensive picture of the interaction of charge carriers with sp^3 defects and defect-localized excitons was still missing. Better control over both spectroscopic and charge transport properties of SWCNTs with luminescent defects is a crucial step towards their application in electrically-driven, NIR-emitting devices.

Chapter 4 demonstrated that SWCNT networks with luminescent E_{11}^* defects can be integrated as charge transport and emission layers in ambipolar, light-emitting field-effect transistor (LEFET) structures with high carrier mobilities. A gradual, yet relatively low decrease in electron and hole mobilities was observed with increasing defect density. Nevertheless, fully operational devices with good switching behaviour were achieved even for highly functionalized SWCNT networks. These excellent electrical characteristics enabled the observation of EL from sp^3 defects that was red-shifted from the native E_{11} emission and stable over a wide range of currents. Furthermore, defect-state EL was tunable in intensity *via* the defect concentration, with $> 80\%$ of photons emitted through the defect channel for high degrees of functionalization. Unfortunately, only a limited increase in the overall EL emission efficiency was observed for LEFETs with a low sp^3 defect density.

As corroborated by charge modulation PL spectroscopy, defect sites directly interact with mobile charge carriers and thus, functionalized SWCNT segments actively contribute to the charge transport through the networks. Yet, static voltage-dependent PL and temperature-dependent transport measurements suggested that sp^3 defects might act as shallow charge traps that increase the intra-nanotube resistance. Charge carriers might become localized at the defects in a similar fashion as excitons, but can readily be detrapped from the shallow trapping potentials at room temperature, thus explaining the limited reduction in overall network mobilities. At temperatures below ~ 150 K, however, thermal detrapping is slowed down and the impact of the defects becomes larger. The observed differences in the temperature dependence of pristine and functionalized network mobilities indicated that charge transport in SWCNT networks is not solely limited by carrier hopping across inter-nanotube junctions, but that the contribution of intra-nanotube transport is significant as well.²⁶⁶

The impact of sp^3 defects on the intrinsic charge transport properties and carrier dynamics in SWCNTs was further investigated in Chapter 5 by using time-resolved optical-pump terahertz-probe (OPTP) spectroscopy. As a direct, contact-less and quantitative technique,³²⁰ OPTP proved to be ideally suited to study the local charge transport in covalently functionalized SWCNTs on short length scales of tens of nanometers and on sub-picosecond time scales. Measurements of individual SWCNTs in dispersion revealed a moderate decrease in intra-nanotube conductivity, charge carrier mobility, and carrier lifetime upon introduction of luminescent defects. Importantly, the minor reduction in local carrier mobility of $< 15\%$ for low and medium defect densities highlights the potential of functionalized SWCNTs to be used in applications that require both excellent spectroscopic and charge transport properties such as, *e.g.*, electrically-pumped single-photon sources.

Temperature-dependent OPTP measurements further showed that sp^3 defects diminish the increase of intra-nanotube carrier mobility due to reduced phonon scattering at lower temperatures,^{213,236} thus further corroborating the direct impact of covalent SWCNT functionalization on intrinsic charge transport. In agreement with the spectroscopic data from Chapter 4, the decrease in photoconductivity lifetime and temperature dependence of local carrier mobility upon functionalization as revealed by OPTP spectroscopy point towards charge carrier localization at luminescent defects. The comparable impact of functionalization on the short-range, intra-nanotube mobilities and long-range charge transport in SWCNT network transistors provide additional evidence for the contribution of intrinsic nanotube conductivity to the overall carrier mobility within the network. Overall, the combination of OPTP spectroscopy of SWCNT dispersions and films with measurements of nanotube network transistors corroborate that a superposition of intra-nanotube transport (affected by sp^3 defects) and inter-nanotube hopping (largely unaffected by functionalization) is required to adequately describe charge transport in randomly oriented SWCNT networks.^{188,266}

Aside from a fundamental understanding of charge transport in covalently functionalized SWCNTs, their application in light-emitting devices demands a high degree of control over their emission spectra when deposited on substrates. Owing to the sensitivity of nanotube excitons to their local environment,^{96,352} however, the spectroscopic properties of SWCNTs in thin films on surfaces can be markedly different to those in dispersion, and their emission spectra are often compromised by peak broadening and emission from lower-energy sidebands.¹¹² To this end, Chapter 6 introduced substrate surface passivation with the cross-linked, low dielectric constant polymer BCB (B-staged divinyltetramethylsiloxane-bis-benzocyclobutene) as a powerful approach to accomplish near-intrinsic luminescence from pristine and functionalized (6,5) SWCNT thin films. BCB passivation strongly reduced unwanted sideband emission (especially from the Y_1 band, whose origin remained elusive thus far) that was found to emerge upon annealing of SWCNT thin films on commonly used glass and Si/SiO₂ substrates. As corroborated by Raman and temperature-dependent PL

spectroscopy, the Y_1 sideband was attributed to shallow excitonic traps that originate from nanotube lattice defects. Such defects most likely originate from the interaction of SWCNTs with the polar, oxygen-containing terminal groups on the substrate surfaces. Gaining control over SWCNT functionalization with luminescent oxygen defects on reactive oxidic surfaces, *e.g.*, with spatial precision under light irradiation,³⁷⁵ might thus open up new possibilities to tune their emission properties.

A comparable effect to BCB passivation was observed for (6,5) SWCNTs deposited on high-quality flakes of hexagonal boron nitride (*h*-BN) that have been widely used as encapsulation layers to study the intrinsic photophysics of 2D materials^{362,364} and individual nanotubes.^{126,127} However, the scalability of this approach over larger areas is limited, and *h*-BN crystals with the required quality are not easily accessible.²⁹¹ In contrast to that, BCB is a commercially available material with applications in semiconductor industry,³⁶⁸ and can be easily applied over large areas *via* a simple spin-on and annealing process. The realization of pristine and functionalized SWCNT network LEFETs with near-intrinsic EL spectra and enhanced emission efficiencies on BCB-passivated glass substrates highlighted the compatibility of BCB with standard processing steps employed in semiconductor device fabrication. As manifested in the narrowband defect emission peaks, BCB passivation greatly improves the application potential of SWCNT thin films with luminescent sp^3 defects as solid-state NIR emitters.

As a further step to control the spectrally diverse emission from functionalized SWCNT thin films and devices, Chapter 7 demonstrated the realization of SWCNT network LEFETs with further red-shifted E_{11}^{*-} defects. These defects were introduced to small-diameter (6,5) and (7,5) SWCNTs *via* a recently developed approach²³ with a high degree of selectivity towards a specific defect binding configuration on the nanotube lattice and thus, emission wavelength. Despite a moderate decrease in charge carrier mobilities upon E_{11}^{*-} -functionalization, all devices exhibited excellent ambipolar transport and switching behaviour. The impact of E_{11}^{*-} defects on charge transport in SWCNT networks was more pronounced compared to E_{11}^* defects in Chapters 4 and 5, which points towards an influence of the defect structure on the interaction with carriers and possibly the magnitude of charge trapping.

LEFETs with functionalized (6,5) and (7,5) SWCNT networks on BCB-passivated substrates exhibited efficient, narrowband E_{11}^{*-} defect EL emission in the telecommunication O-band at ~ 1280 nm and ~ 1300 nm, respectively. These results highlight the tunability of the emission spectrum of covalently functionalized SWCNTs through combination of the nanotube diameter-dependent optical transition energies with the selective introduction of luminescent defects with a specific binding configuration. Utilizing this approach, the emission wavelength can be shifted across the NIR spectral range, which greatly enhances the potential of defect-tailored SWCNTs for applications as electrically-driven NIR emitters, for example in light-emitting thin film devices¹⁰ and quantum light sources.^{21,387}

In summary, this thesis explored and revealed the high sensitivity of defect-localized excitons and their emission characteristics towards changes in the local environment, and especially the presence of charge carriers. To gain deeper insights, future studies should be directed at short-channel transistors³¹⁹ with individual functionalized SWCNTs or aligned nanotube arrays.³⁸⁸ This way, the impact of luminescent defects on intra-nanotube charge transport can be studied without the question of inter-tube junction resistance. Electrical measurements of a large number of such transistors could enable the unambiguous and quantitative analysis of the changes in intrinsic nanotube conductivity upon covalent functionalization depending on the defect binding configuration and SWCNT chirality. Furthermore, this approach allows for fundamental investigations of defect-state emission characteristics in active optoelectronic devices under electrical excitation.³⁰³

In addition to the top-gate LEFET structure employed in this thesis, SWCNT networks can also be integrated in water-gated transistors where they may act as transducing layers for sensing applications.³⁸⁹⁻³⁹¹ To achieve selectivity towards a specific analyte, a variety of non-covalent nanotube functionalization methods, *e.g.*, by wrapping with DNA³⁹² or π - π stacking with pyrenes attached to nanobodies,³⁹³ were previously reported. On the other hand, covalent attachment of defect moieties with specific recognition units presents a powerful approach to enhance the sensing capabilities of SWCNTs, as was demonstrated for single-nanotube transistors functionalized with nucleic acid strands for DNA detection.³⁹⁴ Hence, future studies should focus on the highly versatile concept of using covalent defects in SWCNTs as anchor groups for the conjugation of biomolecules.³⁹⁵ In addition to changes in the gating behaviour of functionalized SWCNTs, the emission intensity and wavelength of sp^3 defects were previously shown to respond to molecular recognition events at the attached defect group¹⁶⁹ or the presence of biomolecular analytes,³⁹⁶ and thus could be utilized as highly sensitive probes. Monitoring the optical response as well as the subtle changes in nanotube conductance upon defect-analyte interactions might enable the realization of dual-signal optical and electrical biosensors based on water-gated transistors with sp^3 -functionalized SWCNTs.

Moreover, the high degrees of photon antibunching and single-photon indistinguishability that were observed for functionalized SWCNTs integrated in plasmonic nanocavities²⁰ hold promise for their application as solid-state single-photon emitters for quantum computing or quantum cryptography. Covalent functionalization of SWCNTs with larger diameters and consequently smaller bandgaps, ideally through selective introduction of deep E_{11}^{*-} exciton traps,²³ will shift their emission wavelength further to the telecommunication C-band, which dramatically increases their application potential. Given the recent demonstration of defect-state EL from single-nanotube transistors,³⁰³ the integration of functionalized SWCNTs into more complex photonic structures^{387,397} will enable the realization of electrically-pumped, room-temperature single-photon emission from luminescent nanotube defects at telecom-

munication wavelengths. Overall, the tailored covalent functionalization of semiconducting SWCNTs has opened a wide range of applications as well as new ways to investigate their fundamental charge transport and optical properties.

Bibliography

- (1) Senior, J. M., *Optical Fiber Communications: Principles and Practice*; Pearson Education: Harlow, 2009.
- (2) Sillard, P.; Molin, D. In *Fibre Optic Communication*, Venghaus, H., Grote, N., Eds.; Springer: Cham, 2017, pp 49–102.
- (3) Grote, N.; Möhrle, M.; Ortsiefer, M. In *Fibre Optic Communication*, Venghaus, H., Grote, N., Eds.; Springer: Cham, 2017, pp 103–149.
- (4) Aharonovich, I.; Englund, D.; Toth, M. *Nat. Photonics* **2016**, *10*, 631–641.
- (5) Franklin, A. D. *Science* **2015**, *349*, aab2750.
- (6) Zaumseil, J. *Adv. Electron. Mater.* **2019**, *5*, 1800514.
- (7) Zaumseil, J. *Semicond. Sci. Technol.* **2015**, *30*, 074001.
- (8) Wieland, S.; El Yumin, A. A.; Gotthardt, J. M.; Zaumseil, J. *J. Phys. Chem. C* **2023**, *127*, 3112–3122.
- (9) Graf, A.; Held, M.; Zakharko, Y.; Tropic, L.; Gather, M. C.; Zaumseil, J. *Nat. Mater.* **2017**, *16*, 911–917.
- (10) Graf, A.; Murawski, C.; Zakharko, Y.; Zaumseil, J.; Gather, M. C. *Adv. Mater.* **2018**, *30*, 1706711.
- (11) Brozena, A. H.; Kim, M.; Powell, L. R.; Wang, Y. *Nat. Rev. Chem.* **2019**, *3*, 375–392.
- (12) Shiraki, T.; Miyauchi, Y.; Matsuda, K.; Nakashima, N. *Acc. Chem. Res.* **2020**, *53*, 1846–1859.
- (13) Gifford, B. J.; Kilina, S.; Htoon, H.; Doorn, S. K.; Tretiak, S. *Acc. Chem. Res.* **2020**, *53*, 1791–1801.
- (14) Zaumseil, J. *Adv. Opt. Mater.* **2022**, *10*, 2101576.
- (15) Hartmann, N. F.; Yalcin, S. E.; Adamska, L.; Hároz, E. H.; Ma, X.; Tretiak, S.; Htoon, H.; Doorn, S. K. *Nanoscale* **2015**, *7*, 20521–20530.
- (16) Piao, Y.; Meany, B.; Powell, L. R.; Valley, N.; Kwon, H.; Schatz, G. C.; Wang, Y. *Nat. Chem.* **2013**, *5*, 840–845.
- (17) Saha, A.; Gifford, B. J.; He, X.; Ao, G.; Zheng, M.; Kataura, H.; Htoon, H.; Kilina, S.; Tretiak, S.; Doorn, S. K. *Nat. Chem.* **2018**, *10*, 1089–1095.
- (18) Ma, X.; Hartmann, N. F.; Baldwin, J. K. S.; Doorn, S. K.; Htoon, H. *Nat. Nanotechnol.* **2015**, *10*, 671–675.

- (19) He, X.; Hartmann, N. F.; Ma, X.; Kim, Y.; Ihly, R.; Blackburn, J. L.; Gao, W.; Kono, J.; Yomogida, Y.; Hirano, A.; Tanaka, T.; Kataura, H.; Htoon, H.; Doorn, S. K. *Nat. Photonics* **2017**, *11*, 577.
- (20) Luo, Y.; He, X.; Kim, Y.; Blackburn, J. L.; Doorn, S. K.; Htoon, H.; Strauf, S. *Nano Lett.* **2019**, *19*, 9037–9044.
- (21) He, X.; Htoon, H.; Doorn, S. K.; Pernice, W. H. P.; Pyatkov, F.; Krupke, R.; Jeantet, A.; Chassagneux, Y.; Voisin, C. *Nat. Mater.* **2018**, *17*, 663–670.
- (22) Berger, F. J.; Lüttgens, J.; Nowack, T.; Kutsch, T.; Lindenthal, S.; Kistner, L.; Müller, C. C.; Bongartz, L. M.; Lumsargis, V. A.; Zakharko, Y.; Zaumseil, J. *ACS Nano* **2019**, *13*, 9259–9269.
- (23) Settele, S.; Berger, F. J.; Lindenthal, S.; Zhao, S.; El Yumin, A. A.; Zorn, N. F.; Asyuda, A.; Zharnikov, M.; Högele, A.; Zaumseil, J. *Nat. Commun.* **2021**, *12*, 2119.
- (24) Hirsch, A. *Nat. Mater.* **2010**, *9*, 868–871.
- (25) Kroto, H. W.; Heath, J. R.; O'Brien, S. C.; Curl, R. F.; Smalley, R. E. *Nature* **1985**, *318*, 162–163.
- (26) Buseck, P. R.; Tsipursky, S. J.; Hettich, R. *Science* **1992**, *257*, 215–217.
- (27) Cami, J.; Bernard-Salas, J.; Peeters, E.; Malek, S. E. *Science* **2010**, *329*, 1180–1182.
- (28) Partha, R.; Conyers, J. *Int. J. Nanomedicine* **2009**, *4*, 261–275.
- (29) Nelson, J. *Mater. Today* **2011**, *14*, 462–470.
- (30) Novoselov, K. S.; Geim, A. K.; Morozov, S. V.; Jiang, D.; Zhang, Y.; Dubonos, S. V.; Grigorieva, I. V.; Firsov, A. A. *Science* **2004**, *306*, 666–669.
- (31) Geim, A. K.; Novoselov, K. S. *Nat. Mater.* **2007**, *6*, 183–191.
- (32) Bonaccorso, F.; Sun, Z.; Hasan, T.; Ferrari, A. C. *Nat. Photonics* **2010**, *4*, 611–622.
- (33) Balandin, A. A. *Nat. Mater.* **2011**, *10*, 569–581.
- (34) Iijima, S. *Nature* **1991**, *354*, 56–58.
- (35) Avouris, P.; Chen, Z.; Perebeinos, V. *Nat. Nanotechnol.* **2007**, *2*, 605–615.
- (36) Avouris, P.; Freitag, M.; Perebeinos, V. *Nat. Photonics* **2008**, *2*, 341–350.
- (37) Wong, H.-S. P.; Akinwande, D., *Carbon nanotube and graphene device physics*; Cambridge University Press: Cambridge, 2011.
- (38) Dresselhaus, M. S.; Dresselhaus, G.; Saito, R. *Carbon* **1995**, *33*, 883–891.
- (39) Charlier, J.-C.; Blase, X.; Roche, S. *Rev. Mod. Phys.* **2007**, *79*, 677–732.
- (40) Odom, T. W.; Huang, J.-L.; Kim, P.; Lieber, C. M. *J. Phys. Chem. B* **2000**, *104*, 2794–2809.
- (41) Ao, G.; Streit, J. K.; Fagan, J. A.; Zheng, M. *J. Am. Chem. Soc.* **2016**, *138*, 16677–16685.
- (42) Kataura, H.; Kumazawa, Y.; Maniwa, Y.; Ohtsuka, Y.; Sen, R.; Suzuki, S.; Achiba, Y. *Carbon* **2000**, *38*, 1691–1697.
- (43) Prasek, J.; Drbohlavova, J.; Chomoucka, J.; Hubalek, J.; Jasek, O.; Adam, V.; Kizek, R. *J. Mater. Chem.* **2011**, *21*, 15872–15884.

- (44) Kim, K. S.; Cota-Sanchez, G.; Kingston, C. T.; Imris, M.; Simard, B.; Soucy, G. *J. Phys. Chem.* **2007**, *40*, 2375.
- (45) Guo, T.; Nikolaev, P.; Thess, A.; Colbert, D. T.; Smalley, R. E. *Chem. Phys. Lett.* **1995**, *243*, 49–54.
- (46) Journet, C.; Maser, W. K.; Bernier, P.; Loiseau, A.; de la Chapelle, M. L.; Lefrant, S.; Deniard, P.; Lee, R.; Fischer, J. E. *Nature* **1997**, *388*, 756–758.
- (47) Kitiyanan, B.; Alvarez, W. E.; Harwell, J. H.; Resasco, D. E. *Chem. Phys. Lett.* **2000**, *317*, 497–503.
- (48) Bachilo, S. M.; Balzano, L.; Herrera, J. E.; Pompeo, F.; Resasco, D. E.; Weisman, R. B. *J. Am. Chem. Soc.* **2003**, *125*, 11186–11187.
- (49) Lolli, G.; Zhang, L.; Balzano, L.; Sakulchaicharoen, N.; Tan, Y.; Resasco, D. E. *J. Phys. Chem. B* **2006**, *110*, 2108–2115.
- (50) Liu, B.; Wu, F.; Gui, H.; Zheng, M.; Zhou, C. *ACS Nano* **2017**, *11*, 31–53.
- (51) Yang, F. et al. *Nature* **2014**, *510*, 522–524.
- (52) Yang, F.; Wang, X.; Zhang, D.; Qi, K.; Yang, J.; Xu, Z.; Li, M.; Zhao, X.; Bai, X.; Li, Y. *J. Am. Chem. Soc.* **2015**, *137*, 8688–8691.
- (53) Sanchez-Valencia, J. R.; Dienel, T.; Gröning, O.; Shorubalko, I.; Mueller, A.; Jansen, M.; Amsharov, K.; Ruffieux, P.; Fasel, R. *Nature* **2014**, *512*, 61–64.
- (54) Coleman, J. N. *Adv. Funct. Mater.* **2009**, *19*, 3680–3695.
- (55) Bergin, S. D.; Nicolosi, V.; Streich, P. V.; Giordani, S.; Sun, Z.; Windle, A. H.; Ryan, P.; Niraj, N. P. P.; Wang, Z.-T. T.; Carpenter, L.; Blau, W. J.; Boland, J. J.; Hamilton, J. P.; Coleman, J. N. *Adv. Mater.* **2008**, *20*, 1876–1881.
- (56) Bergin, S. D.; Sun, Z.; Streich, P.; Hamilton, J.; Coleman, J. N. *J. Phys. Chem. C* **2010**, *114*, 231–237.
- (57) Janas, D. *Mater. Chem. Front.* **2018**, *2*, 36–63.
- (58) O’Connell, M. J.; Bachilo, S. M.; Huffman, C. B.; Moore, V. C.; Strano, M. S.; Haroz, E. H.; Rialon, K. L.; Boul, P. J.; Noon, W. H.; Kittrell, C.; Ma, J.; Hauge, R. H.; Weisman, R. B.; Smalley, R. E. *Science* **2002**, *297*, 593–596.
- (59) Zheng, M.; Jagota, A.; Semke, E. D.; Diner, B. A.; McLean, R. S.; Lustig, S. R.; Richardson, R. E.; Tassi, N. G. *Nat. Mater.* **2003**, *2*, 338–342.
- (60) Hersam, M. C. *Nat. Nanotechnol.* **2008**, *3*, 387–394.
- (61) Arnold, M. S.; Green, A. A.; Hulvat, J. F.; Stupp, S. I.; Hersam, M. C. *Nat. Nanotechnol.* **2006**, *1*, 60–65.
- (62) Ghosh, S.; Bachilo, S. M.; Weisman, R. B. *Nat. Nanotechnol.* **2010**, *5*, 443–450.
- (63) Liu, H.; Nishide, D.; Tanaka, T.; Kataura, H. *Nat. Commun.* **2011**, *2*, 309.
- (64) Yomogida, Y.; Tanaka, T.; Zhang, M.; Yudasaka, M.; Wei, X.; Kataura, H. *Nat. Commun.* **2016**, *7*, 12056.
- (65) Krupke, R.; Hennrich, F.; Löhneysen, H. v.; Kappes, M. M. *Science* **2003**, *301*, 344–347.

- (66) Fagan, J. A. *Nanoscale Adv.* **2019**, *1*, 3307–3324.
- (67) Khripin, C. Y.; Fagan, J. A.; Zheng, M. *J. Am. Chem. Soc.* **2013**, *135*, 6822–6825.
- (68) Li, H.; Gordeev, G.; Garrity, O.; Reich, S.; Flavel, B. S. *ACS Nano* **2019**, *13*, 2567–2578.
- (69) Li, H.; Gordeev, G.; Garrity, O.; Peyyety, N. A.; Selvasundaram, P. B.; Dehm, S.; Krupke, R.; Cambre, S.; Wenseleers, W.; Reich, S.; Zheng, M.; Fagan, J. A.; Flavel, B. S. *ACS Nano* **2019**, *14*, 948–963.
- (70) Li, H.; Sims, C. M.; Kang, R.; Biedermann, F.; Fagan, J. A.; Flavel, B. S. *Carbon* **2023**, *204*, 475–483.
- (71) Wei, L.; Flavel, B. S.; Li, W.; Krupke, R.; Chen, Y. *Nanoscale* **2017**, *9*, 11640–11646.
- (72) Nish, A.; Hwang, J.-Y.; Doig, J.; Nicholas, R. J. *Nat. Nanotechnol.* **2007**, *2*, 640–646.
- (73) Samanta, S. K.; Fritsch, M.; Scherf, U.; Gomulya, W.; Bisri, S. Z.; Loi, M. A. *Acc. Chem. Res.* **2014**, *47*, 2446–2456.
- (74) Gao, J.; Loi, M. A.; Carvalho, E. J. F. d.; dos Santos, M. C. *ACS Nano* **2011**, *5*, 3993–3999.
- (75) Gomulya, W.; Costanzo, G. D.; Carvalho, E. J. F. d.; Bisri, S. Z.; Derenskyi, V.; Fritsch, M.; Fröhlich, N.; Allard, S.; Gordiichuk, P.; Herrmann, A.; Marrink, S. J.; dos Santos, M. C.; Scherf, U.; Loi, M. A. *Adv. Mater.* **2013**, *25*, 2948–2956.
- (76) Ozawa, H.; Ide, N.; Fujigaya, T.; Niidome, Y.; Nakashima, N. *Chem. Lett.* **2011**, *40*, 239–241.
- (77) Hennrich, F.; Li, W.; Fischer, R.; Lebedkin, S.; Krupke, R.; Kappes, M. M. *ACS Nano* **2016**, *10*, 1888–1895.
- (78) Schießl, S. P.; Fröhlich, N.; Held, M.; Gannott, F.; Schweiger, M.; Forster, M.; Scherf, U.; Zaumseil, J. *ACS Appl. Mater. Interfaces* **2015**, *7*, 682–689.
- (79) Lee, H. W. et al. *Nat. Commun.* **2011**, *2*, 541.
- (80) Lemasson, F. A.; Strunk, T.; Gerstel, P.; Hennrich, F.; Lebedkin, S.; Barner-Kowollik, C.; Wenzel, W.; Kappes, M. M.; Mayor, M. *J. Am. Chem. Soc.* **2011**, *133*, 652–655.
- (81) Lei, T.; Pitner, G.; Chen, X.; Hong, G.; Park, S.; Hayoz, P.; Weitz, R. T.; Wong, H.-S. P.; Bao, Z. *Adv. Electron. Mater.* **2016**, *2*, 1500299.
- (82) Jakubka, F.; Schießl, S. P.; Martin, S.; Englert, J. M.; Hauke, F.; Hirsch, A.; Zaumseil, J. *ACS Macro Lett.* **2012**, *1*, 815–819.
- (83) Hwang, J.-Y.; Nish, A.; Doig, J.; Douven, S.; Chen, C.-W.; Chen, L.-C.; Nicholas, R. J. *J. Am. Chem. Soc.* **2008**, *130*, 3543–3553.
- (84) Ding, J.; Li, Z.; Lefebvre, J.; Du, X.; Malenfant, P. R. L. *J. Phys. Chem. C* **2016**, *120*, 21946–21954.
- (85) Brohmann, M.; Rother, M.; Schießl, S. P.; Preis, E.; Allard, S.; Scherf, U.; Zaumseil, J. *J. Phys. Chem. C* **2018**, *122*, 19886–19896.
- (86) Naumov, A. V.; Tsyboulski, D. A.; Bachilo, S. M.; Weisman, R. B. *Chem. Phys.* **2013**, *422*, 255–263.

- (87) Graf, A.; Zakharko, Y.; Schiebl, S. P.; Backes, C.; Pfohl, M.; Flavel, B. S.; Zaumseil, J. *Carbon* **2016**, *105*, 593–599.
- (88) Reich, S.; Maultzsch, J.; Thomsen, C.; Ordejón, P. *Phys. Rev. B* **2002**, *66*, 035412.
- (89) Saito, R.; Dresselhaus, G.; Dresselhaus, M. S. *Phys. Rev. B* **2000**, *61*, 2981–2990.
- (90) Saito, R.; Fujita, M.; Dresselhaus, G.; Dresselhaus, M. S. *Appl. Phys. Lett.* **1992**, *60*, 2204–2206.
- (91) Kleiner, A.; Eggert, S. *Phys. Rev. B* **2001**, *64*, 113402.
- (92) Wilder, J. W. G.; Venema, L. C.; Rinzler, A. G.; Smalley, R. E.; Dekker, C. *Nature* **1998**, *391*, 59–62.
- (93) Schiebl, S. P.; Vries, X. d.; Rother, M.; Massé, A.; Brohmann, M.; Bobbert, P. A.; Zaumseil, J. *Phys. Rev. Mater.* **2017**, *1*, 046003.
- (94) Statz, M.; Schneider, S.; Berger, F. J.; Lai, L.; Wood, W. A.; Abdi-Jalebi, M.; Leingang, S.; Himmel, H.-J.; Zaumseil, J.; Siringhaus, H. *ACS Nano* **2020**, *14*, 15552–15565.
- (95) Weisman, R. B.; Bachilo, S. M. *Nano Lett.* **2003**, *3*, 1235–1238.
- (96) Amori, A. R.; Hou, Z.; Krauss, T. D. *Annu. Rev. Phys. Chem.* **2018**, *69*, 81–99.
- (97) Blancon, J.-C.; Paillet, M.; Tran, H. N.; Than, X. T.; Guebrou, S. A.; Ayari, A.; Miguel, A. S.; Phan, N.-M.; Zahab, A.-A.; Sauvajol, J.-L.; Fatti, N. D.; Vallée, F. *Nat. Commun.* **2013**, *4*, 2542.
- (98) Kane, C. L.; Mele, E. J. *Phys. Rev. Lett.* **2003**, *90*, 207401.
- (99) Plentz, F.; Ribeiro, H. B.; Jorio, A.; Strano, M. S.; Pimenta, M. A. *Phys. Rev. Lett.* **2005**, *95*, 247401.
- (100) Spataru, C. D.; Ismail-Beigi, S.; Benedict, L. X.; Louie, S. G. *Phys. Rev. Lett.* **2004**, *92*, 077402.
- (101) Wang, F.; Dukovic, G.; Brus, L. E.; Heinz, T. F. *Science* **2005**, *308*, 838–841.
- (102) Maultzsch, J.; Pomraenke, R.; Reich, S.; Chang, E.; Prezzi, D.; Ruini, A.; Molinari, E.; Strano, M. S.; Thomsen, C.; Lienau, C. *Phys. Rev. B* **2005**, *72*, 6680.
- (103) Dresselhaus, M. S.; Dresselhaus, G.; Saito, R.; Jorio, A. *Annu. Rev. Phys. Chem.* **2007**, *58*, 719–747.
- (104) Mortimer, I. B.; Nicholas, R. J. *Phys. Rev. Lett.* **2007**, *98*, 027404.
- (105) Blackburn, J. L.; Holt, J. M.; Irurzun, V. M.; Resasco, D. E.; Rumbles, G. *Nano Lett.* **2012**, *12*, 1398–1403.
- (106) Perebeinos, V.; Tersoff, J.; Avouris, P. *Nano Lett.* **2005**, *5*, 2495–2499.
- (107) Soavi, G.; Scotognella, F.; Lanzani, G.; Cerullo, G. *Adv. Opt. Mater.* **2016**, *4*, 1670–1688.
- (108) Harrah, D. M.; Schneck, J. R.; Green, A. A.; Hersam, M. C.; Ziegler, L. D.; Swan, A. K. *ACS Nano* **2011**, *5*, 9898–9906.
- (109) Chen, J.; Perebeinos, V.; Freitag, M.; Tsang, J.; Fu, Q.; Liu, J.; Avouris, P. *Science* **2005**, *310*, 1171–1174.

- (110) Misewich, J. A.; Martel, R.; Avouris, P.; Tsang, J. C.; Heinze, S.; Tersoff, J. *Science* **2003**, *300*, 783–786.
- (111) Jones, M.; Engtrakul, C.; Metzger, W. K.; Ellingson, R. J.; Nozik, A. J.; Heben, M. J.; Rumbles, G. *Phys. Rev. B* **2005**, *71*, 115426.
- (112) Kadria-Vili, Y.; Bachilo, S. M.; Blackburn, J. L.; Weisman, R. B. *J. Phys. Chem. C* **2016**, *120*, 23898–23904.
- (113) Lüttgens, J. M.; Berger, F. J.; Zaumseil, J. *ACS Photonics* **2020**, *8*, 182–193.
- (114) Amori, A. R.; Rossi, J. E.; Landi, B. J.; Krauss, T. D. *J. Phys. Chem. C* **2018**, *122*, 3599–3607.
- (115) Tumiel, T. M.; Amin, M.; Krauss, T. D. *J. Phys. Chem. C* **2021**, *125*, 25022–25029.
- (116) Hertel, T.; Himmelein, S.; Ackermann, T.; Stich, D.; Crochet, J. *ACS Nano* **2010**, *4*, 7161–7168.
- (117) Crochet, J. J.; Duque, J. G.; Werner, J. H.; Lounis, B.; Cognet, L.; Doorn, S. K. *Nano Lett.* **2012**, *12*, 5091–5096.
- (118) Birkmeier, K.; Hertel, T.; Hartschuh, A. *Nat. Commun.* **2022**, *13*, 6290.
- (119) Mehlenbacher, R. D.; McDonough, T. J.; Grechko, M.; Wu, M.-Y.; Arnold, M. S.; Zanni, M. T. *Nat. Commun.* **2015**, *6*, 321.
- (120) Mehlenbacher, R. D.; Wang, J.; Kearns, N. M.; Shea, M. J.; Flach, J. T.; McDonough, T. J.; Wu, M.-Y.; Arnold, M. S.; Zanni, M. T. *J. Phys. Chem. Lett.* **2016**, 2024–2031.
- (121) Ohno, Y.; Iwasaki, S.; Murakami, Y.; Kishimoto, S.; Maruyama, S.; Mizutani, T. *Phys. Status Solidi B* **2007**, *244*, 4002–4005.
- (122) Larsen, B. A.; Deria, P.; Holt, J. M.; Stanton, I. N.; Heben, M. J.; Therien, M. J.; Blackburn, J. L. *J. Am. Chem. Soc.* **2012**, *134*, 12485–12491.
- (123) Ishii, A.; Yoshida, M.; Kato, Y. K. *Phys. Rev. B* **2015**, *91*, 125427.
- (124) Schweiger, M.; Zakharko, Y.; Gannott, F.; Grimm, S. B.; Zaumseil, J. *Nanoscale* **2015**, *7*, 16715–16720.
- (125) Sarpkaya, I.; Zhang, Z.; Walden-Newman, W.; Wang, X.; Hone, J.; Wong, C. W.; Strauf, S. *Nat. Commun.* **2013**, *4*, 2152.
- (126) Noé, J. C.; Nutz, M.; Reschauer, J.; Morell, N.; Tsioutsios, I.; Reserbat-Plantey, A.; Watanabe, K.; Taniguchi, T.; Bachtold, A.; Högele, A. *Nano Lett.* **2018**, *18*, 4136–4140.
- (127) Fang, N.; Otsuka, K.; Ishii, A.; Taniguchi, T.; Watanabe, K.; Nagashio, K.; Kato, Y. K. *ACS Photonics* **2020**, *7*, 1773–1779.
- (128) Kinder, J. M.; Mele, E. J. *Phys. Rev. B* **2008**, *78*, 155429.
- (129) Perebeinos, V.; Avouris, P. *Phys. Rev. Lett.* **2008**, *101*, 057401.
- (130) Matsunaga, R.; Matsuda, K.; Kanemitsu, Y. *Phys. Rev. Lett.* **2011**, *106*, 037404.
- (131) Yoshida, M.; Popert, A.; Kato, Y. K. *Phys. Rev. B* **2016**, *93*, 041402.
- (132) Park, J. S.; Hirana, Y.; Mouri, S.; Miyauchi, Y.; Nakashima, N.; Matsuda, K. *J. Am. Chem. Soc.* **2012**, *134*, 14461–14466.

- (133) Jakubka, F.; Grimm, S. B.; Zakharko, Y.; Gannott, F.; Zaumseil, J. *ACS Nano* **2014**, *8*, 8477–8486.
- (134) El Yumin, A. A.; Zorn, N. F.; Berger, F. J.; Heimfarth, D.; Zaumseil, J. *Carbon* **2023**, *202*, 547–553.
- (135) Zhao, H.; Mazumdar, S. *Phys. Rev. Lett.* **2004**, *93*, 157402.
- (136) Cognet, L.; Tsyboulski, D. A.; Rocha, J.-D. R.; Doyle, C. D.; Tour, J. M.; Weisman, R. B. *Science* **2007**, *316*, 1465–1468.
- (137) Cambré, S.; Santos, S. M.; Wenseleers, W.; Nugraha, A. R. T.; Saito, R.; Cognet, L.; Lounis, B. *ACS Nano* **2012**, *6*, 2649–2655.
- (138) Ghosh, S.; Bachilo, S. M.; Simonette, R. A.; Beckingham, K. M.; Weisman, R. B. *Science* **2010**, *330*, 1656–1659.
- (139) Hartmann, N. F.; Velizhanin, K. A.; Haroz, E. H.; Kim, M.; Ma, X.; Wang, Y.; Htoon, H.; Doorn, S. K. *ACS Nano* **2016**, *10*, 8355–8365.
- (140) Kilina, S.; Ramirez, J.; Tretiak, S. *Nano Lett.* **2012**, *12*, 2306–2312.
- (141) Sykes, M. E.; Kim, M.; Wu, X.; Wiederrecht, G. P.; Peng, L.; Wang, Y.; Gosztola, D. J.; Ma, X. *ACS Nano* **2019**, *13*, 13264–13270.
- (142) Kim, M.; Adamska, L.; Hartmann, N. F.; Kwon, H.; Liu, J.; Velizhanin, K. A.; Piao, Y.; Powell, L. R.; Meany, B.; Doorn, S. K.; Tretiak, S.; Wang, Y. *J. Phys. Chem. C* **2016**, *120*, 11268–11276.
- (143) Spataru, C. D.; Ismail-Beigi, S.; Capaz, R. B.; Louie, S. G. *Phys. Rev. Lett.* **2005**, *95*, 247402.
- (144) He, X.; Velizhanin, K. A.; Bullard, G.; Bai, Y.; Olivier, J.-H.; Hartmann, N. F.; Gifford, B. J.; Kilina, S.; Tretiak, S.; Htoon, H.; Therien, M. J.; Doorn, S. K. *ACS Nano* **2018**, *12*, 8060–8070.
- (145) Miyauchi, Y.; Iwamura, M.; Mouri, S.; Kawazoe, T.; Ohtsu, M.; Matsuda, K. *Nat. Photonics* **2013**, *7*, 715–719.
- (146) Kozawa, D.; Wu, X.; Ishii, A.; Fortner, J.; Otsuka, K.; Xiang, R.; Inoue, T.; Maruyama, S.; Wang, Y.; Kato, Y. K. *Nat. Commun.* **2022**, *13*, 2814.
- (147) Sebastian, F. L.; Zorn, N. F.; Settele, S.; Lindenthal, S.; Berger, F. J.; Bendel, C.; Li, H.; Flavel, B. S.; Zaumseil, J. *J. Phys. Chem. Lett.* **2022**, *13*, 3542–3548.
- (148) Aharoni, A.; Oron, D.; Banin, U.; Rabani, E.; Jortner, J. *Phys. Rev. Lett.* **2008**, *100*, 057404.
- (149) Wen, Q.; Kershaw, S. V.; Kalytchuk, S.; Zhovtiuk, O.; Reckmeier, C.; Vasilevskiy, M. I.; Rogach, A. L. *ACS Nano* **2016**, *10*, 4301–4311.
- (150) He, X.; Sun, L.; Gifford, B. J.; Tretiak, S.; Piryatinski, A.; Li, X.; Htoon, H.; Doorn, S. K. *Nanoscale* **2019**, *11*, 9125–9132.
- (151) Gifford, B. J.; Kilina, S.; Htoon, H.; Doorn, S. K.; Tretiak, S. *J. Phys. Chem. C* **2018**, *122*, 1828–1838.

- (152) Ma, X.; Adamska, L.; Yamaguchi, H.; Yalcin, S. E.; Tretiak, S.; Doorn, S. K.; Htoon, H. *ACS Nano* **2014**, *8*, 10782–10789.
- (153) Kwon, H.; Kim, M.; Nutz, M.; Hartmann, N. F.; Perrin, V.; Meany, B.; Hofmann, M. S.; Clark, C. W.; Htoon, H.; Doorn, S. K.; Högele, A.; Wang, Y. *ACS Cent. Sci.* **2019**, *5*, 1786–1794.
- (154) Nutz, M.; Zhang, J.; Kim, M.; Kwon, H.; Wu, X.; Wang, Y.; Högele, A. *Nano Lett.* **2019**, *19*, 7078–7084.
- (155) Kim, Y.; Velizhanin, K. A.; He, X.; Sarpkaya, I.; Yomogida, Y.; Tanaka, T.; Kataura, H.; Doorn, S. K.; Htoon, H. *J. Phys. Chem. Lett.* **2019**, *10*, 1423–1430.
- (156) Iwamura, M.; Akizuki, N.; Miyauchi, Y.; Mouri, S.; Shaver, J.; Gao, Z.; Cognet, L.; Lounis, B.; Matsuda, K. *ACS Nano* **2014**, *8*, 11254–11260.
- (157) Shiraishi, T.; Shiraki, T.; Nakashima, N. *Nanoscale* **2017**, *9*, 16900–16907.
- (158) He, X.; Gifford, B. J.; Hartmann, N. F.; Ihly, R.; Ma, X.; Kilina, S. V.; Luo, Y.; Shayan, K.; Strauf, S.; Blackburn, J. L.; Tretiak, S.; Doorn, S. K.; Htoon, H. *ACS Nano* **2017**, *11*, 10785–10796.
- (159) Shiraishi, T.; Juhász, G.; Shiraki, T.; Akizuki, N.; Miyauchi, Y.; Matsuda, K.; Nakashima, N. *J. Phys. Chem. C* **2016**, *120*, 15632–15639.
- (160) Wang, P.; Fortner, J.; Luo, H.; Klos, J.; Wu, X.; Qu, H.; Chen, F.; Li, Y.; Wang, Y. *J. Am. Chem. Soc.* **2022**, *144*, 13234–13241.
- (161) Kwon, H.; Furmanchuk, A.; Kim, M.; Meany, B.; Guo, Y.; Schatz, G. C.; Wang, Y. *J. Am. Chem. Soc.* **2016**, *138*, 6878–6885.
- (162) Gifford, B. J.; He, X.; Kim, M.; Kwon, H.; Saha, A.; Sifain, A. E.; Wang, Y.; Htoon, H.; Kilina, S.; Doorn, S. K.; Tretiak, S. *Chem. Mat.* **2019**, *31*, 6950–6961.
- (163) Ma, X.; Baldwin, J. K. S.; Hartmann, N. F.; Doorn, S. K.; Htoon, H. *Adv. Funct. Mater.* **2015**, *25*, 6157–6164.
- (164) Janas, D. *Mater. Horiz.* **2020**, *7*, 2860–2881.
- (165) Lin, C.-W.; Bachilo, S. M.; Zheng, Y.; Tsedev, U.; Huang, S.; Weisman, R. B.; Belcher, A. M. *Nat. Commun.* **2019**, *10*, 2874.
- (166) Wu, X.; Kim, M.; Kwon, H.; Wang, Y. *Angew. Chem. Int. Ed.* **2018**, *57*, 648–653.
- (167) He, X.; Kevlishvili, I.; Murcek, K.; Liu, P.; Star, A. *ACS Nano* **2021**, *15*, 4833–4844.
- (168) Glückert, J. T.; Adamska, L.; Schinner, W.; Hofmann, M. S.; Doorn, S. K.; Tretiak, S.; Högele, A. *Phys. Rev. B* **2018**, *98*, 195413.
- (169) Shiraki, T.; Onitsuka, H.; Shiraishi, T.; Nakashima, N. *Chem. Commun.* **2016**, *52*, 12972–12975.
- (170) Kwon, H.; Kim, M.; Meany, B.; Piao, Y.; Powell, L. R.; Wang, Y. *J. Phys. Chem. C* **2015**, *119*, 3733–3739.
- (171) Powell, L. R.; Piao, Y.; Wang, Y. *J. Phys. Chem. Lett.* **2016**, *7*, 3690–3694.
- (172) Luo, H.-B.; Wang, P.; Wu, X.; Qu, H.; Ren, X.; Wang, Y. *ACS Nano* **2019**, *13*, 8417–8424.

- (173) Zheng, Y.; Bachilo, S. M.; Weisman, R. B. *ACS Nano* **2019**, *14*, 715–723.
- (174) Zhang, Y.; Valley, N.; Brozena, A. H.; Piao, Y.; Song, X.; Schatz, G. C.; Wang, Y. *J. Phys. Chem. Lett.* **2013**, *4*, 826–830.
- (175) Deng, S.; Zhang, Y.; Brozena, A. H.; Mayes, M. L.; Banerjee, P.; Chiou, W.-A.; Rubloff, G. W.; Schatz, G. C.; Wang, Y. *Nat. Commun.* **2011**, *2*, 382.
- (176) Maeda, Y.; Minami, S.; Takehana, Y.; Dang, J.-S.; Aota, S.; Matsuda, K.; Miyauchi, Y.; Yamada, M.; Suzuki, M.; Zhao, R.-S.; Zhao, X.; Nagase, S. *Nanoscale* **2016**, *8*, 16916–16921.
- (177) Yu, B.; Naka, S.; Aoki, H.; Kato, K.; Yamashita, D.; Fujii, S.; Kato, Y. K.; Fujigaya, T.; Shiraki, T. *ACS Nano* **2022**, *16*, 21452–21461.
- (178) Wilson, H.; Ripp, S.; Prisbrey, L.; Brown, M. A.; Sharf, T.; Myles, D. J. T.; Blank, K. G.; Minot, E. D. *J. Phys. Chem. C* **2016**, *120*, 1971–1976.
- (179) Bouilly, D.; Hon, J.; Daly, N. S.; Trocchia, S.; Vernick, S.; Yu, J.; Warren, S.; Wu, Y.; Gonzalez, R. L.; Shepard, K. L.; Nuckolls, C. *Nano Lett.* **2016**, *16*, 4679–4685.
- (180) Lee, Y.-S.; Nardelli, M. B.; Marzari, N. *Phys. Rev. Lett.* **2005**, *95*, 076804.
- (181) Goldsmith, B. R.; Coroneus, J. G.; Khalap, V. R.; Kane, A. A.; Weiss, G. A.; Collins, P. G. *Science* **2007**, *315*, 77–81.
- (182) Goldsmith, B. R.; Coroneus, J. G.; Kane, A. A.; Weiss, G. A.; Collins, P. G. *Nano Lett.* **2008**, *8*, 189–194.
- (183) Sorgenfrei, S.; Chiu, C.-y.; Gonzalez, R. L.; Yu, Y.-J.; Kim, P.; Nuckolls, C.; Shepard, K. L. *Nat. Nanotechnol.* **2011**, *6*, 126–132.
- (184) Lee, Y.; Trocchia, S. M.; Warren, S. B.; Young, E. F.; Vernick, S.; Shepard, K. L. *ACS Nano* **2018**, *12*, 9922–9930.
- (185) Bouilly, D.; Cabana, J.; Martel, R. *Appl. Phys. Lett.* **2012**, *101*, 053116.
- (186) Hills, G.; Lau, C.; Wright, A.; Fuller, S.; Bishop, M. D.; Srimani, T.; Kanhaiya, P.; Ho, R.; Amer, A.; Stein, Y.; Murphy, D.; Arvind; Chandrakasan, A.; Shulaker, M. M. *Nature* **2019**, *572*, 595–602.
- (187) Liang, X.; Xia, J.; Dong, G.; Tian, B.; Peng, L. *Top. Curr. Chem.* **2016**, *374*, 80.
- (188) Zorn, N. F.; Zaumseil, J. *Appl. Phys. Rev.* **2021**, *8*, 041318.
- (189) Zaumseil, J.; Sirringhaus, H. *Chem. Rev.* **2007**, *107*, 1296–1323.
- (190) Klauk, H. *Chem. Soc. Rev.* **2010**, *39*, 2643–2666.
- (191) Kang, M. S.; Frisbie, C. D. *ChemPhysChem* **2013**, *14*, 1547–1552.
- (192) Chua, L.-L.; Ho, P. K. H.; Sirringhaus, H.; Friend, R. H. *Appl. Phys. Lett.* **2004**, *84*, 3400–3402.
- (193) Choi, H. H.; Cho, K.; Frisbie, C. D.; Sirringhaus, H.; Podzorov, V. *Nat. Mater.* **2017**, *17*, 2–7.
- (194) Klauk, H. *Adv. Electron. Mater.* **2018**, *4*, 1700474.
- (195) Pesavento, P. V.; Puntambekar, K. P.; Frisbie, C. D.; McKeen, J. C.; Ruden, P. P. *J. Appl. Phys.* **2006**, *99*, 094504.

- (196) Choi, H. H.; Rodionov, Y. I.; Paterson, A. F.; Panidi, J.; Saranin, D.; Kharlamov, N.; Didenko, S. I.; Anthopoulos, T. D.; Cho, K.; Podzorov, V. *Adv. Funct. Mater.* **2018**, *28*, 1707105.
- (197) Schießl, S. P.; Rother, M.; Lüttgens, J.; Zaumseil, J. *Appl. Phys. Lett.* **2017**, *111*, 193301.
- (198) Chua, L.-L.; Zaumseil, J.; Chang, J.-F.; Ou, E. C.-W.; Ho, P. K.-H.; Sirringhaus, H.; Friend, R. H. *Nature* **2005**, *434*, 194–199.
- (199) Smits, E. C. P.; Anthopoulos, T. D.; Setayesh, S.; van Veenendaal, E.; Coehoorn, R.; Blom, P. W. M.; de Boer, B.; de Leeuw, D. M. *Phys. Rev. B* **2006**, *73*, 205316.
- (200) Zaumseil, J. *Adv. Funct. Mater.* **2020**, *30*, 1905269.
- (201) Kemerink, M.; Charrier, D. S. H.; Smits, E. C. P.; Mathijssen, S. G. J.; de Leeuw, D. M.; Janssen, R. A. J. *Appl. Phys. Lett.* **2008**, *93*, 033312.
- (202) Zaumseil, J.; Friend, R. H.; Sirringhaus, H. *Nat. Mater.* **2006**, *5*, 69–74.
- (203) Zaumseil, J.; Kline, R. J.; Sirringhaus, H. *Appl. Phys. Lett.* **2008**, *92*, 073304.
- (204) Hepp, A.; Heil, H.; Weise, W.; Ahles, M.; Schmechel, R.; von Seggern, H. *Phys. Rev. Lett.* **2003**, *91*, 157406.
- (205) Hotta, S.; Yamao, T.; Bisri, S. Z.; Takenobu, T.; Iwasa, Y. *J. Mater. Chem. C* **2014**, *2*, 965–980.
- (206) Zaumseil, J.; Donley, C. L.; Kim, J.-S.; Friend, R. H.; Sirringhaus, H. *Adv. Mater.* **2006**, *18*, 2708–2712.
- (207) Schornbaum, J.; Zakharko, Y.; Held, M.; Thiemann, S.; Gannott, F.; Zaumseil, J. *Nano Lett.* **2015**, *15*, 1822–1828.
- (208) Ross, J. S.; Klement, P.; Jones, A. M.; Ghimire, N. J.; Yan, J.; Mandrus, D. G.; Taniguchi, T.; Watanabe, K.; Kitamura, K.; Yao, W.; Cobden, D. H.; Xu, X. *Nat. Nanotechnol.* **2014**, *9*, 268–272.
- (209) Freitag, M.; Chen, J.; Tersoff, J.; Tsang, J. C.; Fu, Q.; Liu, J.; Avouris, P. *Phys. Rev. Lett.* **2004**, *93*, 076803.
- (210) Zaumseil, J.; Ho, X.; Guest, J. R.; Wiederrecht, G. P.; Rogers, J. A. *ACS Nano* **2009**, *3*, 2225–2234.
- (211) Muccini, M. *Nat. Mater.* **2006**, *5*, 605–613.
- (212) Franklin, A. D.; Hersam, M. C.; Wong, H. S. P. *Science* **2022**, *378*, 726–732.
- (213) Zhou, X.; Park, J.-Y.; Huang, S.; Liu, J.; McEuen, P. L. *Phys. Rev. Lett.* **2005**, *95*, 146805.
- (214) Franklin, A. D.; Luisier, M.; Han, S.-J.; Tulevski, G.; Breslin, C. M.; Gignac, L.; Lundstrom, M. S.; Haensch, W. *Nano Lett.* **2012**, *12*, 758–762.
- (215) Cao, Q.; Han, S.-j.; Tulevski, G. S.; Zhu, Y.; Lu, D. D.; Haensch, W. *Nat. Nanotechnol.* **2013**, *8*, 180–186.
- (216) Liu, L.; Han, J.; Xu, L.; Zhou, J.; Zhao, C.; Ding, S.; Shi, H.; Xiao, M.; Ding, L.; Ma, Z.; Jin, C.; Zhang, Z.; Peng, L.-M. *Science* **2020**, *368*, 850–856.

- (217) Lu, S.; Zheng, J.; Cardenas, J. A.; Williams, N. X.; Lin, Y.-C.; Franklin, A. D. *ACS Appl. Mater. Interfaces* **2020**, *12*, 43083–43089.
- (218) Rother, M.; Brohmann, M.; Yang, S.; Grimm, S. B.; Schießl, S. P.; Graf, A.; Zaumseil, J. *Adv. Electron. Mater.* **2017**, *3*, 1700080.
- (219) Kim, B.; Jang, S.; Geier, M. L.; Prabhumirashi, P. L.; Hersam, M. C.; Dodabalapur, A. *Nano Lett.* **2014**, *14*, 3683–3687.
- (220) Bucella, S. G.; Salazar-Rios, J. M.; Derenskyi, V.; Fritsch, M.; Scherf, U.; Loi, M. A.; Caironi, M. *Adv. Electron. Mater.* **2016**, *2*, 1600094.
- (221) Lau, P. H.; Takei, K.; Wang, C.; Ju, Y.; Kim, J.; Yu, Z.; Takahashi, T.; Cho, G.; Javey, A. *Nano Lett.* **2013**, *13*, 3864–3869.
- (222) Gotthardt, J. M.; Schneider, S.; Brohmann, M.; Leingang, S.; Sauter, E.; Zharnikov, M.; Himmel, H.-J.; Zaumseil, J. *ACS Appl. Electron. Mater.* **2021**, *3*, 804–812.
- (223) Qian, Q.; Li, G.; Jin, Y.; Liu, J.; Zou, Y.; Jiang, K.; Fan, S.; Li, Q. *ACS Nano* **2014**, *8*, 9597–9605.
- (224) Ding, J.; Li, Z.; Lefebvre, J.; Cheng, F.; Dubey, G.; Zou, S.; Finnie, P.; Hrdina, A.; Scoles, L.; Lopinski, G. P.; Kingston, C. T.; Simard, B.; Malenfant, P. R. L. *Nanoscale* **2014**, *6*, 2328–2339.
- (225) Liu, L.; Ding, L.; Zhong, D.; Han, J.; Wang, S.; Meng, Q.; Qiu, C.; Zhang, X.; Peng, L.-M.; Zhang, Z. *ACS Nano* **2019**, *13*, 2526–2535.
- (226) Cao, Q.; Kim, H.-s.; Pimparkar, N.; Kulkarni, J. P.; Wang, C.; Shim, M.; Roy, K.; Alam, M. A.; Rogers, J. A. *Nature* **2008**, *454*, 495–500.
- (227) Cui, X.; Freitag, M.; Martel, R.; Brus, L.; Avouris, P. *Nano Lett.* **2003**, *3*, 783–787.
- (228) Heinze, S.; Tersoff, J.; Martel, R.; Derycke, V.; Appenzeller, J.; Avouris, P. *Phys. Rev. Lett.* **2002**, *89*, 106801.
- (229) Chen, Z.; Appenzeller, J.; Knoch, J.; Lin, Y.-m.; Avouris, P. *Nano Lett.* **2005**, *5*, 1497–1502.
- (230) Adam, E.; Aguirre, C. M.; Marty, L.; St-Antoine, B. C.; Meunier, F.; Desjardins, P.; Ménard, D.; Martel, R. *Nano Lett.* **2008**, *8*, 2351–2355.
- (231) Jakubka, F.; Backes, C.; Gannott, F.; Mundloch, U.; Hauke, F.; Hirsch, A.; Zaumseil, J. *ACS Nano* **2013**, *7*, 7428–7435.
- (232) Rother, M.; Schießl, S. P.; Zakharko, Y.; Gannott, F.; Zaumseil, J. *ACS Appl. Mater. Interfaces* **2016**, *8*, 5571–5579.
- (233) Liang, S.; Wei, N.; Ma, Z.; Wang, F.; Liu, H.; Wang, S.; Peng, L.-M. *ACS Photonics* **2017**, *4*, 435–442.
- (234) Xiang, L.; Zhang, H.; Dong, G.; Zhong, D.; Han, J.; Liang, X.; Zhang, Z.; Peng, L.-M.; Hu, Y. *Nat. Electron.* **2018**, *1*, 237–245.
- (235) Javey, A.; Guo, J.; Wang, Q.; Lundstrom, M.; Dai, H. *Nature* **2003**, *424*, 654–657.
- (236) Perebeinos, V.; Tersoff, J.; Avouris, P. *Phys. Rev. Lett.* **2005**, *94*, 086802.

- (237) Ilani, S.; Donev, L. A. K.; Kindermann, M.; McEuen, P. L. *Nat. Phys.* **2006**, *2*, 687–691.
- (238) Shimotani, H.; Tsuda, S.; Yuan, H.; Yomogida, Y.; Moriya, R.; Takenobu, T.; Yanagi, K.; Iwasa, Y. *Adv. Funct. Mater.* **2014**, *24*, 3305–3311.
- (239) Perebeinos, V.; Tersoff, J.; Avouris, P. *Nano Lett.* **2006**, *6*, 205–208.
- (240) Rosenblatt, S.; Yaish, Y.; Park, J.; Gore, J.; Sazonova, V.; McEuen, P. L. *Nano Lett.* **2002**, *2*, 869–872.
- (241) Cao, Q.; Xia, M.; Kocabas, C.; Shim, M.; Rogers, J. A.; Rotkin, S. V. *Appl. Phys. Lett.* **2007**, *90*, 023516.
- (242) Nan, C.-W.; Shen, Y.; Ma, J. *Annu. Rev. Mater. Res.* **2010**, *40*, 131–151.
- (243) Behnam, A.; Guo, J.; Ural, A. *J. Appl. Phys.* **2007**, *102*, 044313.
- (244) Islam, A. E.; Rogers, J. A.; Alam, M. A. *Adv. Mater.* **2015**, *27*, 7908–7937.
- (245) Perebeinos, V.; Rotkin, S. V.; Petrov, A. G.; Avouris, P. *Nano Lett.* **2009**, *9*, 312–316.
- (246) Lee, S.-H.; Xu, Y.; Khim, D.; Park, W.-T.; Kim, D.-Y.; Noh, Y.-Y. *ACS Appl. Mater. Interfaces* **2016**, *8*, 32421–32431.
- (247) Held, M.; Schiebl, S. P.; Miehler, D.; Gannott, F.; Zaumseil, J. *Appl. Phys. Lett.* **2015**, *107*, 083301.
- (248) Hwang, D. K.; Fuentes-Hernandez, C.; Kim, J. B.; Potscavage, W. J.; Kippelen, B. *Org. Electron.* **2011**, *12*, 1108–1113.
- (249) Scuratti, F.; Salazar-Rios, J. M.; Luzio, A.; Kowalski, S.; Allard, S.; Jung, S.; Scherf, U.; Loi, M. A.; Caironi, M. *Adv. Funct. Mater.* **2021**, *31*, 2006895.
- (250) Mirka, B.; Rice, N. A.; Williams, P.; Tousignant, M. N.; Boileau, N. T.; Bodnaryk, W. J.; Fong, D.; Adronov, A.; Lessard, B. H. *ACS Nano* **2021**, *15*, 8252–8266.
- (251) Norton-Baker, B.; Ihly, R.; Gould, I. E.; Avery, A. D.; Owczarczyk, Z. R.; Ferguson, A. J.; Blackburn, J. L. *ACS Energy Lett.* **2016**, *1*, 1212–1220.
- (252) Chortos, A.; Pochorovski, I.; Lin, P.; Pitner, G.; Yan, X.; Gao, T. Z.; To, J. W. F.; Lei, T.; Will, J. W.; Wong, H. S. P.; Bao, Z. *ACS Nano* **2017**, *11*, 5660–5669.
- (253) Joo, Y.; Brady, G. J.; Kanimozhi, C.; Ko, J.; Shea, M. J.; Strand, M. T.; Arnold, M. S.; Gopalan, P. *ACS Appl. Mater. Interfaces* **2017**, *9*, 28859–28867.
- (254) Nirmalraj, P. N.; Lyons, P. E.; De, S.; Coleman, J. N.; Boland, J. J. *Nano Lett.* **2009**, *9*, 3890–3895.
- (255) Fuhrer, M. S.; Nygard, J.; Shih, L.; Forero, M.; Yoon, Y. G.; Mazzone, M. S.; Choi, H. J.; Ihm, J.; Louie, S. G.; Zettl, A.; McEuen, P. L. *Science* **2000**, *288*, 494–497.
- (256) Znidarsic, A.; Kaskela, A.; Laiho, P.; Gaberscek, M.; Ohno, Y.; Nasibulin, A. G.; Kauppinen, E. I.; Hassanien, A. *J. Phys. Chem. C* **2013**, *117*, 13324–13330.
- (257) Sano, E.; Tanaka, T. *J. Appl. Phys.* **2014**, *115*, 154507.
- (258) Li, Z.; Ouyang, J.; Ding, J. *ACS Appl. Electron. Mater.* **2022**, *4*, 6335–6344.
- (259) Gao, J.; Loo, Y.-L. *Adv. Funct. Mater.* **2015**, *25*, 105–110.

- (260) Kaiser, A. B.; Skákalová, V. *Chem. Soc. Rev.* **2011**, *40*, 3786–3801.
- (261) Tessler, N.; Preezant, Y.; Rappaport, N.; Roichman, Y. *Adv. Mater.* **2009**, *21*, 2741–2761.
- (262) Itkis, M. E.; Pekker, A.; Tian, X.; Bekyarova, E.; Haddon, R. C. *Acc. Chem. Res.* **2015**, *48*, 2270–2279.
- (263) Luo, S.; Liu, T.; Benjamin, S. M.; Brooks, J. S. *Langmuir* **2013**, *29*, 8694–8702.
- (264) Yanagi, K.; Udoguchi, H.; Sagitani, S.; Oshima, Y.; Takenobu, T.; Kataura, H.; Ishida, T.; Matsuda, K.; Maniwa, Y. *ACS Nano* **2010**, *4*, 4027–4032.
- (265) Gao, W.; Adinehloo, D.; Li, X.; Mojibpour, A.; Yomogida, Y.; Hirano, A.; Tanaka, T.; Kataura, H.; Zheng, M.; Perebeinos, V.; Kono, J. *Carbon* **2021**, *183*, 774–779.
- (266) Brohmann, M.; Berger, F. J.; Matthiesen, M.; Schiefl, S. P.; Schneider, S.; Zaumseil, J. *ACS Nano* **2019**, *13*, 7323–7332.
- (267) Sheng, P. *Phys. Rev. B* **1980**, *21*, 2180–2195.
- (268) Sheng, P.; Sichel, E. K.; Gittleman, J. I. *Phys. Rev. Lett.* **1978**, *40*, 1197–1200.
- (269) Tripathy, S.; Bose, B.; Chakrabarti, P. P.; Bhattacharyya, T. K. *IEEE Trans. Electron Devices* **2020**, *67*, 5676–5684.
- (270) Dash, A.; Scheunemann, D.; Kemerink, M. *Phys. Rev. Applied* **2022**, *18*, 064022.
- (271) Podzorov, V.; Menard, E.; Rogers, J. A.; Gershenson, M. E. *Phys. Rev. Lett.* **2005**, *95*, 226601.
- (272) Kaiser, A. B. *Adv. Mater.* **2001**, *13*, 927–941.
- (273) Zorn, N. F.; Scuratti, F.; Berger, F. J.; Perinot, A.; Heimfarth, D.; Caironi, M.; Zaumseil, J. *ACS Nano* **2020**, *14*, 2412–2423.
- (274) Sirringhaus, H.; Brown, P. J.; Friend, R. H.; Nielsen, M. M.; Bechgaard, K.; Langeveld-Voss, B. M. W.; Spiering, A. J. H.; Janssen, R. A. J.; Meijer, E. W.; Herwig, P.; Leeuw, D. M. d. *Nature* **1999**, *401*, 685–688.
- (275) Pace, G.; Bargigia, I.; Noh, Y.-Y.; Silva, C.; Caironi, M. *Nat. Commun.* **2019**, *10*, 5226.
- (276) Caironi, M.; Bird, M.; Fazzi, D.; Chen, Z.; Di Pietro, R.; Newman, C.; Facchetti, A.; Sirringhaus, H. *Adv. Funct. Mater.* **2011**, *21*, 3371–3381.
- (277) Zhao, N.; Noh, Y.-Y.; Chang, J.-F.; Heeney, M.; McCulloch, I.; Sirringhaus, H. *Adv. Mater.* **2009**, *21*, 3759–3763.
- (278) Sakanoue, T.; Sirringhaus, H. *Nat. Mater.* **2010**, *9*, 736–740.
- (279) Meneau, A. Y. B.; Olivier, Y.; Backlund, T.; James, M.; Breiby, D. W.; Andreasen, J. W.; Sirringhaus, H. *Adv. Funct. Mater.* **2016**, *26*, 2326–2333.
- (280) Sciascia, C.; Martino, N.; Schuettfort, T.; Watts, B.; Grancini, G.; Antognazza, M. R.; Zavelani-Rossi, M.; McNeill, C. R.; Caironi, M. *Adv. Mater.* **2011**, *23*, 5086–5090.
- (281) Jiang, M.; Pecorario, S.; Zorn, N. F.; Zaumseil, J.; Caironi, M. *Adv. Mater. Interfaces* **2023**, DOI: 10.1002/admi.20220245.

- (282) Brohmann, M.; Wieland, S.; Angstenberger, S.; Herrmann, N. J.; Lüttgens, J.; Fazzi, D.; Zaumseil, J. *ACS Appl. Mater. Interfaces* **2020**, *12*, 28392–28403.
- (283) Ferguson, A. J.; Reid, O. G.; Nanayakkara, S. U.; Ihly, R.; Blackburn, J. L. *J. Phys. Chem. Lett.* **2018**, *9*, 6864–6870.
- (284) Park, J.; Reid, O. G.; Blackburn, J. L.; Rumbles, G. *Nat. Commun.* **2015**, *6*, 8809.
- (285) Ferguson, A. J.; Dowgiallo, A.-M.; Bindl, D. J.; Mistry, K. S.; Reid, O. G.; Kopidakis, N.; Arnold, M. S.; Blackburn, J. L. *Phys. Rev. B* **2015**, *91*, 245311.
- (286) Jensen, S. A.; Ulbricht, R.; Narita, A.; Feng, X.; Müllen, K.; Hertel, T.; Turchinovich, D.; Bonn, M. *Nano Lett.* **2013**, *13*, 5925–5930.
- (287) Beard, M. C.; Blackburn, J. L.; Heben, M. J. *Nano Lett.* **2008**, *8*, 4238–4242.
- (288) Maeng, I.; Lim, S.; Chae, S. J.; Lee, Y. H.; Choi, H.; Son, J.-H. *Nano Lett.* **2012**, *12*, 551–555.
- (289) Wang, Z.-Y.; Di Virgilio, L.; Yao, Z.-F.; Yu, Z.-D.; Wang, X.-Y.; Zhou, Y.-Y.; Li, Q.-Y.; Lu, Y.; Zou, L.; Wang, H. I.; Wang, X.-Y.; Wang, J.-Y.; Pei, J. *Angew. Chem. Int. Ed.* **2021**, *60*, 20483–20488.
- (290) Ippolito, S.; Urban, F.; Zheng, W.; Mazzarisi, O.; Valentini, C.; Kelly, A. G.; Gali, S. M.; Bonn, M.; Beljonne, D.; Corberi, F.; Coleman, J. N.; Wang, H. I.; Samori, P. *Adv. Mater.* **2023**, 2211157.
- (291) Taniguchi, T.; Watanabe, K. *J. Cryst. Growth* **2007**, *303*, 525–529.
- (292) De Mello, J. C.; Wittmann, H. F.; Friend, R. H. *Adv. Mater.* **1997**, *9*, 230–232.
- (293) Ahn, T.-S.; Al-Kaysi, R. O.; Müller, A. M.; Wentz, K. M.; Bardeen, C. J. *Rev. Sci. Instrum.* **2007**, *78*, 086105.
- (294) Zheng, W.; Zorn, N. F.; Bonn, M.; Zaumseil, J.; Wang, H. I. *ACS Nano* **2022**, *16*, 9401–9409.
- (295) Dresselhaus, M. S.; Jorio, A.; Hofmann, M.; Dresselhaus, G.; Saito, R. *Nano Lett.* **2010**, *10*, 751–758.
- (296) Grimm, S.; Schiebl, S. P.; Zakharko, Y.; Rother, M.; Brohmann, M.; Zaumseil, J. *Carbon* **2017**, *118*, 261–267.
- (297) Dresselhaus, M. S.; Jorio, A.; Souza Filho, A. G.; Saito, R. *Philos. Trans. Royal Soc.* **2010**, *368*, 5355–5377.
- (298) Zorn, N. F.; Berger, F. J.; Zaumseil, J. *ACS Nano* **2021**, *15*, 10451–10463.
- (299) Schirowski, M.; Hauke, F.; Hirsch, A. *Chem. Eur. J.* **2019**, *25*, 12761–12768.
- (300) Kim, W.; Javey, A.; Vermesh, O.; Wang, Q.; Li, Y.; Dai, H. *Nano Lett.* **2003**, *3*, 193–198.
- (301) Gwinner, M. C.; Kabra, D.; Roberts, M.; Brenner, T. J. K.; Wallikewitz, B. H.; McNeill, C. R.; Friend, R. H.; Sirringhaus, H. *Adv. Mater.* **2012**, *24*, 2728–2734.
- (302) Gaulke, M.; Janissek, A.; Peyyety, N. A.; Alamgir, I.; Riaz, A.; Dehm, S.; Li, H.; Lemmer, U.; Flavel, B. S.; Kappes, M. M.; Hennrich, F.; Wei, L.; Chen, Y.; Pyatkov, F.; Krupke, R. *ACS Nano* **2020**, *14*, 2709–2717.

- (303) Li, M. K.; Riaz, A.; Wederhake, M.; Fink, K.; Saha, A.; Dehm, S.; He, X.; Schöppler, F.; Kappes, M. M.; Htoon, H.; Popov, V. N.; Doorn, S. K.; Hertel, T.; Hennrich, F.; Krupke, R. *ACS Nano* **2022**, *16*, 11742–11754.
- (304) Xu, B.; Wu, X.; Kim, M.; Wang, P.; Wang, Y. *J. Appl. Phys.* **2021**, *129*, 044305.
- (305) Naber, R. C. G.; Bird, M.; Siringhaus, H. *Appl. Phys. Lett.* **2008**, *93*, 023301.
- (306) Shiraki, T.; Shiraishi, T.; Juhász, G.; Nakashima, N. *Sci. Rep.* **2016**, *6*, 28393.
- (307) Zaumseil, J.; Groves, C.; Winfield, J. M.; Greenham, N. C.; Siringhaus, H. *Adv. Funct. Mater.* **2008**, *18*, 3630–3637.
- (308) Held, M.; Zakharko, Y.; Wang, M.; Jakubka, F.; Gannott, F.; Rumer, J. W.; Ashraf, R. S.; McCulloch, I.; Zaumseil, J. *Org. Electron.* **2016**, *32*, 220–227.
- (309) Grimm, S. B.; Jakubka, F.; Schiebl, S. P.; Gannott, F.; Zaumseil, J. *Adv. Mater.* **2014**, *26*, 7986–7992.
- (310) Murawski, C.; Leo, K.; Gather, M. C. *Adv. Mater.* **2013**, *25*, 6801–6827.
- (311) Hartleb, H.; Späth, F.; Hertel, T. *ACS Nano* **2015**, *9*, 10461–10470.
- (312) Eckstein, K. H.; Oberndorfer, F.; Achsnich, M. M.; Schöppler, F.; Hertel, T. *J. Phys. Chem. C* **2019**, *123*, 30001–30006.
- (313) Wang, F.; Dukovic, G.; Knoesel, E.; Brus, L. E.; Heinz, T. F. *Phys. Rev. B* **2004**, *70*, 241403.
- (314) Wang, F.; Wu, Y.; Hybertsen, M. S.; Heinz, T. F. *Phys. Rev. B* **2006**, *73*, 245424.
- (315) Brown, P. J.; Siringhaus, H.; Harrison, M.; Shkunov, M.; Friend, R. H. *Phys. Rev. B* **2001**, *63*, 4108.
- (316) Pesavento, P. V.; Chesterfield, R. J.; Newman, C. R.; Frisbie, C. D. *J. Appl. Phys.* **2004**, *96*, 7312–7324.
- (317) Kalb, W. L.; Batlogg, B. *Phys. Rev. B* **2010**, *81*, 035327.
- (318) Wang, J.; Shea, M. J.; Flach, J. T.; McDonough, T. J.; Way, A. J.; Zanni, M. T.; Arnold, M. S. *J. Phys. Chem. C* **2017**, *121*, 8310–8318.
- (319) Hartmann, M.; Tittmann-Otto, J.; Böttger, S.; Heldt, G.; Claus, M.; Schulz, S. E.; Schröter, M.; Hermann, S. *ACS Appl. Mater. Interfaces* **2020**, *12*, 27461–27466.
- (320) Ulbricht, R.; Hendry, E.; Shan, J.; Heinz, T. F.; Bonn, M. *Rev. Mod. Phys.* **2011**, *83*, 543–586.
- (321) Burdanova, M. G.; Tsapenko, A. P.; Kharlamova, M. V.; Kauppinen, E. I.; Gorshunov, B. P.; Kono, J.; Lloyd-Hughes, J. *Adv. Opt. Mater.* **2021**, 2101042.
- (322) Zheng, W.; Bonn, M.; Wang, H. I. *Nano Lett.* **2020**, *20*, 5807–5813.
- (323) Zhang, H.; Debroye, E.; Zheng, W.; Fu, S.; Virgilio, L. D.; Kumar, P.; Bonn, M.; Wang, H. I. *Sci. Adv.* **2021**, *7*, eabj9066.
- (324) Němec, H.; Kužel, P.; Sundström, V. *J. Photochem. Photobiol. A: Chem.* **2010**, *215*, 123–139.
- (325) Narita, A. et al. *Nat. Chem.* **2014**, *6*, 126–132.
- (326) Dong, R. et al. *Nat. Mater.* **2018**, *17*, 1027–1032.

- (327) Kumamoto, Y.; Yoshida, M.; Ishii, A.; Yokoyama, A.; Shimada, T.; Kato, Y. K. *Phys. Rev. Lett.* **2014**, *112*, 117401.
- (328) Karlsen, P.; Shuba, M. V.; Kuzhir, P. P.; Nasibulin, A. G.; Lamberti, P.; Hendry, E. *Phys. Rev. B* **2018**, *98*, 241404.
- (329) Smith, N. V. *Phys. Rev. B* **2001**, *64*, 155106.
- (330) Cocker, T. L.; Baillie, D.; Buruma, M.; Titova, L. V.; Sydora, R. D.; Marsiglio, F.; Hegmann, F. A. *Phys. Rev. B* **2017**, *96*, 205439.
- (331) Blackburn, J. L. *ACS Energy Lett.* **2017**, *2*, 1598–1613.
- (332) Pfohl, M.; Glaser, K.; Graf, A.; Mertens, A.; Tune, D. D.; Puerckhauer, T.; Alam, A.; Wei, L.; Chen, Y.; Zaumseil, J.; Colsmann, A.; Krupke, R.; Flavel, B. S. *Adv. Energy Mater.* **2016**, *6*, 1600890.
- (333) Bindl, D. J.; Wu, M.-Y.; Prehn, F. C.; Arnold, M. S. *Nano Lett.* **2010**, *11*, 455–460.
- (334) Bindl, D. J.; Ferguson, A. J.; Wu, M.-Y.; Kopidakis, N.; Blackburn, J. L.; Arnold, M. S. *J. Phys. Chem. Lett.* **2013**, *4*, 3550–3559.
- (335) Jain, R. M.; Howden, R.; Tvrdy, K.; Shimizu, S.; Hilmer, A. J.; McNicholas, T. P.; Gleason, K. K.; Strano, M. S. *Adv. Mater.* **2012**, *24*, 4436–4439.
- (336) Bernardi, M.; Lohrman, J.; Kumar, P. V.; Kirkeminde, A.; Ferralis, N.; Grossman, J. C.; Ren, S. *ACS Nano* **2012**, *6*, 8896–8903.
- (337) Bai, Y.; Bullard, G.; Olivier, J.-H.; Therien, M. J. *J. Am. Chem. Soc.* **2018**, *140*, 14619–14626.
- (338) Crochet, J. J.; Hoseinkhani, S.; Lüer, L.; Hertel, T.; Doorn, S. K.; Lanzani, G. *Phys. Rev. Lett.* **2011**, *107*, 257402.
- (339) Santos, S. M.; Yuma, B.; Berciaud, S.; Shaver, J.; Gallart, M.; Gilliot, P.; Cagnet, L.; Lounis, B. *Phys. Rev. Lett.* **2011**, *107*, 187401.
- (340) Yuma, B.; Berciaud, S.; Besbas, J.; Shaver, J.; Santos, S.; Ghosh, S.; Weisman, R. B.; Cagnet, L.; Gallart, M.; Ziegler, M.; Hönerlage, B.; Lounis, B.; Gilliot, P. *Phys. Rev. B* **2013**, *87*, 205412.
- (341) Soavi, G.; Scotognella, F.; Brida, D.; Hefner, T.; Späth, F.; Antognazza, M. R.; Hertel, T.; Lanzani, G.; Cerullo, G. *J. Phys. Chem. C* **2013**, *117*, 10849–10855.
- (342) Xu, X.; Chuang, K.; Nicholas, R. J.; Johnston, M. B.; Herz, L. M. *J. Phys. Chem. C* **2009**, *113*, 18106–18109.
- (343) Luo, L.; Chatzakis, I.; Patz, A.; Wang, J. *Phys. Rev. Lett.* **2015**, *114*, 107402.
- (344) Tries, A.; Osella, S.; Zhang, P.; Xu, F.; Ramanan, C.; Kläui, M.; Mai, Y.; Beljonne, D.; Wang, H. I. *Nano Lett.* **2020**, *20*, 2993–3002.
- (345) Steinhoff, A.; Florian, M.; Rösner, M.; Schönhoff, G.; Wehling, T. O.; Jahnke, F. *Nat. Commun.* **2017**, *8*, 1166.
- (346) D’Innocenzo, V.; Grancini, G.; Alcocer, M. J. P.; Kandada, A. R. S.; Stranks, S. D.; Lee, M. M.; Lanzani, G.; Snaith, H. J.; Petrozza, A. *Nat. Commun.* **2014**, *5*, 3586.

- (347) Kaindl, R. A.; Hägele, D.; Carnahan, M. A.; Chemla, D. S. *Phys. Rev. B* **2009**, *79*, 045320.
- (348) Lloyd-Hughes, J.; Richards, T.; Sirringhaus, H.; Johnston, M. B.; Herz, L. M. *Phys. Rev. B* **2008**, *77*, 125203.
- (349) Streit, J. K.; Bachilo, S. M.; Ghosh, S.; Lin, C.-W.; Weisman, R. B. *Nano Lett.* **2014**, *14*, 1530–1536.
- (350) Hendry, E.; Koeberg, M.; Schins, J. M.; Nienhuys, H. K.; Sundström, V.; Siebbeles, L. D. A.; Bonn, M. *Phys. Rev. B* **2005**, *71*, 125201.
- (351) Zorn, N. F.; Settele, S.; Zhao, S.; Lindenthal, S.; El Yumin, A. A.; Wedl, T.; Li, H.; Flavel, B. S.; Högele, A.; Zaumseil, J. *Adv. Opt. Mater.* **2023**, DOI: 10.1002/adom.202300236.
- (352) Miyauchi, Y. *J. Mater. Chem. C* **2013**, *1*, 6499–6521.
- (353) Lefebvre, J.; Fraser, J. M.; Homma, Y.; Finnie, P. *Appl. Phys. A* **2004**, *78*, 1107–1110.
- (354) Silvera-Batista, C. A.; Wang, R. K.; Weinberg, P.; Ziegler, K. J. *Phys. Chem. Chem. Phys.* **2010**, *12*, 6990–6998.
- (355) Sims, C. M.; Fagan, J. A. *Carbon* **2020**, *165*, 196–203.
- (356) Xie, L.; Liu, C.; Zhang, J.; Zhang, Y.; Jiao, L.; Jiang, L.; Dai, L.; Liu, Z. *J. Am. Chem. Soc.* **2007**, *129*, 12382–12383.
- (357) Lefebvre, J.; Homma, Y.; Finnie, P. *Phys. Rev. Lett.* **2003**, *90*, 217401.
- (358) Moritsubo, S.; Murai, T.; Shimada, T.; Murakami, Y.; Chiashi, S.; Maruyama, S.; Kato, Y. K. *Phys. Rev. Lett.* **2010**, *104*, 247402.
- (359) Walden-Newman, W.; Sarpkaya, I.; Strauf, S. *Nano Lett.* **2012**, *12*, 1934–1941.
- (360) Berger, F. J.; de Sousa, J. A.; Zhao, S.; Zorn, N. F.; El Yumin, A. A.; Quintana Garcia, A.; Settele, S.; Högele, A.; Crivillers, N.; Zaumseil, J. *ACS Nano* **2021**, *15*, 5147–5157.
- (361) Dean, C. R.; Young, A. F.; Meric, I.; Lee, C.; Wang, L.; Sorgenfrei, S.; Watanabe, K.; Taniguchi, T.; Kim, P.; Shepard, K. L.; Hone, J. *Nat. Nanotechnol.* **2010**, *5*, 722–726.
- (362) Ajayi, O. A.; Ardelean, J. V.; Shepard, G. D.; Wang, J.; Antony, A.; Taniguchi, T.; Watanabe, K.; Heinz, T. F.; Strauf, S.; Zhu, X. Y.; Hone, J. C. *2D Mater.* **2017**, *4*, 031011.
- (363) Calman, E. V.; Fogler, M. M.; Butov, L. V.; Hu, S.; Mishchenko, A.; Geim, A. K. *Nat. Commun.* **2018**, *9*, 1895.
- (364) Cadiz, F. et al. *Phys. Rev. X* **2017**, *7*, 021026.
- (365) Ciarrocchi, A.; Unuchek, D.; Avsar, A.; Watanabe, K.; Taniguchi, T.; Kis, A. *Nat. Photonics* **2019**, *13*, 131–136.
- (366) Kalkan, S. B.; Najafidehaghani, E.; Gan, Z. Y.; Drewniok, J.; Lichtenegger, M. F.; Huebner, U.; Urban, A. S.; George, A.; Turchanin, A.; Nickel, B. *Adv. Opt. Mater.* **2023**, *11*, 2201653.

- (367) Zhang, C.; Wang, P.; Barnes, B.; Fortner, J.; Wang, Y. *Chem. Mat.* **2021**, *33*, 4551–4557.
- (368) Mills, M. E.; Townsend, P.; Castillo, D.; Martin, S.; Achen, A. *Microelectron. Eng.* **1997**, *33*, 327–334.
- (369) Larson, B. W.; Thurman, K. A.; Kang, H. S.; Ferguson, A. J.; Blackburn, J. L.; Steger, M. *ACS Appl. Nano Mater.* **2022**, *5*, 3502–3511.
- (370) Zheng, Y.; Bachilo, S. M.; Weisman, R. B. *ACS Nano* **2019**, *13*, 8222–8228.
- (371) Zheng, Y.; Weight, B. M.; Jones, A. C.; Chandrasekaran, V.; Gifford, B. J.; Tretiak, S.; Doorn, S. K.; Htoon, H. *ACS Nano* **2021**, *15*, 923–933.
- (372) Lin, Z.; Beltran, L. C.; De los Santos, Z. A.; Li, Y.; Adel, T.; Fagan, J. A.; Hight Walker, A. R.; Egelman, E. H.; Zheng, M. *Science* **2022**, *377*, 535–539.
- (373) Hofmann, M. S.; Noé, J.; Kneer, A.; Crochet, J. J.; Högele, A. *Nano Lett.* **2016**, *16*, 2958–2962.
- (374) Belotcerkovtceva, D.; Maciel, R. P.; Berggren, E.; Maddu, R.; Sarkar, T.; Kvashnin, Y. O.; Thonig, D.; Lindblad, A.; Eriksson, O.; Kamalakar, M. V. *ACS Appl. Mater. Interfaces* **2022**, *14*, 36209–36216.
- (375) Huang, Z.; Powell, L. R.; Wu, X.; Kim, M.; Qu, H.; Wang, P.; Fortner, J. L.; Xu, B.; Ng, A. L.; Wang, Y. *Adv. Mater.* **2020**, *32*, 1906517.
- (376) Laturia, A.; Van de Put, M. L.; Vandenberghe, W. G. *npj 2D Mater. Appl.* **2018**, *2*, 6.
- (377) Quellmalz, A. et al. *Nat. Commun.* **2021**, *12*, 917.
- (378) Duque, J. G.; Pasquali, M.; Cagnet, L.; Lounis, B. *ACS Nano* **2009**, *3*, 2153–2156.
- (379) Miyauchi, Y.; Matsuda, K.; Kanemitsu, Y. *Phys. Rev. B* **2009**, *80*, 235433.
- (380) Way, A. J.; Jacobberger, R. M.; Guisinger, N. P.; Saraswat, V.; Zheng, X.; Suresh, A.; Dwyer, J. H.; Gopalan, P.; Arnold, M. S. *Nat. Commun.* **2022**, *13*, 2992.
- (381) Di Bartolomeo, A.; Genovese, L.; Giubileo, F.; Iemmo, L.; Luongo, G.; Foller, T.; Schleberger, M. *2D Mater.* **2018**, *5*, 015014.
- (382) Steiner, M.; Freitag, M.; Perebeinos, V.; Naumov, A.; Small, J. P.; Bol, A. A.; Avouris, P. *Nano Lett.* **2009**, *9*, 3477–3481.
- (383) Freitag, M.; Steiner, M.; Naumov, A.; Small, J. P.; Bol, A. A.; Perebeinos, V.; Avouris, P. *ACS Nano* **2009**, *3*, 3744–3748.
- (384) Brozena, A. H.; Leeds, J. D.; Zhang, Y.; Fourkas, J. T.; Wang, Y. *ACS Nano* **2014**, *8*, 4239–4247.
- (385) Tanaka, Y.; Hirana, Y.; Niidome, Y.; Kato, K.; Saito, S.; Nakashima, N. *Angew. Chem. Int. Ed.* **2009**, *48*, 7655–7659.
- (386) Heimfarth, D.; Balcı Leinen, M.; Klein, P.; Allard, S.; Scherf, U.; Zaumseil, J. *ACS Appl. Mater. Interfaces* **2022**, *14*, 8209–8217.

- (387) Khasminskaya, S.; Pyatkov, F.; Słowik, K.; Ferrari, S.; Kahl, O.; Kovalyuk, V.; Rath, P.; Vetter, A.; Hennrich, F.; Kappes, M. M.; Gol'tsman, G.; Korneev, A.; Rockstuhl, C.; Krupke, R.; Pernice, W. H. P. *Nat. Photonics* **2016**, *10*, 727–732.
- (388) Jinkins, K. R.; Foradori, S. M.; Saraswat, V.; Jacobberger, R. M.; Dwyer, J. H.; Gopalan, P.; Berson, A.; Arnold, M. S. *Sci. Adv.* **2021**, *7*, eabh0640.
- (389) Molazemhosseini, A.; Viola, F. A.; Berger, F. J.; Zorn, N. F.; Zaumseil, J.; Caironi, M. *ACS Appl. Electron. Mater.* **2021**, *3*, 3106–3113.
- (390) Balcı Leinen, M.; Lindenthal, S.; Heimfarth, D.; Zaumseil, J. *Nanoscale* **2022**, *14*, 13542–13550.
- (391) Scuratti, F.; Bonacchini, G. E.; Bossio, C.; Salazar-Rios, J. M.; Talsma, W.; Loi, M. A.; Antognazza, M. R.; Caironi, M. *ACS Appl. Mater. Interfaces* **2019**, *11*, 37966–37972.
- (392) Yaari, Z.; Yang, Y.; Apfelbaum, E.; Cupo, C.; Settle, A. H.; Cullen, Q.; Cai, W.; Roche, K. L.; Levine, D. A.; Fleisher, M.; Ramanathan, L.; Zheng, M.; Jagota, A.; Heller, D. A. *Sci. Adv.* **2021**, *7*, eabj0852.
- (393) Filipiak, M. S.; Rother, M.; Andoy, N. M.; Knudsen, A. C.; Grimm, S.; Bachran, C.; Swee, L. K.; Zaumseil, J.; Tarasov, A. *Sens. Actuators B Chem.* **2018**, *255*, 1507–1516.
- (394) Vernick, S.; Trocchia, S. M.; Warren, S. B.; Young, E. F.; Bouilly, D.; Gonzalez, R. L.; Nuckolls, C.; Shepard, K. L. *Nat. Commun.* **2017**, *8*, 15450.
- (395) Mann, F. A.; Herrmann, N.; Opazo, F.; Kruss, S. *Angew. Chem. Int. Ed.* **2020**, *59*, 17732–17738.
- (396) Spreinat, A.; Dohmen, M. M.; Lüttgens, J.; Herrmann, N.; Klepzig, L. F.; Nißler, R.; Weber, S.; Mann, F. A.; Lauth, J.; Kruss, S. *J. Phys. Chem. C* **2021**, *125*, 18341–18351.
- (397) Pyatkov, F.; Fütterling, V.; Khasminskaya, S.; Flavel, B. S.; Hennrich, F.; Kappes, M. M.; Krupke, R.; Pernice, W. H. P. *Nat. Photonics* **2016**, *10*, 420–427.

Eidesstattliche Versicherung gemäß §8 der Promotionsordnung für die Gesamtfakultät für Mathematik, Ingenieur- und Naturwissenschaften der Universität Heidelberg

1. Bei der eingereichten Dissertation zu dem Thema *Charge Transport in and Luminescence from Covalently Functionalized Carbon Nanotube Networks* handelt es sich um meine eigenständig erbrachte Leistung.
2. Ich habe nur die angegebenen Quellen und Hilfsmittel benutzt und mich keiner unzulässigen Hilfe Dritter bedient. Insbesondere habe ich wörtlich oder sinngemäß aus anderen Werken übernommene Inhalte als solche kenntlich gemacht.
3. Die Arbeit oder Teile davon habe ich bislang nicht an einer Hochschule des In- oder Auslands als Bestandteil einer Prüfungs- oder Qualifikationsleistung vorgelegt.
4. Die Richtigkeit der vorstehenden Erklärungen bestätige ich.
5. Die Bedeutung der eidesstattlichen Versicherung und die strafrechtlichen Folgen einer unrichtigen oder unvollständigen eidesstattlichen Versicherung sind mir bekannt.

Ich versichere an Eides statt, dass ich nach bestem Wissen die reine Wahrheit erklärt und nichts verschwiegen habe.

Heidelberg, 30. März 2023

Nicolas Frederic Zorn